UNIVERSITY OF SOUTHAMPTON

FACULTY OF ENGINEERING AND THE ENVIRONMENT

Electro-Mechanical Engineering Research Group

The Influence of Scatter and Beam Hardening in X-ray Computed Tomography for Dimensional Metrology

by

Joseph J Lifton

Thesis for the degree of Doctor of Philosophy

April 2015

UNIVERSITY OF SOUTHAMPTON

ABSTRACT

FACULTY OF ENGINEERING AND THE ENVIRONMENT

Electro-Mechanical Engineering Research Group

Thesis for the degree of Doctor of Philosophy

THE INFLUENCE OF SCATTER AND BEAM HARDENING IN X-RAY COMPUTED TOMOGRAPHY FOR DIMENSIONAL METROLOGY

Joseph John Lifton

This thesis is concerned with the use of X-ray computed tomography (CT) for making dimensional measurements. Scattered radiation and beam hardening are two phenomena that are well-known to severely degrade the quality of cone-beam CT data; however, the impact they have on dimensional measurements is not well understood. The aim of this work is to better understand how scatter and beam hardening influence dimensional measurements.

The influence that scattered radiation and beam hardening have on internal and external dimensional measurements is investigated for two surface determination methods: the ISO50 method and a local gradient-based method. The work includes both experiment and simulation. The influence of scatter is assessed through the use of source collimation and the beam stop array scatter correction method, whilst the influence of beam hardening is assessed using spectrum pre-filtration. The simulation makes use of empirically derived X-ray spectra and scatter signals; good agreement between measured and simulated data is seen.

The results show the presence of scatter and beam hardening decreases the measured size of internal features and increases the measured size of external features. This effect is seen for both surface determination methods, with the local method being more robust for outer features. The ISO50 surface determination method fails to give the ‘correct’ surface position for both inner and outer features in the presence of scatter and/or beam hardening. For the local surface determination method, scatter and beam hardening change the turning point of the edge gradient, this being the property by which surface points are defined for the local method; it is therefore through this change in turning point that scatter and beam hardening influence dimensional measurements.

Table of Contents

List of tables v

List of figures vii

DECLARATION OF AUTHORSHIP xiii

Acknowledgements xv

Chapter 1 Introduction 1

1.1 The Need for Dimensional Measurements 1
1.2 Basic Terms and Concepts in Metrology 2
1.3 Limitations of Tactile and Optical Instruments 3
1.4 X-ray Computed Tomography 6
1.5 X-ray Computed Tomography for Dimensional Metrology 8
1.6 Limitations of X-ray CT for Dimensional Metrology 10
1.7 Aim and Objectives 15
1.8 Structure of the Thesis 15

Chapter 2 X-ray CT for Dimensional Metrology 17

2.1 Basics of X-ray Physics 17
2.1.1 Atomic Structure 17
2.1.2 X-ray Production 18
2.1.3 X-ray Detection 19
2.1.4 X-ray Interactions with Matter 20
2.1.5 Attenuation 23
2.2 Components of a CT System 25
2.2.1 Microfocus X-ray Source 26
2.2.2 Flat Panel X-ray Detector 28
2.2.3 Motion Control 30
2.3 Reconstruction 31
2.3.1 Analytic Reconstruction 32
2.3.2 Iterative Reconstruction 35
2.4 Artefacts 37
2.4.1 Beam Hardening 37
2.4.2 Scatter 44
2.4.3 Feldkamp 48
2.4.4 Geometric Misalignment 49
2.5 Estimating Surfaces from Volumetric Data 51
2.5.1 Gradient-Based Edge Detection (Local Method) 52
2.5.2 Histogram-Based Edge Detection (ISO50 Method) 57
2.5.3 Surface Determination for Dimensional Measurements 59
2.6 Chapter Summery 60

Chapter 3 Reference Workpieces and CT Measurement Strategy.....63

3.1 Review of Existing Reference Workpieces 63
3.2 Reference Workpiece 1: The Ruby Sphere Workpiece 66
3.2.1 Function and Design 66
3.2.2 Reference Dimensions 67
3.2.3 Reference Measurement Strategy.....68
3.2.4 Reference Measurement Uncertainty.....70
3.2.5 CT Measurement Strategy 74
3.3 Reference Workpiece 2: Multi Cross-Section Workpieces 79
3.3.1 Function and Design 79
3.3.2 Reference Dimensions 79
3.3.3 Reference Measurement Strategy.....81
3.3.4 Reference Measurement Uncertainty.....82
3.3.5 CT Measurement Strategy 85
3.4 Reference Workpiece 3: Plastic Brick 87
3.4.1 Function and Design 87
3.4.2 Reference Dimensions 88
3.4.3 CT Measurement Strategy 90
3.5 Chapter Summary 92

Chapter 4 Voxel Size Determination 93

4.1 Geometric Magnification and Voxel Size.....93
4.2 Estimating the SDD and Mag Axis Offset 95
4.2.1 Method 95
4.2.2 Results.....98
4.3 Voxel Size Correction 99
4.3.1 CT Scans 100
4.3.2 Method 101
4.3.3 Results.....102
4.4 Chapter Summary 104

Chapter 5 Experimental Studies on Scatter and Beam Hardening.....105

5.1 Attenuation Measurements 105
5.1.1 Method 106
5.1.2 Results.....108
5.2 Scans with Collimation and Pre-Filtration.....110
5.2.1 Estimating Scatter Signals 110
5.2.2 Comparing CT Images 112
5.3 Dimensional Measurements with Collimation and Pre-Filtration 118
5.3.1 Method 119
5.3.2 Results.....119
5.4 Beam Stop Array Scatter Correction 121

5.4.1 Beam Stop Array Method 121
5.4.2 Veiling Glare PSF Theory 124
5.4.3 Veiling Glare PSF Measurements 126
5.4.4 Veiling Glare PSF Estimate 126
5.4.5 Implementing the Beam Stop Array Method 129
5.4.6 Scatter Correction Results 131
5.5 Dimensional Measurements with Scatter Correction and Pre-Filtration 136
5.5.1 Method 136
5.5.2 Results 137
5.6 Chapter Summary 140
Chapter 6 Simulation Studies on Scatter and Beam Hardening 141
6.1 Overview of the Simulation Tool 142
6.1.1 Ray Tracing 143
6.1.2 X-ray Source and Detector Energy Dependence 145
6.1.3 Scatter 150
6.1.4 Noise 151
6.1.5 Simulation Validation 152
6.2 The Influence of Beam Hardening on Dimensional Measurements 153
6.2.1 Method 153
6.2.2 Results 156
6.2.3 The Influence of Beam Hardening for the ISO50 Method 162
6.2.4 The Influence of Beam Hardening for the Local Method 164
6.3 The Influence of Scatter on Dimensional Measurements 167
6.3.1 Method 167
6.3.2 Results 167
6.3.3 The Influence of Scatter for the ISO50 Method 170
6.3.4 The Influence of Scatter for the Local Method 171
6.4 Chapter Summary 172
Chapter 7 Measurement Uncertainty due to Surface Determination . 175
7.1 Basic Concept 175
7.2 Estimating the Uncertainty of Surface Points 176
7.3 Edge Model 177
7.4 Monte Carlo Simulation 179
7.5 Monte Carlo Simulation Results 180
7.6 Uncertainty due to Surface Determination 183
7.7 Method Verification 185
7.8 Evaluation on Measured Data 186
7.9 Chapter Discussion 189

Chapter 8 Summary, Conclusions and Future Work 191

List of References 197

List of tables

Table 1.1 Simplified classification of factors that influence dimensional measurements. 11
Table 3.1 Overview of reference dimensions for the ruby sphere workpiece. 67
Table 3.2 Reference measurement results for the ruby sphere workpiece. 73
Table 3.3 YXLON Y.FOX X-ray CT system specification. 75
Table 3.4 CT acquisition settings for the ruby sphere workpiece 77
Table 3.5 Reconstruction settings for the ruby sphere workpiece. 77
Table 3.6 Overview of reference dimensions for the multi cross-section workpiece. 80
Table 3.7 Datum definition of the multi cross-section workpieces 82
Table 3.8 Reference measurement results for titanium and aluminium multi cross-section workpiece. 84
Table 3.9 CT acquisition settings for the multi cross-section workpieces. 86
Table 3.10 Reconstruction settings for the multi cross-section workpieces. 86
Table 3.11 Overview of reference dimensions for the plastic brick. 88
Table 3.12 Reference measurement results for the plastic brick [146]. 89
Table 3.13 CT acquisition settings for the plastic brick. 91
Table 3.14 Reconstruction settings for the plastic brick. 91
Table 3.15 Datum definition of the plastic brick. 92
Table 5.1 X-ray source settings for attenuation measurements using step wedges. 107
Table 5.2 X-ray source settings for scans with and without the BSA and source pre-filtration. 131
Table 7.1 Monte Carlo edge parameters for inner feature of measured data. 187
Table 7.2 Monte Carlo edge parameters for outer features of measured data. 187

List of figures

Figure 1.1 (a) The effect of using a stylus with a spherical tip. (b) Example of a stylus tip measuring a re-entrant feature. Figures taken from [14]. 4
Figure 1.2 Illustration of projection acquisition for a cone-beam (top) and fan-beam CT system (mid), alongside subsequent reconstruction and visualisation of CT images and a CT volume (bottom). 7
Figure 1.3 Workflow for a CT-based dimensional measurement. 9
Figure 1.4 Demonstration of scatter and beam hardening artefacts for simulated CT data of an aluminium object approximately 40 mm in diameter. Scatter and beam hardening cause streaks, raised intensity values at outer edges and a general loss of image contrast. Colour bars represent the range of grey values in each CT image. 13
Figure 2.1 Graph showing the difference in photon energy distribution of characteristic X-rays and bremsstrahlung. Plot generated using SpekCalc [64] for a tungsten target and an acceleration voltage of 100 kV. 19
Figure 2.2 Illustration of electronic band structure for scintillator materials, adapted from [65]. 20
Figure 2.3 Graph showing the probability of each X-ray-matter interaction occurring for aluminium, for photon energies from 1 keV to 1 MeV. 21
Figure 2.4 Graph showing the probability of a photon scattering at a given angle by a single electron. Probability in units of $r_e^2 \approx 7.94 \times 10^{-26}$ cm^2. 23
Figure 2.5 Setup for measuring X-ray transmission, with and without source collimation [65]. 25
Figure 2.6 Diagram of a microfocus X-ray source. Three different target types are shown. 27
Figure 2.7 Operating principle of an indirect TFT detector using a structured CsI scintillator. 28
Figure 2.8 Illustration of an array of detector elements alongside read-out and digitisation electronics, adapted from [76]. 29
Figure 2.9 Environmental scanning electron micrograph of the surface of a CsI scintillator with micro structured columns. Scale bar = 50 μm. Image taken from [77] 29
Figure 2.10 Illustration of the motion stages of a typical, circular trajectory, industrial CT system. 31
Figure 2.11 Illustration of the Fourier slice theorem for a single parallel projection [59]. 32
Figure 2.12 Sampling pattern in the Fourier domain for the Fouier slice theorem [59]. 33
Figure 2.13 Illustration of backprojection. Projection values are added to the image along ray paths for all angular positions. 34
Figure 2.14 Ramp filter with a lower intensity at low spatial frequencies and a higher intensity at high spatial frequencies to weight projections prior to backprojection. 35
Figure 2.15 Graphs showing how an X-ray spectrum changes after penetrating different thicknesses of material. The y-axis of each plot changes to highlight the different energy distributions. The total number of photons will reduce as material thickness increases. 38
Figure 2.16 Graph showing the nonlinear relationship between scatter free polychromatic attenuation and material thickness for aluminium. Also

shown is the linear relationship between monochromatic attenuation and material thickness 39
Figure 2.17 Comparison of line profiles drawn across CT images of an aluminium sphere. Both pre-filtration and beam hardening correction remove the cupping artefact. 40
Figure 2.18 Streaking artefact induced by beam hardening between two copper rods. Figure taken from [87]. 41
Figure 2.19 Illustration of an anti-scatter grid, adapted from Schorner [57]. 46
Figure 2.20 Leftmost: test object for demonstrating Feldkamp artefacts. From left to right: CT data acquired with a cone angle of 30, 11 and 5°. Images taken from QRM GmbH [112]. 48
Figure 2.21 Illustration of helical scan trajectory. This trajectory requires both translation and rotation. 49
Figure 2.22 Top: CT image reconstructed with correct alignment. Bottom: CT image reconstructed with incorrect alignment of CT hardware. Taken from Yang et al. [117]. 50
Figure 2.23 Illustration of cone-beam CT geometry. The six misalignment parameters are $\Delta x, \Delta y, \Delta z, \alpha, \beta, \eta$. 51
Figure 2.24 Gradient-based approach for detecting sub-pixel edge position. The top two images show the true position of the edge and its discrete representation. The bottom two images show the intensity profile and its first derivative. Figure adapted from [118]. 53
Figure 2.25 Vector representation of 2D and 3D gradient components, resultant gradient magnitued and gradient direction. 53
Figure 2.26 Illustration of non-maximum suppression and sup-pixel refinement for a 2D image. 54
Figure 2.27 Step by step processing of the local surface determination method used throughout this work. 56
Figure 2.28 Illustration of an ideal grey value histogram of an image/volume composed of two grey value classes; background and material. The data can be segmented based on an isovalue. 57
Figure 2.29 Illustration of sub-pixel refinement of the ISO50 method. 58
Figure 2.30 Step by step processing of the ISO50 surface determination method used throughout this work. 59
Figure 3.1 A selection of existing CT reference workpieces 65
Figure 3.2 Photograph of the ruby sphere workpiece, ruler for scale. 66
Figure 3.3 Overview of reference geometries for the ruby sphere workpiece, all dimensions in mm. 67
Figure 3.4 The ruby sphere workpiece being measured with a CMM. 69
Figure 3.5 Probing strategy for ruby spheres. Dashed lines represent probe trajectory. 69
Figure 3.6 Magnitude of uncertainty components for calculating the uncertainty of D14 73
Figure 3.7 Internal layout of the YXLON Y.FOX CT system. 75
Figure 3.8 CT measurement setup for the ruby sphere workpiece. 76
Figure 3.9 Data evaluation for the ruby sphere workpiece. 78
Figure 3.10 Photograph of the multi cross-section workpieces, ruler for scale. 79
Figure 3.11 Measurement details for the multi cross-section workpiece. All dimensions in mm. 80
Figure 3.12 Measurement setup of multi cross-section workpiece on the CMM. ... 81
Figure 3.13 Datum definition of the multi cross-section workpieces. 81
Figure 3.14 Calibrated standard used to evaluate the measurement uncertainty for the multi cross-section workpieces. 82
Figure 3.15 Uncertainty components for calculating the uncertainty of OD1. 85

Figure 3.16 CT measurement setup for the multi cross section workpiece. 85
Figure 3.17 Volume rendering of the multi cross-section workpiece. 86
Figure 3.18 Cross-sections of the aluminium multi cross-section workpiece evaluated using GOM inspect. 87
Figure 3.19 Photograph of the plastic brick, ruler for scale. 88
Figure 3.20 Reference dimensions for the plastic brick [146]. 89
Figure 3.21 CT measurement setup for the plastic brick. 90
Figure 3.22 Volume rendering of the plastic brick. 91
Figure 4.1 Idealised geometry of a CT system on the central plane. 94
Figure 4.2 Projections and magnification details for scans of the ruby sphere workpiece. 97
Figure 4.3 Plot of ziverses 1/mag. Mag values are derived in the image using the ruby sphere workpiece, and zi is the mag axis encoder position. 98
Figure 4.4 Residual error of ruby sphere workpiece measurements when scanned over a range of magnifications 99
Figure 4.5 Projections of the plastic brick workpiece in three different orientations alongside the ruby sphere workpiece for voxel size correction. 100
Figure 4.6 Plot of CT versus CMM measurements of the ruby sphere workpiece. Gradient of the best-fit line is the voxel size correction δ. 101
Figure 4.7 Measurement error for L1 of the plastic brick workpiece. Comparison between a global approach to correcting errors in magnification and a one-time correction. 103
Figure 4.8 Measurement error D1 of the plastic brick workpiece. Comparison between a global approach to correcting errors in magnification and a one-time correction. 103
Figure 5.1 Titanium (left) and aluminium (right) step wedges, step increment is 1 mm. 107
Figure 5.2 Copper collimator with 300 µm slit. 108
Figure 5.3 Bright field image with source collimation. 108
Figure 5.4 Attenuation versus thickness graph for aluminium, with and without pre-filtration and collimation. 109
Figure 5.5 Attenuation versus thickness graph for titanium, with and without pre-filtration and collimation. 110
Figure 5.6 Open field projection of the aluminium multi cross-section workpiece. Red line corresponds to line profile in Figure 5.8. 111
Figure 5.7 Collimated projection of the aluminium multi cross-section workpiece. Red line corresponds to line profile in Figure 5.8. 111
Figure 5.8 Line profiles across projections of the aluminium multi cross-section workpiece with and without collimation. Difference in edge ‘sharpness’ highlighted. 112
Figure 5.9 Comparison of CT images of the aluminium multi cross-section workpiece acquired with and without collimation and pre-filtration. Red lines correspond to line profiles in Figure 5.11 113
Figure 5.10 Comparison of CT images of the titanium multi cross-section workpiece acquired with and without collimation and pre-filtration. Red lines correspond to line profiles in Figure 5.12. 114
Figure 5.11 Comparison of line profiles form Figure 5.9. Line profiles drawn across the aluminium cylinder wall. 115
Figure 5.12 Comparison of line profiles from Figure 5.10. Line profiles drawn across titanium cylinder wall. 115
Figure 5.13 Grey value histograms of the aluminium CT images in Figure 5.9. 117
Figure 5.14 Grey value histograms of the titanium CT images in Figure 5.10. 118

Figure 5.15 Influence of scatter and beam hardening on internal radius measurements of the aluminium multi cross-section workpiece. Error bars represent range of 3 repeats. 120
Figure 5.16 Influence of scatter and beam hardening on external radius measurements of the aluminium multi cross-section workpiece. Error bars represent range of 3 repeats. 121
Figure 5.17 Illustration of the BSA method for directly measuring scatter. Figure adapted from Schorner et al. [57]. 122
Figure 5.18 Illustration showing how veiling glare can raise intensity values in the shadows of beam stops. 123
Figure 5.19 Contrast ratio versus lead disk radius; best fit line gives veiling glare PSF model parameters. 127
Figure 5.20 Spatial extent of veiling glare PSF. 127
Figure 5.21 Inverse frequency filter to remove veiling glare from intensity measurements. 127
Figure 5.22 Intensity profiles from lead disk images before (black line) and after (grey line) veiling glare correction. 128
Figure 5.23 Array of lead cylinders 1 mm in diameter, 3 mm in depth, mounted in an acrylic plate, termed a beam stop array (BSA). 130
Figure 5.24 BSA positioned between the X-ray source and object on an acrylic mounting table. 130
Figure 5.25 Projection of multi cross-section workpiece with BSA. 130
Figure 5.26 Scatter estimate from BSA scatter correction method. 130
Figure 5.27 Comparison between scatter estimated using collimation and BSA method. 131
Figure 5.28 Comparison of line profiles drawn across cylinder wall of CT images in Figure 5.29 and Figure 5.30. 132
Figure 5.29 Comparison of scatter contaminated CT images with and without pre-filtration. Red lines correspond to line profiles in Figure 5.28. 133
Figure 5.30 Comparison of scatter corrected CT images with and without pre-filtration. Red lines correspond to line profiles in Figure 5.28. 134
Figure 5.31 Comparison of histograms evaluated from CT volumes with and without pre-filtration and scatter correction. 135
Figure 5.32 Surfaces of the multi cross-section workpiece as evaluated in GOM Inspect. 137
Figure 5.33 Radius measurement error for internal features of the multi cross-section workpiece. 139
Figure 5.34 Radius measurement error for outer features of the multi cross-section workpiece. 139
Figure 6.1 Illustration of ray-tracing for calculating X-ray path lengths through each workpiece cross-section. 144
Figure 6.2 Illustration of the finite size of the X-ray source and detector pixels. Rays are traced from multiple point sources whilst point detectors are down-sampled. 144
Figure 6.3 Validation of method for estimating $W(E)$. Graph shows a comparison between the actual spectrum, the estimated spectrum and the initial guess. 147
Figure 6.4 Comparison of actual transmission values and those calculated with the estimated spectrum in Figure 6.3. 148
Figure 6.5 Convergence of spectrum estimate, based on the sum of the absolute difference between actual and estimated transmission values in Figure 6.4. 148
Figure 6.6 Estimate of the energy dependence $W(E)$ of the CT system used in this work. 149

Figure 6.7 Comparison between measured and simulated X-ray transmission for aluminium, titanium and steel. 150
Figure 6.8 Comparison of simulated intensity values with and without scatter. 151
Figure 6.9 Derivation of noise model parameters based on intensity measurements from Section 5.1. 152
Figure 6.10 Comparison of line profiles drawn across cylinder wall of CT images reconstructed from measured and simulated data. 153
Figure 6.11 Polychromatic and monochromatic attenuation versus material thickness for aluminium. 155
Figure 6.12 Function for correcting polychromatic to monochromatic attenuation for aluminium (beam hardening correction curve) approximated by a 6^{th} order polynomial. 155
Figure 6.13 CT images reconstructed from simulated data with varying degrees of beam hardening. Red lines correspond to the position of line profiles in Figure 6.14. 157
Figure 6.14 Line profiles across CT images of the OCIC cross-section reconstructed from noiseless data with varying degrees of beam hardening. 158
Figure 6.15 Comparison of radius measurement error for the OCIC cross-section. Error bars represent the range of the three repeats 159
Figure 6.16 Comparison of radius measurement error for the OCIC cross-section simulated and reconstructed at three different pixel sizes: low-resolution (LR), medium-resolution (MR) and high-resolution (HR). Respective detector pixel sizes are 254, 127 and 63 μm. Respective CT image pixel sizes are 98, 49 and 24.5 μm. 160
Figure 6.17 Comparison of radius measurement error for the OCIC cross-section in aluminium and titanium. 161
Figure 6.18 Comparison of inner & outer radius measurement error for various threshold values for BH corrected data and polychromatic data. Experiment replicated from Carmignato et al. [46]. 163
Figure 6.19 Comparison of inner and outer ERFs for polychromatic and monochromatic data. 164
Figure 6.20 Comparison of ERFs for inner and outer edges of data with various degrees of beam hardening 165
Figure 6.21 Comparison of LSFs for inner and outer edges of data with various degrees of beam hardening. The shift in the LSF turning point influences dimensional measurements. 166
Figure 6.22 Inner and outer dimensions act in opposition because their edges have opposing grey value gradient directions. Illustration of an object with internal and external edges, arrows represent the grey value gradient direction. Figure inspired by Nixon et al. [124]. 167
Figure 6.23 CT images reconstructed from simulated scatter-corrupted data 168
Figure 6.24 Line profiles across CT images reconstructed from simulated data. . 168
Figure 6.25 Influence of scatter and beam hardening on measurements of the inner and outer features of the OCIC cross-section. 169
Figure 6.26 Comparison of inner and outer ERFs in the presence and absence of scatter 170
Figure 6.27 Comparison of ERFs for inner and outer edges evaluated from data with and without scatter and beam hardening. 171
Figure 6.28 Comparison of LSFs for inner and outer edges evaluated from data with and without scatter contamination. Notice scatter and beam hardening cause the turning points of the LSFs to shift. 172
Figure 7.1 Illustration of the measurement uncertainty due to surface determination. 176

Figure 7.2 Magnified edge from a measured CT image. The edge is not a step edge but is blurred across several pixels. 178
Figure 7.3 Rockett's step edge model [120]. 178
Figure 7.4 Flow chart showing each step in the Monte Carlo simulation for estimating the uncertainty of an edge's position. 179
Figure 7.5 Input and output of the Monte Carlo simulation for estimating the uncertainty of an edge's position. 180
Figure 7.6 Graphs showing how the edge's positional error varies as a function of edge displacement t and edge orientation θ in the absence (a) and presence (b) of noise. 181
Figure 7.7 (a) Graph showing how the standard deviation of the xy edge coordinates vary with t and θ. (b) Maximum envelope of (a). 183
Figure 7.8 Radius distribution based on the output of the second Monte Carlo simulation. Standard deviation is 0.007 pixels which corresponds to 0.343 μm for a 49 μm pixel size. 184
Figure 7.9 Comparison of measurement uncertainty due to surface determination estimated from repeated simulations and the proposed model. 186
Figure 7.10 Measurement uncertainty due to surface determination for measured data, estimated using proposed model. 187

DECLARATION OF AUTHORSHIP

I, Joseph Lifton, declare that this thesis entitled The Influence of Scatter and Beam Hardening in X-ray Computed Tomography for Dimensional Metrology and the work presented in it are my own and has been generated by me as the result of my own original research. I confirm that:

1. This work was done wholly or mainly while in candidature for a research degree at this University;
2. Where any part of this thesis has previously been submitted for a degree or any other qualification at this University or any other institution, this has been clearly stated;
3. Where I have consulted the published work of others, this is always clearly attributed;
4. Where I have quoted from the work of others, the source is always given. With the exception of such quotations, this thesis is entirely my own work;
5. I have acknowledged all main sources of help;
6. Where the thesis is based on work done by myself jointly with others, I have made clear exactly what was done by others and what I have contributed myself;
7. Parts of this work have been published as:

   J. J. Lifton, A. A. Malcolm, J. W. McBride, A Simulation-Based Study on the Influence of Beam Hardening in X-ray Computed Tomography for Dimensional Metrology, Journal of X-ray Science and Technology, 23(1), 65-82, 2015.

   J. J. Lifton, A. A. Malcolm, J. W. McBride, On the Uncertainty of Surface Determination in X-ray Computed Tomography for Dimensional Metrology, Measurement Science and Technology, 26(3), 035003, 2015.

Signed:.....

Date:.....

Acknowledgements

Having spent the first year of this project at the University of Southampton, followed by two years at the Singapore Institute of Manufacturing Technology (SIMTech), I have been fortunate enough to meet a number of truly wonderful people, and visited parts of the world that I may not have otherwise seen. The past three years have been a most excellent adventure.

I would like to thank my supervisor John McBride for his support throughout this work, Andy Malcolm for providing day to day supervision in Singapore, Kevin Cross who provided supervision during the first year of this work, and Thomas Blumensath who provided supervision towards the end of this work. I would also like to thank the μ-vis team at the University of Southampton, namely Ian Sinclair, Mark Mavrogordato, Richard Boardman and Dmitry Grinev.

I would like to thank the Precision Measurements Group at SIMTech. Particular thanks go to Liu Yuchan and Kok Shaw Wei for their help with the CMM, Liu Tong for being a wonderful critic of this work and Ha Thi Mai Hoa for useful discussions on Monte Carlo simulations and spectrum measurements. I would also like to thank my fellow students at SIMTech for being so welcoming and for making my time in Singapore one that I shall never forget.

I would like to thank my parents for their endless support and for providing me with such a great start in life. Final thanks go to my brothers, for not really knowing where or what I'm doing; I love you all.

Chapter 1 Introduction

1.1 The Need for Dimensional Measurements

Metrology is the science of measurement and its application [1], whilst dimensional metrology is concerned with the measurement of an object's geometric features, such as size, distance, angle and form [2]. Dimensional metrology plays a central role in manufacturing industries for the purpose of quality assurance, interchangeability of components and controlling manufacturing processes.

When manufacturing a component, measurements are made to check the component is manufactured within the dimensional tolerances specified by the designer. This ensures the component is able to fulfil its intended function, and demonstrates to a customer they receive the component they contracted for.

Measurements are also made to monitor and control manufacturing processes. Consider a turned component: a drift in the size of the component may identify the wear of the cutting tool. By monitoring the manufacturing process corrective action can be taken before the component's dimensions exceed the allowable tolerance [2].

It is often the case that the dimensions of a component dictate its functional performance. For example, the optical power of a lens is controlled by the radius of the surface [3], the shape of a turbine blade dictates its aerodynamic properties and centre of mass [4], and the surface texture of a cylinder bore influences the fuel efficiency and power of a combustion engine [5]. It is clear that in order to control the function of a component, the manufacturing process must be controlled, which in turn requires measurement.

Dimensional measurement is not only of significance to manufacturing industries, but plays an important role in many aspects of scientific research. In science, measurements are made to enhance understanding. For example, one may wish to understand how the size and position of pores in a metallic casting influence its fatigue behaviour [6], or to understand how the complex structure of shark's skin reduces drag allowing it to swim more efficiently [7].

Clearly dimensional metrology has been, and will continue to be fundamental in all aspects of technological innovation and scientific development.

1.2 Basic Terms and Concepts in Metrology

In order to ensure an instrument is able to make accurate measurements, it is often checked or calibrated against a more accurate instrument, or a reference standard. Take for example a micrometer; the length measurement of a micrometer can be compared against a gauge block. Suppose the gauge block has been measured using a laser interferometer; if the laser of the interferometer has been calibrated against the iodine-stabilised laser that realises the definition of the metre then an unbroken chain of comparisons has been ensured ending in the definition of the metre, thus the measurements of the micrometer can be claimed to be accurate. This chain of unbroken comparisons is termed traceability and is one of the most fundamental concepts in metrology, its formal definition can be found in the International Vocabulary of Metrology (VIM) [1].

Traceability ensures measurements are consistent within a company and around the world. If individual components of a product are manufactured in different countries, it is crucial that measurements are traceable such that the components can be assembled to form the final product.

All real world measurements are subject to some degree of imperfection, thus a measurement result is not complete unless accompanied by a statement of uncertainty, where a statement of uncertainty describes quantitatively the imperfection of the measurement result. It therefore follows that a statement of uncertainty is required in order to meaningfully compare any two measurement results, and is thus inseparable from traceability [8].

The definitive text on uncertainty evaluation is the Guide to the Expression of Uncertainty in Measurement (GUM) [9]. To evaluate the measurement uncertainty the measurand, Y, is considered a function of several input quantities, X_i, such that:

$$Y = f(X_1, X_2, \dots, X_n). \tag{1.1}$$

The input quantities include all factors that can influence the measurement. These include effects associated with the measurement instrument, the object being measured, the measurement process, and ‘imported’ effects such as data from calibration certificates and handbooks. The combined standard uncertainty of the measurement result is calculated by propagating the estimated standard uncertainty of each input quantity. The combined standard uncertainty is then multiplied by a

coverage factor, k, for a specified confidence probability [10]. Implementations of this approach are given in Sections 3.2.4 and 3.3.4.

The vocabulary used in the field of metrology is defined in the VIM [1], key terms used throughout this work are defined here for those who may be unaware of their correct definition. Accuracy is a qualitative term indicating how well a measurement result agrees with the true value. The precision of a measurement is the dispersion of measurement results when making repeated measurements under specified measurement conditions. The error of a measurement is the difference between the measured value and the value of a reference standard. Calibration is the comparison of an instrument against a more accurate instrument, or a reference standard, to find and correct any errors in its measurement result. For completeness, the metre is defined as the length of the path travelled by light in a vacuum in a time interval of $1/c$ of a second, where c is the speed of light which is 299 792 458 $m \cdot s^{-1}$.

1.3 Limitations of Tactile and Optical Instruments

Measurements are required over many length-scales: from the nanometre measurements required for micro-electro-mechanical systems (MEMS), to measurements over tens of metres required for the blades of a wind turbine. Obviously no single instrument can cater for all length scales, but rather, different measurement techniques are available for different measurement needs, each with associated advantages and disadvantages. The techniques described in this section are broadly classified as tactile and optical.

Tactile instruments use a probe to touch the surface of an object. An object's geometric features can be resolved by probing the surface and recording the coordinates of each probing point [11]. The probe may be dragged across the object's surface, as per a surface profilometer, whereby a transducer converts the probes height displacement into an electrical signal [12]. Such instruments are used to measure small scale surface features such as surface roughness [13]. The limitations of tactile surface profilers include long acquisition times due to surfaces being measured on a line-by-line basis. Due to the finite radius of the probe tip, sharp peaks of a profile become rounded and the depth of the profile valleys are reduced [14], which can influence surface parameters evaluated from the surface measurement [15], see Figure 1.1(a). The force exerted on the surface by the stylus tip can also influence a measurement result; if too high, the surface may be damaged, if too low, the measurement speed must be

reduced to avoid ‘stylus flight’ [8]. The cone angle of the probe tip limits the maximum surface slope that can be measured [14], and because the stylus detects the surface profile by moving down, it cannot detect re-entrant features, as shown in Figure 1.1(b).

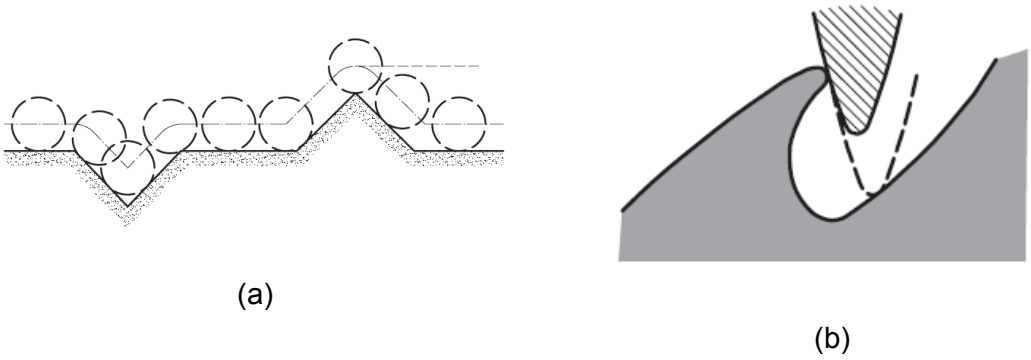

(a) (b)

Figure 1.1 (a) The effect of using a stylus with a spherical tip. (b) Example of a stylus tip measuring a re-entrant feature. Figures taken from [14].

Single coordinate points may be recorded by bringing a touch-trigger probe in contact with an object’s surface, as the probe touches the surface it deflects and triggers the xyz coordinate information to be recorded, as per a coordinate measuring machine (CMM) [10]. Note that CMMs can acquire data in a scanning fashion also [16]. Such instruments are used to measure the geometric form of larger scale objects such as components from the automotive, aerospace and shipping industries [2]. CMMs have proved very popular for the measurement of complex components with multiple features such as engine blocks; this is in part due to the significant reduction in measurement times compared to manual processes. CMMs range in size from small machines with a measurement volume of 300 mm^3 cube, to huge machines that may be 20 m or more along the main axis of the machine [2]. Driven by decreasing product sizes and tighter tolerances, micro-coordinate measuring machines have been developed in recent years [17]. Such instruments typically have ranges of tens of millimetres, and accuracies of tens of nanometres in the x, y and z directions [8]. One major limitation of micro-coordinate measuring machines is the miniaturisation of probe heads [11]. Not only are probe tips likely to plastically deform the workpiece, but micro-scale probes may adhere to an object’s surface due to surface interaction forces such as electrostatic, liquid film and van der Waals forces [18] [8].

The non-contact measurements possible with optical instruments overcome issues of object deformation posed by tactile methods, and can therefore be used to measure soft or deformable objects. The non-contact approach can also lead to much faster

measurement times than tactile methods. Optical instruments may be based on interferometry [19], focus variation [20], confocal microscopy [21], laser triangulation [22] or structured light [23] to name, but a few. Generally speaking, optical methods use properties of light reflected from an object's surface to measure surface height or position; a detailed description of different optical measurement techniques can be found in refs [8], [15], [24]. The interaction of light with a surface is much more complicated than that of a stylus tip; as such, more care must be taken when interpreting data from an optical measurement [8]. Optical instruments are affected to varying degrees by surface reflectivity and surface contamination, such as dust, water and oil [25]. As for tactile profilometers, the ability of an optical instrument to measure sloped surfaces is limited; for steeply sloped features the reflected light may miss the objective lens leading to missing data or spurious results [21].

Modern manufacturing techniques enable the fabrication of components with ever increasing dimensional complexity; as such, new measurement techniques are required [3]. This is especially true for complex cast components, injection moulded components, assembled parts and components fabricated using additive manufacturing techniques [26]. Such components often have internal structures that simply cannot be accessed using tactile or optical techniques unless the component is cut open, termed destructive inspection. Cast components often have internal cavities that require dimensional measurement [27]; examples include wall thickness measurements of turbine blades [26] and the measurement of internal channels of cylinder heads [28]. Machined parts may have small, long, intersecting internal channels, or re-entrant cavities that required dimensional measurement, such as the hydraulic manifold of a race car [26]. Additive manufacturing enables the fabrication of parts with internal cavities, such as thin lattice structures for lightweight aerospace structures, and porous medical scaffolds for bone regeneration [29]. Assembled components may also require measurement or inspection, this is to ensure individual components fit together such that the product functions as intended [26]. All these types of components and structures are inherently difficult to measure using conventional tactile and optical instruments due to their limited measuring ranges and the accessibility of features. There is a clear need to be able to perform internal metrology. One promising measurement technique that is able to measure both internal structures and external structures, non-destructively, in a single scan, is X-ray computed tomography (CT).

1.4 X-ray Computed Tomography

Rather than probing an object's surface or reflecting light from it, X-ray CT measures through an object, revealing both its internal and external structure. By acquiring X-ray transmission images of an object from different angular positions, cross-sectional images of the object can be calculated using a numerical algorithm. These cross-sectional images reveal an object's internal structure, just as if it had been cut, or sliced open as per destructive inspection. The word 'tomography' is derived from the Greek words 'tomos' meaning slice or section and 'graphy' meaning writing or recording.

Referring to Figure 1.2, the X-ray CT measurement process can be summarised as follows: an X-ray source emits a cone or fan beam of X-rays that are attenuated as they propagate through an object. X-rays that fully penetrate the object fall incident on a detector, the output of which is a transmission image, termed a projection. Projections are made for multiple angular positions of the object, based on these projections, cross-sectional images of the object are calculated. The cross-sectional images, termed CT images, describe the material distribution of the object in the considered plane. The process of calculating CT images from projections is termed reconstruction. Individual CT images can be visualised as grey value images, alternatively, multiple CT images can be "stacked", thus forming a CT volume, in which three-dimensional pixels are termed voxels. A much more detailed description of CT is given in the next chapter.

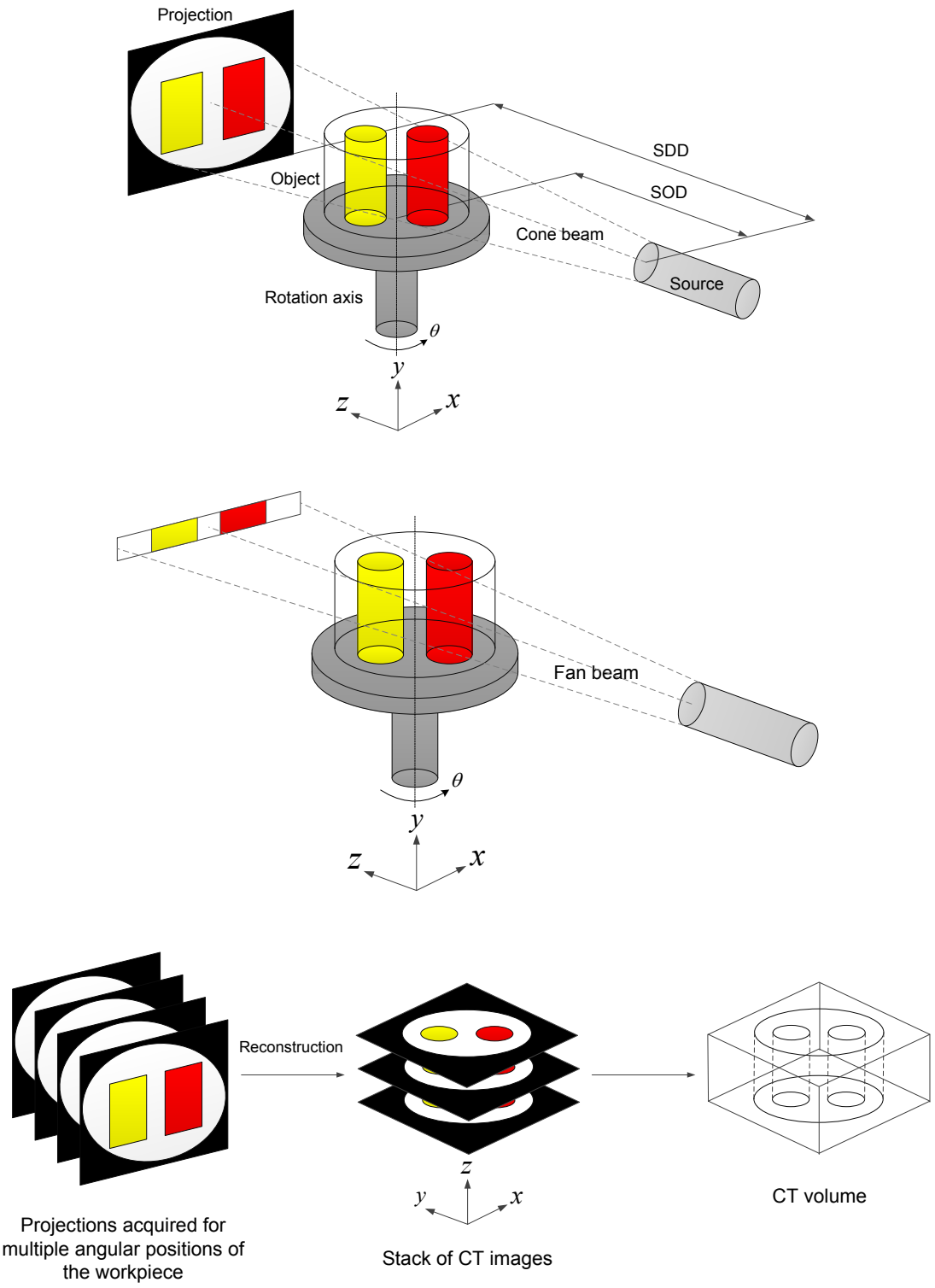

Figure 1.2 Illustration of projection acquisition for a cone-beam (top) and fan-beam CT system (mid), alongside subsequent reconstruction and visualisation of CT images and a CT volume (bottom).

X-ray CT was pioneered by Godfrey Hounsfield whilst working at EMI in the UK. He described a complete CT system in his 1968 patent application, which was subsequently granted in 1972 [30]; a detailed description of the system followed in a 1973 publication [31]. Prior to, and independent of Hounsfield's work, Allan Cormack derived mathematical methods to calculate the density of different materials given measurements of their combined X-ray attenuation. He published two papers on the subject in 1963 [32] and 1964 [33].

The invention of X-ray CT enabled the internal structure of the brain to be visualised with the kind of detail only previously possible at autopsy, and lead to breakthroughs in the diagnosis and treatment of neurological diseases. For their contributions toward the development of X-ray CT, Cormack and Hounsfield were awarded the Nobel Prize in physiology or medicine in 1979 [34].

Naturally, the insight gained through imaging an object's internal structure led to X-ray CT being used for various imaging tasks outside the medical industry. X-ray CT remains a popular tool for materials characterisation; applications of its use include the characterisation of advanced aerospace composites [35], granular materials, pyrotechnics, textiles, CT has even been used to virtually unwrap an Egyptian mummy [36]. X-ray CT is also a well-established technique for non-destructive testing, revealing the spatial distribution of defects in manufactured structures, allowing engineers to improve their manufacturing processes and ensure components are structurally sound.

1.5 X-ray Computed Tomography for Dimensional Metrology

The evaluation of dimensional information from CT data dates back to the early 90's [27], whilst the first commercially available metrology CT system became available in 2005 [26]. Early CT-based measurements were of large aluminium castings used in the automotive industry [37], but with advances in both CT hardware and software, and a greater awareness of what CT has to offer, the number of measurement tasks being solved with X-ray CT continues to grow. A number of examples of measurement tasks that have been solved using X-ray CT are given in refs [26] and [38], these include small (centimetre) scale injection moulded plastic components, large (tens of centimetres) scale metallic cast components and a range of multi-material assemblies.

The general workflow for evaluating dimensional measurements from CT data is outlined in Figure 1.3. First the object is CT scanned which yields a set of projections, these are then reconstructed giving the cross-sectional images of the object. The next step is termed surface determination, this step is very important in X-ray CT for dimensional metrology as it is the process by which the object's surfaces are estimated. That is, a CT data set is essentially a 2D or 3D image composed of pixels or voxels that describe the object's material distribution, it is not a direct measurement of an object's surface. Nevertheless, certain edge detection algorithms are employed to estimate the object's surface from the CT data. With an estimate of the object's surface, geometric primitives are fitted to the discrete surface points and the dimensions of the object's features evaluated. More detailed explanations of reconstruction and surface determination are given in the next chapter.

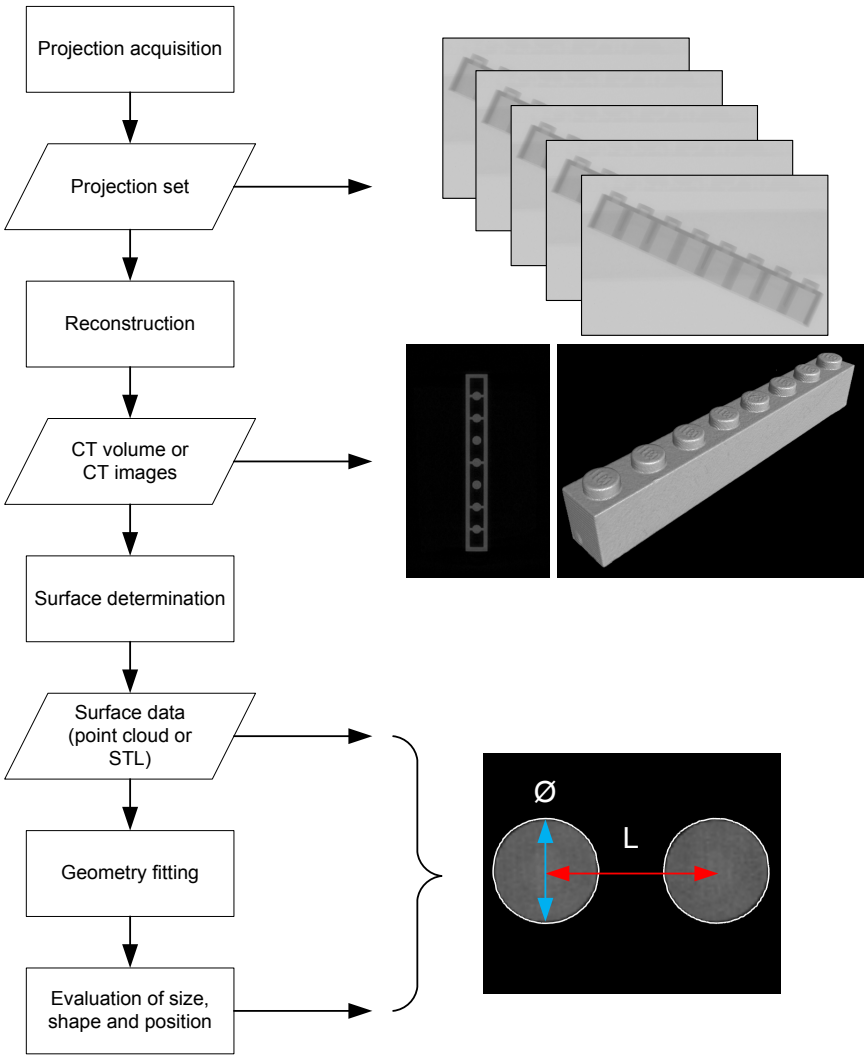

Figure 1.3 Workflow for a CT-based dimensional measurement.

When performing a CT scan there are a number of parameters that require setting. These include the X-ray power, number of projections, detector exposure time, number of projection averages and the object orientation to name, but a few. These settings are largely dictated by the size, material and structure of the object to be scanned. The position of the object relative to the source and detector is also an important parameter as it defines the geometric magnification of the scan. The magnification determines the effective pixel size of the projections and hence the voxel size of the reconstructed data. Geometric magnification m is calculated as:

$$m = \frac{D_{sd}}{D_{so}} \tag{1.2}$$

where D_{sd} is the source-to-detector distance (SDD) and D_{so} is the source-to-object distance (SOD), both of which are shown in Figure 1.2. Assuming the data is reconstructed at the same resolution as the acquired data, voxel size V is calculated as:

$$V = \frac{P}{m} \tag{1.3}$$

where P is the detector pixel size.

The voxel size represents the scale of a CT volume and its correct definition is essential for making accurate dimensional measurements. Voxel size determination is described in some detail in Chapter 4.

1.6 Limitations of X-ray CT for Dimensional Metrology

The result of a measurement is complete only if it includes a statement of measurement uncertainty [9]. Hence, for dimensional measurements evaluated via X-ray CT to be deemed complete, a statement of measurement uncertainty is required. Evaluating the task specific measurement uncertainty of CT measurements is where much of the research effort in the field of X-ray CT for dimensional metrology is concentrated [39]–[43]. To evaluate the measurement uncertainty, the doubt or imperfection of the measurement result needs to be evaluated. This requires that all factors that can influence a measurement result be understood, and their influence quantified. In many cases it is unknown how different factors influence a CT-based measurement result.

A comprehensive list of influencing factors can be found in the German guideline on X-ray CT for dimensional metrology, VDI/VDE 2630 Part 1.2 [44]. In this guideline influencing factors are classified as being due to: the CT device, the application, the analysis, the ambient conditions and the operator. A total of 64 influencing factors are identified, but the list is claimed not to be exhaustive. Several authors have compiled simplified lists of their own, all of which vary slightly [40], [42], [45], [46]. The author's own simplified classification of influencing factors is given in Table 1.1.

Table 1.1 Simplified classification of factors that influence dimensional measurements.

Category	Influencing factor
Hardware	X-ray source
	Detector
	Axes
	Radiation Cabinet
Measurement task	Object
	Scan settings
	User
Data processing	Reconstruction
	Surface determination
	Registration
	Form fitting
Environment	Temperature
	Humidity
	Vibration

The present work is concerned with two influencing factors that have been acknowledged and discussed throughout the literature; these are scattered radiation and beam hardening. Scattered X-rays are those that have deviated from their incident path and contribute an unwanted background signal to projections. Whilst beam hardening is the preferential attenuation of low energy X-rays; detailed descriptions of both phenomena are given in Sections 2.4.2 and 2.4.1 respectively. Both scattered radiation and beam hardening introduce nonlinearities in the physics of projection acquisition, and since most reconstruction algorithms rely on a linear acquisition model, artefacts (artificial features) are introduced to the reconstructed data. Scattered radiation and beam hardening introduce streaks between attenuating structures, raised intensity values at outer edges, lowered intensity values at the centre of objects and a general loss of image contrast, all of which ultimately degrade the quality of CT data. The impact that scatter and beam hardening have on CT data is shown in Figure 1.4.

The importance of the problem posed by scatter and beam hardening is reflected by the number of publications on the topic. Research on correcting scatter and beam hardening artefacts dates back to the mid-70s [47]–[50] and continues to the present day [51]–[53]. Scatter and beam hardening originally caused problems in medical CT, but when it comes to CT scanning common engineering metals such as aluminium, titanium and steel, scatter and beam hardening artefacts become much more problematic due to the higher atomic numbers and densities of the materials. Since objects manufactured from these materials require CT metrology it is important the influence that scatter and beam hardening have on dimensional measurements be studied.

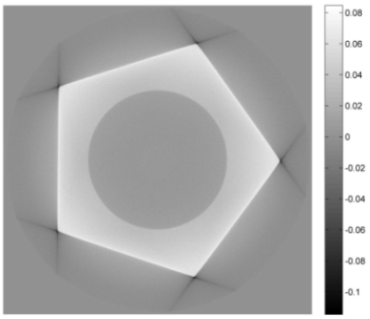

(a) CT image with both scatter and beam hardening.

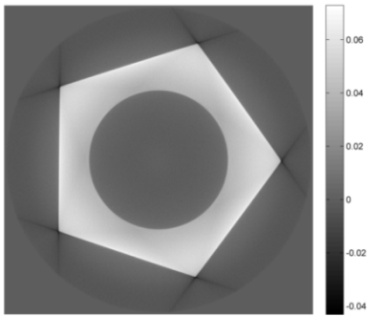

(b) CT image with scatter only.

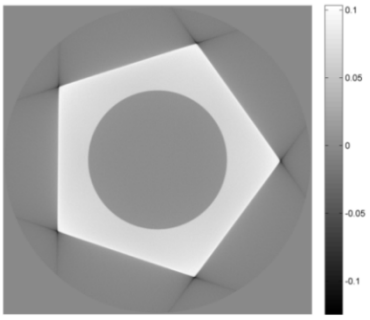

(c) CT image with beam hardening only.

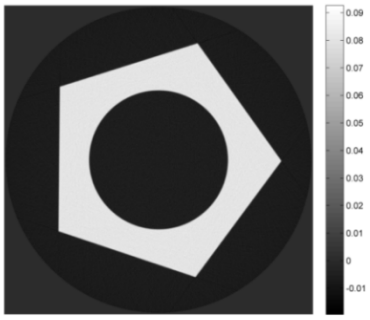

(d) CT image with no scatter and no beam hardening.

Figure 1.4 Demonstration of scatter and beam hardening artefacts for simulated CT data of an aluminium object approximately 40 mm in diameter. Scatter and beam hardening cause streaks, raised intensity values at outer edges and a general loss of image contrast. Colour bars represent the range of grey values in each CT image.

The influence of beam hardening correction on dimensional measurements has been considered by a number of authors in parallel to this work. The group of Dewulf et al. [54], [55] showed that an incorrect beam hardening correction can increase measurement error; Dewulf et al., Zhang et al. [56] and Nishihata et al. [51] have since derived beam hardening corrections that do not have this unwanted effect. On the other hand, Bartscher et al. [43] considered the influence beam hardening correction has on tests for verifying the performance of a CT system for dimensional metrology. Bartscher et al. stated that when a CT system's performance is assessed the influence beam hardening correction has on the measurement result should be taken into consideration. These studies have largely made use of 'black box' corrections provided by CT software companies, and only go so far as to look at the end effect of beam hardening correction. The core of the problem has therefore not been addressed; it is not clear how beam hardening influences dimensional measurements. Beam hardening clearly influences grey values in CT data, but what effect does it have on the edges/surfaces of CT data? Does it cause them to move? Or does it lead to an incorrectly defined surface, which in turn influences dimensional measurements? The purpose of this work is to answer these questions, not only for beam hardening, but for scatter also.

Scatter has been acknowledged by a number of authors to influence dimensional measurements; however, no dedicated studies on the subject have been published. Schorner et al. [57], [58] studied a number of scatter correction approaches for industrial CT and suggested that the presence of scatter may influence dimensional measurements, but no quantitative results were given.

Even though scatter and beam hardening manifest themselves in a similar way, they are two very different phenomena and should therefore be corrected/studied separately. This being a major shortcoming of the aforementioned work of Dewulf, Zhang and Bartscher et al., all of which neglect the presence of scatter and assume all artefacts are wholly attributable to beam hardening.

Based on the above reasoning, the aim of this thesis is stated in the next section.

1.7 Aim and Objectives

The mechanisms through which scattered radiation and beam hardening influence dimensional measurements are poorly understood; the aim of this thesis is to develop a better understanding of how these two phenomena influence surface determination and hence dimensional measurements through the use of both measured and simulated data.

The objectives of this thesis are as follows:

- To develop reference workpieces to test and correct for systematic errors in CT based dimensional measurements (Section 3.2 and 3.4).

- To develop reference workpieces with both internal and external threshold sensitive dimensions to evaluate the influence of scatter and beam hardening on dimensional measurements (Section 3.3).

- To implement scatter and beam hardening correction/minimisation techniques to quantify the influence these artefacts have on dimensional measurements (Chapter 5).

- Give explanations as to how scatter and beam hardening influence dimensional measurements for both the ISO50 and local surface determination methods (Sections 6.2 and 6.3).

- Give recommendations on the use of artefact correction/minimisation in the context of X-ray CT for dimensional metrology (Chapter 8).

1.8 Structure of the Thesis

The remainder of this thesis is organised as follows:

In Chapter 2 a detailed description of X-ray CT is presented with a focus on its use for making dimensional measurements. The chapter begins with some basic X-ray physics, followed by a description of the main components of a CT system. The principle of image reconstruction is presented alongside a description of different

artefacts that degrade the quality of CT images. Two surface determination algorithms are then reviewed and finally a chapter summary is given.

In Chapter 3 three reference workpieces are introduced. Two of the workpieces are used for voxel size determination in Chapter 4, whilst the third is designed to induce scatter and beam hardening artefacts and is made use of in Chapter 5. Reference measurements of each workpiece are made with a CMM and the measurement uncertainty evaluated. The strategy for measuring each workpiece via X-ray CT is then described, covering details such as the acquisition setup, reconstruction method, surface determination method, datum definition and alignment.

In order to study the influence of scatter and beam hardening experimentally, errors in the voxel size must first be minimised. In Chapter 4 the methods employed for voxel size determination are presented and tested for an object that presents negligible scatter and beam hardening artefacts.

In Chapter 5 the influence that scatter and beam hardening have on dimensional measurements is evaluated experimentally. Measurements of the inner and outer radii of cylindrical cross-sections are compared before and after scatter and beam hardening correction/minimisation. A systematic effect is observed: in the presence of scatter and beam hardening the measured size of internal features decreases and the measured size of external features increases.

In Chapter 6 the experimental study is repeated, but in simulation. The simulation results show the same opposing inner/outer relationship as the experimental results. Explanations of this effect are then given for both surface determination methods.

Scatter and beam hardening do not influence dimensional measurements directly, they influence the determined surface. As such, the measurement uncertainty due to surface determination is evaluated in Chapter 7, and the impact scatter and beam hardening have on this uncertainty contributor assessed.

Finally, in Chapter 8 the developments of each chapter are restated, important findings discussed, and future research directions suggested.

Chapter 2 X-ray CT for Dimensional Metrology

In this chapter an overview of X-ray CT is presented and literature concerning the use of CT for metrology is reviewed. Many of the topics covered can be found in any introductory text to X-ray CT e.g. [59], [60], however, these tend to be written with a focus on medical CT. The chapter begins by introducing the basic physics of CT, and then covers the main components of a CT system. The principle of image reconstruction is presented alongside a description of different artefacts that degrade the quality of CT images. The basics of edge detection are reviewed since it is through edge detection that surfaces are estimated from volumetric data. Finally, a chapter summery is given and gaps in the knowledge identified.

2.1 Basics of X-ray Physics

In this section the basic physics of radiography are introduced based on the texts of Evans [61] and Bushberg et al. [60]. The structure of the atom is first described followed by X-ray production and detection. The dominant interactions that occur between X-rays and matter at the considered energy range are then described alongside the governing equations of X-ray attenuation.

2.1.1 Atomic Structure

According to the simplified Bohr model, the atom consists of a central nucleus orbited by electrons. Electrons occupy orbits, or shells, around the nucleus. These orbits/shells are labelled K, for the innermost, and L, M, N progressing outwards. These shells can only be occupied by a certain number of electrons, and when an electron is removed from a shell, a positive ion results. Electrons are held in their orbits by the Coulomb force of attraction between their negative charge and the positive charge of the nucleus; the binding energy is the energy required to overcome this force. The binding energy is strongest for the K-shell and gets weaker the further an electron is from the nucleus. The binding energy for a tungsten K-shell electron is 69.5 keV, where 1 eV is equivalent to 1.6×10^{-19} J. So, to remove a K-shell electron from a tungsten atom energy in excess of 69.5 keV is required.

When an electron is removed from the K-shell, an electron from an outer shell can drop down to fill the vacancy. This process is accompanied by the emission of electromagnetic radiation with an energy equal to the difference in the binding energies

of the shells involved. This type of electromagnetic radiation is termed characteristic radiation, as it is characteristic of the element which produces it. X-ray production is covered in more detail in the next section.

2.1.2 X-ray Production

Electromagnetic radiation produced as a result of electrons transiting between energy levels was described in the previous section. Electromagnetic radiation can be characterised by its wavelength (λ), frequency (f), and energy (E) with the following two equations:

$$E = hf \tag{2.1}$$

and

$$c = f\lambda \tag{2.2}$$

where h is Plank's constant and c is the speed of light in a vacuum.

Characterising electromagnetic radiation by frequency or wavelength forms the electromagnetic spectrum, which includes in order of increasing frequency: radio waves, microwaves, infrared radiation, visible light, ultraviolet light, X-rays and gamma rays. X-rays are classified as having a wavelength in the range of 10 nm to 0.01 nm [62].

This thesis is concerned with X-rays, discovered by Wilhelm Röntgen in 1895. X-rays are divided into two types: (i) characteristic X-rays and (ii) continuous X-rays, or bremsstrahlung. The production of characteristic X-rays has already been described. Continuous X-rays/bremsstrahlung are produced by the acceleration or deceleration of charged particles, such as free electrons or ions. This acceleration or deceleration may occur due to a charged particle interacting with the electric fields of atomic electrons or nuclei. Free electrons can be generated by passing a current through a filament in a vacuum such that electrons are boiled off the surface of the filament by thermionic emission. If these electrons are accelerated and bombard a target, the target will emit X-rays, both characteristic and bremsstrahlung. It is in this manner that X-rays are generated in most industrial CT systems. A more detailed description of this type of X-ray source is given in section 2.2.1. A typical X-ray spectrum emitted by a tungsten target is shown in Figure 2.1.

X-rays may also be generated by a synchrotron, a type of particle accelerator, whereby charged particles are accelerated radially and therefore emit bremsstrahlung X-rays. Furthermore, X-rays can be generated by linear accelerators, another type of particle accelerator, whereby charged particles are accelerated along linear beamlines. It has also been reported that X-rays can be generated when peeling adhesive tape in a vacuum [63]. However, this work is not concerned with X-rays produced in these ways so they are discussed no further.

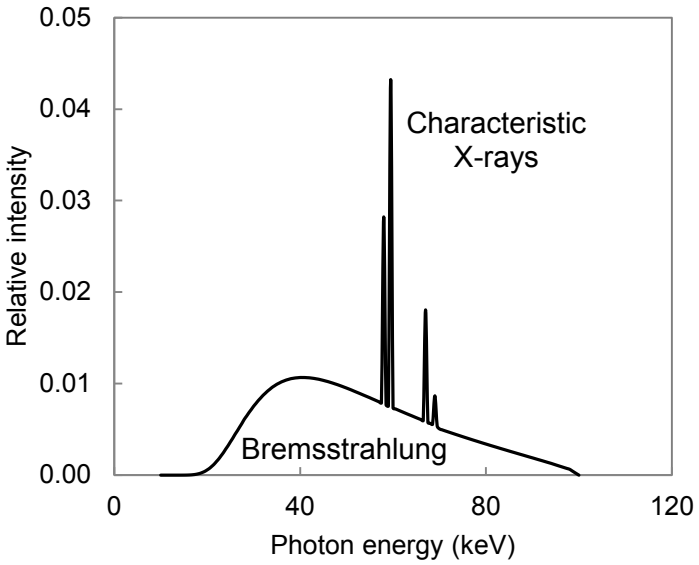

Figure 2.1 Graph showing the difference in photon energy distribution of characteristic X-rays and bremsstrahlung. Plot generated using SpekCalc [64] for a tungsten target and an acceleration voltage of 100 kV.

2.1.3 X-ray Detection

Röntgen discovered X-rays after noticing a screen painted with barium platinocyanide scintillated whilst he experimented with a vacuum tube; where scintillations are small flashes of light. Scintillators are materials that emit light after absorbing radiation; this property is made use of in most X-ray detectors used in industrial CT systems.

Scintillation can be explained using energy band theory [65]. Electrons in crystalline solids can be grouped into energy bands, the valence band and the conduction band. These are separated by a forbidden energy region termed the energy gap. The outer shell electrons of the material's atoms occupy the valence band, whilst the conduction band is generally empty. X-ray absorption can cause many electrons to be excited into the conduction band. These electrons may immediately drop back down to the valence

band, which is accompanied by the emission of a large number of visible and/or ultraviolet photons; this is illustrated in Figure 2.2. These photons are directed on to a photodiode and converted into an electrical signal, this being the principle behind indirect digital detectors, more on these in section 2.2.2. The excited electrons may alternatively be collected directly using materials such as amorphous selenium; this process is exploited in direct digital detectors.

The ionisation of high-pressure inert gas by X-rays is another detection method, such detectors have been used in medical CT systems, but since this work is not concerned with these types of detectors they are discussed no further.

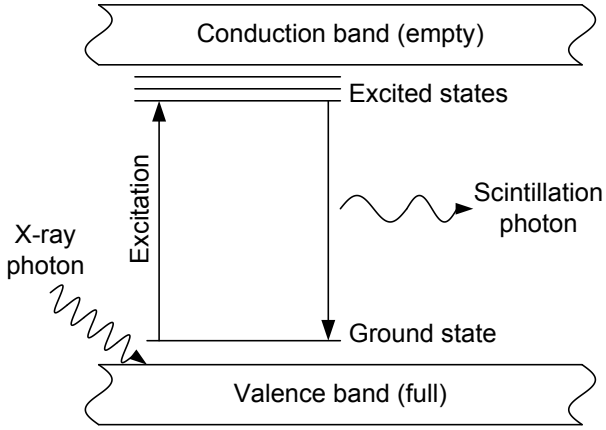

Figure 2.2 Illustration of electronic band structure for scintillator materials, adapted from [65].

2.1.4 X-ray Interactions with Matter

For energies between a few keV to less than 1 MeV there are three primary processes by which X-rays interact with matter. These are the photoelectric effect, Compton scattering and Rayleigh scattering. Their relative importance is illustrated in Figure 2.3 in which the mass attenuation coefficient (μ/ρ) for aluminium is plotted as a function of photon energy. The linear attenuation coefficient μ, defined in equation 2.10, is a measure of the probability of an X-ray interacting in a given material. It depends on the atomic number Z and density ρ of the absorbing material and varies strongly with X-ray energy E. It has contributions from all three interaction processes, each having its own energy dependence and Z dependence.

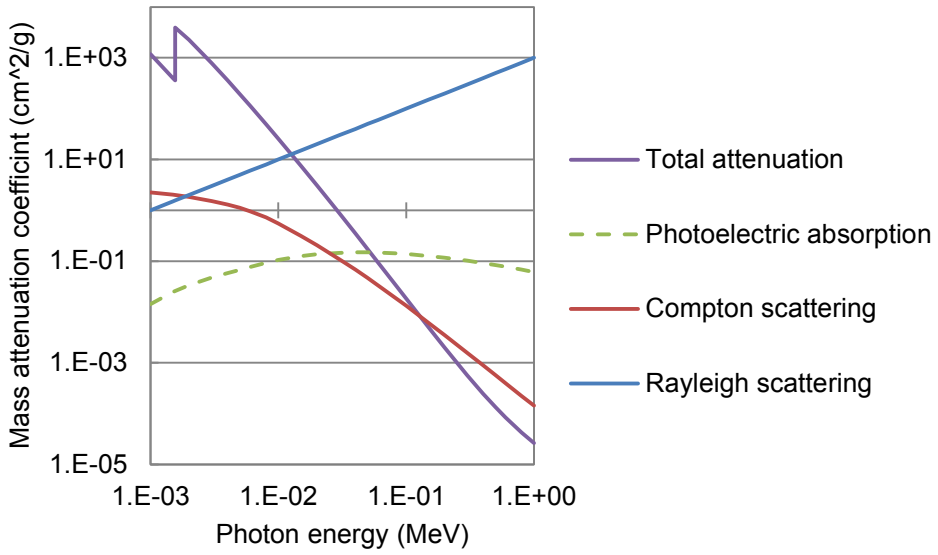

Figure 2.3 Graph showing the probability of each X-ray-matter interaction occurring for aluminium, for photon energies from 1 keV to 1 MeV.

Photoelectric absorption occurs when a photon's energy is converted to release an electron from its orbit, usually an inner shell electron. The emitted electron is termed a photoelectron and has a kinetic energy equal to $E - B_e$, where E is the energy of the incident photon and B_e is the binding energy of the electron. An electron from a higher shell may fill the vacancy, which is accompanied by the emission of a characteristic X-ray.

The probability of a particular interaction occurring is termed a cross section and has units of centimetre squared. The probability of photoelectric absorption occurring is therefore termed the photoelectric cross section σ_{PE} and varies strongly with X-ray energy and the atomic number of the material. An approximate expression of the photoelectric cross-section for energies of a few hundred keV is given by [65]:

$$\sigma_{PE} \approx Z^5/E^{3.5}. \qquad 2.3$$

Equation 2.3 shows photoelectric absorption is more likely for higher Z materials but decreases with photon energy.

Compton scattering occurs when a photon scatters with an outer shell electron. The result of the interaction is a photon of lower energy and a recoil electron. The energy of the scattered photon E' is given by:

$$E' = \frac{E}{1 + (E/mc^2)(1 - \cos\theta)} \quad 2.4$$

where E is the energy of the incident photon, mc^2 is the rest mass energy of the recoil electron and θ is the scattering angle. Thus the energy of the scattered photon is unchanged for $\theta = 0°$ and a minimum for $\theta = 180°$.

The probability of a photon scattering at a given angle is illustrated in Figure 2.4 for various photon energies. Note the fraction of forward-scattered photons increases with E. The angular distribution in Figure 2.4 is termed the differential Compton cross section; its analytical form can be found elsewhere [61]. Integrating the differential cross section over all possible scattering angles gives the average Compton cross section, per electron, derived by Otto Klein and Yoshio Nishina in 1928:

$$\sigma_C = 2\pi r_e^2 \left\{ \frac{1+\alpha}{\alpha^2} \left[\frac{2(1+\alpha)}{1+2\alpha} - \frac{1}{\alpha} \ln(1+2\alpha) \right] + \frac{1}{2\alpha} \ln(1+2\alpha) - \frac{1+3\alpha}{(1+2\alpha)^2} \right\} \quad 2.5$$

where $\alpha = E/mc^2$ and r_e is the classical electron radius. σ_C has units of cm^2 / electron.

The probability of Compton scattering is less dependent on E and Z than photoelectric absorption, but is strongly dependent on the density of electrons in the medium. Equation 2.5 predicts the probability of Compton scattering decreases with E.

Rayleigh scattering occurs when an X-ray interacts with the entire atom and is scattered from its incident path without loss of energy. The incident electromagnetic wave sets the atom into a forced resonant oscillation. The motion of the electrons results in the emission of X-rays of the same energy as the incident photon, but with a slightly different direction. Most X-rays are scattered forward, with small angles.

The average cross-section for Rayleigh scattering is evaluated by integrating the differential cross section over all scattering angles:

$$\sigma_R = \pi r_e^2 \int_0^{2\pi} \sin\theta \, (1 + \cos^2\theta) FF^2(q, Z) \, \mathrm{d}\theta, \quad 2.6$$

where $FF(q, Z)$is the atomic form factor, and $q = 2E \sin(\theta/2)$. Atomic form factors take into account the energy and material dependence of Rayleigh scattering [57]. At low energies, form factors do not influence the angular distribution of Rayleigh scattering, but at higher energies they become forward peaked.

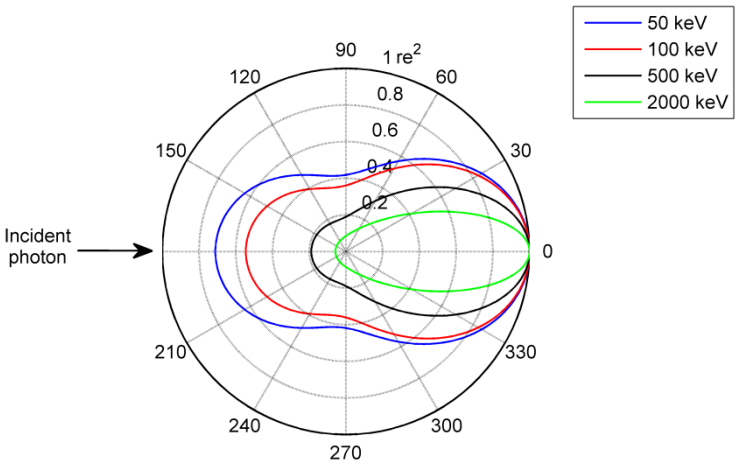

Figure 2.4 Graph showing the probability of a photon scattering at a given angle by a single electron. Probability in units of $r_e^2 \approx 7.94 \times 10^{-26}$ cm^2.

2.1.5 Attenuation

For a collimated[1] beam of X-rays, the three interactions described in the previous section will cause the beam to be attenuated as it passes through matter. Photons that undergo photoelectric absorption are removed from the beam entirely, whist those that are scattered are deflected from their incident path and fail to reach the detector. This is illustrated in Figure 2.5.

Consider a collimated beam of X-rays, cross sectional area of 1 cm^2, of a single energy E. Let I_0 photons per second fall incident on a slab of material of thickness $\mathrm{d}x$ and with an atomic density of N (atoms/cm^3). If the total interaction cross-section per atom of the material is σ, and $I_0 - dI$ photons are transmitted per second, the rate of removal of photons from the beam is given by:

$$-\frac{dI}{I_0} = N\sigma \mathrm{d}x \qquad 2.7$$

where the total cross-section σ has contributions from all three interactions previously described, that is:

$$\sigma = \sigma_{PE} + Z\sigma_C + \sigma_R \,. \qquad 2.8$$

[1] For X-rays, a collimator limits the beam so that only the X-rays travelling parallel to a specified direction are allowed through.

Integrating equation 2.7 over the thickness of the material gives:

$$-\ln\left(\frac{I}{I_0}\right) = N\sigma x \qquad 2.9$$

and by letting:

$$\mu = N\sigma \qquad 2.10$$

equation 2.9 is rewritten to give the well-known Beer-Lambert law:

$$-\ln\left(\frac{I}{I_0}\right) = \mu x\,. \qquad 2.11$$

The term μ is known as the linear attenuation coefficient and has units cm^{-1}. Equation 2.11 shows that X-ray attenuation is a linear function of material thickness. This relationship is seen experimentally for a collimated beam of X-rays of a single energy (a monochromatic beam), see Figure 2.5(a). However, if the beam is not collimated then X-rays scattered by the material may fall incident on the detector, raising the measured intensity and causing the relationship to deviate from this ideal case, Figure 2.5(b).

In the previous section it was shown that each of the dominant X-ray - matter interactions are functions of X-ray energy, thus μ is also a function of X-ray energy. Figure 2.3 shows that μ varies considerably with X-ray energy, this means that each X-ray energy is attenuated differently. For an X-ray beam composed of many different X-ray energies (a polychromatic beam) the total attenuation becomes the sum of attenuation for each X-ray energy. Rewriting equation 2.11 to consider this energy dependence yields:

$$I = I_0 \int_{E\,min}^{E\,max} W(E)\exp(-\mu(E)x)\,dE \qquad 2.12$$

where $W(E)$ is a function describing the relative intensity of each X-ray energy, and I and I_0 are the total transmitted and incident X-ray intensities respectively. Rewriting equation 2.12 in terms of attenuation gives:

$$-\ln\left(\frac{I}{I_0}\right) = -\ln\left(\int_{E\,min}^{E\,max} W(E)\exp(-\mu(E)x)\,dE\right). \qquad 2.13$$

Clearly polychromatic attenuation is not a linear function of material thickness.

The ideal experimental setup illustrated in Figure 2.5(a) is far removed from the apparatus used in industrial CT. Industrial X-ray sources emit a poorly collimated beam of polychromatic X-rays, and as a consequence, the X-ray attenuation measured in industrial CT differs strongly from that governed by the Beer-Lambert law. In Section 2.3 it will be shown that the mathematics of reconstruction are derived based on the assumption that X-ray attenuation follows the Beer-Lambert law, whilst in Section 2.4 it will be shown that polychromatic X-ray attenuation and scattered X-rays lead to errors, or artefacts in the reconstructed data that severely degrade the quality of CT data.

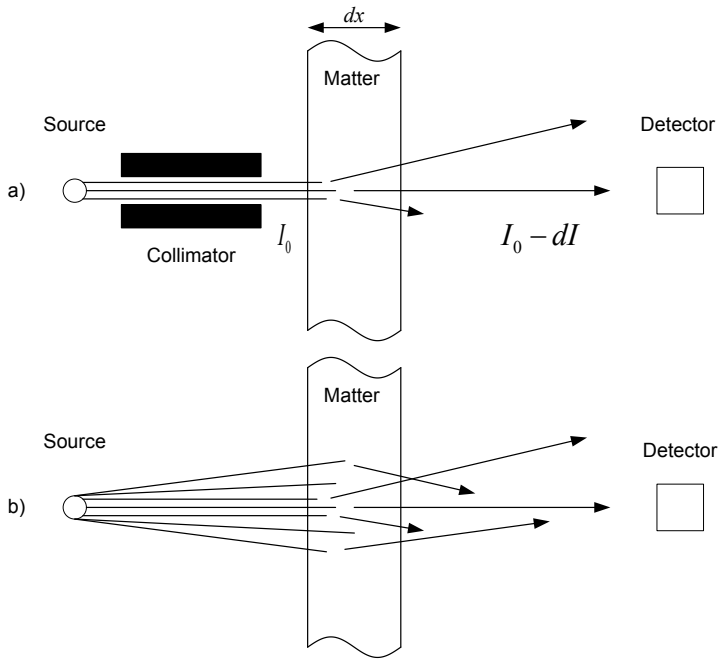

Figure 2.5 Setup for measuring X-ray transmission, with and without source collimation [65].

2.2 Components of a CT System

An industrial CT system is composed of four main components: (i) an X-ray source, (ii) an X-ray detector, (iii) a set of mechanical axes for positioning the object between the source and detector and providing the rotation required for CT, and (iv) a computer for acquiring data, reconstructing the data and subsequent data analysis. The characteristics and performance of the first three components directly influence the quality of the acquired data. As such, these components are described in some detail in the next sections.

2.2.1 Microfocus X-ray Source

Industrial CT systems typically employ a microfocus X-ray source; that is, the size of the X-ray focal spot is in the order of microns. Nanofocus X-ray focal spot sizes are possible, however, maintaining this spot size over a long period of time whilst emitting sufficiently high intensity X-rays is an ongoing research topic [66].

As described in Section 2.1.2, X-rays can be produced by bombarding a target with high speed electrons. Figure 2.6 shows this process in a little more detail. An electron cloud is generated by passing a current through a filament. The electron cloud is electrostatically focussed into a narrow electron beam by a control grid. The electron beam is then accelerated by the anode and enters the drift chamber. The high speed electron beam is then further focussed into a narrower beam by a set of electro-magnets, termed the focusing coils. A set of deflection coils then control the lateral position of the electron beam as it impinges upon the target [67]. Only a very small part of the energy used to accelerate the electrons is converted into X-rays; the majority of the energy is dissipated as heat. Extremely high temperatures can therefore be reached that can permanently damage the target, reducing its operating efficiency and lifetime.

Figure 2.6 shows an electron beam incident on three different target types: transmission, reflection and rotating. Transmission targets are ‘slide-like’ and covered in a thin layer of tungsten, ~ 1 to 10 μm depending on the application [68]. X-rays are generated within the tungsten layer, and transmitted through the target. The maximum power of a transmission X-ray source is limited by the thermal conductivity of the target material since the heat generated as the electron beam bombards the target may cause the target to melt. For this reason transmission targets are typically backed with carbon to aid heat dissipation.

Reflection targets are ‘massive’ targets that may be cooled directly and can therefore handle higher electron beam powers. Additionally, the target surface that the electron beam falls incident upon is angled, such that the heat generated is dispersed over a larger area.

Rotating targets are reflection targets that are rotated at high speeds (~10,000 rpm and higher) such that the electron beam impinges upon a constantly changing region of the target to aid heat dispersion. However, at high rotational speeds and in the presence of high temperatures, large stresses are placed on the bearings and drive assembly of the

target. This can contribute to instabilities in the target rotation, causing unpredictable movement and positioning of the focal spot on the target, which ultimately degrades the resulting X-ray image quality [69].

One solution to the problem of heat dissipation is to use a jet of liquid metal as the target; since the target is already molten, the melting point of the target is no longer the factor that limits the source power [70]. Such X-ray sources claim focal spot sizes of 5 to 40 μm, with sub-micron focal spot stability. Other X-ray source manufactures claim with improved internal cooling, transmission type sources can also achieve focal spot movement of less than a micron for extended periods of time [71]. One approach to overcome resolution limits imposed by the size and drift of the focal spot is to use X-ray optics. A condenser lens is used to focus the X-ray beam on the sample, a Fresnel zone plate objective then forms a magnified image of the sample on a high resolution X-ray detector. This approach is used in X-ray microscopes but has been adopted for use in X-ray CT to resolve structures in CT images in the order of 50 nm [72].

A number of studies have been conducted whereby the extent of the focal spot drift has been measured for extended periods of time [71], [73]–[75]. These studies suggest focal spot drift is largest whilst the X-ray source warms up, and is minimal once the X-ray source has reached thermal equilibrium. In terms of the impact this has on dimensional measurements, spot drift will influence geometric magnification, and cause projections to shift horizontally and vertically on the detector. This will cause blurring of reconstructed data and may influence both size and form measurements.

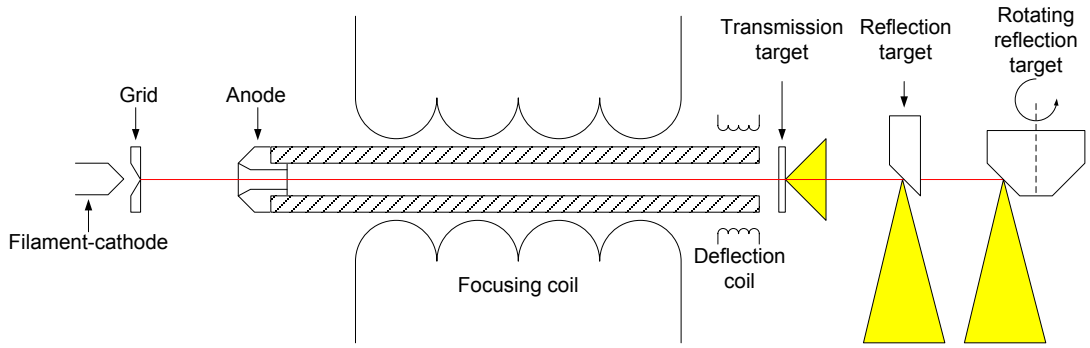

Figure 2.6 Diagram of a microfocus X-ray source. Three different target types are shown.

2.2.2 Flat Panel X-ray Detector

Most industrial CT systems use flat panel, indirect, scintillation-based X-ray detectors. The basic physics of scintillation have been described in Section 2.1.3. The working principle of this type of detector is illustrated in Figure 2.7. A scintillator converts X-ray photons into visible light photons. The light photons fall incident on photodiodes, which produce a corresponding charge; this charge is stored during X-ray exposure. Once exposure is terminated, a thin film transistor (TFT) switches, allowing the stored charge to flow to a charge amplifier for subsequent analogue to digital conversion. Each detector element therefore consists of a charge collection electrode, a storage capacitor and a TFT [76]. For an indirect detector the charge collection electrode is a photodiode. For a direct detector the charge collection electrode is a semiconductor sandwiched between two electrodes, such that absorbed X-rays directly generate ion pairs. This architecture is illustrated in Figure 2.8.

Scintillator materials used in flat panel X-ray detectors can be classified as being unstructured, or structured. Caesium iodide (CsI) is a scintillating material that can be grown in micro-structured columns, see Figure 2.9. The micro-columns guide light by total internal reflection; this reduces light spread compared to unstructured scintillating materials such as gadolinium oxysulfide [77].

Modern flat panel X-ray detectors are expected to have a high level of spatial uniformity, with negligible image distortion. However, it has been proposed that the scintillator deposition process may in fact warp the detector panel. Additionally, the angular orientation of the CsI micro-columns may vary across the detector, thus introducing variations in the detector signal. Weiß et al. [78] estimated the image distortion in a flat panel detector; the mean distortion was found to be approximately 0.05 pixels. Subsequent correction of the image distortion on a projection by projection basis reduced measurement error of a calibrated workpiece by a few microns.

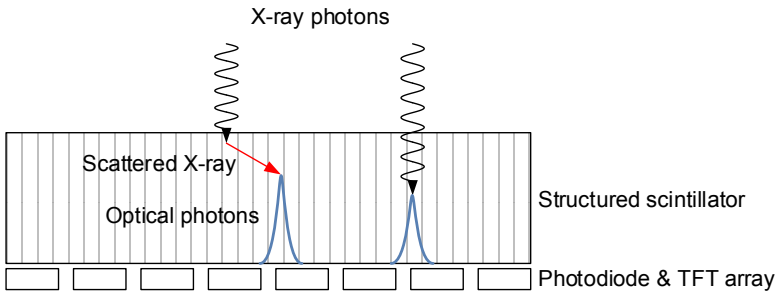

Figure 2.7 Operating principle of an indirect TFT detector using a structured CsI scintillator.

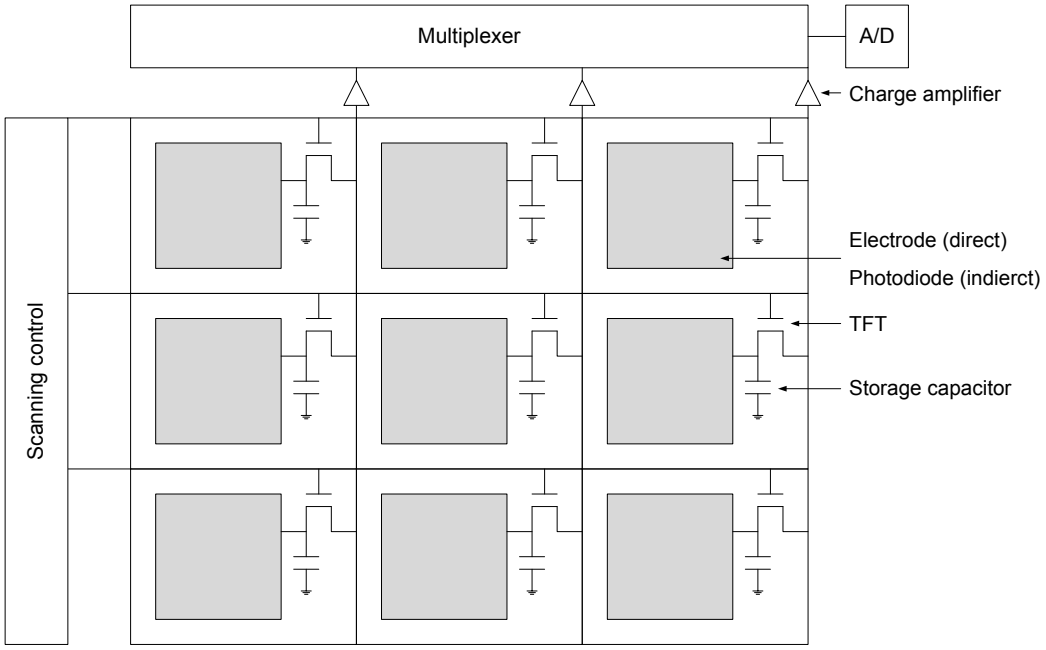

Figure 2.8 Illustration of an array of detector elements alongside read-out and digitisation electronics, adapted from [76].

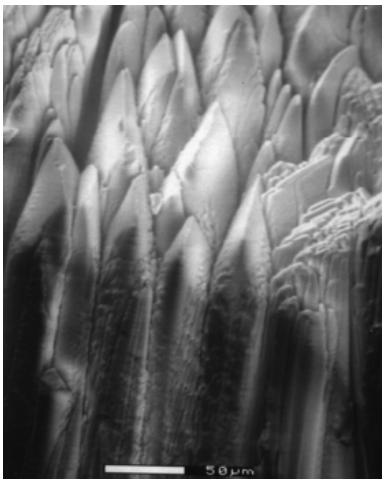

Figure 2.9 Environmental scanning electron micrograph of the surface of a CsI scintillator with micro structured columns. Scale bar = 50 µm. Image taken from [77]

2.2.3 Motion Control

For circular trajectory cone-beam CT only the workpiece need be rotated relative to a stationary X-ray source and detector. In theory this rotation needs only to be through 180°, but in practice the rotation is typically through 360° to improve the signal-to-noise ratio of the reconstructed data. Other acquisition trajectories are possible, such as spiral/helical CT, these will be discussed briefly in Section 2.4.3.

An industrial CT system will typically have linear axes to position the workpiece within the X-ray cone-beam. The x and y axes position the workpiece's projection within the detector plane, whilst the z axis changes the geometric magnification, see Figure 2.10. Since geometric magnification is calculated based on the z axis encoder read out, it is desirable for this axis to have low positional errors and high bidirectional repeatability.

The rotation stage is the only axis that moves during scanning. The rotation may be continuous for fast in-line scanning, or discrete for longer, high precision scans. The eccentricity or radial run out of the rotation stage should be as low as possible. At high magnifications, when the effective pixel size is in the order of microns, radial run out will become significant and will cause blurring in the reconstructed data. Furthermore, the tilt of the rotation surface should be minimal. That is, the rotation axis should be parallel to the central column of the detector. Geometric alignment of the CT system and its influence on dimensional measurements is described in detail in Section 2.4.4.

Studies have shown the encoder position of the magnification axis can be subject to large errors. Positional errors of up to 350 μm were measured for axis travel over 700 mm in one study [45], and errors of ±800 μm for axis travel of up to 600 mm in a separate study [79]. Errors in the magnification axis position, and hence the SOD, are typically minimised by scanning a reference object with a calibrated length before, after or during a measurement task; by comparing the CT-based measurement to the calibrated value the magnification can be calculated for the given axis position. This will be discussed in more detail in Chapter 4.

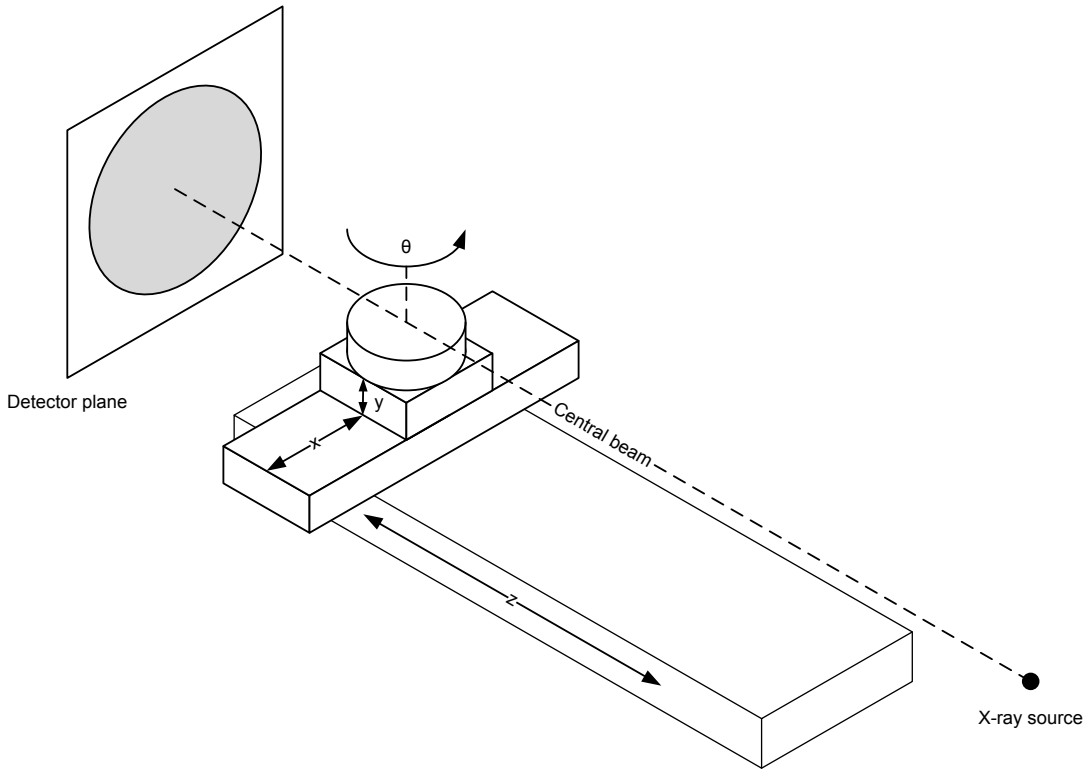

Figure 2.10 Illustration of the motion stages of a typical, circular trajectory, industrial CT system.

2.3 Reconstruction

Reconstruction is the process of estimating an object's cross-sections from its projections. Broadly speaking there are two approaches to solving the inverse problem posed by reconstruction: (i) try to formulate the solution in a closed-form equation, often referred to as the analytic approach, (ii) try to formulate the result as the solution to an optimisation problem, which is often solved in an iterative fashion, and referred to as the iterative approach [80]. Both analytic and iterative approaches have pros and cons. In general, analytical approaches are computationally more efficient, whilst iterative approaches can improve CT image quality.

In this section the basics of both approaches to image reconstruction are described.

2.3.1 Analytic Reconstruction

Analytic reconstruction methods are based on the Fourier slice theorem, no mathematical derivation is given here since it is well covered in other texts [59], [81]. Instead, an illustrative description of analytic reconstruction is given.

The cross-section of the object to be reconstructed is considered a two dimensional function $f(x,y)$, whilst the X-ray attenuation measured at each detector pixel is considered a line integral of the object function, and is denoted $P(\theta,t)$, where θ is the projection angle, and t the detector column, see Figure 2.11. The Fourier slice theorem states that the 1D Fourier transform of a projection $S(\omega)$ is equivalent to a radial line of the 2D Fourier transform of the original object $F(u,v)$. This is more easily understood by looking to Figure 2.11. This result is remarkable, in that by acquiring projections of the object at a number of angular positions, the 2D Fourier transform of the object can be filled and inverse transformed to yield the original object function. This is a very elegant solution to the reconstruction problem, however, practical implementation requires a slightly different approach.

It should be noted that $P(\theta,t)$ is termed the Radon transform of the function $f(x,y)$. In 1917 Johann Radon derived mathematics to calculate the integral of a function over straight lines; Radon also derived an inverse transform to calculate $f(x,y)$ from its Radon transform.

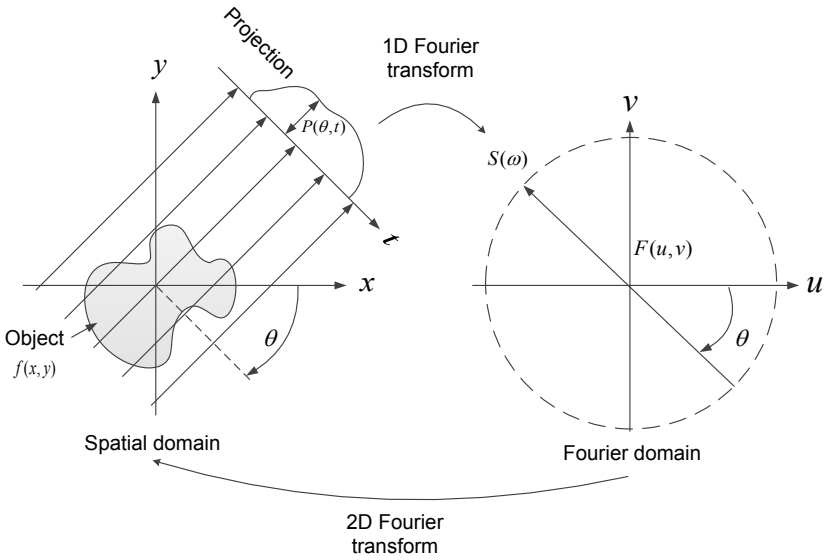

Figure 2.11 Illustration of the Fourier slice theorem for a single parallel projection [59].

The algorithm used for almost all CT reconstruction tasks is the Filtered backprojection algorithm (FBP). The filtered backprojection algorithm can be described by noting two issues presented by the Fourier slice theorem. Firstly, Figure 2.12 shows that the 2D Fourier transform of $f(x, y)$ is only sampled along a finite number of radial lines. In order to use this result the radial points need to be interpolated onto a square grid. Since the density of the radial points becomes sparser as one gets further away from the centre, the interpolation error will become larger. This causes a greater error in the high frequency components of the image than the low frequency ones, which leads to image degradation. This is overcome by performing the summation of the object's projections in the spatial domain rather than the Fourier domain; this is preferable since spatial interpolation is usually more accurate than the Fourier domain interpolation. When the projection summation is performed in the spatial domain it is termed backprojection. Backprojection consists of adding each projection value to the reconstruction image along ray paths for each angular position, and is illustrated in Figure 2.13.

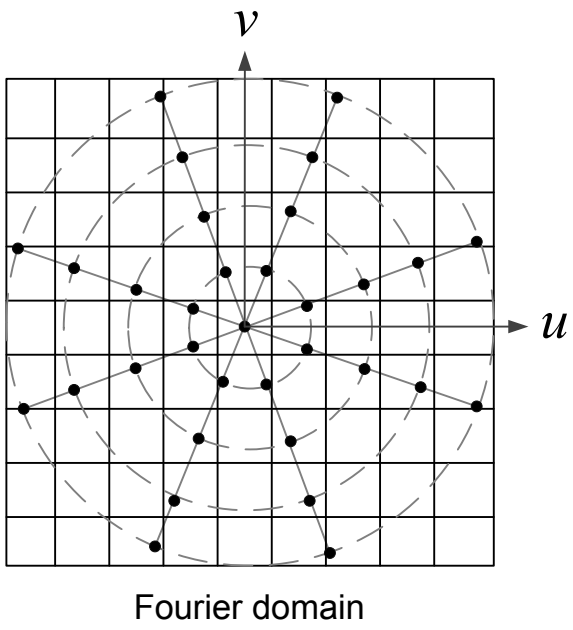

Figure 2.12 Sampling pattern in the Fourier domain for the Fouier slice theorem [59].

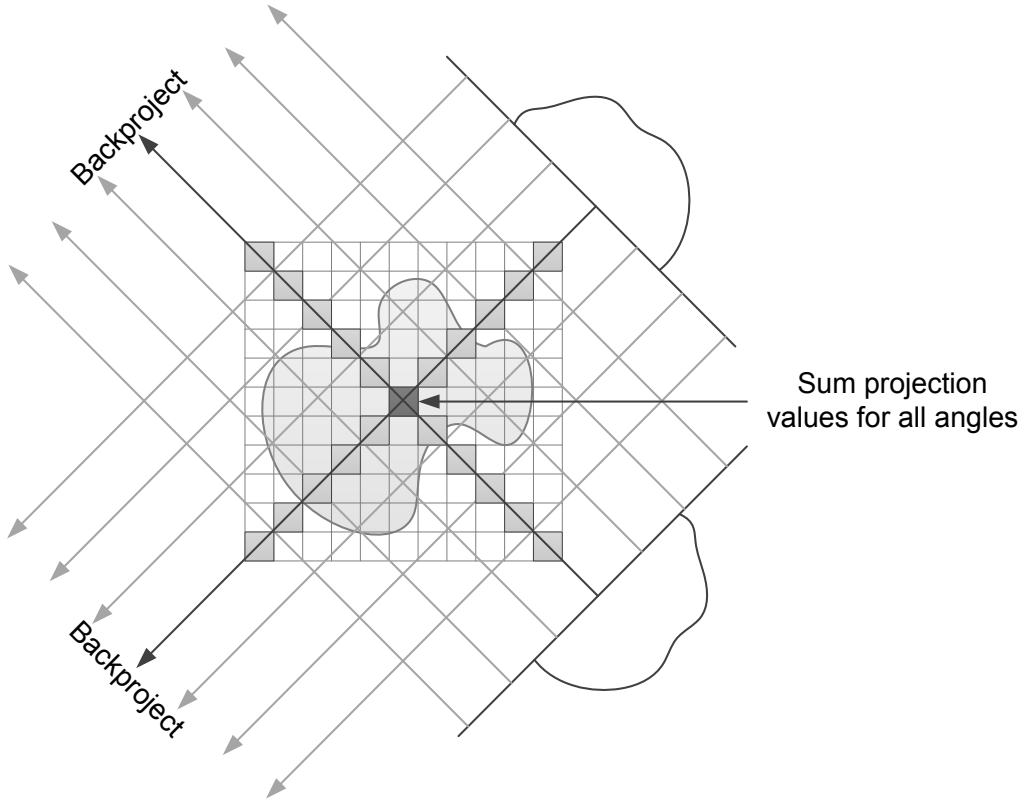

Figure 2.13 Illustration of backprojection. Projection values are added to the image along ray paths for all angular positions.

The second issue with the Fourier slice theorem is also illustrated in Figure 2.12, if we simply sum up the Fourier transforms of all the uniformly spaced projections, the DC term would be artificially enhanced whilst the outer regions would be underrepresented. This is overcome by multiplying the Fourier transform of each projection with a function that has a lower intensity at low spatial frequencies and a higher intensity at high spatial frequencies. Such a weighting function, or Fourier domain filter is plotted in Figure 2.14. It is clear that weighting each projection in this manner corresponds to the filtering part of the filtered backprojection algorithm.

Cone-beam and fan-beam reconstruction algorithms differ from the parallel-beam geometry illustrated in Figure 2.11 in that a modified backprojection formula is used to accommodate for the different ray-paths. Due to its simplicity of implementation, the most popular cone-beam reconstruction algorithm is that introduced by Feldkamp, Davis and Kress (FDK) [82]. Irrespective of its popularity, the FDK algorithm is considered an approximate algorithm, since the reconstruction result always deviates

from the measured object regardless of the measurement resolution. For small cone beam angles these differences are often negligible in terms of image quality. However, it has been shown that these differences can influence dimensional measurements [83], [84]. The approximation in the FDK algorithm stems from the fact that circular-trajectory cone-beam CT scans yield incomplete sampling of the object in the Fourier domain. Helical/spiral trajectories yield complete sampling of the object and therefore overcome this influence. The errors introduced by this approximation are termed Feldkamp artefacts and are described in Section 2.4.3.

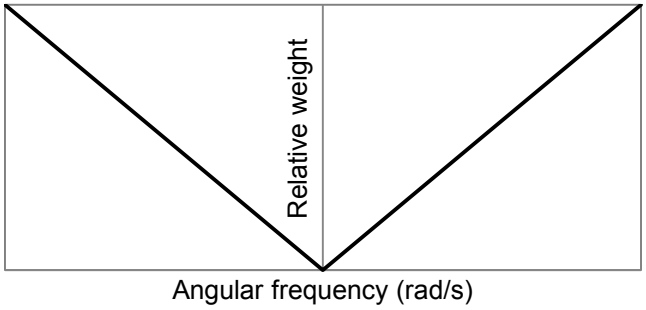

Figure 2.14 Ramp filter with a lower intensity at low spatial frequencies and a higher intensity at high spatial frequencies to weight projections prior to backprojection.

2.3.2 Iterative Reconstruction

X-ray CT has its origins in the medical industry, the long reconstruction times associated with iterative reconstruction methods were therefore unacceptable for clinical workflow. For this reason analytical reconstruction methods were preferred in the early days of CT due to shorter reconstruction times on standard computer workstations. Advances in modern computing and a relaxation of reconstruction times for industrial CT have since spurred a rediscovery of iterative methods [85].

Iterative reconstruction methods can be considered to consist of three steps repeated in an iterative loop: (i) forward projection through the reconstruction matrix, which generates artificial projections; (ii) comparison between artificial projections and actual projections, from which a correction term is calculated; (iii) reconstruction matrix update based on the correction term. The iterative loop is considered complete when a certain number of iterations have taken place, or the correction term converges to a predefined criteria.

The simplest form of iterative reconstruction is the algebraic reconstruction technique (ART) which is based on Kaczmarz' method for solving systems of linear equations. ART works on single X-rays and single projection values, whilst the simultaneous iterative reconstruction technique (SIRT) works through the entire projection set before updating the reconstruction matrix with the average update for each pixel. In the simultaneous algebraic reconstruction technique (SART) the reconstruction matrix is updated on a projection by projection basis [81].

With ART-based methods it is possible to model the geometry and physics of projection acquisition in the forward projection step; this is something that cannot be done using FBP. The acquisition model is used to improve the forward projection step, thus artificial projections better match real projections, leading to improved correction terms and ultimately better reconstructions. A projection acquisition model may consider the X-ray focal spot size, detector pixel size, polychromatic attenuation, scattering, and photon statistics. It is clear that as the model complexity increases the computational demand increases. As such, a balance between model complexity and reconstructed image improvement is required. Furthermore, the ability to model many of these physical processes is dependent on the availability of prior knowledge of the CT system and the object being scanned.

The advantages offered by iterative reconstruction methods are already being taken advantage of in the medical industry [59], and are beginning to be used in industrial CT [52]. However, iterative reconstruction methods have yet to be exploited for the purpose of dimensional metrology. Although, in a study by Yin et al. [86] an iterative reconstruction method for dimensional metrology has been proposed that directly reconstructs surfaces of single material objects. This direct surface reconstruction approach is very appealing for CT metrology because it mitigates the surface determination step required in the present workflow.

2.4 Artefacts

Artefacts are artificial features that appear in CT data but do not correspond to physical features of the object, and are considered detrimental to the quality of CT data. Artefacts arise from many different sources, including the hardware, the scanned object and the reconstruction algorithm. The artefacts described in this section have been identified in the literature as being significant to the field of X-ray CT for dimensional metrology. Descriptions of other less important artefacts can be found in ref. [59].

2.4.1 Beam Hardening

Beam hardening is the name given to the preferential attenuation of low energy X-rays. As a polychromatic beam of X-rays passes through matter, low energy photons are preferentially absorbed causing the mean energy of the X-ray spectrum to increase [48]. The more material an X-ray beam penetrates, the more low energy photons are removed from the spectrum, which makes it increasingly difficult to further attenuate the beam. This means the X-ray beam becomes more penetrating, or “harder”, at higher penetration depths, hence the term beam hardening. This effect is more easily understood by looking at how an X-ray spectrum changes after being attenuated by different thicknesses of material. Figure 2.15(a) to (c) show a 100 keV X-ray spectrum after penetrating different thicknesses of material. Figure 2.15(a) shows the original spectrum, Figure 2.15(b) shows the spectrum after penetrating 15 mm of aluminium; notice much of the low energy X-rays have been attenuated. Figure 2.15(c) shows the spectrum after penetrating 30 mm of aluminium; notice most of the X-rays are now above 55 keV. The mean energy of the spectrum increases from 42 to 58 to 65 keV.

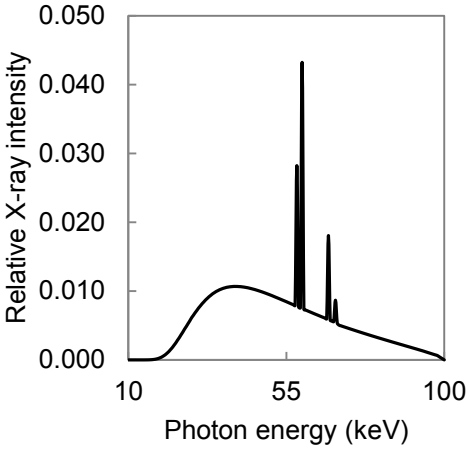

(a) 100 keV X-ray spectrum for a reflection type tungsten target with no additional filtration. Mean energy 42 keV.

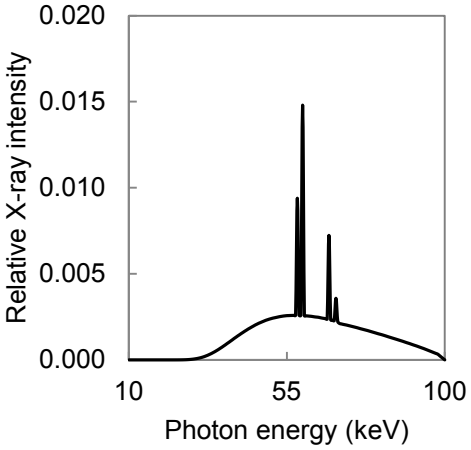

(b) Spectrum after penetrating 15 mm of aluminium. Mean energy 58 keV.

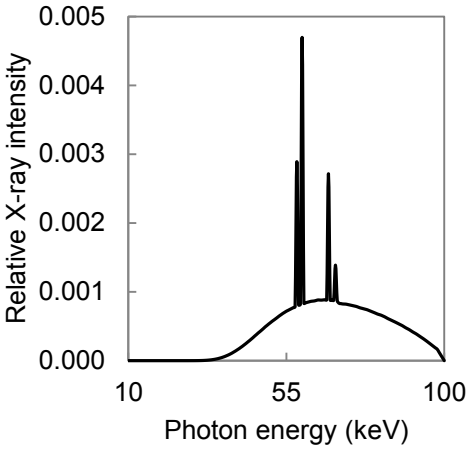

(c) Spectrum after penetrating 30 mm of aluminium. Mean energy 65 keV.

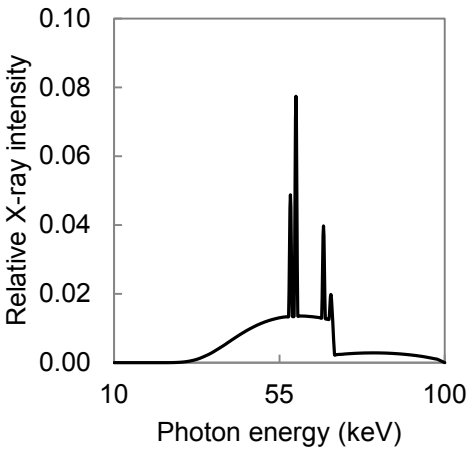

(d) Spectrum pre-filtered by 0.1 mm of tungsten. Mean energy 56 keV.

Figure 2.15 Graphs showing how an X-ray spectrum changes after penetrating different thicknesses of material. The y-axis of each plot changes to highlight the different energy distributions. The total number of photons will reduce as material thickness increases.

In Section 2.3.1 it was stated that analytic reconstruction methods consider projection values to be line integrals of the object function, i.e. X-ray attenuation is proportional to the thickness of material the X-ray beam has passed through. For a collimated beam of monochromatic X-rays this assumption holds and is governed by the Beer-Lambert law of attenuation, see Section 2.1.5, where the coefficient of proportionality is the materials linear attenuation coefficient μ. As a consequence of beam hardening, polychromatic X-ray attenuation is not proportional to X-ray path length, instead, a nonlinear relationship is seen between the two.

The results of measuring polychromatic X-ray attenuation for increasing thicknesses of aluminium are plotted in Figure 2.16. For the first few millimetres of material the relationship is particularly nonlinear, after which the relationship becomes increasingly linear. If the X-ray spectrum were to remain unchanged as it propagated through the increasing thickness of material, a linear relationship would be seen, as per the monochromatic line in Figure 2.16.

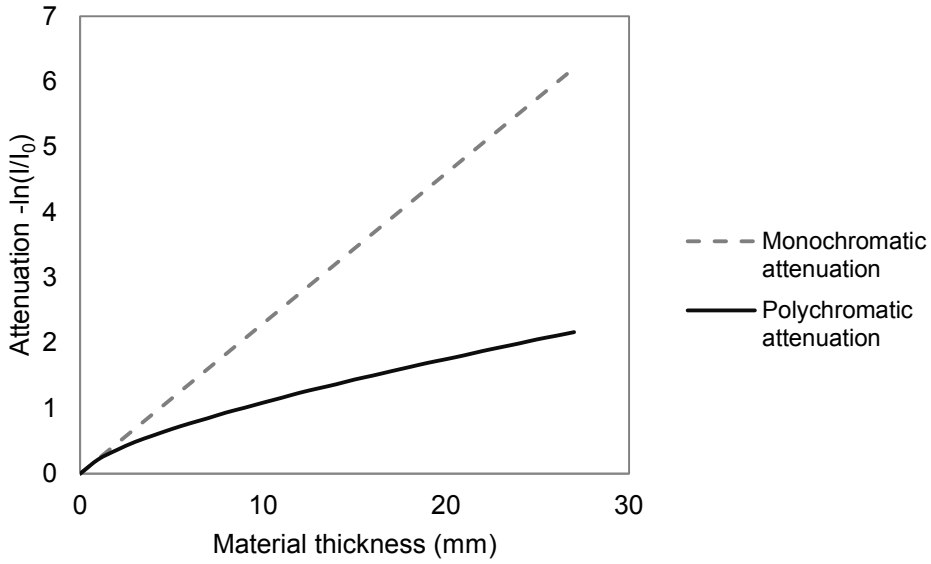

Figure 2.16 Graph showing the nonlinear relationship between scatter free polychromatic attenuation and material thickness for aluminium. Also shown is the linear relationship between monochromatic attenuation and material thickness.

As a consequence of beam hardening the outer edges of objects are reconstructed as being more attenuating than those at higher penetration depths. This effect occurs because the first few millimetres of material rapidly attenuate lower energy photons from the incident spectrum, whilst material at higher penetration depths are irradiated by harder X-rays. This effect is shown in Figure 2.17(a): the CT image shows a cross-section through an aluminium sphere with a nominal radius of 8 mm. An intensity profile drawn across the CT image is shown in Figure 2.17(d) displaying the raised intensity values at the outer edges of the sphere and lowered intensity values towards the centre. This artefact is termed cupping and gives a false impression of material density. Beam hardening also causes lowered intensity values between highly attenuating structures, this effect is shown in Figure 2.18 and is termed streaking. This effect occurs because highly attenuating structures harden the incident beam such that subsequent material, encountered after the structure, does little to further attenuate the beam, and is therefore reconstructed as having lower attenuation coefficients.

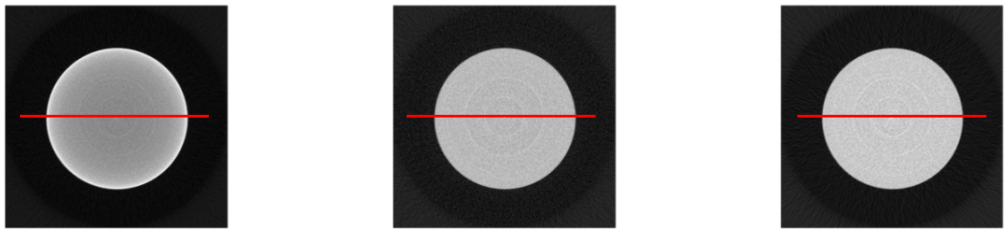

(a) Polychromatic data.

(b) Pre-filtered with 0.5 mm of copper.

(c) Corrected with a linearisation BHC.

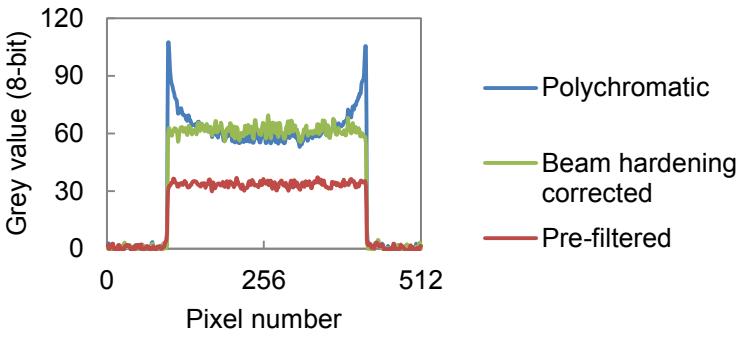

(d)

Figure 2.17 Comparison of line profiles drawn across CT images of an aluminium sphere. Both pre-filtration and beam hardening correction remove the cupping artefact.

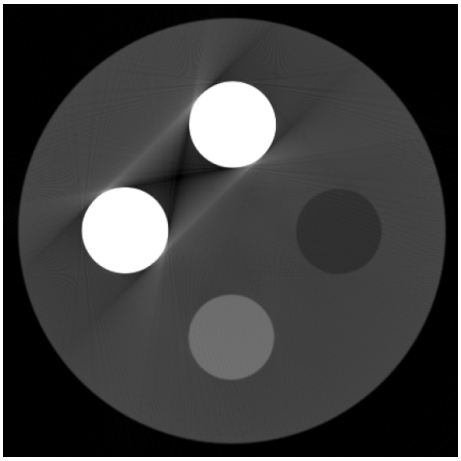

Figure 2.18 Streaking artefact induced by beam hardening between two copper rods. Figure taken from [87].

The importance of the problem posed by beam hardening is reflected in the high number of publications on the topic, with strategies for correcting the effect of beam hardening dating back to the early 70's [47]–[49]. The different approaches to correct beam hardening artefacts can be broadly classified as: hardware-based, pre-reconstruction and post-reconstruction.

Hardware-based methods are considered preventative in that they minimise beam hardening by removing low energy photons from the X-ray spectrum. This is achieved by placing a piece of attenuating material, termed a pre-filter, between the X-ray source and the object being scanned. The pre-filter acts to absorb low energy X-rays such that the beam incident on the object is pre-hardened. Typical filter materials include aluminium, copper and brass. Pre-filtering is able to suppress cupping artefacts, as shown in Figure 2.17(b) and (d).

More advanced so-called K-edge filters are employed in the field of mammography (radiographic imaging of the human breast) [88], [89]. A K-absorption edge is a sudden increase in the linear attenuation coefficient occurring at energies just above the binding energy of the K-shell electrons for a given material. K-absorption edges are used to suppress both low and high energy portions of the X-ray spectrum, yielding a narrow bandwidth X-ray spectrum such as that plotted in Figure 2.15(d). The 100 keV X-ray spectrum has been pre-filtered with 0.1 mm of tungsten, which acts as a band-pass filter giving a quasi-monochromatic X-ray spectrum.

The main disadvantage of using pre-filters is the subsequent reduction in X-ray intensity, which reduces the signal-to-noise ratio in the acquired projections and hence the reconstruction. This can be remedied by increasing the source current, or detector exposure time which increases the focal spot size and scan time respectively.

Perhaps the most widely adopted method to correct beam hardening artefacts is the linearisation method proposed in 1979 by Herman [47]. Linearisation is a pre-reconstruction method that aims to convert polychromatic attenuation into monochromatic attenuation. The required correction function is typically derived by measuring attenuation through a step wedge made of the same material as the scanned object and with the same source settings. A polychromatic attenuation verses thickness curve is then plotted, as per Figure 2.16. The straight line in Figure 2.16 represents the desired monochromatic attenuation; plotting polychromatic attenuation against monochromatic attenuation yields the required correction function which is typically approximated by a polynomial. Linearisation is very effective at removing cupping artefacts as shown in Figure 2.17(c) and (d). The two major drawbacks of linearisation are the requirement for the step wedge to be made from the same material as the actual object to be scanned, and the method only being suitable for single material objects. There are many variations of the method, most of which try to derive the required beam hardening correction function without the need for the additional step wedge measurement [51], [90]–[92].

Nalcioglu and Lou [49] proposed another long-standing approach to correct beam hardening artefacts for multi-material objects, termed the post-reconstruction method. The method relies on segmenting a CT image into its constituent materials and then estimating path lengths through each material by means of ray-tracing. With ray path lengths and knowledge of each material's attenuation coefficient, monochromatic projections can be estimated. The difference between the monochromatic and polychromatic projections gives the required correction term. Adding the correction term to the polychromatic projections and reconstructing yields artefact free CT images. Krumm et al. [90] proposed a variation of this method requiring no prior knowledge of the object's attenuation coefficients, as did Van Gompel et al. [91]. The main limitations of these iterative methods are the computational cost and achieving a good segmentation of the beam hardening contaminated data: If the beam hardening artefacts are severe, the segmentation will fail along with the beam hardening correction. Yang et al. [53] improved the speed of the post-reconstruction method by low-pass filtering and down-sampling the reconstruction

prior to segmentation. Yang et al. claim this leads to faster convergence of the algorithm because cupping artefacts are generally low frequency signals that require more iterations than high spatial frequency signals.

As mentioned in Section 2.3.2, one of the major attractions of iterative reconstruction methods is the ability to incorporate physical models in the forward projection step. Brabant et al. [52] significantly reduced the presence of beam hardening artefacts in CT data by incorporating a polychromatic attenuation model in the simultaneous algebraic reconstruction technique (SART). Other examples of incorporating polychromatic attenuation models in iterative reconstruction methods include the work of Elbakri et al. [93].

Beam hardening is a major source of image degradation. Correction or suppression of beam hardening artefacts certainly improves the appearance of CT data, which may aid subsequent qualitative visual inspection of the data. Inspection tasks that require the data to be segmented for quantitative analysis may also benefit from beam hardening correction, since streaking and/or cupping artefacts may prevent correct segmentation. It is for this reason beam hardening is thought to influence dimensional measurements: if beam hardening artefacts influence surface determination, it follows they influence dimensional measurements; surface determination is described in detail in Section 2.5.

A number of papers identify beam hardening as a factor that influences dimensional measurements [38], [45], [94]; however, few have attempted to study the influence in any detail. Wenig et al. [95] acknowledged the link between beam hardening and surface determination; a simulation-based study showed reducing beam hardening by spectrum pre-filtering improved measurement accuracy, this was attributed to the suppression of cupping artefacts. Suppes et al. [96] reasoned the grey value inhomogeneity caused by beam hardening influenced the position of the determined surface; an experimental study showed correcting for beam hardening reduced both errors in form and length measurements. The most comprehensive work on the subject is that of Dewulf et al. which has been published in parallel with this work. In their first of two papers on the subject [54], the diameter of a precision rod was measured before and after being surrounded by an aluminium cylinder, then by a steel cylinder. Introducing the different surrounding materials had little influence on the measurement of the rod's diameter. However, after applying a linearisation beam hardening correction, introducing the different surrounding materials significantly changed the

radius measurement; the beam hardening correction introduced a measurement error up to 30 μm for a rod diameter of 4 mm ± 1 μm. In the follow up paper [55] the experiment was repeated but in simulation and the same effect was observed. Dewulf et al. concluded that applying an incorrect beam hardening correction can lead to large measurement errors and proposed a method to derive a beam hardening correction that does not have this unwanted effect.

In addition to the group of Dewulf et al., Zhang et al. [56] have derived a beam hardening correction for CT metrology. Zhang et al. show their beam hardening correction reduces errors when measuring the diameter of precision steel spheres and reduces length measurement errors for more complex workpieces. Bartscher et al. [43] have studied how applying 'soft' and 'hard' beam hardening corrections influence size and form measurements of internal dimensional features. Their results show that beam hardening correction predominantly influences threshold sensitive dimensions such as the radius of a cylinder, whereas threshold independent dimensions such as the distance between the centres of two cylinders are affected to a lesser degree (see Section 2.5 for a description of threshold dependent/independent dimensions).

The main shortcoming of the work of Dewulf et al. and Bartscher et al. is the use of low (2^{nd}) order polynomials for the linearisation beam hardening correction; low order polynomial corrections are only sufficient for low-resolution medical CT images [47], for industrial materials such as aluminium and steel, polynomials of at least 8^{th} order should be used [97]. Additionally, in both studies the beam hardening corrections are not justified; the correction functions should be derived based on scatter-free attenuation measurements made under the same conditions as the actual scan, or using a validated polychromatic attenuation model. Finally, all the aforementioned experimental studies neglect the contribution of scatter to the nonlinearity of measured attenuation. Scatter must not be overlooked in this way otherwise beam hardening will be overcorrected. The effects of scatter are described in the next section.

2.4.2 Scatter

Scattered X-rays are those that have undergone one or more scattering interaction (see Section 2.1.4) and have therefore deviated from their intended incident path, whilst primary X-rays are those that have not undergone a scattering interaction. Scattered radiation may originate from the object being scanned, from the environment (X-ray chamber, manipulator and detector housing), or within the detector itself.

Scattered X-rays that fall incident on the detector contribute a significant, but unwanted, signal to the detector output. For common engineering metals such as aluminium, titanium and steel, the interaction probability of Compton scattering is greater than that of photoelectric absorption for energies greater than 100 keV. Scatter signals raise intensity values and therefore lower attenuation values leading to an additional nonlinearity in the relationship between X-ray attenuation and material thickness. As a consequence, scatter induces similar artefacts to those caused by beam hardening; namely cupping and streaking. Furthermore, since scatter has been shown to be a low spatial frequency background signal in projections, scattered radiation also induces a general loss of contrast in CT data [57].

The problem posed by scattered radiation is as long-standing as that of beam hardening. However, the problem of scatter has perhaps become worse of late through the use of cone-beam CT. Scatter signals are larger for cone-beam CT than fan-beam CT because a larger portion of the object is irradiated in the former, leading to an increased number of potential scattering sources.

As for beam hardening, the importance of the problem of scatter is reflected by the attention its correction and suppression have received in the literature, methods for correcting the effect of scatter date back to the early 80's [50], [98], [99]. Broadly speaking, scatter is either suppressed by employing apparatus to prevent scattered radiation reaching the detector, or scatter signals are estimated by various means and subtracted from projections prior to reconstruction.

A simple approach to reduce detected scatter signals is to increase the object to detector distance, termed the air-gap. This method is quite effective because X-ray intensity follows the inverse square law; by increasing the air gap, the intensity of scatter signal decreases. However, increasing the air-gap also reduces the intensity of primary X-rays, so one has to carefully choose an air-gap to minimise the ratio between scattered and primary X-rays.

Anti-scatter grids are a long-standing hardware-based approach to minimise scatter signals. An anti-scatter grid is an array of high aspect ratio lamellae of highly X-ray absorbent material, such as lead, tungsten or gold that is placed directly in front of the detector. Assuming the lamellae are aligned with the direction of the primary X-rays, any X-rays that deviate from this direction will be absorbed, see Figure 2.19. Clearly if the lamellae are not well aligned, primary radiation will also be absorbed. In the medical industry, anti-scatter grids employed in fan-beam CT systems have been

shown to reduce scatter-to-primary ratios and increase signal-to-noise ratios [100]. However, anti-scatter grids employed in cone-beam CT have been shown to have the unwanted effect of reducing SNRs, but have been successful in reducing the presence of cupping artefacts [101].

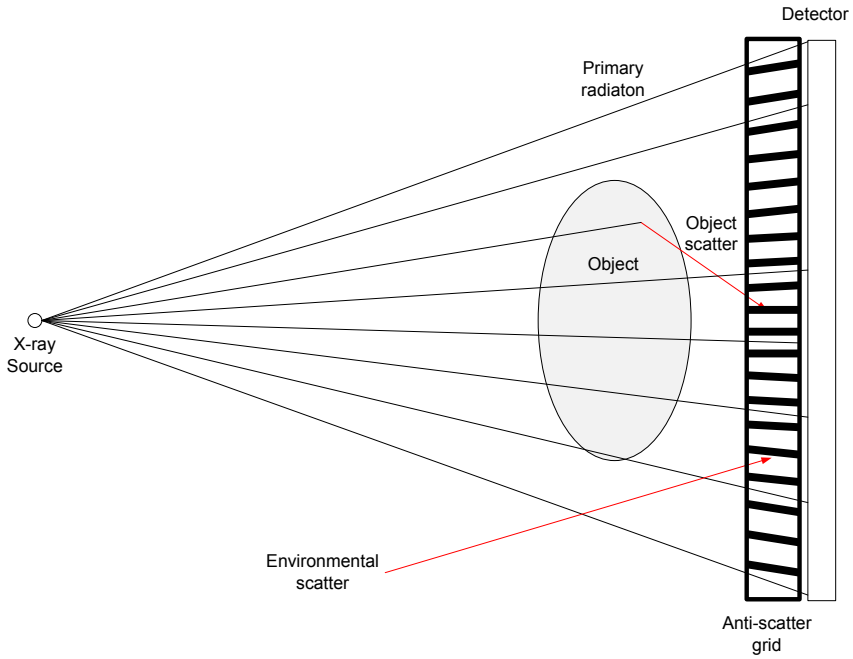

Figure 2.19 Illustration of an anti-scatter grid, adapted from Schorner [57].

Generally speaking, scatter correction schemes aim to estimate the scatter signal in each projection. Subsequent subtraction of the scatter estimate from each projection yields the required primary-only signal that leads to reconstructions free from scatter artefacts. Scatter signals have been estimated by direct measurement, analytical simulation, Monte Carlo simulation, or by approximation with point spread functions.

Direct measurement of scatter signals generally involves placing a lead disk between the X-ray source and the object; assuming the lead disk absorbs all X-rays incident upon it, any signal measured in it's shadow must be due to scattered radiation. Such methods have a long history of use and are well understood [98]. With an array of stoppers, scatter can be measured across the field of view, these scatter measurements may then be interpolated to give a scatter estimate for an entire projection [58], [102], [103].

Equations to calculate the probability of a photon scattering at a given angle, for a given material, and a given photon energy are given in Section 2.1.4. These equations may be used to calculate scatter signals analytically, provided the object's material

distribution is known in advance. Analytical simulations are typically limited to first order scattering interactions, else the complexity of the simulation grows rapidly. Studies have shown analytical scatter simulations to be in good agreement with Monte Carlo simulations [104], which are generally regarded as the gold standard for investigating X-ray scattering. Advances in computer processing power enable comprehensive Monte Carlo simulations that include scatter signals generated by the object, the environment and the detector. Schuetz et al. [105] conducted a very thorough investigation on the impact of environmental scatter for industrial CT using Monte Carlo simulation. A number of 'hybrid' simulations have been proposed that combine coarse Monte Carlo simulations with deterministic simulations; these have shown good agreement when compared to full-scale Monte Carlo simulations [106].

Scatter signals have been modelled as primary signals convolved with a scattering point spread function (PSF) [107]. With an estimate of the scattering PSF, the primary signal can be recovered via deconvolution. Scattering PSFs have been estimated by direct measurement, analytical calculation and Monte Carlo techniques. Deconvolution methods are simple to implement, but they rely on the assumptions of a symmetric, spatially invariant PSF with an amplitude that depends on object thickness. Sun et al. [108] have shown scattering PSFs broaden with increasing material thickness, and that symmetric, spatially invariant PSFs do not consider the attenuation suffered by scattered X-rays as they propagate through the object. Sun et al. overcame these limitations by developing an adaptive scatter PSF that requires additional empirically derived parameters.

As for beam hardening, there are a number of papers that identify scattered radiation as a factor that can influence CT dimensional measurements. It has been suggested that scatter blurs edges and renders flat surfaces bent [26], [57], [109]; however, to the authors' best knowledge there are no dedicated studies on the influence of scatter in X-ray CT for dimensional metrology. Although one paper suggests a study on this topic [110], it contains not one dimensional measurement. Clearly, given the impact scattered radiation has on CT image quality, there is much work to be done in this area.

2.4.3 Feldkamp

For circular-trajectory cone-beam CT the acquired data is inherently incomplete, in that some of the object's three-dimensional Fourier transform is not sampled. This means the reconstruction result always deviates from the measured object, regardless of the measurement resolution. For circular-trajectory cone-beam CT only the Fourier data on the central slice is sampled completely, whilst the sampling of data further from the central slice becomes increasingly incomplete [111]. As such, so-called Feldkamp artefacts are seen at the top and bottom of reconstructed volumes, see Figure 2.20. However, for small cone-beam angles these differences are often negligible in terms of image quality.

A helical scan trajectory yields complete sampling of the object's three-dimensional Fourier transform and thus overcomes Feldkamp artefacts. A helical scan trajectory combines simultaneous rotation and translation of the object relative to the stationary X-ray source and detector and is illustrated in Figure 2.21. There are other scan trajectories that yield complete Fourier sampling, but helical scanning seems to be the most popular. Helical scanning is slowly being adopted by instrument manufacturers, but the benefit for dimensional measurements is still unclear. Muller [42] claimed Feldkamp artefacts caused larger measurement errors in high magnification scans (large cone-angle) compared to lower magnification scans (smaller cone-angle). Two simulation-based studies compared measurements of length, size and form for data acquired with circular and helical-trajectories. However, the results of the two studies are contradictory: in one study helical CT reduced length error and increased form error compared to circular CT [84]. Whilst in the second study helical CT increased size error but reduced form error [83]. Clearly more work needs to be conducted in this area, but since helical scanning and the respective reconstruction algorithms are not commonplace, progress in this area is likely to be slow.

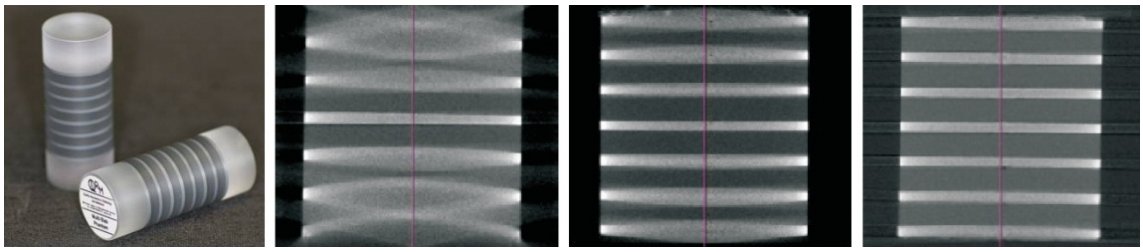

Figure 2.20 Leftmost: test object for demonstrating Feldkamp artefacts. From left to right: CT data acquired with a cone angle of 30, 11 and 5°. Images taken from QRM GmbH [112].

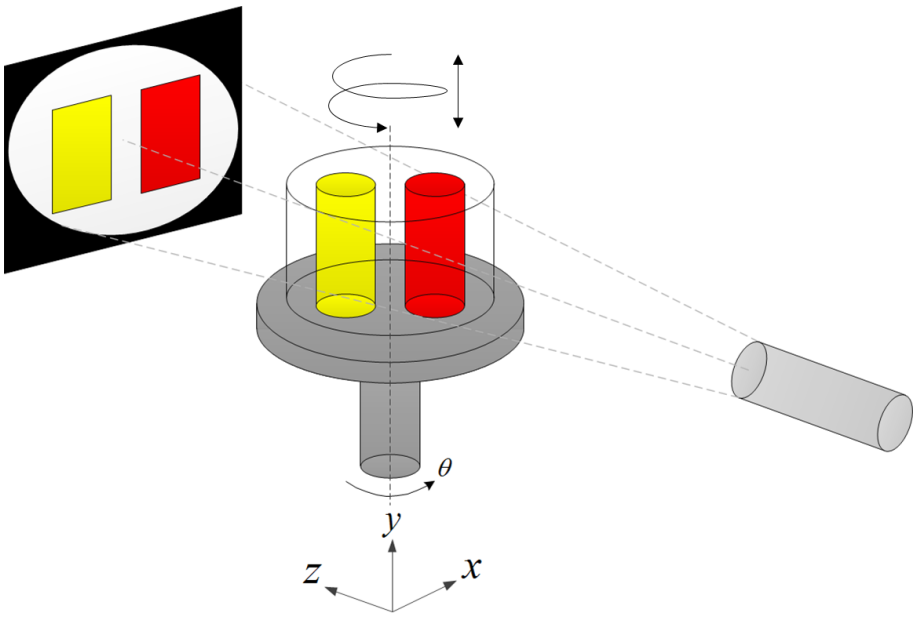

Figure 2.21 Illustration of helical scan trajectory. This trajectory requires both translation and rotation.

2.4.4 Geometric Misalignment

The standard FDK backprojection formula assumes perfect alignment between the X-ray focal spot, axis of rotation and the detector; hence the quality of CT data relies strongly on minimising misalignments in the system's geometry. In practice it is impossible to avoid misalignment, thus several authors have developed procedures and algorithms to estimate misalignment parameters [74], [113], [114].

Having estimated these misalignment parameters, precise translation or rotation of the detector, X-ray source and rotation axis is not always possible unless such adjustment is built into the system. As a consequence of this limited flexibility, misalignments may be corrected through the use of a modified backprojection algorithm, as per Sun et al. [115]. Most reconstruction software packages are able to estimate the position and tilt of the projected axis of rotation; knowledge of these two parameters is sufficient to reconstruct CT data of a quality acceptable for most inspection tasks.

If geometric misalignment is not corrected for, artefacts will be present in the CT data. Depending on which misalignments are present, artefacts vary from the doubling of edges, changes of magnification throughout the CT volume, and a general loss of spatial resolution, see Figure 2.22.

Sun et al. [113] show mathematically the geometry of a CT system can be fully described by six parameters, these being the six degrees of freedom of the detector: three-translations and three rotations. For an ideal CT system the X-ray focal spot, centre of rotation and the centre of the detector all fall on a straight line. The axis of rotation is projected onto the central column of the detector and is perpendicular to the detector rows, implying there is no in-plane detector tilt. The detector is not rotated about any of its columns or rows, implying there are no out of plane detector tilts. The distance between the X-ray focal spot and the centre of the detector are known, as is the distance between the X-ray focal spot and the centre of rotation, these geometric parameters are illustrated in Figure 2.23.

Minimising geometric misalignment is of great importance in X-ray CT for dimensional metrology. A very thorough simulation-based study by Kumar et al. [116] showed the influence each misalignment has on length measurement error. The results showed out of plane detector tilts have a significant influence on dimensional measurements. Kumar et al. recommend these tilts need to be less than 1° for accurate dimensional measurements. This is an interesting result as many of the aforementioned methods for estimating geometric misalignment state the out of plane detector tilts have little impact of CT image quality.

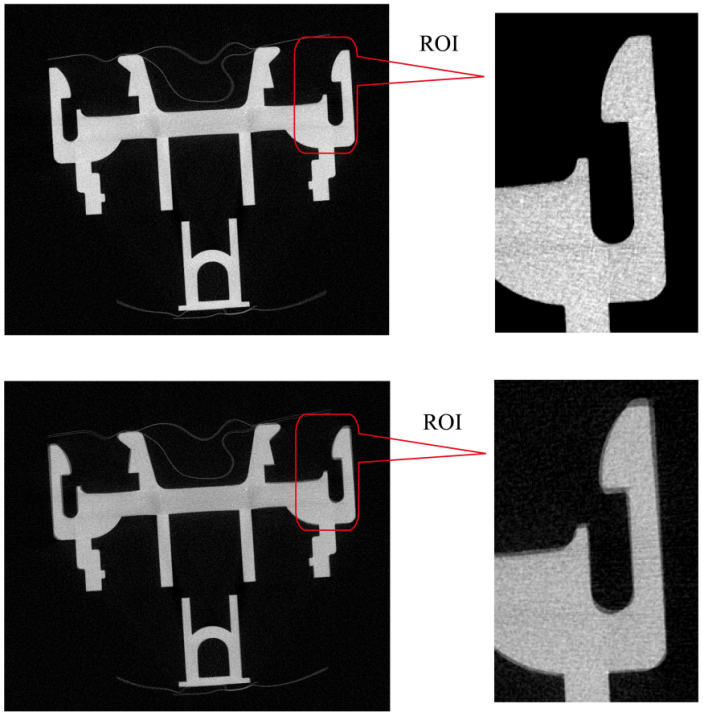

Figure 2.22 Top: CT image reconstructed with correct alignment. Bottom: CT image reconstructed with incorrect alignment of CT hardware. Taken from Yang et al. [117].

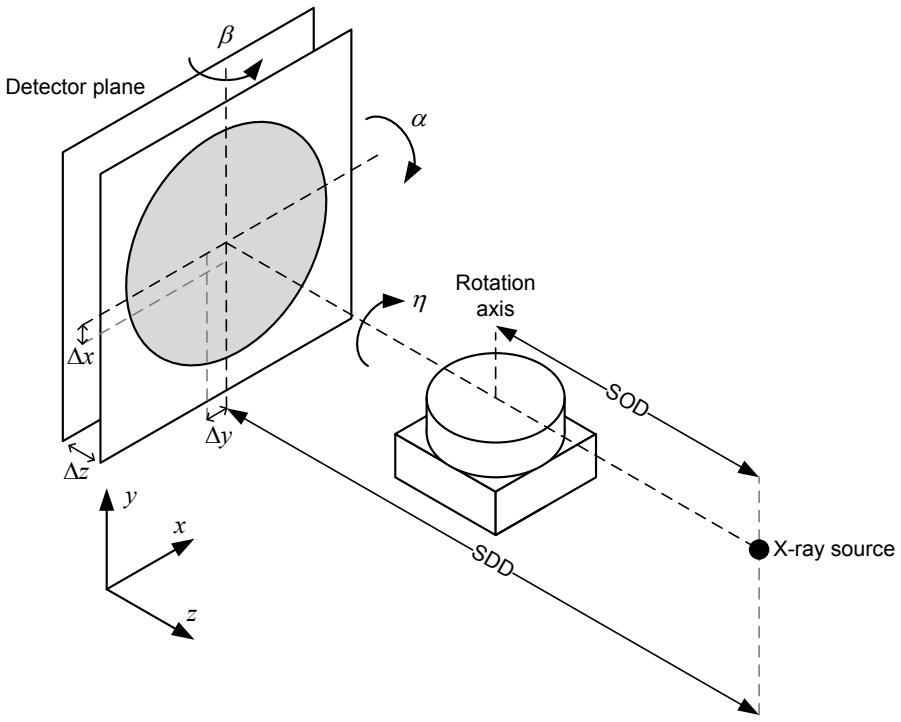

Figure 2.23 Illustration of cone-beam CT geometry. The six misalignment parameters are $\Delta x, \Delta y, \Delta z, \alpha, \beta, \eta$.

2.5 Estimating Surfaces from Volumetric Data

Having acquired a set of projections and reconstructed them into a CT volume, the object's surfaces need to be estimated such that its dimensions can be evaluated. Estimating surfaces from a CT volume or CT image is referred to here as surface determination, but is essentially 3D or 2D edge detection.

Edge detection is a long-standing research topic in the field of image processing and has been reviewed elsewhere [118]. As such, only two approaches to edge detection are described here, these being the two most commonly used in X-ray CT for dimensional metrology. The methods include a histogram-based image segmentation approach termed the ISO50 method, and an edge detection method that evaluates the grey value gradient in a small neighbourhood of pixels or voxels termed the local method.

The reason these two surface determination methods are used for CT metrology is because they are the methods provided by CT metrology software companies such as VGStudio MAX (Volume Graphics GmbH, Heidelberg, Germany) [119]. Obviously the commercial algorithms are proprietary, so details of their inner workings are not disclosed to users. In order to understand how scatter and beam hardening influence dimensional measurements the finer details of the surface determination algorithms need to be known. To overcome the 'black box' posed by commercial algorithms the following descriptions are of the authors own algorithms used throughout the thesis. They are implemented based on the literature and have been tested against commercial algorithms and found to be in good agreement.

2.5.1 Gradient-Based Edge Detection (Local Method)

An edge in a 1D, 2D or 3D image is defined as the position at which a change in contrast occurs. In CT the intensity of a pixel or voxel corresponds to the linear attenuation coefficient μ; hence a change in contrast corresponds to a change in material. The point at which this change occurs must therefore represent a point on the object's surface. The terms edge and surface are used interchangeably throughout this work. To detect the position of an edge first order differentiation is typically used since this emphasises change.

In Figure 2.24 the true position of a 1D edge is depicted alongside its discretised version. Taking the first derivative of the discrete intensity signal gives a signal where the largest response corresponds to the largest change in intensity. A classic approach to estimate the sub-pixel edge position is to fit a polynomial to the gradient values in a small (3 to 5 pixel) neighbourhood, the turning point of the polynomial gives the sub-pixel edge position [120]. Alternatively, Gaussian functions have been used instead of polynomials [118].

This gradient-based approach lends itself to edge detection in images of higher dimensions. The 2D gradient magnitude is calculated as $\sqrt{Gx^2 + Gy^2}$ where Gx and Gy are the 1D gradients in the x and y directions. For a 3D image the additional z gradient is computed. In the 2D and 3D case, edges also have a direction, given by $\theta = \tan^{-1}(Gy/Gx)$ and $\phi = \tan^{-1}\left(Gz/\sqrt{Gx^2 + Gy^2}\right)$ where θ and ϕ are illustrated in Figure 2.25. Since applying a gradient operator amplifies noise in an image, the data is typically smoothed first. The gradient magnitude of a measured CT image is shown in Figure 2.27(b).

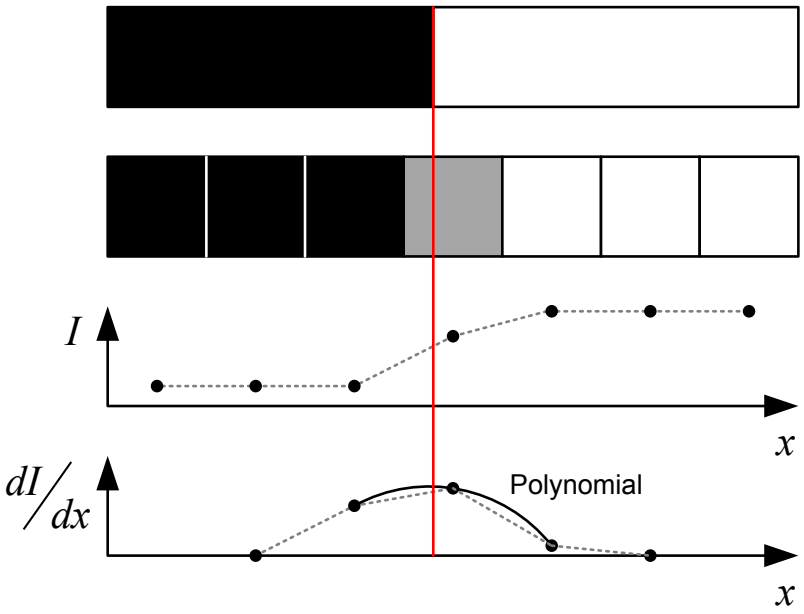

Figure 2.24 Gradient-based approach for detecting sub-pixel edge position. The top two images show the true position of the edge and its discrete representation. The bottom two images show the intensity profile and its first derivative. Figure adapted from [118].

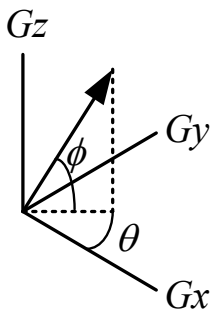

Figure 2.25 Vector representation of 2D and 3D gradient components, resultant gradient magnitued and gradient direction.

In order to minimise the number of false edges identified, the gradient operation is followed by an edge thinning algorithm called non-maximum suppression (NMS). NMS identifies pixels where the gradient magnitude is a maximum. This is achieved by comparing the magnitude of each gradient value to its neighbours, if it is the biggest in its neighbourhood, it is the local maximum. A scheme for 2D NMS is illustrated for a 3 by 3 pixel region in Figure 2.26. The gradient magnitude is interpolated in the positive and negative gradient directions, if these interpolated values are both less than the magnitude of the central pixel, the central pixel is a local maximum, else the pixel value is set to zero. Having performed NMS both strong and weak edges that are thin should remain; thin implies one pixel thick, or one voxel thick. A non-maximum suppressed gradient magnitude image is shown in Figure 2.27(c).

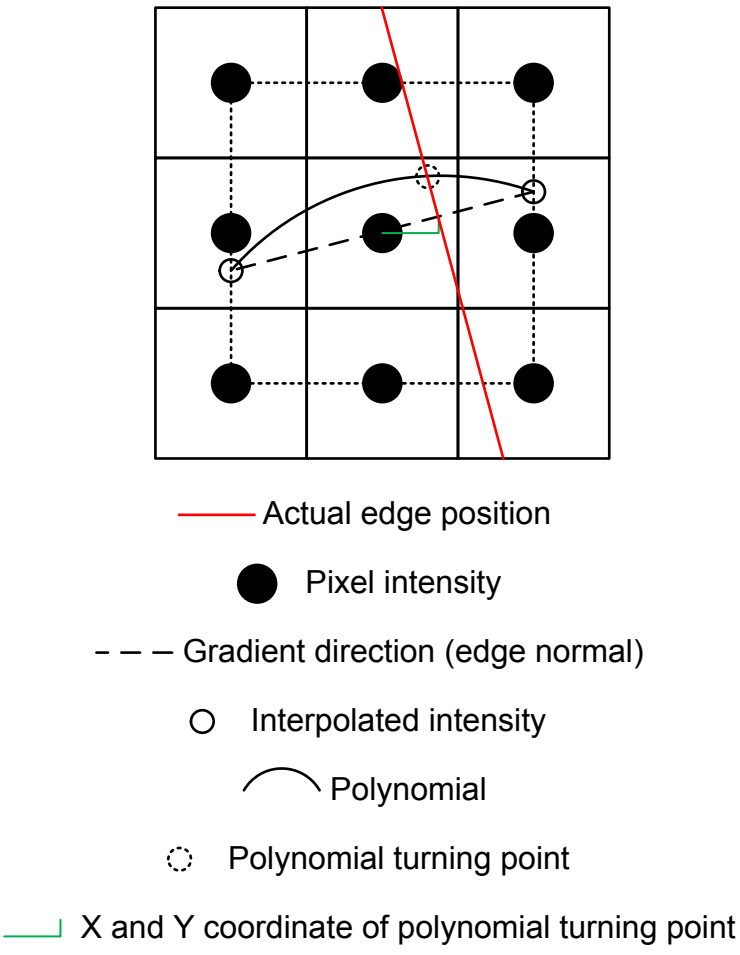

Figure 2.26 Illustration of non-maximum suppression and sup-pixel refinement for a 2D image.

To suppress any remaining noise in the gradient magnitude image, thresholding is performed with hysteresis. In hysteresis thresholding two thresholds are defined, an upper and a lower. All pixels or voxels with values greater than the upper threshold are considered edge points, as are any pixels or voxels that are connected to those points that are above the lower threshold. The application of thresholding to the non-maximum supressed image is shown in Figure 2.27(d).

The result of the above steps is an image or a volume of thin edges. For each edge point the sub-pixel refinement can then be performed. This process is also illustrated in Figure 2.26. A second order polynomial is fitted to the interpolated gradient magnitude in the positive and negative gradient direction. The turning point of the polynomial gives the sub-pixel edge position. The resulting sub-pixel surface points of the CT image are shown in Figure 2.27(e).

The general approach to edge detection described above was largely laid out by Canny in his Masters thesis and is known as the Canny edge detector [121]. In terms of practical implementation, the smoothing operation can be performed by convolving the image or volume with a Gaussian operator, whilst the gradient operation can be performed by convolving the image with the derivative of the Gaussian operator. The size of these operators influences both the precision and the accuracy of the edge detector. Larger operators suppress noise but compromise accuracy, i.e. edges are detected in the wrong position. Throughout this work a 5×5 operator is used for 2D data and a 5×5×5 operator for 3D data. The size of the operator was chosen based on experimentation; ideally a 3×3 operator would be chosen, but this size of operator led to noisy surfaces.

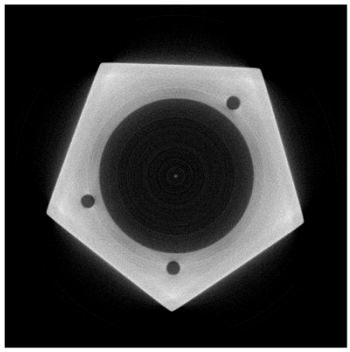

(a) Grey value CT image.

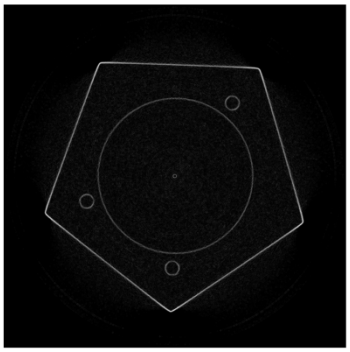

(b) Magnitude of grey value gradient.

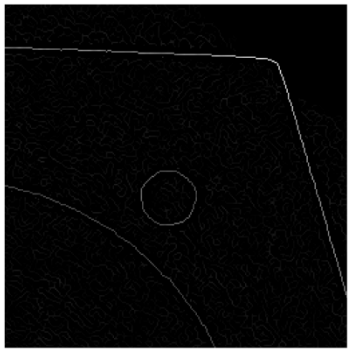

(c) Magnitude of grey value gradient after non-maximum suppression.

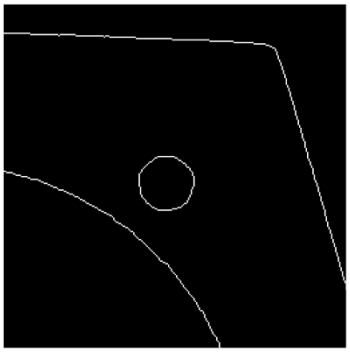

(d) Hysteresis thresholding gives thin binary edges.

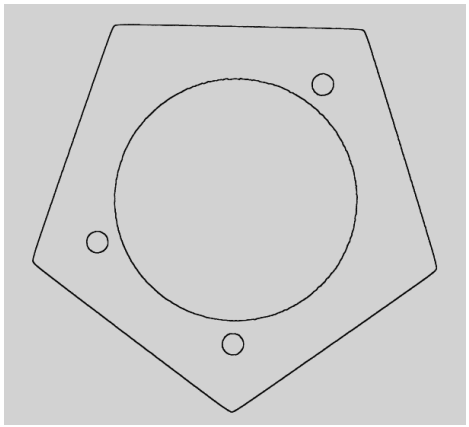

(e) Sub-pixel refinement gives surface points.

Figure 2.27 Step by step processing of the local surface determination method used throughout this work.

2.5.2 Histogram-Based Edge Detection (ISO50 Method)

In classic 2D image processing a grey value histogram may be used to select a threshold to segment an image, thus extracting an object from its background [122]. Early approaches to visualising volumetric CT data relied on the generation of an isosurface: a surface that connects points that have the same value. Algorithms for generating isosurfaces include the marching cubes algorithm [123], which requires a user defined threshold, or isovalue. Having identified this isovalue, highly detailed triangulated surfaces can be generated revealing complex 3D structures of the scanned object. A grey value histogram is an efficient way to select an isovalue. An ideal grey value histogram will have two well defined peaks, one for the background (air) grey values, and one for the object (material) grey values, this assumes an object of a single material, see Figure 2.28. Between the two peaks exists a valley which corresponds to a grey value that segments the data. Alternatively, the point halfway between the two peaks is calculated, this being termed the ISO50 value, which is often used to define the surfaces of a single material object in X-ray CT for dimensional metrology.

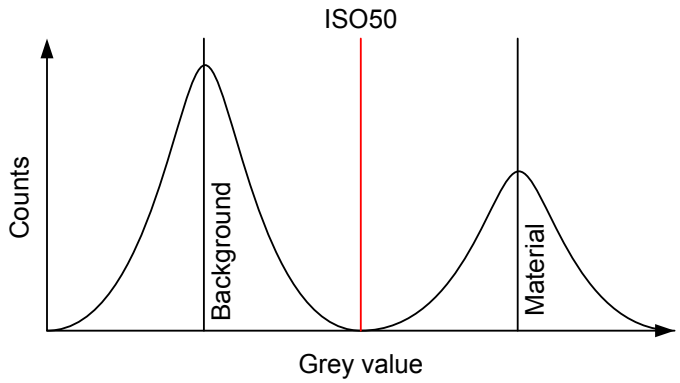

Figure 2.28 Illustration of an ideal grey value histogram of an image/volume composed of two grey value classes; background and material. The data can be segmented based on an isovalue.

In order to use the ISO50 value to generate a set of sub-voxel surface points, the following steps may be taken. First, the volume is segmented into material or background based on the ISO50 value: if the voxel contains a grey value greater than or equal to the threshold it is considered material, else it is background. This yields a binary volume. A binary edge is evaluated by subtracting an eroded binary volume from the original binary volume, were erosion is a morphological operator [124]. Having evaluated the grey value gradient direction as per the local method, intensity values are interpolated in the gradient direction for each voxel that lies on the binary edge. Figure 2.29 shows the 2D equivalent of this interpolation step. Finally, the point at which the ISO50 value lies on the interpolant is found and corresponds to a surface point. The application of this method to real CT data is shown in Figure 2.30(a) through (d).

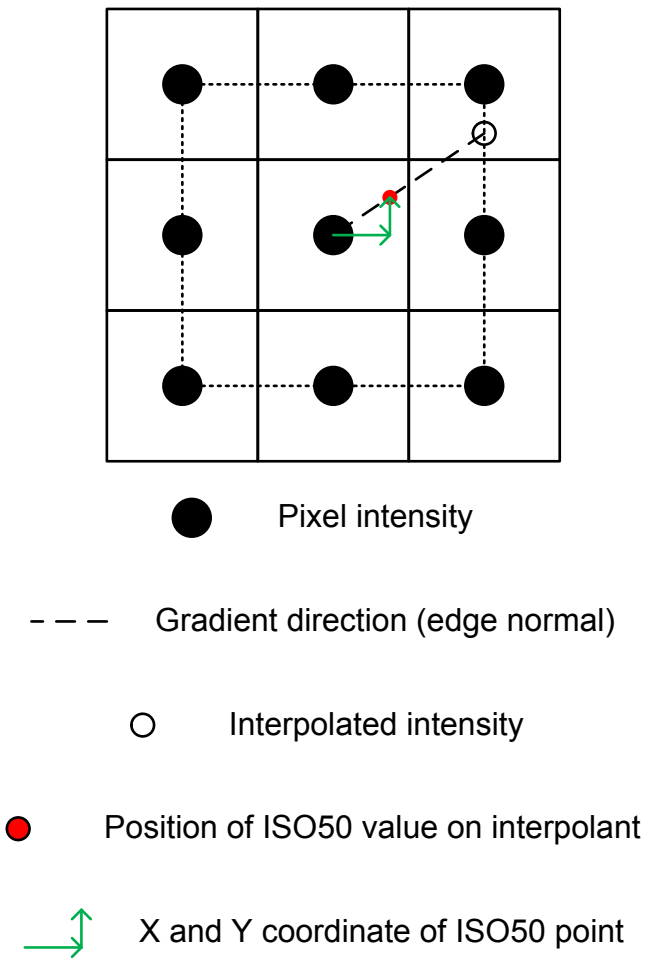

Figure 2.29 Illustration of sub-pixel refinement of the ISO50 method.

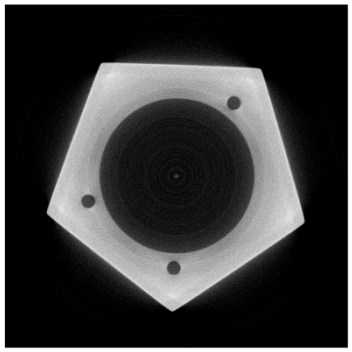

(a) Grey value CT image.

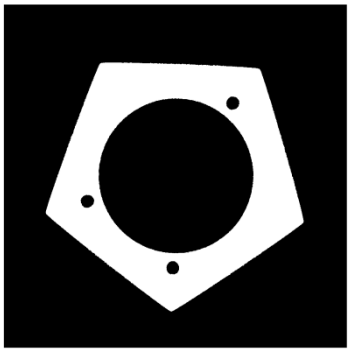

(b) Binarised CT image.

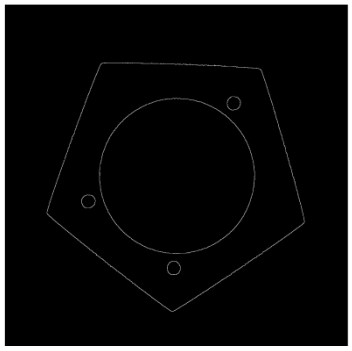

(c) Thin binary edge.

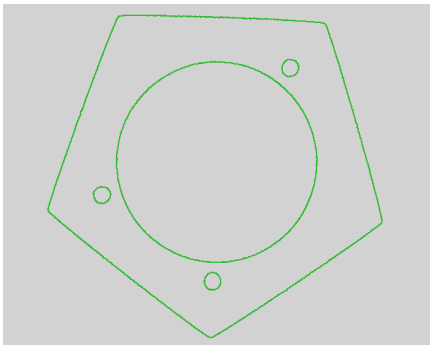

(d) Sub-pixel refinement gives surface points.

Figure 2.30 Step by step processing of the ISO50 surface determination method used throughout this work.

2.5.3 Surface Determination for Dimensional Measurements

Approaches to surface determination other than those just described include the generation of triangulated surfaces using advanced surface generation algorithms for both single [125], [126] and multi-material objects [127]. A study by Yague-Fabra et al. [128] showed that using a local surface determination method leads to more repeatable measurements than an ISO50 method, whilst Carmignatio et al. showed the measured dimensions of and object can change significantly by varying an isovalue threshold [46]. These studies highlight the importance of surface determination in X-ray CT for dimensional metrology; clearly any factor that influences surface determination will influence the measurement result.

A dimensional feature such as the radius of a sphere is considered highly sensitive to the determined surface. Clearly an error in the surface position will directly impact the measured radius. On the other hand, the centre point of the sphere will be less affected, hence the distance between the centres of two spheres is considered robust to the influence of surface determination. Centre-to-centre distances are used throughout X-ray CT for dimensional metrology to test and correct for scale errors and other systematic errors [42]. This type of threshold independent distance is used in Chapter 4 to correct scale errors, whilst the influence of scatter and beam hardening is evaluated using threshold sensitive dimensions.

2.6 Chapter Summery

In this chapter the basics of X-ray physics have been introduced alongside the key components of a CT system. An illustrative example of reconstruction has been given together with a description of how artefacts can degrade the quality of CT data. The last section considered how an object's surfaces may be estimated from CT data.

In each section factors that may influence dimensional measurements have been identified. Those acknowledged include: focal spot drift, geometric distortions in the detector, positional errors and run-out of the mechanical axes, the inexactness of circular-trajectory cone-beam CT, the presence of artefacts in CT data due to beam hardening, scatter and geometric misalignment, and the potential for an object's surfaces to be incorrectly defined. These represent only a few of the factors that can influence a dimensional measurement.

From the reviewed literature it is clear there are a number of gaps in the knowledge. Areas that require further investigation include: the impact the reconstruction method has on dimensional measurements; the influence beam hardening, scatter and Feldkamp artefacts have on dimensional measurements; methods for traceable geometric alignment of the CT system need to be developed; and the influence that surface determination has on dimensional measurements needs to be better understood. In light of these research directions, the influence of scatter and beam hardening are chosen for study in the present work.

Scattered radiation and beam hardening are widely acknowledged as factors that influence dimensional measurements; however, the mechanisms through which they influence dimensional measurements are largely unknown. The purpose of this thesis is to study the influence of scattered radiation and beam hardening and develop a better understanding as to how they influence dimensional measurements.

Chapter 3 Reference Workpieces and CT Measurement Strategy

In this chapter, the three reference workpieces used throughout this thesis are introduced. Two of the workpieces are used for voxel size determination in Chapter 4, whilst the third is designed to induce scatter and beam hardening artefacts and is made use of in Chapter 5. The reference dimensions of each workpiece are measured with a coordinate measuring machine (CMM) and the measurement uncertainty evaluated according to relevant international standards. The specification of the CT system used throughout this thesis is then presented, alongside the strategy for measuring each workpiece via X-ray CT.

3.1 Review of Existing Reference Workpieces

A number of reference workpieces can be found in the literature. The function of these workpieces is usually: (i) to test the accuracy of CT-based measurements under ideal (artefact-free) conditions, and (ii) to test how the workpiece material and geometry influence dimensional measurements. Examples of such workpieces are given in Figure 3.1.

The ‘ideal’ workpieces (left hand column of Figure 3.1) typically feature ruby spheres mounted on a carbon fibre frame. The distance between the centres of two spheres can be measured with low uncertainty using a CMM; by comparing CT and CMM measurements, systematic errors in the CT measurements can be studied and corrected. Ruby spheres are usually chosen as they can be manufactured with low form errors, and carbon fibre is chosen due to its low coefficient of thermal expansion, whilst both ruby and carbon fibre induce minimal artefacts.

The ball plate and CT tree (shown in Figure 3.1) were developed at the Technical University of Denmark [42] for the purpose of testing and characterising CT systems for dimensional metrology. These workpieces are similar in design to conventional ball plates and hole plates used in classical coordinate metrology. The CT tetrahedron was developed at the University of Padova and was used in the first international comparison on X-ray CT for dimensional metrology [129]. The Metrotom-Check is a reference workpiece developed by Zeiss, Germany, and consists of 27 ruby spheres mounted on carbon fibre tubes [130]. The alumina sphere tetrahedron was developed

at the National Physical Laboratory in collaboration with the University of Manchester [131]; the three spheres are not cemented together, but the workpiece is dismountable, the polystyrene base is designed to ensure all three spheres are contacting. The voxel size of a scan can be determined using the distances between the spheres, whilst the calibrated radii of the spheres can be used to determine an isovalue threshold for surface determination.

The workpieces shown in the right hand column of Figure 3.1 resemble industrial components. Such workpieces are used to test the performance of a CT system for real-world measurement tasks. These workpieces are usually machined from aluminium, titanium or steel. The more complex workpiece geometries are designed to vary X-ray path lengths in order to induce scatter and beam hardening artefacts.

The hole plate was developed at the Physikalisch-Technische Bundesanstalt (PTB), Germany in cooperation with the National Metrology Institute Japan (NMIJ). The workpiece features 28 internal cylinders and was designed to evaluate the material influence in CT metrology [43]. Step cylinders have been used in various studies [132]–[134] and are recommended in VDI/VDE 2630 Part 1.3 for evaluating the material and geometric influence of the workpiece in CT metrology [135]. The dismountable workpiece, developed by ACTech GmbH, Germany and the PTB, consists of four segments; dismantling the workpiece allows the internal features to be measured using a CMM [136]. The aluminium block workpiece was originally designed to induce various beam hardening artefacts to test the performance of artefact correction algorithms [137]. It is particularly difficult to measure using CT due to the severity of the artefacts it induces. The sphere calotte cube consists of a regular 5×5 array of calottes arranged on three faces of a titanium cube. The calotte cube and its variants, developed by PTB, have been used to map volumetric anisotropies as well as assessing errors in length, size and form measurements [94], [138].

The workpieces shown in Figure 3.1 are not suitable for use in the present work due to their mounting requirements: the CT system used in this work has a horizontally mounted rotation axis, see Section 3.2.5. Furthermore, the maximum acceleration voltage of the CT system is 160 kV, which limits the maximum material path length that can be penetrated. Finally, the influence of scatter and beam hardening are to be studied for both internal and external dimensional features; only the step cylinder possesses such features, however, due to its rotational symmetry only cupping artefacts will be induced, and not streaking artefacts. As such, we develop our own

workpieces which are better suited for the purpose of this work; these workpieces are described in the sections that follow.

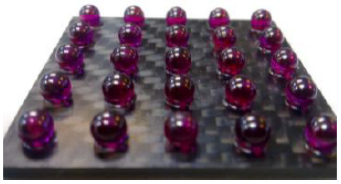

(a) Ball Plate [42].

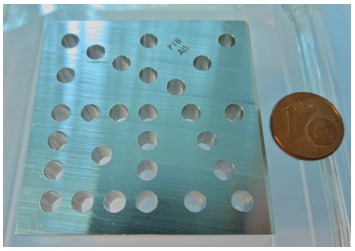

(b) Hole Plate [43].

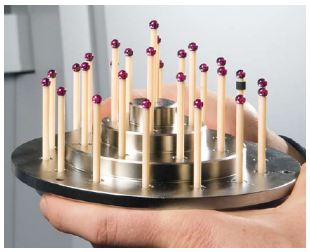

(c) Metrotom-Check [130].

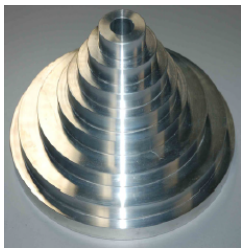

(d) Step Cylinder [139].

(e) CT Tree [42].

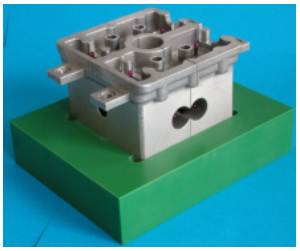

(f) Dismountable Workpiece [136].

(g) CT Tetrahedron [129].

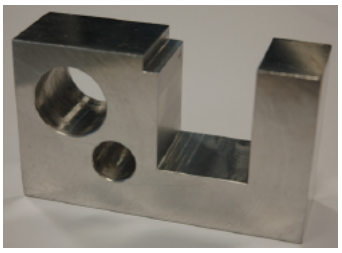

(h) Aluminium Workpiece [137].

(i) Alumina Sphere Tetrahedron [131].

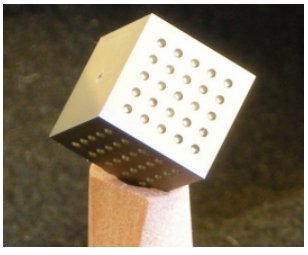

(j) Sphere Calotte Cube [140].

Figure 3.1 A selection of existing CT reference workpieces.

3.2 Reference Workpiece 1: The Ruby Sphere Workpiece

3.2.1 Function and Design

The first reference workpiece is named the ruby sphere workpiece and is shown in Figure 3.2. The ruby sphere workpiece is used in Chapter 4 to correct voxel size errors. The workpiece consists of four 3 mm diameter synthetic ruby spheres that are glued with Araldite® to staggered heights of MACOR®, a machinable glass ceramic. The distance between the centres of any two spheres is considered to be independent of surface determination, see Section 2.5. This type of dimension is useful for correcting systematic scale errors, as will be shown in Chapter 4.

Ruby spheres are chosen for two reasons: firstly, ruby has similar X-ray attenuation properties to aluminium and is therefore visible at acceleration voltages typical of industrial CT, but is not so attenuating as to induce artefacts. Secondly, ruby-spheres can be manufactured with very low form error (sphericity of 0.64 μm) thus reducing the reference and CT measurement uncertainties. MACOR® is chosen for its low density and machinability, but primarily for its low coefficient of thermal expansion (CTE). Prototypes of this workpiece used polyoxymethylene (POM) for the base material; although POM is suitably X-ray transparent, the thermal stability was found to be the dominating uncertainty contributor in the reference measurements; replacing POM with MACOR overcame this issue.

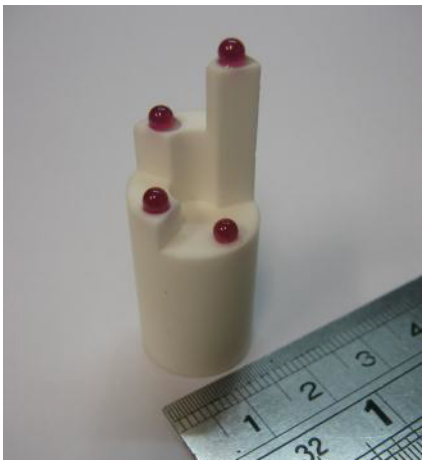

Figure 3.2 Photograph of the ruby sphere workpiece, ruler for scale.

3.2.2 Reference Dimensions

The ruby sphere workpiece features 6 centre-to-centre distances. The staggered heights of the spheres are designed such that no two centre-to-centre distances are the same. Details of the ruby sphere workpiece's geometry are given in Figure 3.3 and summarised in Table 3.1.

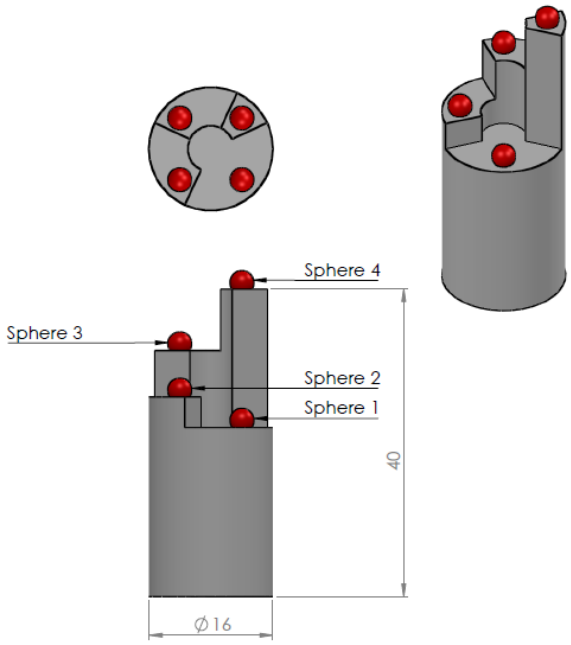

Figure 3.3 Overview of reference geometries for the ruby sphere workpiece, all dimensions in mm.

Table 3.1 Overview of reference dimensions for the ruby sphere workpiece.

Identification	Description
D12	3D distance between sphere 1 & 2
D13	3D distance between sphere 1 & 3
D14	3D distance between sphere 1 & 4
D23	3D distance between sphere 2 & 3
D24	3D distance between sphere 2 & 4
D34	3D distance between sphere 3 & 4

3.2.3 Reference Measurement Strategy

All the reference measurements described in this chapter are performed on a coordinate measuring machine (CMM), where a CMM is defined as: a measuring system with the means to move a probing system and capability to determine spatial coordinates on a workpiece surface [141]. A CMM is chosen as the reference instrument because measurements from CMMs are widely accepted due to international standards supporting their acceptance and reverification [141], and the assessment of task specific measurement uncertainty is well documented [142], [143].

All reference measurements are performed on a Zeiss PRISMO Ultra, this instrument has a maximum permissible error for size measurement (MPE) of 0.6 + L/500 µm where L is the measured size in millimetres. The maximum permissible error of a CMM specifies its length measuring accuracy. It is defined in ISO10360 Part 1 as: the extreme value of the error of indication of a CMM for size measurement permitted by specifications, regulations etc. for a CMM [141]. The CMM software utilised throughout is Calypso V5.2. The instrument is housed in an environmentally controlled metrology lab with the temperature and relative humidity maintained at 21°C ± 0.5°C and 60 % respectively. Each workpiece is allowed to acclimatise for two days before it is measured. All reference workpieces are measured a total of 20 times: five measurements per day over a four day period, with the workpieces repositioned in the measurement volume for each day of measurements. For each round of measurements the CMM is started from the same initial condition: the master probe is first qualified on a master sphere, the master probe is then removed and the working probe installed and qualified in the same fashion.

The measurement setup for the ruby sphere workpiece is depicted in Figure 3.4. Measurements of the ruby sphere workpiece are made with a 1 mm diameter probe and a probing force of 0.1 N. The probing strategy adopted for each sphere is depicted in Figure 3.5: circular profiles are traced at three evenly spaced heights with the CMM operating in scanning mode and a single point is measured on the estimated crown of the sphere. 3600 points are measured per trace and the coordinate set is filtered with a low-pass spline filter with parameter settings of 50 undulations per revolution and a wavelength cut-off of 2.5 mm; these being the default filter settings as defined by Calypso. This probing strategy is chosen to be similar to that of a CT measurement; i.e. the measurement points are evaluated on a given plane of the workpiece. For measuring the diameter of a sphere ISO 10360 Part 5 [144] and NPL Good Practice

Guide No. 42 [145] recommend a 25 point probing strategy, this is too few data points to be compared to a CT measurement, which often yields hundreds to thousands of data points.

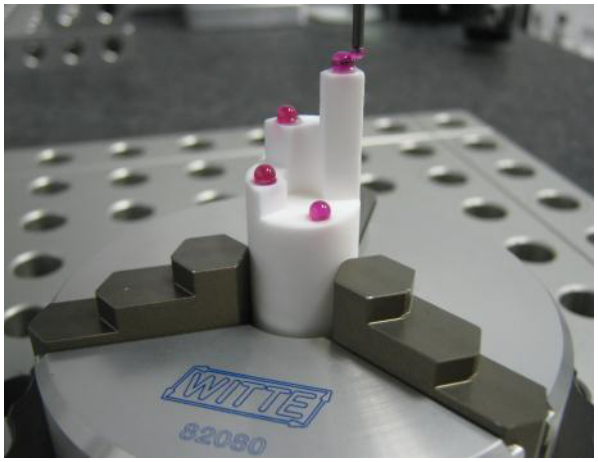

Figure 3.4 The ruby sphere workpiece being measured with a CMM.

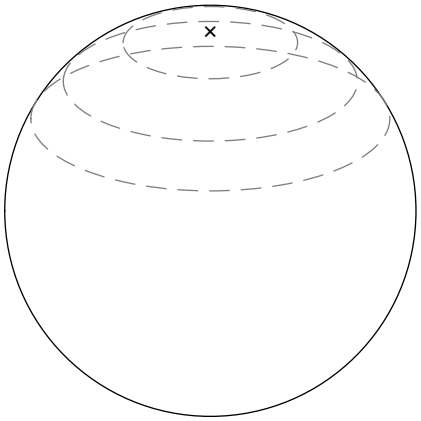

Figure 3.5 Probing strategy for ruby spheres. Dashed lines represent probe trajectory.

3.2.4 Reference Measurement Uncertainty

The task specific measurement uncertainty for the ruby sphere workpiece is evaluated with reference to NPL Good Practice Guide No. 130 [10], alongside ISO 14253 Part 2 [143], and a measurement report from the CIA CT inter-laboratory comparison for industrial computed tomography [146].

According to the GUM [9], uncertainty contributors evaluated using statistical methods are termed Type A, whilst those evaluated by methods other than statistical are termed Type B. All uncertainty contributors have an associated statistical distribution; three common distributions are Gaussian, rectangular and U-distributions. When calculating a Type B uncertainty contributor it is typically the limit of the distribution that is calculated. To convert a limit value to a standard deviation the limit value is divided by a constant corresponding to the distribution it follows. Based on the worked examples given in NPL Good Practice Guide No. 130 [10] all the Type B uncertainty contributors evaluated in the following uncertainty budget can be assumed to follow a rectangular distribution, hence all Type B contributors are divided by $\sqrt{3}$.

The following uncertainty contributors are considered for the ruby sphere workpiece:

- The ruby sphere workpiece is measured n = 20 times and the standard deviation σ of the repeated measurements evaluated. The standard uncertainty due to the measurement procedure is calculated as the standard error of the mean:

$$u_1 = \frac{\sigma}{\sqrt{n}}. \tag{3.1}$$

- The standard uncertainty due to the thermal expansion of the workpiece is calculated as:

$$u_2 = \frac{\alpha_{MACOR} L \Delta T}{\sqrt{3}}, \tag{3.2}$$

$$u_3 = \frac{\alpha_{ruby} r \Delta T}{\sqrt{3}}, \tag{3.3}$$

where α is the thermal expansion coefficient of the subscripted material, L is the nominal centre-to-centre distance, ΔT is the change in temperature and r is the nominal radius of a given ruby sphere.

- The standard uncertainty due to the thermal expansion of the CMM is calculated as:

$$u_4 = \frac{\alpha_{CMM} L \Delta T}{\sqrt{3}}. \quad 3.4$$

- The thermal expansion coefficients are estimated to be known to 1 part per million (ppm) for each material, the standard uncertainty contribution is:

$$u_5 = \frac{u_{\alpha\, MACOR} L \Delta T}{\sqrt{3}} \quad 3.5$$

$$u_6 = \frac{u_{\alpha\, ruby} r \Delta T}{\sqrt{3}} \quad 3.6$$

$$u_7 = \frac{u_{\alpha\, CMM} L \Delta T}{\sqrt{3}}. \quad 3.7$$

- The MPE of the CMM is 0.6 + L/500 μm, the standard uncertainty due to the error of indication of the CMM is:

$$u_8 = \frac{0.6 + \frac{L}{500}}{\sqrt{3}}. \quad 3.8$$

- 20 additional measurements of a calibrated sphere were conducted, the difference between the mean of the 20 measurements and the calibrated value was 0.0002 mm, the contribution to the standard measurement uncertainty is therefore:

$$u_9 = \frac{0.0002}{\sqrt{3}}. \quad 3.9$$

- The thermometer has an accuracy u_T of 0.1°C, the standard uncertainty due to the thermometer is:

$$u_{10} = \frac{u_T \alpha_{MACOR} L}{\sqrt{3}} \quad 3.10$$

$$u_{11} = \frac{u_T \alpha_{ruby} r}{\sqrt{3}} \quad 3.11$$

$$u_{12} = \frac{u_T \alpha_{CMM} L}{\sqrt{3}}. \quad 3.12$$

- During probing of the workpiece, the workpiece and stylus elastically deform. Assuming the workpiece is an elastic plane and the probe is a rigid sphere, the standard uncertainty due to the probing force is:

$$u_{13} = \frac{2\left(\frac{3}{4}Fr^2\left(\frac{1-v^2}{E}\right)\right)^{2/3}}{\sqrt{3}} \quad 3.13$$

where F is the probing force, r is the radius of the probe, v is Poisson's ratio of ruby and E is the Young's modulus of ruby [146].

The expanded uncertainty is therefore calculated as:

$$U = k\sqrt{\sum_{i=1}^{13} {u_i}^2} \quad 3.14$$

where k is a coverage factor equal to 2 and indicates a confidence probability of approximately 95%. The coverage factor can be found by assuming the probability distribution is the *t*-distribution, with the effective degrees of freedom v_{eff} obtained from the Welch-Satterthwaite formula:

$$v_{eff} = \frac{u_c^4}{\sum_{i=1}^{N}\frac{u_i^4}{v_i}} \quad 3.15$$

where u_c is the combined standard uncertainty. To obtain v_{eff} from Equation 3.15 requires the degrees of freedom v_i for each standard uncertainty component. For a component obtained from a Type A evaluation v_i is equal to $n-1$. For a component obtained from a Type B evaluation v_i is obtained from the judged reliability of the value of that component: all Type B evaluations are assumed reliable to about 20% based on the examples given in reference [10], except for the MPE which is known with a high number of degrees of freedom. Using the Welch-Satterthwaite equation the total number of degrees of freedom is calculated as 203, the corresponding k value is obtained from the *t*-distribution table in UKAS document M3003 [147]. This value of v confirms the use of $k = 2$.

The expanded measurement uncertainty for the six reference dimensions of the ruby sphere workpiece are given in Table 3.2. The uncertainties are in the order of 1 μm,

this being an acceptable level of uncertainty for the intended function of the reference workpiece.

Figure 3.6 shows the magnitudes of the uncertainty components used to calculate the expanded measurement uncertainty of D14. Components 8 and 13 are the largest, these being the uncertainty due to the error of indication of the CMM and the uncertainty due to the probing force, respectively; both of these uncertainty components originate from the CMM and not the workpiece. If the reference measurement uncertainty were to be reduced, the reference instrument should be changed. An instrument with an optical probe would mitigate the influence of the probing force, whist an instrument with a smaller measurement volume would potentially reduce the MPE, this should be considered in future work.

Table 3.2 Reference measurement results for the ruby sphere workpiece.

Identification	D12	D13	D14	D23	D24	D34
Mean (mm)	8.994	15.123	19.920	9.990	18.130	11.448
Expanded Uncertainty (μm) ($k = 2$)	0.88	0.92	0.96	0.89	0.95	0.90

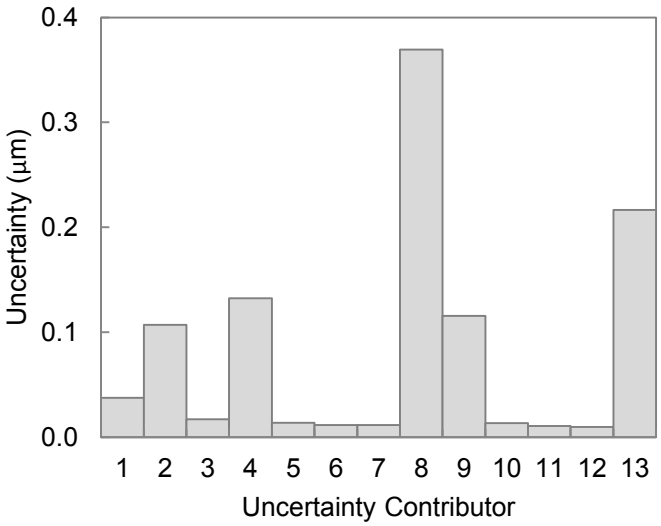

Figure 3.6 Magnitude of uncertainty components for calculating the uncertainty of D14

3.2.5 CT Measurement Strategy

All CT scans are performed with an YXLON/FeinFocus Y.Fox 160.25 (YXLON International GmbH, Garbsen, Germany), the specification for which is given in Table 3.3. The CT system is housed in an air conditioned laboratory with the temperature set to 21°C ± 1°C. The internal layout of the instrument is shown in Figure 3.7: as can be seen, the rotation axis is mounted horizontally with the X-ray source mounted above and the detector below. It should be noted this CT system is not a metrology system, as such, the X-ray chamber is not air conditioned and the axes are not mounted on a granite base. The positional errors and run-out errors of the axes are therefore expected to be larger than those of a dedicated metrology system. Even so, systematic positional errors and thermal offsets can be corrected for, thus the system is deemed adequate for the research topic.

Before each workpiece is CT scanned it is stored in the same lab as the CT system for at least two days in advance and allowed to acclimatise in the CT chamber whilst the system ‘starts-up’. This start-up procedure consists of: an axis home search, the X-ray source ramping up to the maximum voltage and pausing, optimisation of the source filament current, and the source centring characteristics being set for all voltages. A ‘dummy’ scan is performed before each ‘actual’ scan to allow the X-ray tube to reach thermal equilibrium.

Table 3.3 YXLON Y.FOX X-ray CT system specification.

Parameter	Value
X-ray source type	Transmission, tungsten, open
X-ray source model	YXLON FXE 160.51
Max. source voltage (kV)	160
Max. source current (mA)	1
Min. focal spot size (μm)	2
Max. magnification	×2720
Detector type	Indirect, caesium iodide (CsI) & amorphous silicon
Detector model	Varian PaxScan 2520V
Detector pixel size (mm)	0.127
Number of pixels (x, y)	1480, 1848

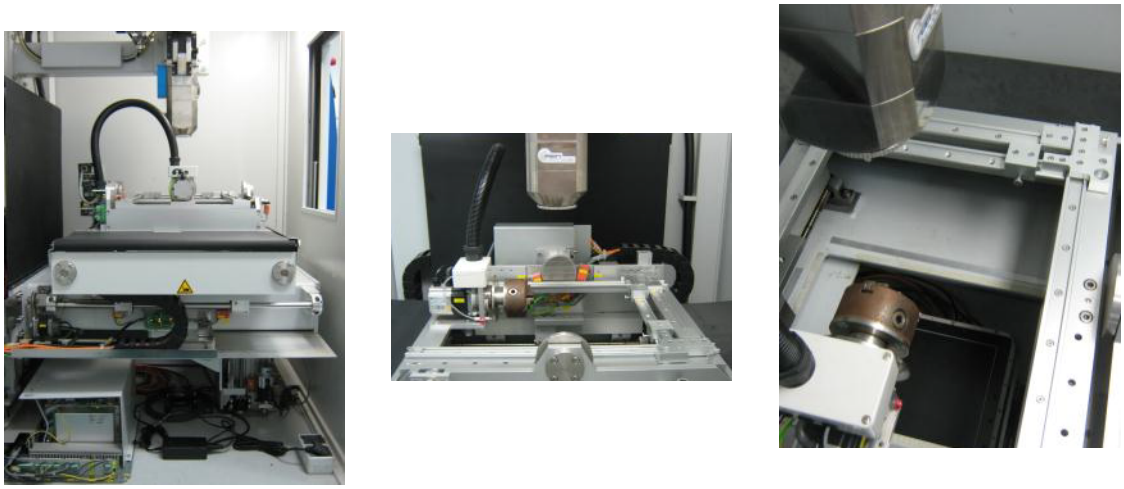

(a) Full internal layout of the CT system.

(b) X-ray source & rotation axis.

(c) X-ray source, rotation axis and detector.

Figure 3.7 Internal layout of the YXLON Y.FOX CT system.

All reconstruction is performed with VGStudio MAX 2.1 (Volume Graphics GmbH, Heidelberg, Germany), or with in-house developed software. Prior to reconstruction, all projection data is corrected for a centre of rotation offset and a tilt about the z axis of the detector. The backprojection filter is chosen as the Shepp-Logan filter for all reconstructions, this filter is selected as it attenuates high spatial frequencies thus reducing noise in the CT-data at a cost of a reduced spatial resolution. All data is reconstructed as 32-bit floating point numbers rather than 16-bit integers. When 16-bit integers are used the CT data is scaled between 0 and 2^{16}, this often means the grey values of two data sets are not directly comparable as they have been scaled differently. In order to overcome this issue of comparability, 32-bit floating point numbers are used throughout.

The CT measurement setup for the ruby sphere workpiece is shown in Figure 3.8; the workpiece is mounted directly in the three-jaw chuck of the rotation axis. All scans of the ruby sphere workpiece are made with the acquisition settings given in Table 3.4. With regards to the number of projections, the reason for acquiring so few projections (360) is to reduce scan time, this minimises thermal drift which reduces the measurement uncertainty due to thermal expansion. Furthermore, Muller et al. [42] and Weckenmann et al. [148] have both shown that increasing the number of projections has little influence on the accuracy of dimensional measurements.

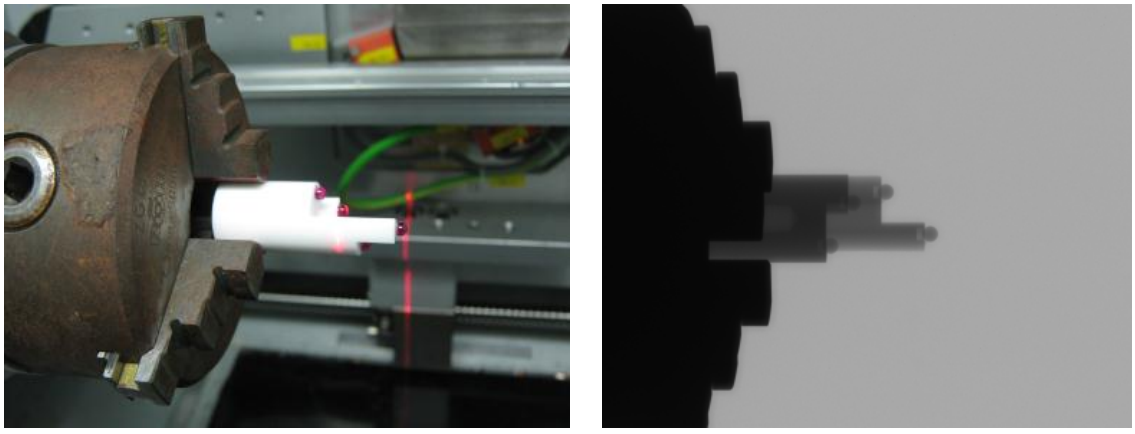

(a) The ruby sphere workpiece mounted in the chuck of the rotation axis of the CT system.

(b) An X-ray projection of the ruby sphere workpiece.

Figure 3.8 CT measurement setup for the ruby sphere workpiece.

Table 3.4 CT acquisition settings for the ruby sphere workpiece

Parameter name	Value
Source voltage (kV)	120
Source current (μA)	22
Pre-filter material	Steel
Pre-filter thickness (mm)	0.5
Detector exposure time (ms)	1000
Averaged projections	1
Number of projections	360
Magnification	Various

Reconstruction settings for the ruby sphere workpiece are given in Table 3.5, whilst a volume rendering of a typical measurement result is shown in Figure 3.9(a). To evaluate the centre-to-centre distances of the ruby sphere workpiece from the CT data the following procedure is adopted and performed using VGStudio MAX 2.1: first, regions of interest (ROIs) of the crown of each sphere are defined by manual selection. Next these ROIs are extracted as shown in Figure 3.9(b). Following which, surface determination is performed for all ROIs using the ISO50 method. Finally, spheres are fitted to all points of each determined surfaces and the centre-to-centre distances evaluated, as shown in Figure 3.9(c).

Table 3.5 Reconstruction settings for the ruby sphere workpiece.

Parameter name	Value
Number of voxels	512^3
Backprojection filter	Shepp-Logan
Interpolation method	Linear
Ring artefact correction	Yes

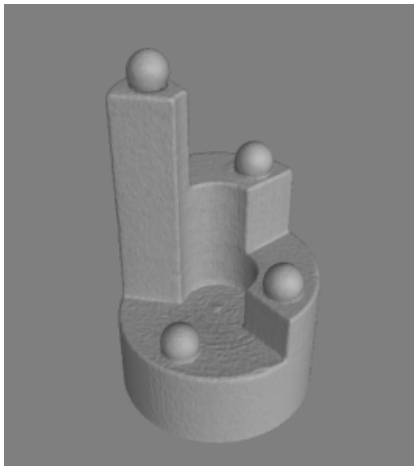

(a) Volume rendering of the ruby sphere workpiece

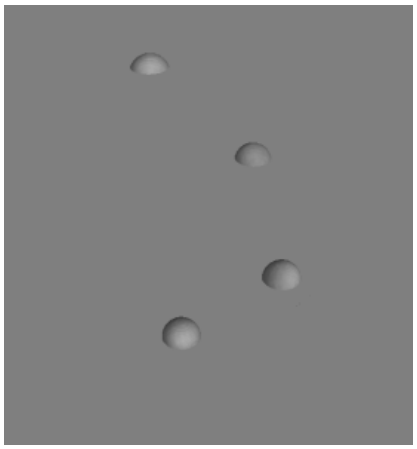

(b) The crown of each sphere extracted as a ROI.

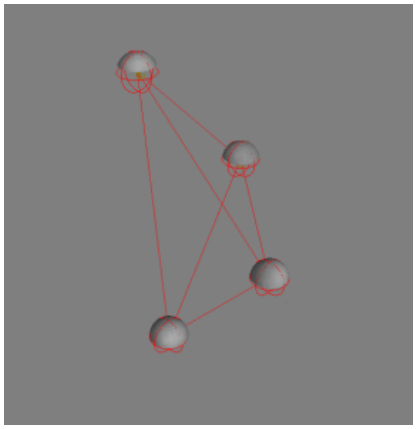

(c) Spheres fitted to each ROI and centre-to-centre distances evaluated.

Figure 3.9 Data evaluation for the ruby sphere workpiece.

3.3 Reference Workpiece 2: Multi Cross-Section Workpieces

3.3.1 Function and Design

The second reference workpiece, or set of workpieces, are the aluminium and titanium multi cross-section workpieces, see Figure 3.10. The function of these workpieces is to induce beam hardening and scattering artefacts such that the influence of these artefacts can be evaluated for both internal and external threshold sensitive dimensional measurements. The different geometric cross-sections are designed to present varying X-ray path lengths to induce various cupping artefacts, whilst the internal and external vertices are designed to induce streaking artefacts. The workpieces are fabricated from aluminium and titanium since these are common manufacturing materials and present different X-ray absorption and scattering properties.

3.3.2 Reference Dimensions

The multi cross-section workpieces have two external radii and two internal radii. These features are considered sensitive to surface determination and should therefore respond to the presence/absence of scatter and beam hardening. The specific dimensions considered in this work are illustrated in Figure 3.11 and are listed in Table 3.6.

Figure 3.10 Photograph of the multi cross-section workpieces, ruler for scale.

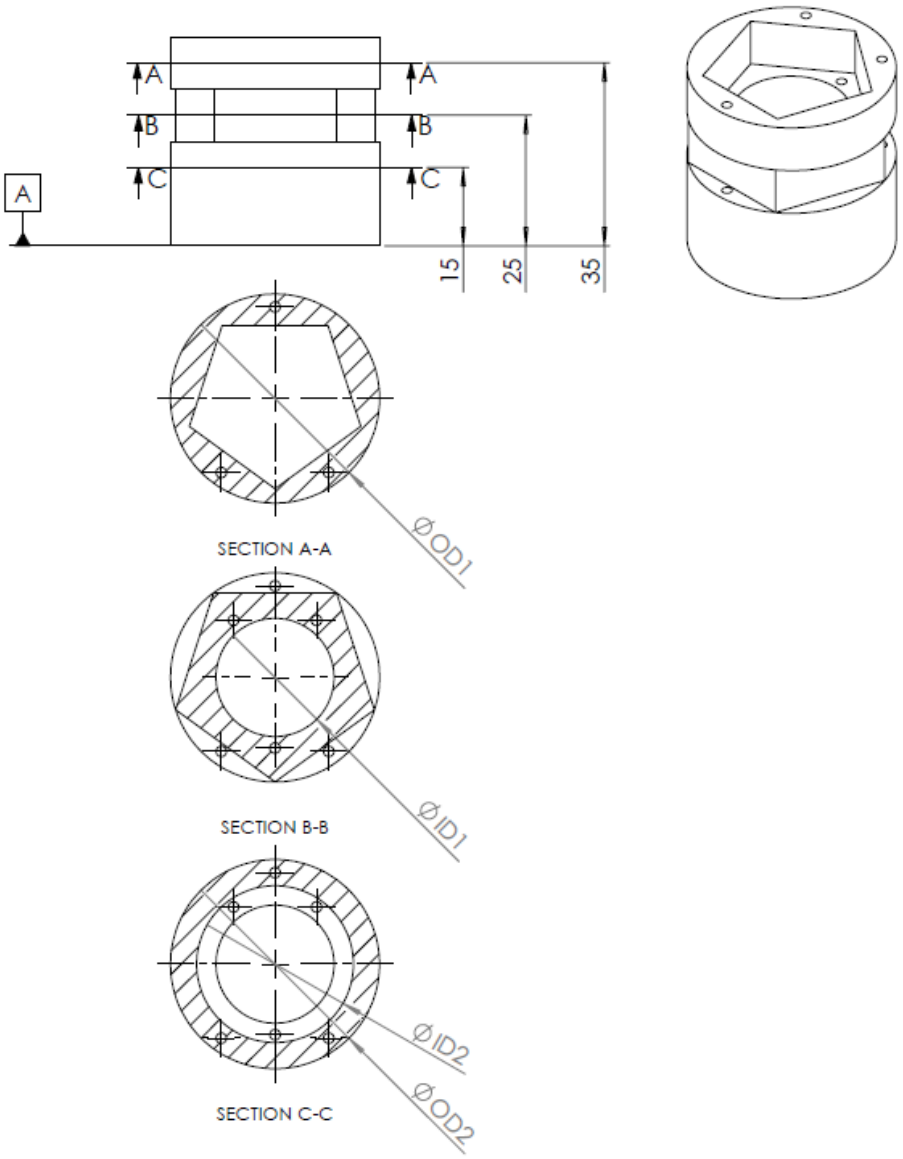

Figure 3.11 Measurement details for the multi cross-section workpiece. All dimensions in mm.

Table 3.6 Overview of reference dimensions for the multi cross-section workpiece.

Identification	Description
OD1	Outer diameter 35 mm from datum A
ID1	Internal diameter 25 mm from datum A
OD2	Outer diameter 15 mm from datum A
ID2	Internal diameter 15 mm from datum A

3.3.3 Reference Measurement Strategy

The reference measurement setup for the multi cross-section workpieces is depicted in Figure 3.12. Measurements are made with a 3 mm diameter probe and a probing force of 0.1 N. Diameter measurements are evaluated from 3600 points acquired with the CMM operating in scanning mode, the coordinate set is filtered with the same low-pass spline filter described in Section 3.2.3. The measurement datum system is shown in Figure 3.13 and is based on the definition of a primary, secondary and tertiary datum; details of each datum are given in Table 3.7.

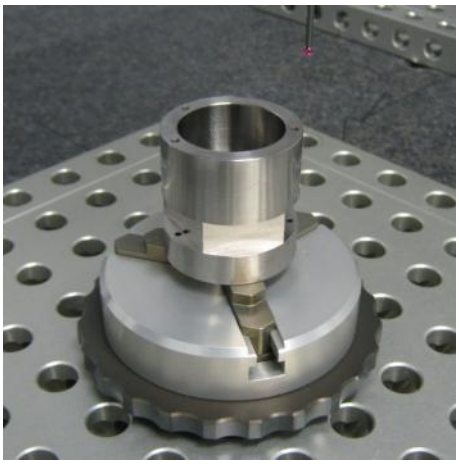

Figure 3.12 Measurement setup of multi cross-section workpiece on the CMM.

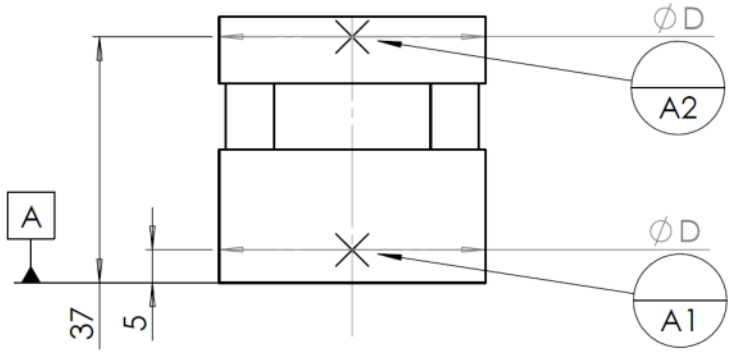

Figure 3.13 Datum definition of the multi cross-section workpieces.

Table 3.7 Datum definition of the multi cross-section workpieces.

Datum	Description
Primary (plane)	Datum A
Secondary (line)	Line formed between circle centres A1 & A2
Tertiary (point)	Intersection between Primary & Secondary Datum

3.3.4 Reference Measurement Uncertainty

The measurement uncertainty for the multi cross-section workpieces is evaluated in accordance with ISO 15530 Part 3 [142], which is termed the substitution method. The method requires that a calibrated standard is measured in the same way and under the same conditions as the actual workpiece. The measurement results of both the calibrated standard and the multi cross-section workpieces are used to estimate the measurement uncertainty. The calibrated standard used is a setting ring gauge from Bowers Metrology (Bowers Group, Surry, UK), see Figure 3.14.

The substitution method requires that at least 20 measurements of the calibrated standard are made in various positions and orientations within the measurement volume. As such, the calibrated standard and the multi cross-section workpieces are each measured five times per day, for four days. Each day the workpiece and calibrated standard are repositioned in the measurement volume.

Figure 3.14 Calibrated standard used to evaluate the measurement uncertainty for the multi cross-section workpieces.

According to the substitution method, the expanded measurement uncertainty U is calculated as:

$$U = k \times \sqrt{u_{cal}^2 + u_p^2 + u_b^2 + u_w^2} \quad 3.16$$

where k is the coverage factor and is specified as $k = 2$ by ISO 15530 Part 3 for a coverage probability of 95%. u_{cal} is the uncertainty of the calibrated standard and is given in the calibration certificate. u_p is the uncertainty due to the measurement procedure and is calculated as the standard deviation of the 20 repeated measurements of the calibrated standard. u_b is the uncertainty of the systematic error and considers the uncertainty of the coefficient of thermal expansion (CTE) of the calibrated standard, it is calculated as:

$$u_b = (T - 20) \times u_{\alpha\, cal} \times L \quad 3.17$$

where T is the reference temperature, $u_{\alpha\, cal}$ is the uncertainty of the CTE of the calibrated standard which is assumed to be 1 part per million (ppm), and L is the size of the measurement. u_w is the uncertainty from the manufacturing process and is calculated as:

$$u_w = \sqrt{u_{wp}^2 + u_{wt}^2} \quad 3.18$$

where u_{wp} is the uncertainty due to the workpiece and considers any difference in form error and surface roughness between the calibration standard and the actual workpiece. For the multi cross-section workpiece there are two contributors to the form error: the alignment of datum A and the roundness of each hole. It is assumed the form error for each reference dimension can be estimated based on the difference between the maximum and minimum diameters D for the 20 repeated measurements of the multi cross-section workpiece, u_{wp} is therefore calculated as:

$$u_{wp} = \Delta D = \max(D) - \min(D). \quad 3.19$$

Finally, u_{wt} is the uncertainty due to the variation of the CTE of the workpiece and is calculated as:

$$u_{wt} = (T - 20) \times u_{\alpha\, wp} \times L \quad 3.20$$

where $u_{\alpha\, wp}$ is the uncertainty of the CTE of the workpiece, again assumed to be 1 ppm.

The measurement results for the titanium and aluminium multi cross-section workpieces are given in Table 3.8. The measurement uncertainties are in the order of 1 to 2 μm, this is an acceptable level of uncertainty for the intended function of these reference workpieces.

Figure 3.15 shows the magnitude of the components used to calculate the uncertainty of OD1 for the titanium and aluminium workpieces. The dominant components are the uncertainty of the calibration standard u_{cal}, the uncertainty of the measurement procedure u_p, and the uncertainty due to the workpiece u_{wp}. u_{cal} could be reduced by using a calibration standard with a lower uncertainty, such as a standard calibrated by a national metrology institute rather than an accredited laboratory that is further down the traceability chain. u_p could be reduced by improving the measurement strategy, for example, a reversal method could be adopted whereby the workpiece is rotated through steps of 90° and re-measured so as to cancel out errors in the axes of the CMM [10]. u_{wp} could be reduced by improving the manufacture of the workpiece.

Table 3.8 Reference measurement results for titanium and aluminium multi cross-section workpiece.

	Identification	OD1	ID1	OD2	ID2
Titanium	Mean (mm)	39.990	30.092	40.001	22.606
	Expanded Uncertainty (μm) ($k = 2$)	1.4	1.5	1.5	1.5
Aluminium	Mean (mm)	39.956	30.107	39.961	22.631
	Expanded Uncertainty (μm) ($k = 2$)	1.6	1.5	1.4	1.5

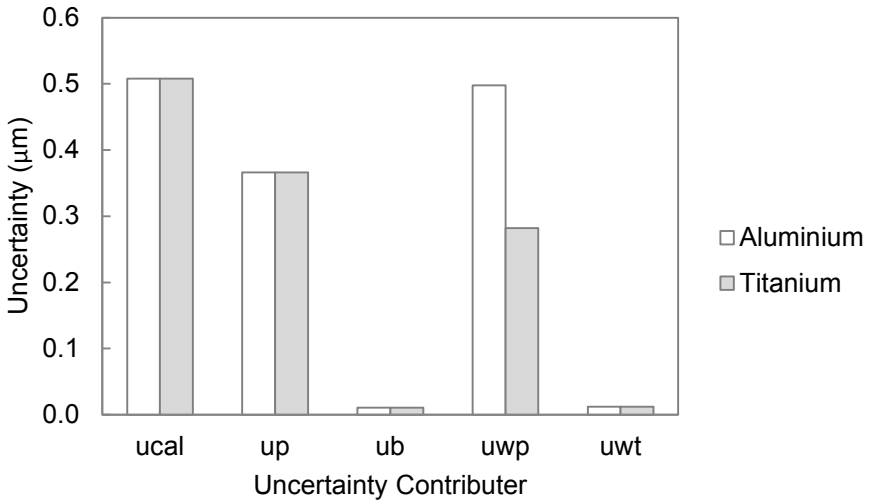

Figure 3.15 Uncertainty components for calculating the uncertainty of OD1.

3.3.5 CT Measurement Strategy

The CT measurement setup for the multi cross-section workpieces is shown in Figure 3.16(a). The workpiece is attached to a polymer mount using an interference fit, the shaft of the mount is then clamped in the three-jaw chuck of the rotation axis. An exemplary projection of the aluminium multi cross-section workpiece is shown in Figure 3.16(b), whilst a volume rendering of a typical measurement result is shown in Figure 3.17.

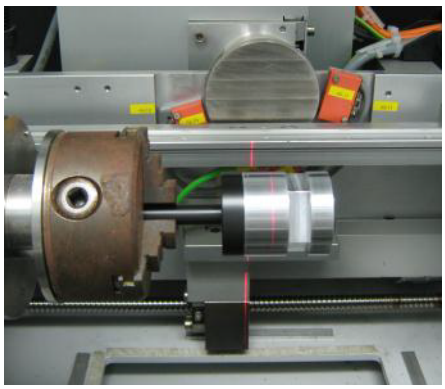

(a) The aluminium multi cross-section workpiece mounted in the chuck of the rotation axis of the CT system.

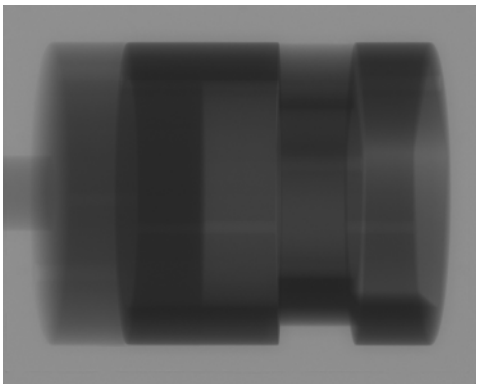

(b) An X-ray projection of the aluminium multi cross-section workpiece.

Figure 3.16 CT measurement setup for the multi cross section workpiece.

Table 3.9 CT acquisition settings for the multi cross-section workpieces.

Parameter name	Value
Source voltage (kV)	160
Detector exposure time (ms)	1000
Averaged projections	2
Number of projections	720
Magnification	×3.76

Table 3.10 Reconstruction settings for the multi cross-section workpieces.

Parameter name	Value
Number of voxels	1024^3
Backprojection filter	Shepp-Logan
Interpolation method	Linear
Ring artefact correction	No
Voxel size (µm)	49

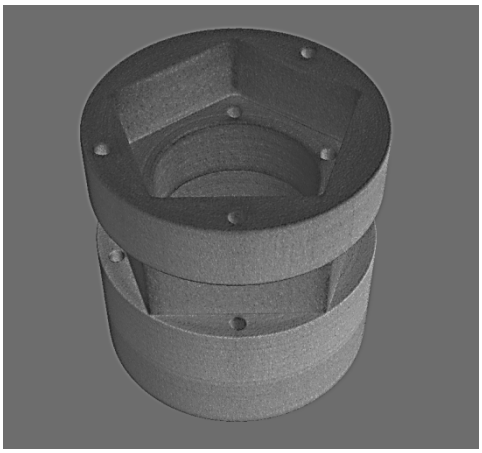

Figure 3.17 Volume rendering of the multi cross-section workpiece.

Following reconstruction surface determination is performed using the algorithms described in Section 2.5 which yields a point cloud of surface points. The point cloud is imported into GOM inspect V8 (GOM mbH, Braunschweig, Germany). The data is aligned by fitting the reference geometries defined in Figure 3.13 and Table 3.7. The reference dimensions of the workpiece are then evaluated by fitting circles by nonlinear least-squares to surface points in the positions indicated in Figure 3.11. Exemplary cross-sections evaluated using GOM inspect are shown in Figure 3.18.

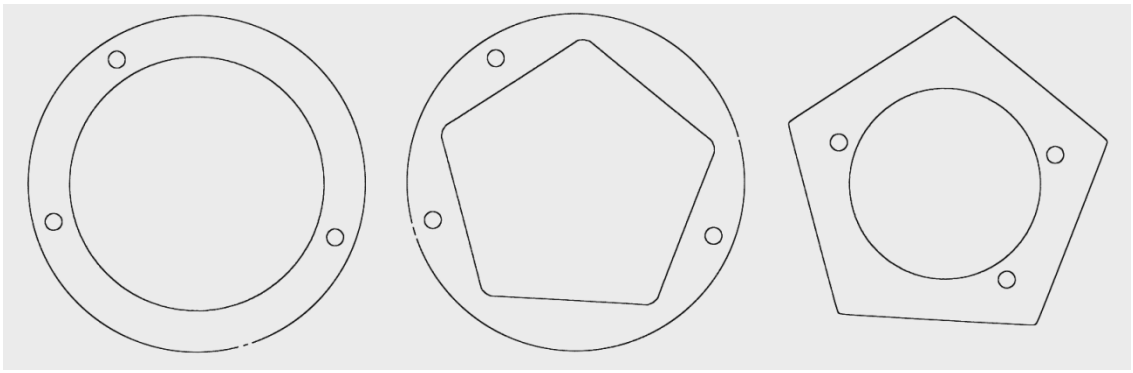

Figure 3.18 Cross-sections of the aluminium multi cross-section workpiece evaluated using GOM inspect.

3.4 Reference Workpiece 3: Plastic Brick

3.4.1 Function and Design

The third and final reference workpiece is a plastic brick, see Figure 3.19. The plastic brick is used in Chapter 4 to evaluate how systematic error corrections influence length measurement error.

The plastic brick originates from the CIA-CT comparison, an inter-laboratory comparison on industrial CT organised by the Technical University of Denmark (DTU) [149]. The participants of the comparison were required to scan two objects, one of which was the plastic brick. After completing the comparison the objects were returned to the participants alongside a measurement report detailing reference measurements of the object's reference dimensions. Details of the reference measurements and measurement uncertainty calculations can be found in reference [146].

The plastic brick is made of Acrylonitrile Butadiene Styrene (ABS) and features eight cylindrical knobs aligned in a row. The low density material of the workpiece results in CT data with minimal beam hardening and scattering artefacts, and thus presents a relatively easy measurement task.

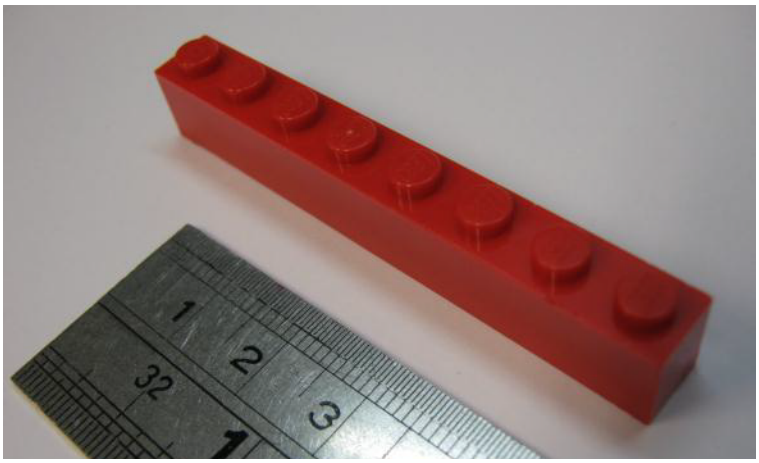

Figure 3.19 Photograph of the plastic brick, ruler for scale.

3.4.2 Reference Dimensions

The plastic brick has two reference dimensions: the centre-to-centre distance between circles fitted to the two outermost knobs, and the radius of one of the central knobs, these dimensions are illustrated in Figure 3.20 and are listed in Table 3.11. The reference measurement results are given in Table 3.12 alongside the measurement uncertainty as documented in ref. [146].

Table 3.11 Overview of reference dimensions for the plastic brick.

Identification	Description
L1	Centre-to-centre distance between circle centres B1 and C1.
R1	Radius of knob shown in section A-A.

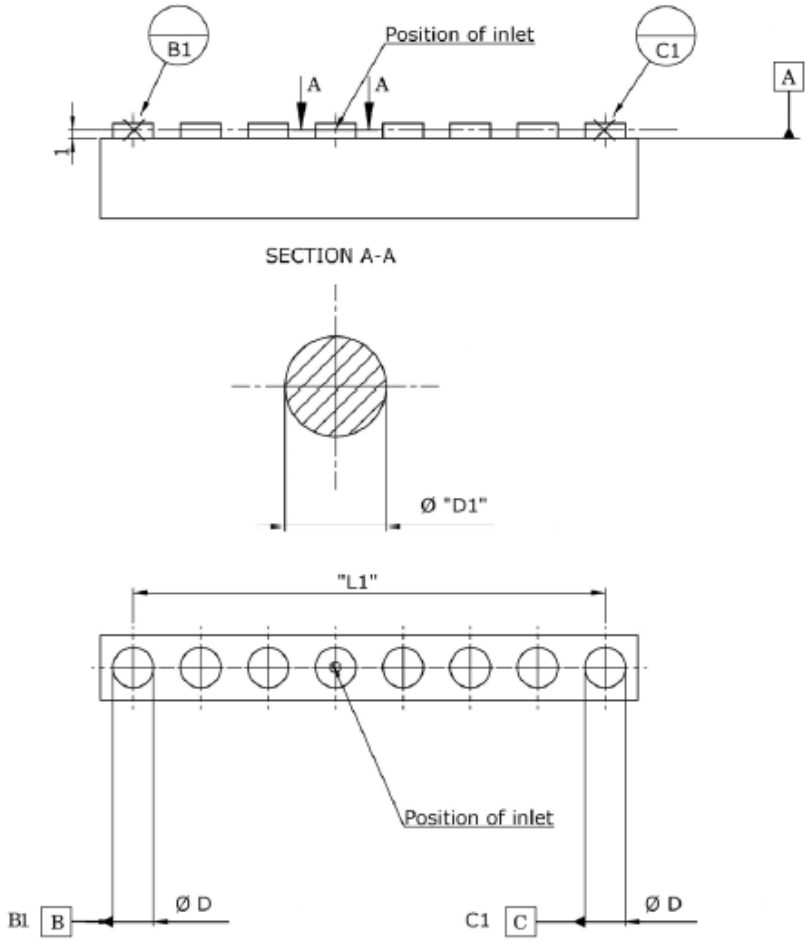

Figure 3.20 Reference dimensions for the plastic brick [146].

Table 3.12 Reference measurement results for the plastic brick [146].

	L1	D1
Mean (mm)	55.9134	4.9028
Expanded Uncertainty (μm) ($k = 2$)	5.5	2.3

3.4.3 CT Measurement Strategy

The CT measurement setup for the plastic brick is shown in Figure 3.21(a) and an exemplary projection of the workpiece is shown in Figure 3.21(b). The scan settings for the plastic brick are given in Table 3.13 and the reconstruction settings in Table 3.14; a volume rendering of a typical measurement result is shown in Figure 3.22.

Following reconstruction, the reference dimensions of the plastic brick are evaluated as follows and performed using VGStudio MAX 2.1: first, surface determination is performed using the ISO50 method, next, the CT data is aligned based on the definition of a primary, secondary and tertiary datum; details of each datum are given in Figure 3.20 and Table 3.15. Based on the aligned data, the reference dimensions of the plastic brick are then evaluated.

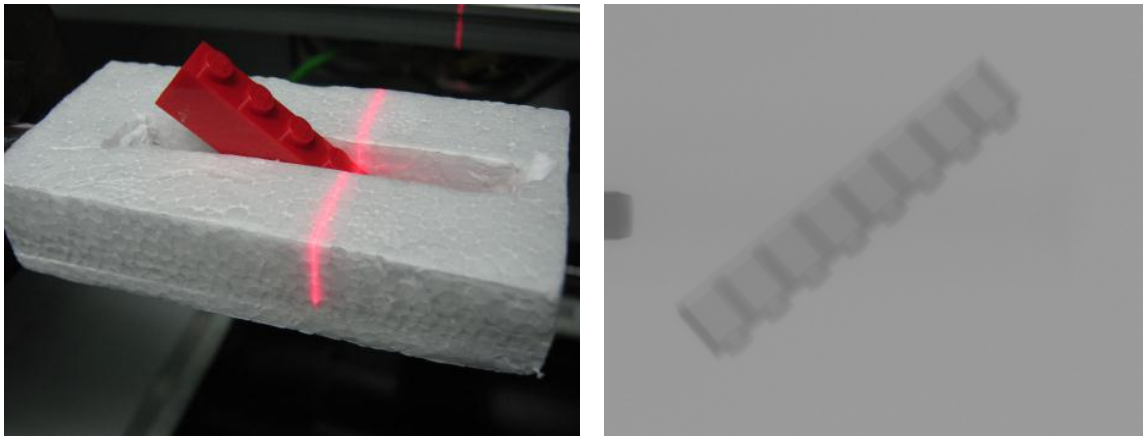

(a) The plastic brick mounted in the rotation axis of the CT system.

(b) An X-ray projection of the plastic brick.

Figure 3.21 CT measurement setup for the plastic brick.

Table 3.13 CT acquisition settings for the plastic brick.

Parameter name	Value
Source voltage (kV)	100
Source current (μA)	10
Detector exposure time (ms)	1000
Averaged projections	2
Number of projections	720
Magnification	×2.77

Table 3.14 Reconstruction settings for the plastic brick.

Parameter name	Value
Number of voxels	512^3
Backprojection filter	Shepp-Logan
Interpolation method	Linear
Ring artefact correction	Yes
Voxel size (μm)	133

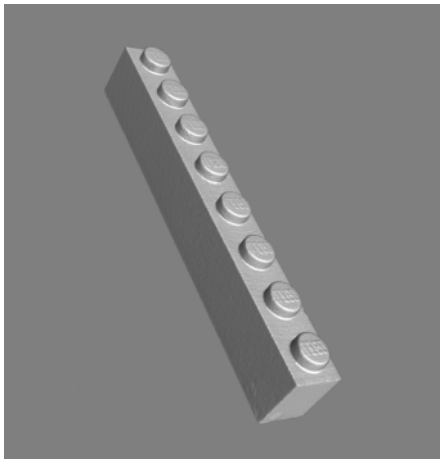

Figure 3.22 Volume rendering of the plastic brick.

Table 3.15 Datum definition of the plastic brick.

Datum	Description
Primary (plane)	Datum A
Secondary (line)	Line formed between circle centres A1 & A2
Tertiary (point)	Intersection between Primary & Secondary Datum

3.5 Chapter Summary

In this chapter three reference workpieces have been introduced and a description given concerning the measurement of each workpiece on a CMM. The uncertainties of the reference measurements have been evaluated according to international standards. Suggestions on how to reduce the uncertainty of the reference measurements have been made and should be considered in future work.

The specification of the CT system used throughout this work has been presented alongside the CT measurement and data evaluation strategy for each workpiece.

In the next chapter the ruby sphere workpiece and plastic brick workpiece are used to minimise systematic errors in magnification/voxel size. Whilst the multi cross-section workpieces are used in Chapter 5 to evaluate the influence scatter and beam hardening have on dimensional measurements.

Chapter 4 Voxel Size Determination

In order to study the influence of scatter and beam hardening experimentally, methods for minimising systematic errors in magnification/voxel size must first be implemented; this being the purpose of the present chapter.

In this chapter the source-to-detector distance (SDD) and the offset of the magnification axis of the considered CT system are estimated using the ruby sphere workpiece; this provides a basic system setup (Section 4.2). The accuracy of measurements made with this setup are then compared to those made using a one-time voxel size correction; the plastic brick workpiece is used for this comparison (Section 4.3).

4.1 Geometric Magnification and Voxel Size

The voxel size is a very important property in X-ray CT for dimensional metrology. When a dimension is evaluated from a CT data-set the measurement can be considered the product of the number of voxels and the voxel size; so if the voxel size is in error, the measurement result will also be in error. The purpose of this chapter is to try and minimise errors in the voxel size, the developed methods are then used when studying the influence of scatter and beam hardening in the next chapter.

With knowledge of the detector pixel size P, the number of detector pixels perpendicular to the rotation axis n_p, the number of voxels into which the data is reconstructed n_v, and the geometric magnification m, the voxel size V of the reconstructed data can be calculated using Equation 4.1.

$$V = \frac{n_p \times P}{n_v \times m} \tag{4.1}$$

Geometric magnification is calculated as the quotient of the source-to-detector distance (SDD) D_{sd} and the source-to-object distance (SOD) D_{so}, see Equation 4.2. These simple equations are based on the assumption that the X-ray focal spot, rotation axis and the centre of the detector all lie on a straight line, as illustrated in Figure 4.1.

$$m = \frac{D_{sd}}{D_{so}} \tag{4.2}$$

Equation 4.1 shows that there are two potential sources of error in calculating the voxel size: (i) the pixel size and (ii) the magnification. It is assumed that the pixel size error is small compared to errors in magnification [78], [150]. Thus in order to minimise the voxel size error, the magnification error needs to be minimised, which in turn requires accurate estimates of SOD and SDD. The SOD is largely dependent on the encoder position of the magnification axis, but requires an estimate of the offset between the axis origin and the focal spot position (z_0 in Figure 4.1). Additionally, the SDD cannot be measured using an external instrument since the focal spot exists within the target. As such, a method for estimating SOD and SDD is described in the next section.

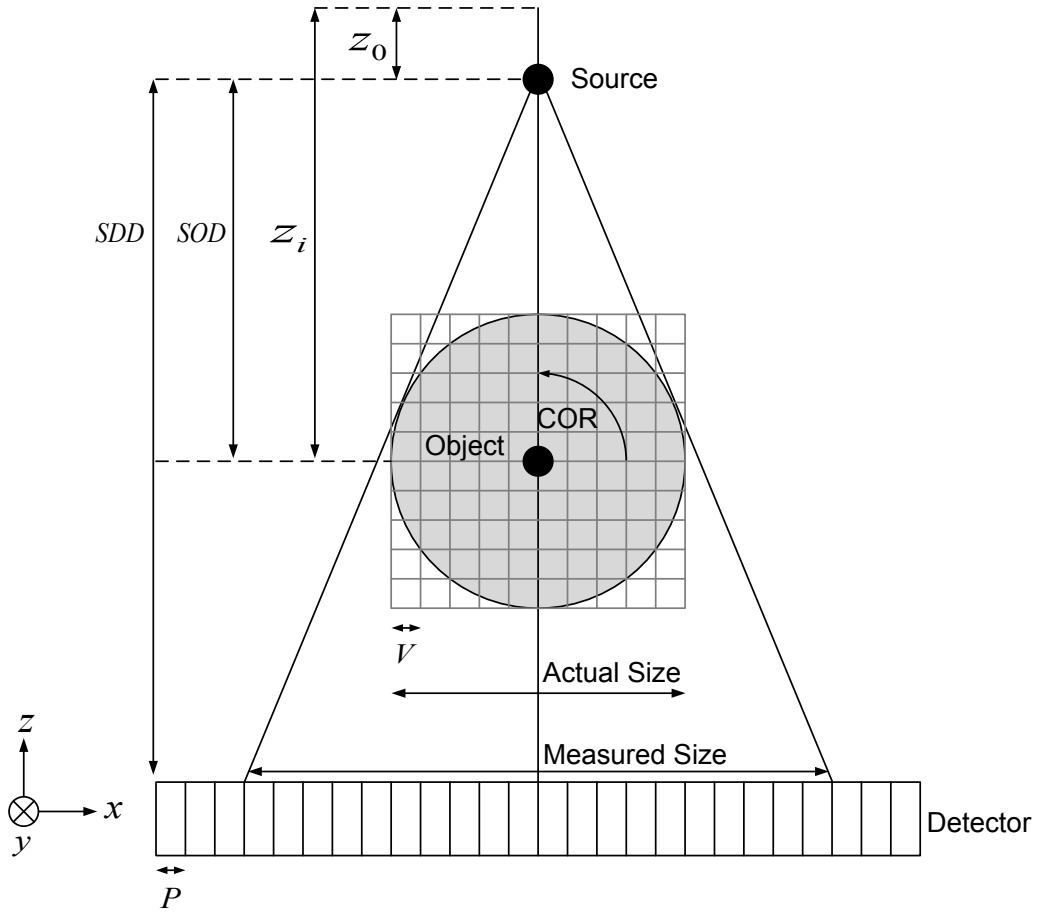

Figure 4.1 Idealised geometry of a CT system on the central plane.

4.2 Estimating the SDD and Mag Axis Offset

The SOD and SDD are subject to a number of error sources, these include thermal expansion of the CT system, focal spot drift, vibration, misalignment, and errors in the magnification axis encoder position. Seeing as it is not possible to directly measure the z position of the focal spot, magnification must be measured 'in the image'. This is achieved by imaging an object of a known size and with knowledge of the detector pixel size. With at least two independent measurements of the magnification the SDD and mag axis offset can be estimated; the method for doing this is described in what follows and is largely based on the work of Yang et al. [114].

4.2.1 Method

A more general formula for geometric magnification is the quotient of 'measured size' (s_m) and 'actual size' (s_a):

$$m = \frac{s_m}{s_a} \tag{4.3}$$

where the terms 'measured size' and 'actual size' are illustrated in Figure 4.1. The calibrated diameter of the object in Figure 4.1 is the 'actual size' and the diameter of the object's projection is the 'measured size'. This calculation of magnification is independent of values of SOD and SDD, so by equating Equation 4.3 and 4.2 SDD can be estimated.

To evaluate Equation 4.3 the 'measured size' needs to be evaluated in the image. Mere projections are not sufficient as one cannot evaluate a 3D length from its 2D projection. The reference dimensions of the ruby sphere workpiece are therefore used for this purpose.

With a CT scan of the ruby sphere workpiece its dimensions can be evaluated as described in Chapter 3. By dividing the dimensions of the ruby-sphere workpiece by the voxel size we have the dimensions in units of voxels (d_v), this mitigates the influence of an incorrect voxel size. These CT-based measurements are used to calculate the 'measured size' using the following equation:

$$s_m = P \times d_v \times \frac{n_p}{n_v} \tag{4.4}$$

Dividing this length by the 'actual size', that is, the CMM reference measurement, the geometric magnification is found:

$$m = \frac{P \times d_v \times n_p}{n_v \times s_a} \quad 4.5$$

Equating Equation 4.5 to Equation 4.2 gives:

$$m = \frac{PS \times d_v \times n_p}{n_v \times s_a} = \frac{D_{sd}}{D_{so}} \quad 4.6$$

Looking to Figure 4.1 it can be seen that SOD is a function of the axis encoder position z_i and the axis origin z_0 such that:

$$D_{so} = z_i - z_0 \quad 4.7$$

rewriting Equation 4.6:

$$m = \frac{D_{sd}}{z_i - z_0} \quad 4.8$$

Rearranging for z_i:

$$z_i = D_{sd}\frac{1}{m} + z_0 \quad 4.9$$

Equation 4.9 now takes the form of a straight line where the gradient is the best-fit SDD and the y-intercept is the offset in the magnification axis.

In order to plot Equation 4.9 and evaluate the fit parameters, the ruby sphere workpiece is scanned at five different magnifications, details of which are given in Figure 4.2. The scan settings, reconstruction settings and data processing steps have already been described in Chapter 3.

All six reference dimensions of the ruby sphere workpiece are evaluated at each of the five magnifications and used to derive the magnification as per Equation 4.5.

(a) Mag 1 = ×3.75,

z_i = 200 mm

Voxel size = 97.7 µm

(b) Mag 2 = ×4.21

z_i = 180 mm

Voxel size = 87.2 µm

(c) Mag 3 = ×4.78

z_i = 160 mm

Voxel size = 76.8 µm

(d) Mag 4 = ×5.54

z_i = 140 mm

Voxel size = 66.3 µm

(e) Mag 5 = ×6.58

z_i = 120 mm

Voxel size = 55.8 µm

Figure 4.2 Projections and magnification details for scans of the ruby sphere workpiece.

4.2.2 Results

The result of plotting the reciprocal of the magnification against the encoder position z_i, is given in Figure 4.3. The parameters of the best fit line give the SDD and the offset in the magnification axis, which are found to be 698.420 mm and 13.344 mm respectively. Figure 4.4 shows that with these values, the dimensions of the ruby sphere workpiece are measured with an error less than ± 15 μm across the five considered magnifications. This represents the residual error in the measurements; this residual error is either due to the CT measurement procedure (1/mag values), or it is due to errors in the magnification axis encoder position (z_i), or a combination of both.

The procedure for estimating the SDD and the offset in the magnification axis is repeated a further two times with a week between measurement runs. The range of the repeated measurements of the SDD and z_0 are 400 μm and 150 μm respectively. This result shows the stability of the CT system is very poor, and the reproducibility of measurements for different magnifications is very low. Welkenhuyzen et al. [79] reported encoder position errors for the magnification axis of up to ± 400 μm for axis travel over 600 mm as measured using laser interferometry, it therefore seems likely that errors in the encoder position are responsible for the variation of the SDD and mag axis offset. In other work, drift of up to 150 μm has been observed for measurements conducted over a 5 week period, the drift was again attributed to the repeatability of the magnification axis [38], [42].

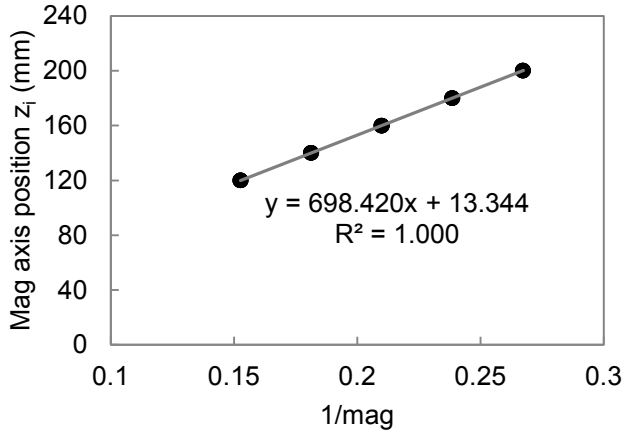

Figure 4.3 Plot of $z_i$verses 1/mag. Mag values are derived in the image using the ruby sphere workpiece, and z_i is the mag axis encoder position.

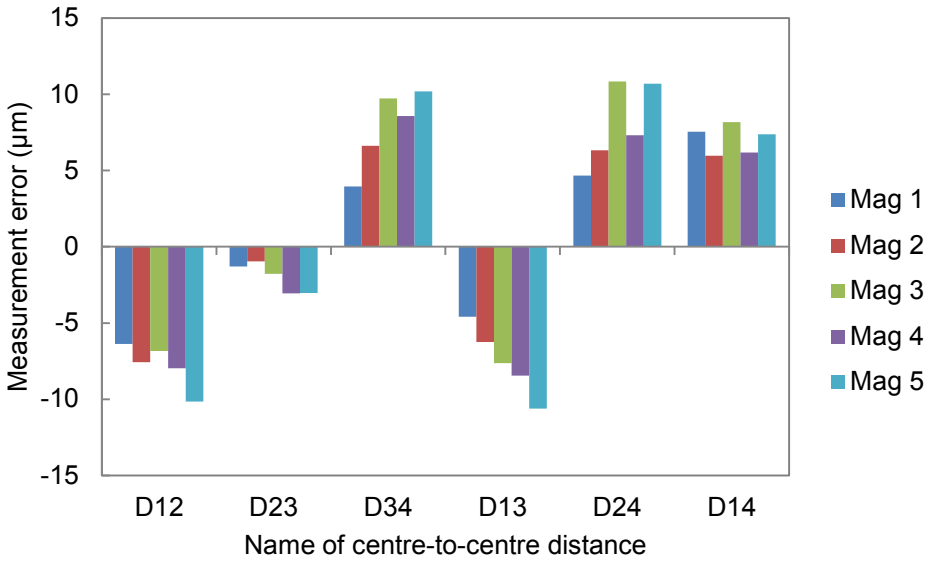

Figure 4.4 Residual error of ruby sphere workpiece measurements when scanned over a range of magnifications.

The main limitation of estimating the SDD and mag axis offset in this way is relying on the magnification axis encoder position. A better approach would be to measure the axis position directly using an external tool such as a laser interferometer, thus mitigating the error in the encoder position. By reducing the error in the z_i values it is expected that more accurate and reproducible estimates of SDD and z_0 will be achieved. This should be considered in future work.

Irrespective of the potential errors in the encoder position, in the next section the performance of the procedure is tested by measuring the plastic brick workpiece. In addition to this system setup, a one-time voxel size correction is evaluated that requires an extra scan of the ruby sphere workpiece after the measurement task.

4.3 Voxel Size Correction

The aim of the approach described in the previous section is to minimise voxel size errors over a range of magnifications, and is hence termed a global approach. In this section the performance of the approach is tested by measuring the plastic brick workpiece.

An alternative approach to minimise voxel size errors is to scan a reference workpiece before, after or during a given measurement task. The voxel size is then corrected by comparing the CT measurements to the reference measurements. This approach is termed a one-time voxel size correction and is also evaluated in this section for measurements of the plastic brick workpiece.

4.3.1 CT Scans

The reference dimensions of the plastic brick workpiece include the distance between the centres of the two outermost knobs, L1, and the radius of one of the central knobs D1. The plastic brick workpiece is scanned in three different orientations, see Figure 4.5. Measuring the workpiece in different orientations should highlight any anisotropy in the measurement volume due to geometric misalignment [148]. The SOD and SDD are defined based on the values derived in the previous section. The scan settings remain the same for all three scans, details of which are given in Section 3.4.3. The scans are conducted consecutively and the magnification axis unmoved. To derive the one-time voxel size correction the ruby sphere workpiece is scanned after the final scan of the plastic brick.

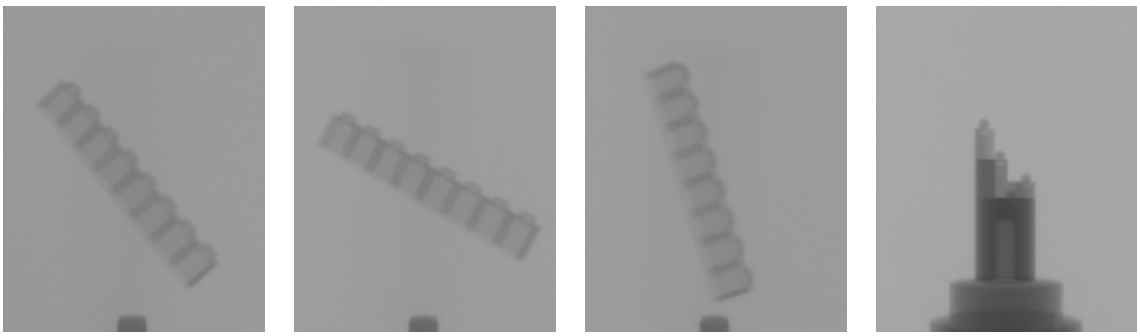

Position 1 | Position 2 | Position 3 | Ruby sphere workpiece

Mag = ×2.77, Voxel Size = 133 µm.

Figure 4.5 Projections of the plastic brick workpiece in three different orientations alongside the ruby sphere workpiece for voxel size correction.

4.3.2 Method

The aim of the one-time voxel size correction is to derive a scaling factor to correct systematic errors in CT measurements through the use of reference dimensions. Consider the reference dimension $D12$ of the ruby sphere workpiece. The reference measurement is denoted $D12_{CMM}$ whilst the CT-based measurement is denoted $D12_{CT}$. The CT-based measurement can be multiplied by a correction factor δ such that it is equal to the reference measurement:

$$D12_{CMM} = \delta D12_{CT}. \tag{4.10}$$

Since the ruby sphere workpiece has six reference dimensions we find the δ that satisfies the following equation in the least-squares sense:

$$\begin{bmatrix} D12_{CMM} \\ D13_{CMM} \\ D14_{CMM} \\ D23_{CMM} \\ D24_{CMM} \\ D34_{CMM} \end{bmatrix} = \delta \begin{bmatrix} D12_{CT} \\ D13_{CT} \\ D14_{CT} \\ D23_{CT} \\ D24_{CT} \\ D34_{CT} \end{bmatrix}. \tag{4.11}$$

This is easily evaluated by plotting the CT-based measurements against the reference measurements and fitting a straight line that passes through the origin, the gradient of the straight line is the correction factor δ, as shown in Figure 4.6. Multiplying the measurement results of the actual workpiece (the plastic brick in this case) by δ will correct the measurement result accordingly.

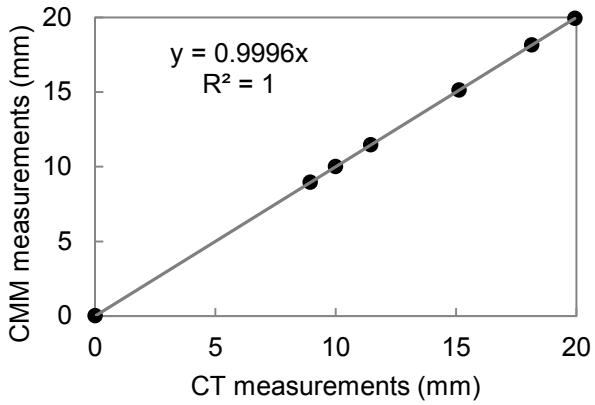

Figure 4.6 Plot of CT versus CMM measurements of the ruby sphere workpiece. Gradient of the best-fit line is the voxel size correction δ.

4.3.3 Results

The measurement error for the reference dimensions L1 and D1 evaluated from the three different workpiece orientations are given in Figure 4.7 and Figure 4.8 respectively. Looking to Figure 4.7, the first thing to notice is all the measurements are made with sub-voxel accuracy. The largest error is 36 μm whilst the nominal voxel size is 133 μm. With the one-time voxel size correction the measurement error is further reduced, and is in the order of microns for positions 1 and 3.

Looking to Figure 4.8, as for L1, all the measurements of D1 are made with sub-voxel accuracy, the largest error being 20 μm. Again, the one-time voxel size correction reduces the measurement error, but the effect is not as dramatic as for L1. This may be due to L1 spanning a much larger portion of the CT volume than D1, so even a small error in the voxel size will lead to large measurement errors.

The measurements of L1 and D1 vary with the orientation of the workpiece. L1 varies by 10 μm, whilst D1 varies by 4 μm. This variation is most likely due to some degree of geometric misalignment in the CT system. L1 seems to be more affected by the orientation; this is to be expected since it spans a larger portion of the measurement volume and will therefore amplify any misalignment in the system.

The results suggest using the one-time correction leads to more accurate measurements. The method is simple to implement and reduces the measurement error well below the voxel size of the CT data. The limitation of the method is the requirement for an additional scan and additional data processing. Furthermore, different size reference workpieces will be required for different magnifications. Nevertheless, the method seems to be quite effective. A similar method was demonstrated by Bartscher et al. [43] whereby a reference workpiece was scanned before and after the actual workpiece. The before and after scan allows any drift in the measurement to be quantified, which could be particularly significant for long scans.

As mentioned in the previous section, the limitation of the global approach is the error in the magnification axis encoder position. The one-time correction is able to overcome this error since the scaling factor is derived independent of the SOD. Nevertheless, the global approach still leads to sub-voxel measurement errors, the method can therefore serve as a good first estimate that can be further refined with the one-time correction.

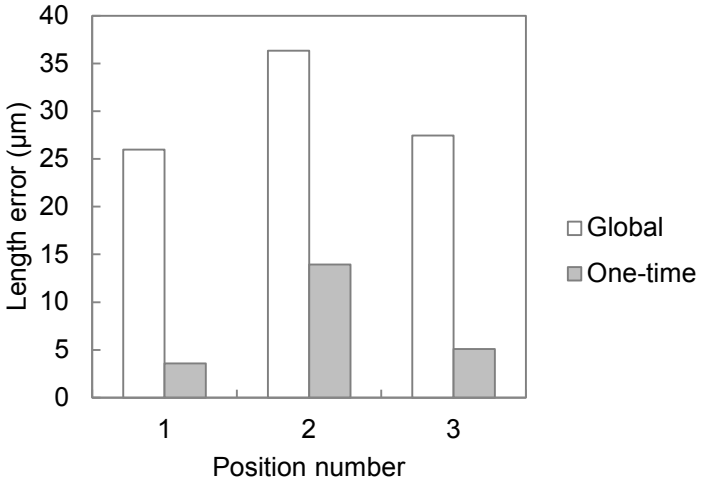

Figure 4.7 Measurement error for L1 of the plastic brick workpiece. Comparison between a global approach to correcting errors in magnification and a one-time correction.

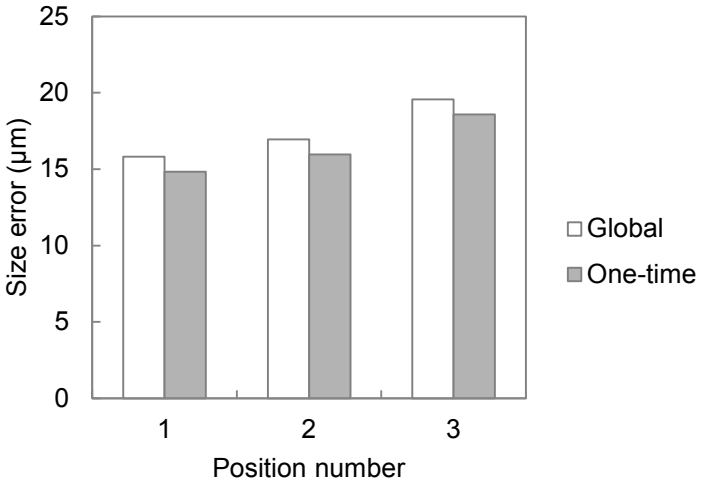

Figure 4.8 Measurement error D1 of the plastic brick workpiece. Comparison between a global approach to correcting errors in magnification and a one-time correction.

4.4 Chapter Summary

In this chapter the SDD and offset of the magnification axis have been estimated using the ruby sphere workpiece. Following this system setup the plastic brick workpiece was measured. It was shown that the system setup leads to reasonable measurement accuracy, but a one-time voxel size correction can further reduce measurement errors.

The methods described in this chapter serve to minimise errors in the voxel size such that the influence of scatter and beam hardening can be studied experimentally in the next chapter.

Chapter 5 Experimental Studies on Scatter and Beam Hardening

Scatter and beam hardening are well known to severely degrade the quality of CT data; however, the impact they have on dimensional measurements is not well understood. The purpose of this chapter is to investigate how scattered radiation and beam hardening influence dimensional measurements through experimentation.

The influence of scatter is assessed through the use of source collimation and the beam stop array scatter correction method, whilst the influence of beam hardening is considered using spectrum pre-filtration.

In this chapter the following contributions are made:

- Both scatter and beam hardening are shown to contribute to the nonlinear relationship between attenuation and material thickness. The contribution of scatter has been neglected in previous studies and the nonlinearity wholly attributed to beam hardening (Section 5.1).
- Scatter and beam hardening artefacts are shown to severely distort the material phase of grey value histograms (Section 5.2).
- Scatter and beam hardening are shown to decrease measurements of the inner radius of the multi-cross section workpiece, and increase measurements of the outer radius compared to when scatter and beam hardening are minimised/corrected (Section 5.3 and 5.5).
- The beam stop array scatter correction method is extended to consider the impact veiling glare has on measured scatter signals (Section 5.4).

5.1 Attenuation Measurements

Scattered radiation and beam hardening directly influence intensity values measured by the detector. The measured intensity is used to calculate X-ray attenuation, which is then backprojected to estimate the object's cross-sections. Understanding the influence scatter and beam hardening have on attenuation measurements is therefore the starting point to understanding how these phenomena influence dimensional measurements.

5.1.1 Method

X-ray attenuation is measured for varying thicknesses of aluminium and titanium using step wedges of each material, see Figure 5.1. The steps of both wedges vary in height from 1 mm to 50 mm in steps of 1 mm ± 0.1 mm, as measured with a micrometer. X-ray attenuation is measured for a maximum material thickness of 27 mm, this being the maximum path length of the multi cross-section workpieces used later on in this chapter.

X-ray attenuation measurements are made under four conditions:

1. The X-ray source collimated to a fan-beam.
2. The X-ray source pre-filtered with 0.5 mm of copper.
3. The X-ray source collimated and pre-filtered.
4. No collimation and no pre-filtration.

Collimating the X-ray source to a fan-beam reduces the number of X-rays incident on both the step wedge and its surrounding environment, thus reducing the number of potential scattered X-rays. A copper collimator is used to realise the collimation, it is 30 mm in height and has an aperture in the form of a 300 µm slit, see Figure 5.2. 30 mm of copper is able to attenuate 99.6 % of 160 keV X-ray photons, whilst the 300 µm slit is the smallest slit that can be fabricated using electrical discharge machining. The resulting collimation for a bright field image is shown in Figure 5.3.

Pre-filtering the source attenuates low energy photons from the X-ray spectrum. After pre-filtering, the X-ray spectrum that falls incident on the step wedge has a higher mean energy, it has been ‘pre-hardened’ and is less polychromatic. This reduces subsequent beam hardening that occurs as the X-ray spectrum propagates through the step wedge. Copper is chosen as the pre-filter material as it is an efficient X-ray attenuator. 0.5 mm of copper is chosen as this is the maximum thickness that can be used for the considered CT system at the specified source settings.

Before placing a step wedge in the chamber of the CT system, the current and acceleration voltage of the X-ray source are set, see Table 5.1, and the detector is corrected for defective pixels and variations in intensity (flat field correction), a bright field image is then captured. One of the step wedges is then positioned between the X-ray source and the detector. For each attenuation measurement the step wedge is repositioned such that the projection of each step falls upon the approximate centre of the detector. Projections of each step are captured and the mean intensity of a 5×5

pixel region is evaluated in the shadow of each step, this being I in the Beer-Lambert law of attenuation:

$$Attenuation = -\ln(I/I_0) \quad 5.1$$

where I_0 is the mean intensity of the same 5×5 pixel region of the bright field image. Each measurement is repeated three times for the four different combinations of source collimation and pre-filtration.

Table 5.1 X-ray source settings for attenuation measurements using step wedges.

	Voltage (kV)	Current (μA)
No collimation, no pre-filter	160	14
No collimation, pre-filter	160	25
Collimation, no pre filter	160	17
Collimation, pre-filter	160	33

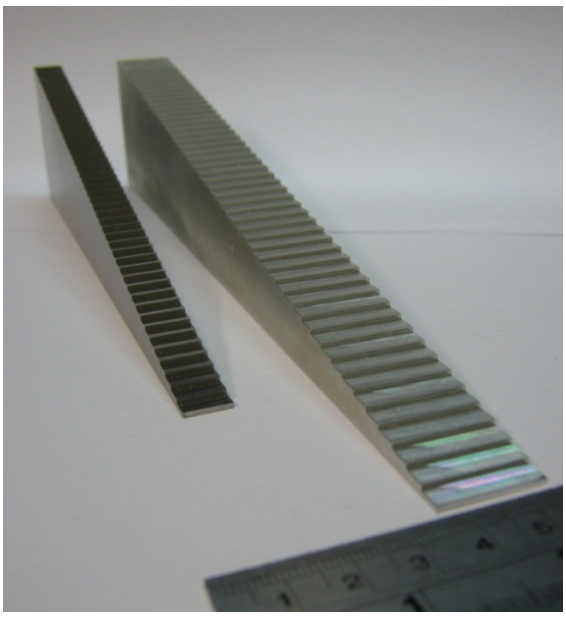

Figure 5.1 Titanium (left) and aluminium (right) step wedges, step increment is 1 mm.

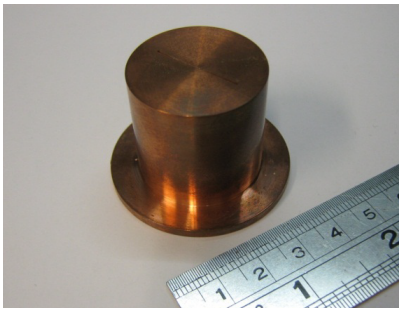

Figure 5.2 Copper collimator with 300 μm slit.

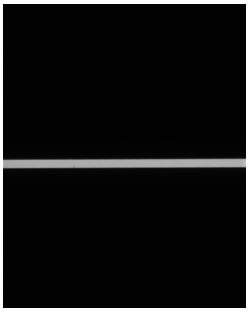

Figure 5.3 Bright field image with source collimation.

5.1.2 Results

Figure 5.4 and Figure 5.5 show the attenuation measurements for the aluminium and titanium step wedges plotted against material thickness respectively. Results for all four conditions are plotted. For ideal monochromatic, scatter-free attenuation measurements a linear relationship would be seen between X-ray attenuation and material thickness. Figure 5.4 and Figure 5.5 show that with no collimation and no pre-filtration both the aluminium and titanium attenuation measurements are, as expected, nonlinear with respect to material thickness. For the aluminium attenuation measurements shown in Figure 5.4, a reasonably linear relationship is seen with both collimation and pre-filtration. For the titanium attenuation measurements shown in Figure 5.5, a nonlinear relationship is seen even with collimation and pre-filtration. The results show that neither collimation nor pre-filtration by themselves are sufficient to minimise the influence of both scatter and beam hardening, but rather a combination of the two is sufficient for aluminium in this case.

In both Figure 5.4 and Figure 5.5 pre-filtration has the effect of lowering attenuation values. This is because the pre-filtered X-rays have a higher mean energy, and are therefore more penetrating, meaning it would take more material to yield the same attenuation as un-filtered X-rays. On the other hand, collimation has the effect of raising attenuation values. This is because scattered X-rays that fall incident on the detector raise intensity values, I, compared to if there were no scattered X-rays. Looking to Equation 5.1, if I increases, attenuation decreases and vice versa. Therefore, scatter and beam hardening act on attenuation values in opposition: beam hardening raises attenuation values and scatter lowers attenuation values, but both

cause the relationship between attenuation and material thickness to become nonlinear.

Scatter and beam hardening are two very different physical phenomena that contribute in different ways to the nonlinearity of polychromatic X-ray attenuation. Unfortunately this seems to have been overlooked in previous studies. It is often the case that attenuation measurements are made using step wedges similar to those used here; the nonlinearity observed is then wholly attributed to beam hardening, and a beam hardening correction then derived. This beam hardening correction will be wrong, as it is derived in the presence of scatter. Scatter is an additional signal, it is stochastic in nature and therefore not as simple to correct as beam hardening. Failing to recognise this is where a number of studies in the field have fallen short.

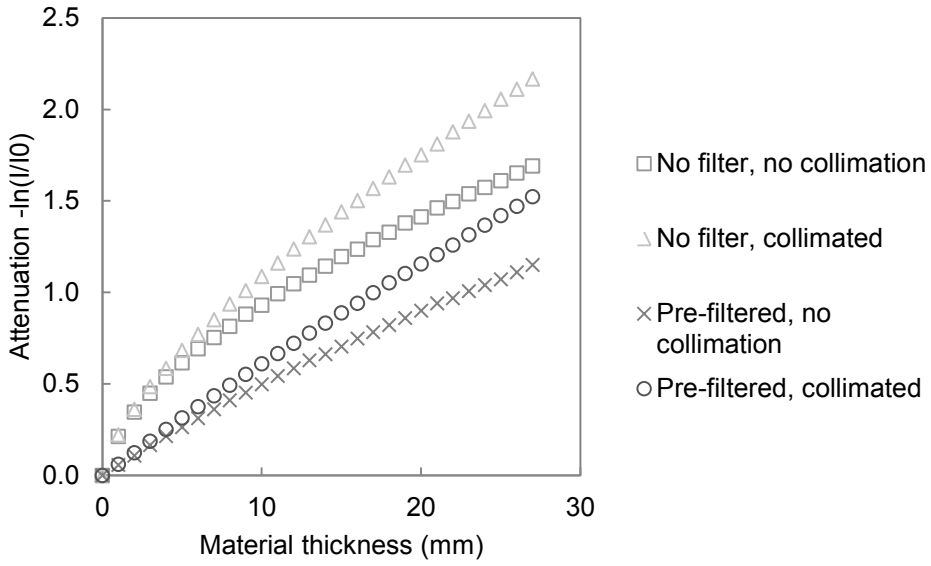

Figure 5.4 Attenuation versus thickness graph for aluminium, with and without pre-filtration and collimation.

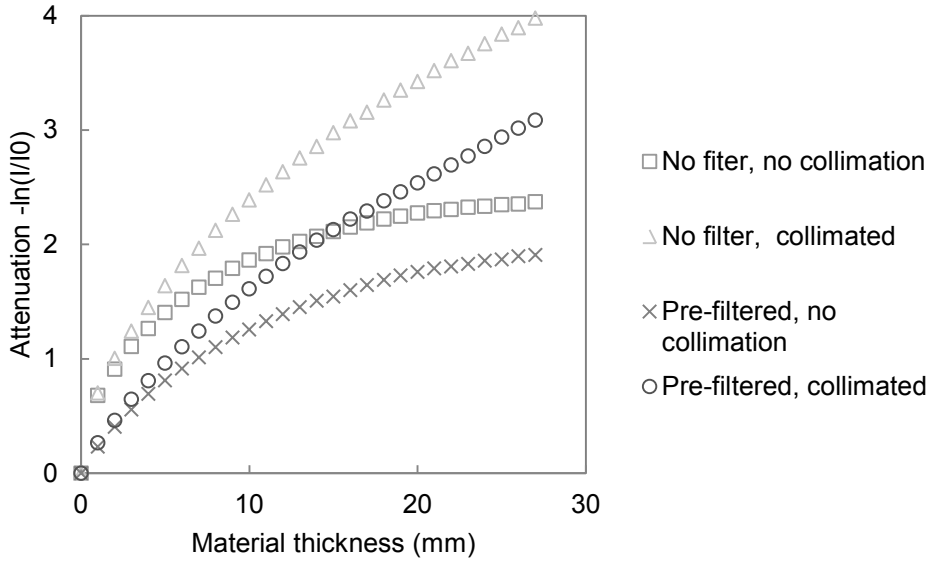

Figure 5.5 Attenuation versus thickness graph for titanium, with and without pre-filtration and collimation.

5.2 Scans with Collimation and Pre-Filtration

In the previous section it was shown that source collimation and pre-filtration were able to minimise the nonlinearity of the aluminium attenuation measurements. Collimation and pre-filtration are next used to minimise scatter and beam hardening for scans of the aluminium and titanium multi cross-section workpieces.

The scatter signal generated by the aluminium workpiece is first estimated using the source collimator to inspect its magnitude and spatial distribution. A comparison is then made between CT images reconstructed from data with and without collimation and pre-filtration.

5.2.1 Estimating Scatter Signals

An open-field projection of the aluminium multi cross-section workpiece is shown in Figure 5.6. This projection consists of both primary photons, P, that have not undergone scattering interactions, and scattered photons, S, that have undergone scattering interactions. Denoting the open-field projection as I_{OF}:

$$I_{OF} = P + S. \qquad 5.2$$

A collimated projection of the wokpiece is shown in Figure 5.7; only the collimator has been added, the workpiece is unmoved and the X-ray settings are unchanged. Denoting the collimated projection as I_{COL}, it is assumed the scatter signal in the collimated projection is small such that $I_{COLL} \approx P$. Therefore the scatter signal can be estimated by subtracting I_{COL} from I_{OF}. Figure 5.8 shows the result of this calculation in the form of line profiles. Intensity values across the centre of the collimator slit for the open-field and collimated projections are plotted alongside the estimated scatter signal. Note the discontinuities in the profiles correspond to drilled holes in the multi cross-section workpiece. Figure 5.8 shows the scatter signal is largest at the edges of the projection where no material is present, and smallest for maximum path lengths through the workpiece. This result is in agreement with the work of Schorner et al. [57] and Peterzol et al. [102] both of whom used beam stop arrays to estimate scatter signals (the beam stop array method is discussed in detail in Section 5.4). Observe also that the edges of the collimated line profile are much 'sharper' than those of the open field, this is likely to influence the quality of the edges in the reconstructed data, and therefore surface determination.

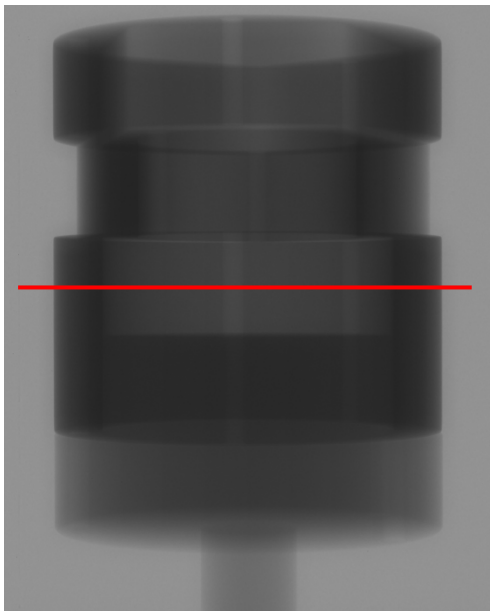

Figure 5.6 Open field projection of the aluminium multi cross-section workpiece. Red line corresponds to line profile in Figure 5.8.

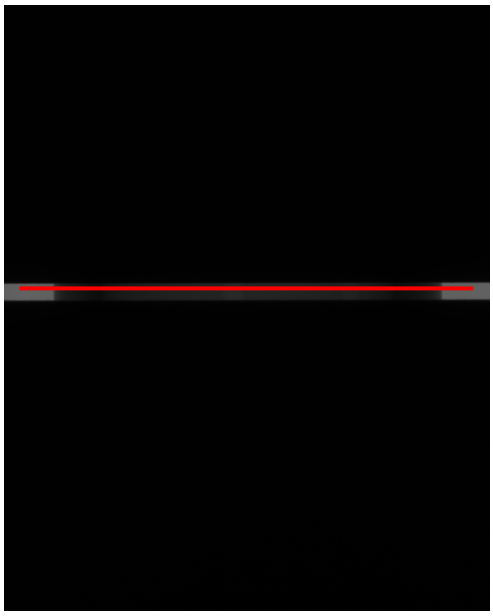

Figure 5.7 Collimated projection of the aluminium multi cross-section workpiece. Red line corresponds to line profile in Figure 5.8.

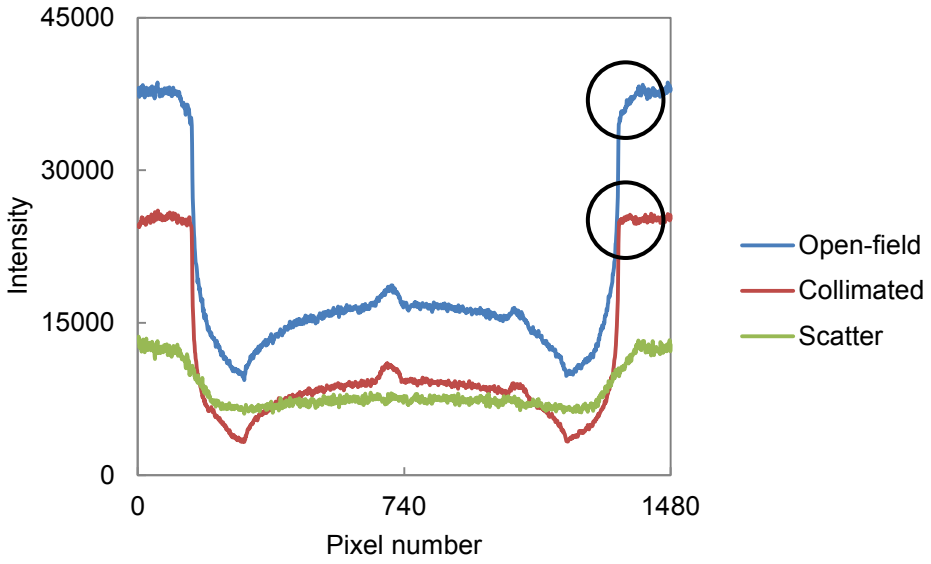

Figure 5.8 Line profiles across projections of the aluminium multi cross-section workpiece with and without collimation. Difference in edge 'sharpness' highlighted.

5.2.2 Comparing CT Images

The aluminium and titanium multi cross-section workpieces are next scanned under the same four conditions as the attenuation measurements in Section 5.1; i.e. with and without collimation and pre-filtration. The scan settings are the same as those given in Table 5.1. The workpieces are not removed from the CT system between scans and each scan is repeated three times per condition. Due to the limited field of view imposed by the collimator, only the CT image corresponding to the central detector row of each scan is reconstructed.

Central CT images of the aluminium and titanium workpieces are shown in Figure 5.9 and Figure 5.10 respectively. Whilst line profiles across the cylinder wall for each reconstruction are shown in Figure 5.11 and Figure 5.12 for the aluminium and titanium data respectively.

Looking to Figure 5.9 and Figure 5.10, the CT images with no collimation and no pre-filtration show raised grey values at outer edges and lowered grey values at inner edges (cupping), alongside a general loss of contrast compared to the data with both collimation and pre-filtration. These artefacts are particularly severe for the titanium data shown in Figure 5.10(a), notice the distortion of the drill holes also.

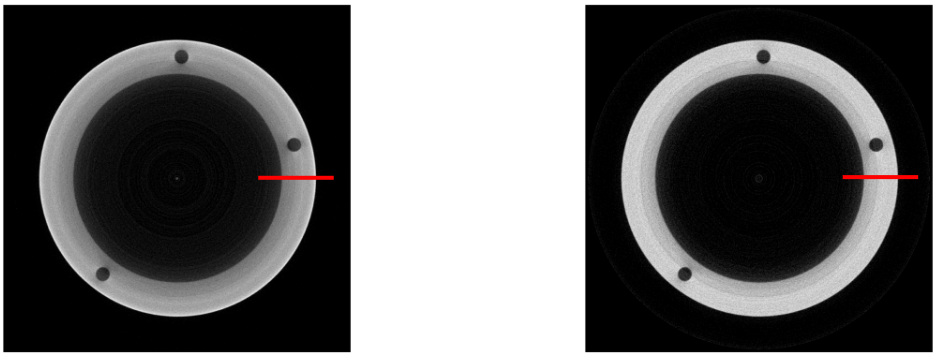

(a) No pre-filter, no collimation.

(b) Pre-filtered, no collimation.

(c) No pre-filter, collimated.

(d) Pre-filtered, collimated.

Figure 5.9 Comparison of CT images of the aluminium multi cross-section workpiece acquired with and without collimation and pre-filtration. Red lines correspond to line profiles in Figure 5.11.

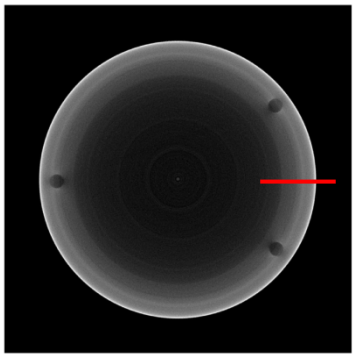

(a) No pre-filter, no collimation.

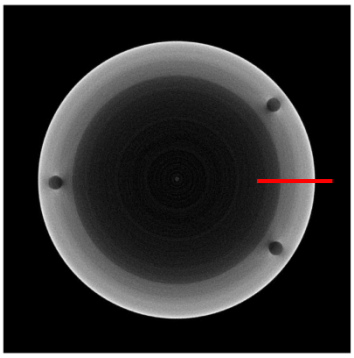

(b) Pre-filtered, no collimation.

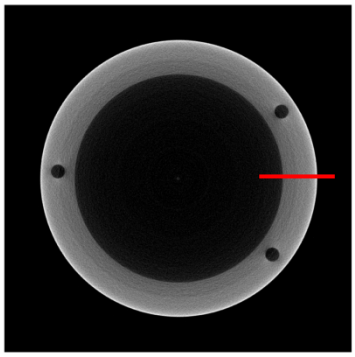

(c) No pre-filter, collimated.

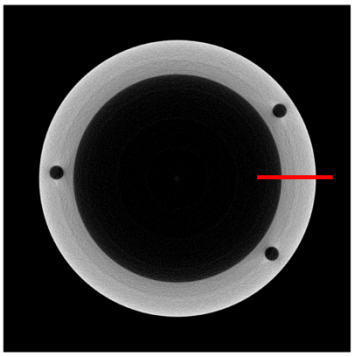

(d) Pre-filtered, collimated.

Figure 5.10 Comparison of CT images of the titanium multi cross-section workpiece acquired with and without collimation and pre-filtration. Red lines correspond to line profiles in Figure 5.12.

The line profiles in Figure 5.11 and Figure 5.12 show that collimation raises the reconstructed values whilst pre-filtration lowers the reconstructed values, this is the same relationship that was seen for the attenuation values in the previous section. Also, looking to the inner (left-hand) edge of the line profiles, the edges of the collimated data appear much more ‘well defined’. This is particularly apparent for the titanium data where the inner edge is barely discernible without collimation. Collimation significantly improves the inner edge profile which suggests the dominant artefact for the titanium workpiece is scatter.

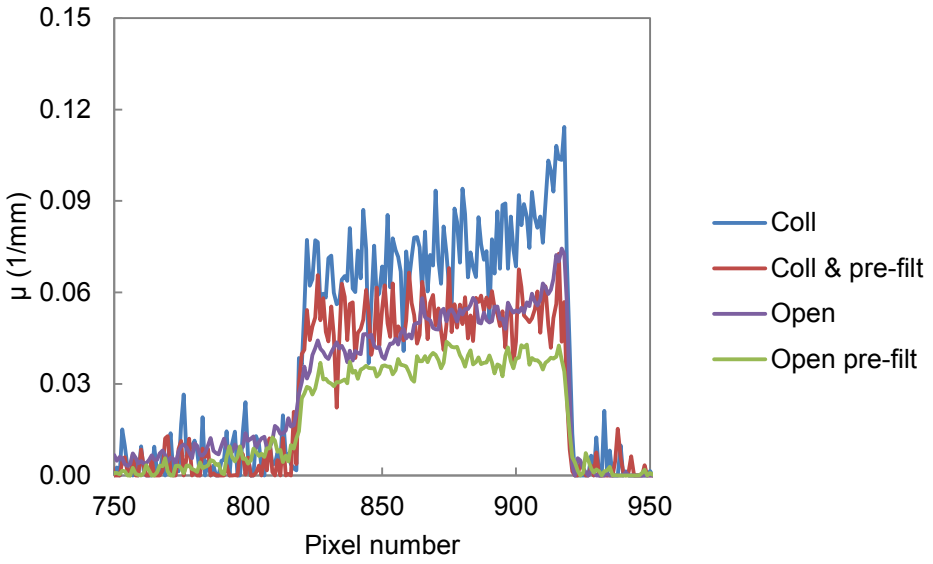

Figure 5.11 Comparison of line profiles form Figure 5.9. Line profiles drawn across the aluminium cylinder wall.

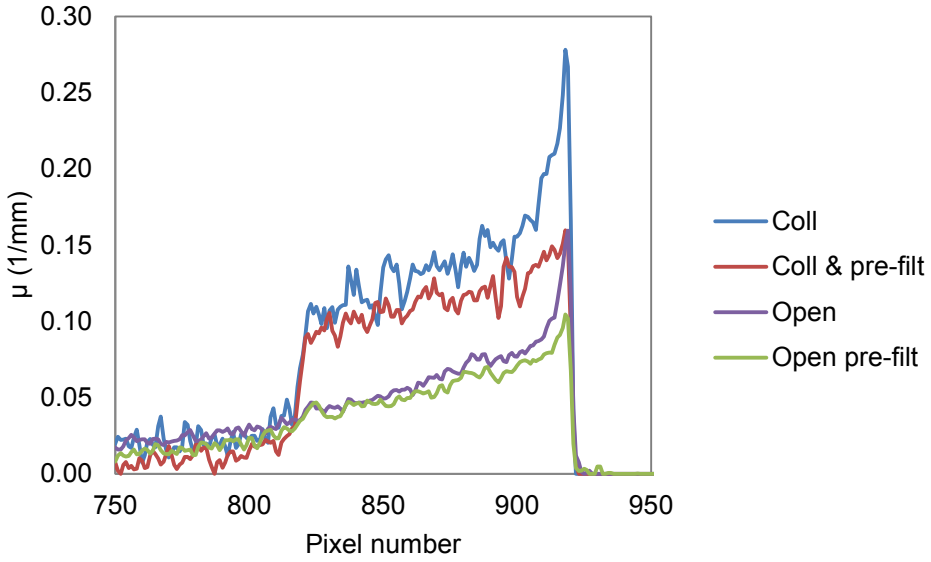

Figure 5.12 Comparison of line profiles from Figure 5.10. Line profiles drawn across titanium cylinder wall.

In order to present a quantitative comparison between CT images any number of image quality statistics could be evaluated. Unfortunately, it is unclear how any of these statistics influence, or relate to, surface determination or dimensional measurements. The contrast-to-noise ratio (CNR) is one statistic that could prove useful, since both edge contrast and noise are likely to influence surface determination. High contrast between air and material will yield a large response from a gradient-based edge operator, whilst low noise will reduce the number of false edges identified. Unfortunately, such a statistic requires a region of interest (ROI) be defined; it is unlikely a ROI will be representative of an entire CT image, or CT volume for that matter. Thus, in order to consider all the information available in the CT images, histograms of each are evaluated. Contrast is considered as the horizontal distance between air and material distribution peaks, whilst noise is considered to be the spread of each distribution. Grey value histograms of the aluminium and titanium CT images are shown in Figure 5.13 and Figure 5.14 respectively.

The histograms reveal a considerable amount of information about each CT image. It appears without collimation or pre-filtration the material phase of the data has multiple peaks, Figure 5.13(a) and Figure 5.14(a). These peaks belong to the raised and lowered grey values induced by scatter and beam hardening for the external and internal surfaces respectively. For the aluminium data, either pre-filtration or collimation removes this undesirable distribution, as shown by Figure 5.13 (c) and (b) respectively; whilst for the titanium data neither collimation nor pre-filtration alone are able to unify the material distribution, Figure 5.14 (c) and (b). For the aluminium data the combination of both collimation and pre-filtration yields a narrow, Gaussian material grey value distribution; whilst for the titanium data even with both collimation and pre-filtration some amount of distortion remains in the material grey value distribution.

The histograms show collimation alone gives the highest contrast, at the expense of a larger spread in the material phase, i.e. greater noise. The next highest contrast belongs to the collimated and pre-filtered data, followed by the un-collimated and un-filtered data, whilst the lowest contrast is seen for the pre-filtered data.

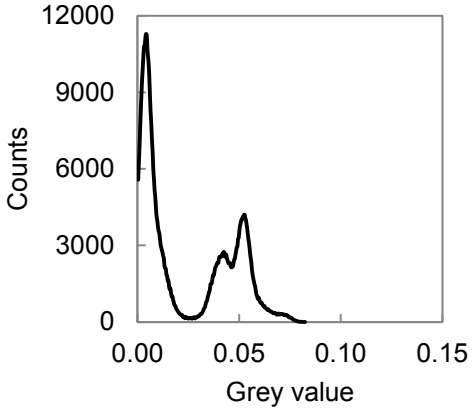

(a) No pre-filter, no collimation. Contrast = 0.047.

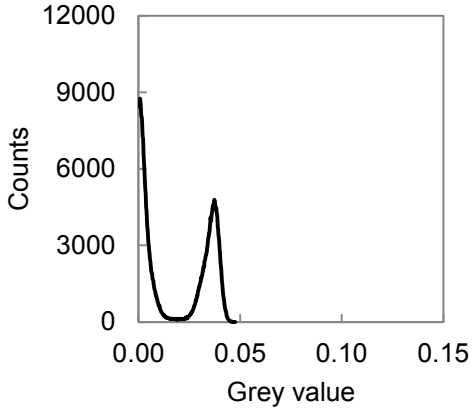

(b) Pre-filtered, no collimation. Contrast = 0.037.

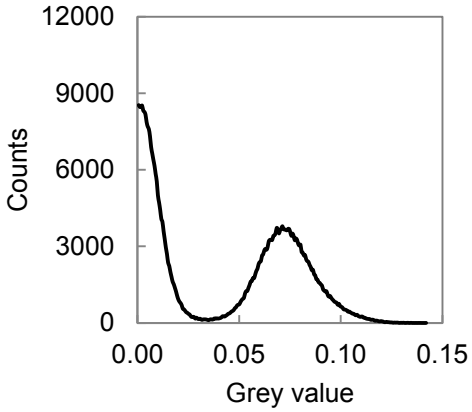

(c) No pre-filter, collimated. Contrast = 0.071.

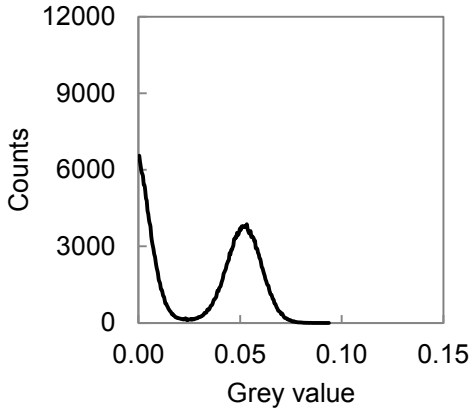

(d) Pre-filtered, collimated. Contrast = 0.053.

Figure 5.13 Grey value histograms of the aluminium CT images in Figure 5.9.

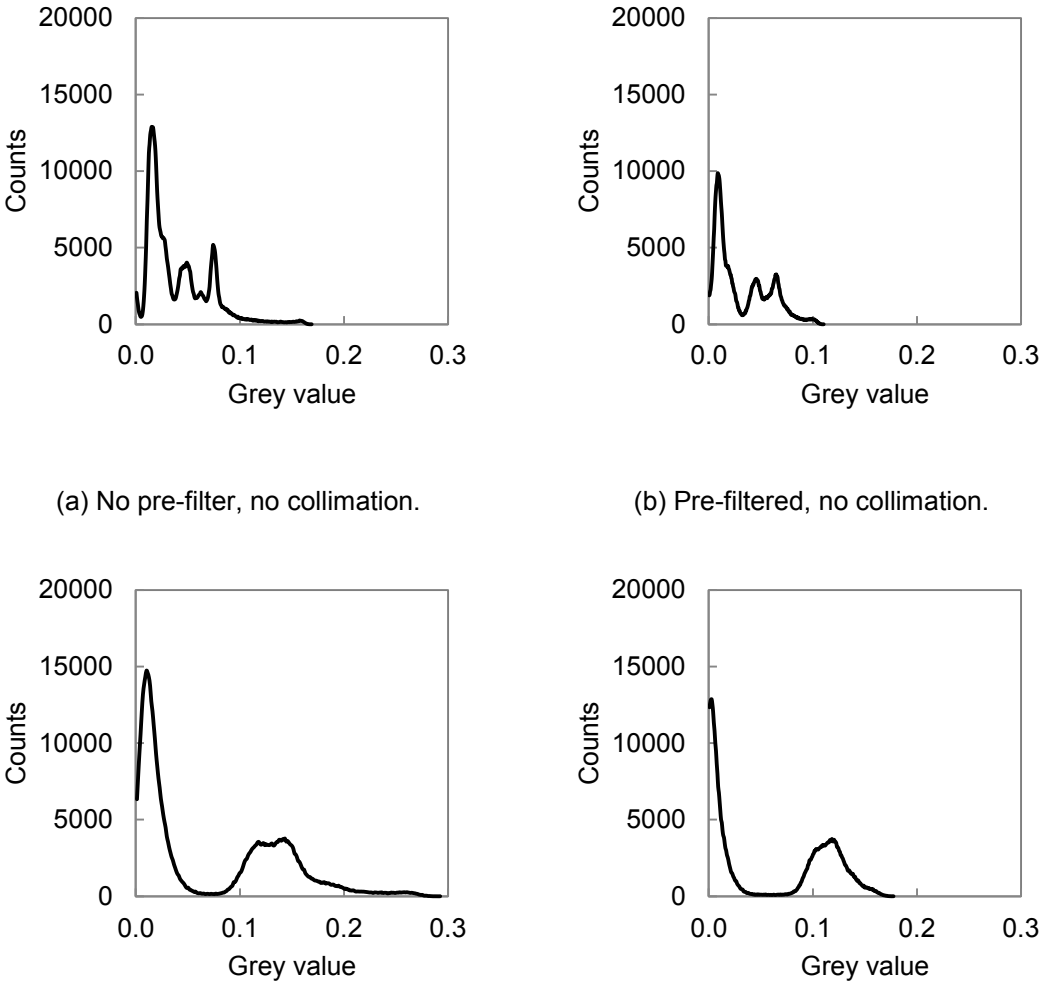

(a) No pre-filter, no collimation.

(b) Pre-filtered, no collimation.

(c) No pre-filter, collimated.

(d) Pre-filtered, collimated.

Figure 5.14 Grey value histograms of the titanium CT images in Figure 5.10.

5.3 Dimensional Measurements with Collimation and Pre-Filtration

In the previous section the influence of collimation and pre-filtration on CT image quality were assessed. The focus of this work is to better understand how scatter and beam hardening influence dimensional measurements. As such, using the scans described in the previous section, the influence of collimation and pre-filtration on measurements of the inner and outer radii of the aluminium multi cross-section workpiece are evaluated. The titanium data is not considered because the scatter and beam hardening artefacts are so severe surface determination is not possible for all the data sets.

5.3.1 Method

Surface determination is performed using both the ISO50 method and the local gradient-based method. Full details of these surface determination algorithms are given in Section 2.5. Both the ISO50 and local surface determination methods are considered because they rely on two different principles to identify an object's surfaces. The ISO50 method relies on a single threshold and treats all features in a data-set the same, whilst the local method considers local grey value properties; the two methods are therefore likely to behave differently to the presence of scatter and beam hardening.

As a result of reconstructing only the central CT image of each data-set, the resulting data cannot be aligned. This means the cross-sections evaluated are not necessarily perpendicular to the cylinder's axis. As such, the measurement results are not compared to the CMM reference measurements. Since the workpiece is not removed from the CT system between scans, nor the translation axes moved, it is assumed the same cross-section is evaluated each time.

5.3.2 Results

The measurement results of the inner and outer radii are given in Figure 5.15 and Figure 5.16 respectively; the error bars represent the range of the three repeated measurements. Figure 5.15 shows that collimation and pre-filtration both act to increase the inner radius estimate. This holds for both the ISO50 and local surface determination methods. Figure 5.16 shows that collimation and pre-filtration act to decrease the outer radius estimate; again this holds for both surface determination methods. Comparing Figure 5.15 and Figure 5.16, for the ISO50 method a greater influence is seen for the outer dimensions than the inner dimensions, furthermore, pre-filtration has a greater influence on the measurement results than collimation. The latter two observations do not hold for the local surface determination method which appears to be more robust to the influence of scatter and beam hardening.

The results clearly show both scatter and beam hardening significantly influence dimensional measurements. It appears scatter and beam hardening influence dimensional measurements in a similar fashion, and act on inner and outer dimensional features in opposition. The magnitude of the influence seems to be quite large; the influence of pre-filtration on the outer radius measurement as evaluated via the ISO50 method is 27 μm. This may seem small compared to the nominal radius of the workpiece (20 mm) but it is approximately half the voxel size of the reconstructed data (49 μm). This shows how changing the X-ray spectrum incident on the workpiece can significantly influence a measurement result.

As a consequence of being unable to align the CT data due to the limited field of view (FOV) imposed by the collimator, the cross-sections evaluated are not necessarily perpendicular to the cylinder's axis, therefore no comment can be made concerning the influence of scatter or beam hardening on the accuracy of dimensional measurements. As such, a method for correcting scatter for the entire FOV is implemented in the next section.

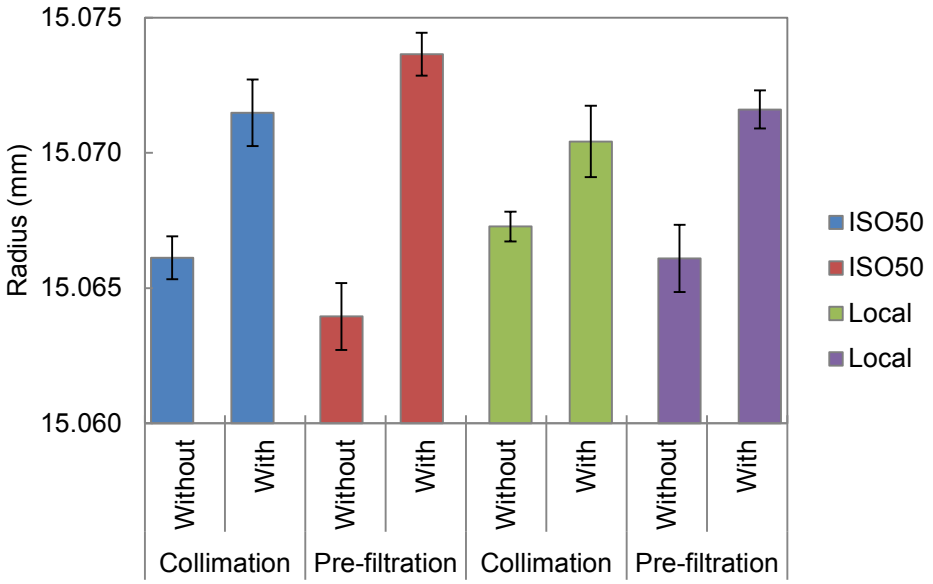

Figure 5.15 Influence of scatter and beam hardening on internal radius measurements of the aluminium multi cross-section workpiece. Error bars represent range of 3 repeats.

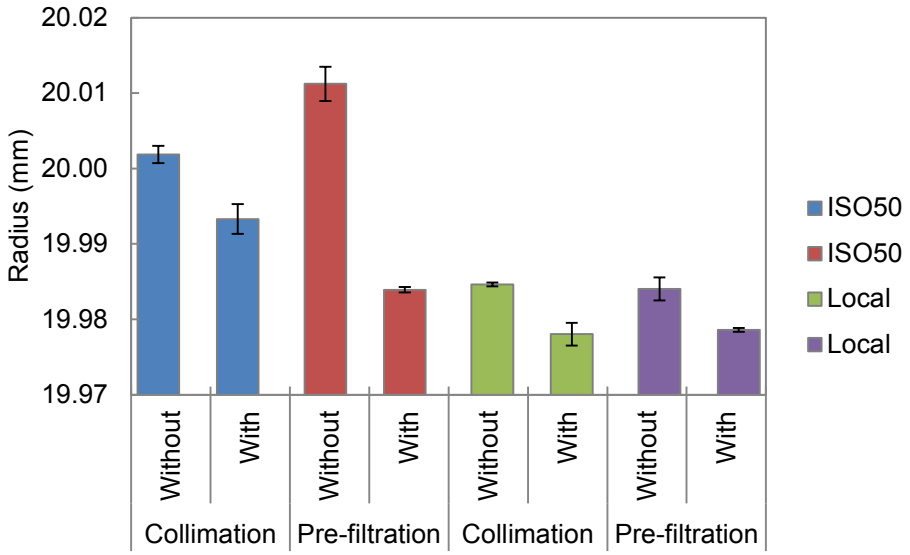

Figure 5.16 Influence of scatter and beam hardening on external radius measurements of the aluminium multi cross-section workpiece. Error bars represent range of 3 repeats.

5.4 Beam Stop Array Scatter Correction

In the previous section the influence of scatter and beam hardening were assessed using collimation and pre-filtration, and were shown to influence dimensional measurements. However, source collimation restricts the field of view (FOV), preventing correct alignment of the CT data. As such, the influence of scatter and beam hardening on measurement error could not be assessed. To overcome this limitation, in this section, scatter is estimated and removed from projections using the beam stop array (BSA) method.

5.4.1 Beam Stop Array Method

The principle behind the BSA method is as follows: lead cylinders (beam stops) are placed between the X-ray source and the object. The beam stops are designed such that primary photons incident upon them are absorbed, any signal detected in their shadow must therefore be due to scattered radiation. By using an array of beam stops, scatter signals can be sampled and interpolated across the FOV, giving a scatter estimate for the entire projection. Scatter is estimated in this way for each projection of a CT scan; subtracting this estimate from a second scan with the BSA removed gives an estimate of primary radiation which is subsequently reconstructed free from scatter artefacts. The BSA principle is illustrated in Figure 5.17.

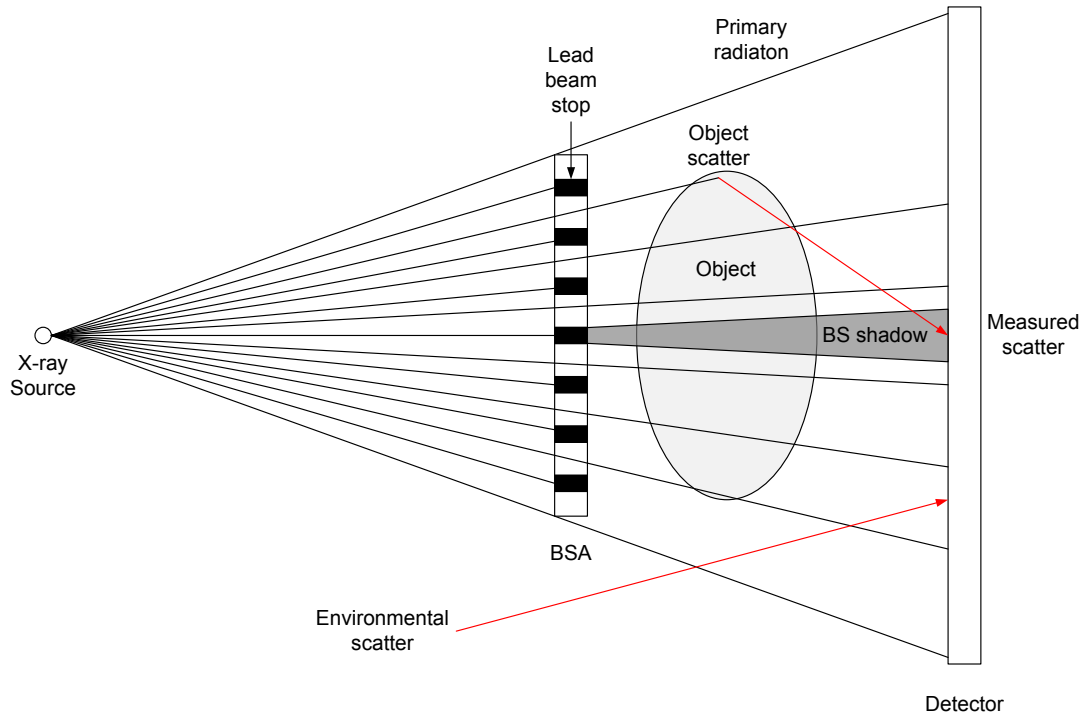

Figure 5.17 Illustration of the BSA method for directly measuring scatter. Figure adapted from Schorner et al. [57].

In terms of implementing the BSA method there are a few practical considerations:

(i) The stoppers block a portion of the X-ray beam incident on the object, this reduces the number of potential scattering interactions originating from the object and its surroundings. The measured scatter signal is therefore underestimated compared to the unblocked case. To take this into consideration, the scatter signals are scaled by a factor equal to the ratio of the blocked area to the unblocked area. As it turns out, this scaling factor is very small.

(ii) The stoppers must be embedded in a support material in order to distribute them in a given plane. This support is typically an acrylic sheet. The acrylic sheet will generate a scatter signal of its own, thus raising the measured scatter signal. To consider this, a 'dummy' acrylic sheet with no stoppers is used in open-field measurements such that the scatter signal becomes a constant that cancels out.

(iii) Concerning X-ray detection, X-ray photons incident on the detector may scatter in the detector panel. Furthermore, once X-ray photons have been converted to light photons by the scintillation layer, these light photons may scatter optically. The resulting blurring is termed veiling glare. Seibert et al. [98] and Lazos et al. [151] showed veiling glare may result in detector signals at distances of millimetres to centimetres from the initial X-ray photon interaction site. Veiling glare therefore raises signals in the shadows of the beam stops, causing scatter signals to be overestimated in the BSA method; this is illustrated in Figure 5.18. In order to correct this over estimation, the veiling glare point spread function (PSF) is estimated and an inverse filter calculated, scatter signals are then restored by deconvolution. This process is described in detail in the following sections.

The extension of the BSA method to consider the impact that veiling glare has on measured scatter signals is a contribution of this work; it has only previously been considered in simulation by Lasos et al. [151].

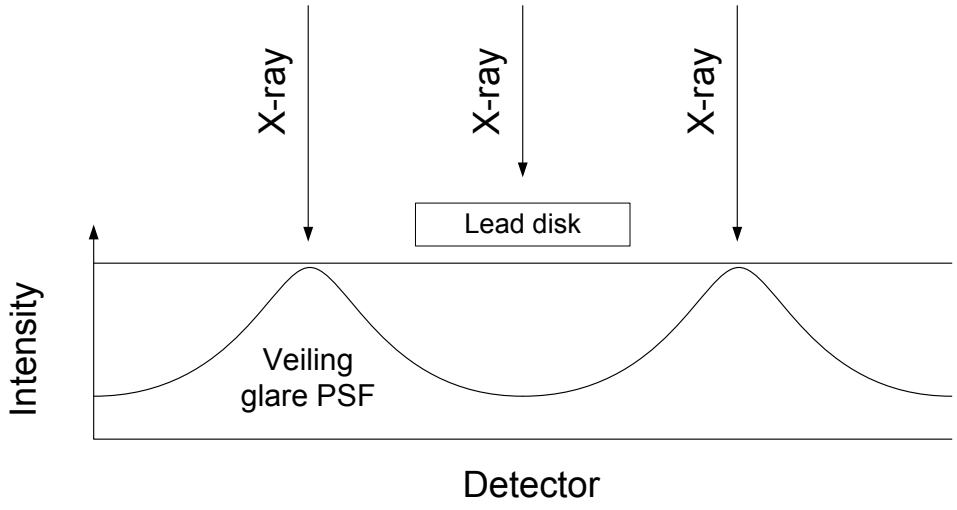

Figure 5.18 Illustration showing how veiling glare can raise intensity values in the shadows of beam stops.

5.4.2 Veiling Glare PSF Theory

In the next sections the PSF due to veiling glare is estimated for the detector used in this work. With an estimate of the veiling glare PSF, an inverse filter is derived. By deconvolving the beam stop scatter measurements with the veiling glare PSF, scatter can be estimated free from the influence of veiling glare, yielding an improved scatter estimate. Putting this mathematically, let V be an intensity measurement contaminated by veiling glare, let v be the un-degraded intensity measurement and h the veiling glare PSF:

$$V = v * h \tag{5.3}$$

where $*$ denotes convolution. The spatial convolution in Equation 5.3 can be represented as a multiplication in the Fourier domain:

$$F\{V\} = F\{v\} \times F\{h\}, \tag{5.4}$$

where F denotes the Fourier transform operator. The un-degraded intensity measurement v can be obtained by estimating the veiling glare PSF h and inverting its Fourier transform $F\{h\}$ as follows:

$$v = F^{-1}\left\{F\{V\} \times \frac{1}{H}\right\}. \tag{5.5}$$

where H is the Fourier transform of h and F^{-1} is the inverse Fourier transform operator. Thus the veiling glare PSF h needs to be estimated alongside its Fourier transform H.

The veiling glare model derived by Seibert et al. [98] is adopted here, full details concerning the derivation of the model and the inverse filter are given in Seibert's original papers [98], [99], the key equations and assumptions are summarised here for completeness.

The model considers that some of the light from the scintillator directly corresponds to an incident X-ray photon, whilst the remaining light spreads radially. The PSF is written:

$$h(r) = (1-\rho)\frac{\delta(r)}{r} + \frac{\rho}{2kr}e^{-r/k}, \tag{5.6}$$

where r is radial distance, $\delta(r)$ is the Dirac delta function, ρ is the fraction of light that is scattered, thus $(1-\rho)$ is the non-scattered light fraction, and k is the mean radial propagation distance of scattered light in the detector.

To estimate the model parameters, ρ and k, measurements are conducted to sample the veiling glare PSF. Intensity measurements are made in the shadow of lead disks of various radii. Placing the lead disks directly in front of the detector ensures environmental scatter signals are minimised, and using disks ensures that intensity signals due to veiling glare contribute symmetrically to the pixels in the centre of the disk's shadow. The signal I_a in the shadow of each lead disk of radius a is written:

$$I_a = I_0 \rho e^{-a/k} \tag{5.7}$$

where I_0 is the intensity value in the absence of the lead disk. Denoting the contrast ratio measured in the shadow of a disk as $C_a = I_0/I_a$, Equation 5.7 is rewritten:

$$C_a = \frac{1}{\rho} e^{a/k}. \tag{5.8}$$

Taking the natural logarithm of both sides:

$$\ln C_a = \frac{1}{k} a - \ln \rho, \tag{5.9}$$

the equation takes the form of a straight line:

$$y = mx + c. \tag{5.10}$$

By plotting $\ln C_a$ against a the PSF parameters ρ and k can be estimated using linear regression, where the gradient of the least-squares line gives $1/k$ and the y-axis intercept gives $-\ln \rho$.

Given the analytical form of the veiling glare PSF $h(r)$, its Fourier transform $H(f)$ can be evaluated analytically [99]. The inverse of $H(f)$ is given by:

$$\frac{1}{H(f)} = \frac{1}{\pi} \left\{ \frac{\sqrt{1 + (2\pi k f)^2}}{\rho + (1-\rho)\sqrt{1 + (2\pi k f)^2}} \right\}, \tag{5.11}$$

where f denotes spatial frequency. With this expression, the inverse filter can be generated and veiling glare removed from intensity measurements. Implementation details and results are given in the next sections.

5.4.3 Veiling Glare PSF Measurements

Contrast measurements are made using five lead disks with radii of 1, 2, 3, 4 and 5 mm and of 3 mm thickness, giving 99.7 % attenuation for 160 keV X-ray photons. The lead disks are placed in the centre of the X-ray detector, alignment is done by eye using laser cross-hairs projected on the detector as guides. The X-ray source settings correspond to the un-collimated, un-filtered settings given in Table 5.1. The mean of a 3×3 pixel region is evaluated in the shadow of each disk with each measurement repeated three times.

With estimates of ρ and k the inverse filter is built directly in the Fourier domain using Equation 5.11. The deconvolution is implemented as a point by point multiplication with the Fourier transform of the intensity image, the result is then inverse Fourier transformed to return to the spatial domain. All processing is done in MATLAB R2014a (MathWorks, Natick, Massachusetts, U.S.A.).

5.4.4 Veiling Glare PSF Estimate

The results of the lead disk contrast measurements are given in Figure 5.19; a reasonably linear relationship between $\ln C$ and disk radius is observed. Using the gradient and intercept of the least-squares line, values of ρ and k are calculated. The scattered light fraction ρ is found to be 0.09, and the mean radial propagation distance of scattered light k is found to be 1.61 cm. Lazos et al. [151] performed these measurements with a similar X-ray detector (same manufacturer and scintillator material), their values of ρ and k are 0.06 and 2.45 cm respectively, acquired at 120 keV; these results suggest less light is scattered, but the light that is scattered travels a further distance. Our increased scattered light fraction may be due to a carbon fibre sheet that lies on top of the scintillator. This was not removed for the veiling glare measurements as it remains in place for all scans. The carbon fibre sheet will generate its own scatter signal, raising the signal in the shadow of the lead disks.

A radial plot of the PSF is given in Figure 5.20 and the Fourier representation of the inverse filter in Figure 5.21. Note the filter acts as a high-pass filter, attenuating low spatial frequencies.

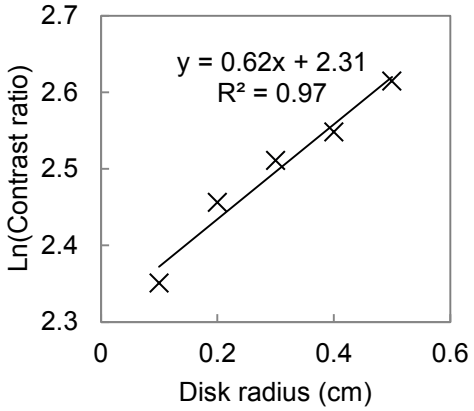

Figure 5.19 Contrast ratio versus lead disk radius; best fit line gives veiling glare PSF model parameters.

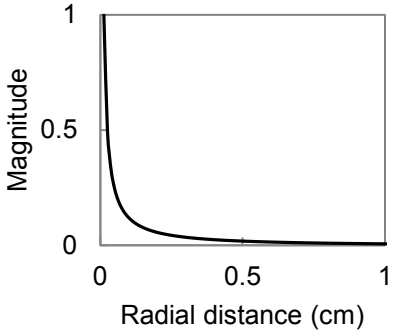

Figure 5.20 Spatial extent of veiling glare PSF.

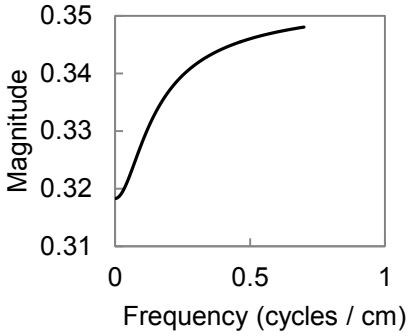

Figure 5.21 Inverse frequency filter to remove veiling glare from intensity measurements.

Figure 5.22(a) to (e) show line profiles across the lead disk measurements before and after removing veiling glare. The filter has the desired effect of lowering intensity values in the shadows of the lead disks. The intensity values do not quite reach zero, this is most likely due to the noise floor of the detector. Comparing Figure 5.22(a) and (e), the influence of veiling glare is greater for the smaller disk size than the larger disk size as expected. Note that after removing veiling glare the intensity profiles become slightly convex. This inverse cupping effect was also observed by Lazos et al. [151] when veiling glare was incorporated in simulated data, but since it only affects the edges of the intensity profile, it is of little concern here.

With the ability to correct the effect of veiling glare on scatter measurements, the BSA method is implemented in the next section.

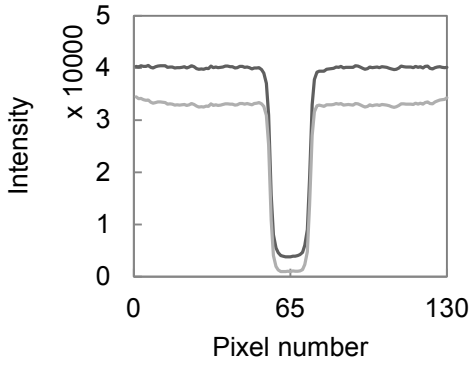

(a) 1 mm disk radius.

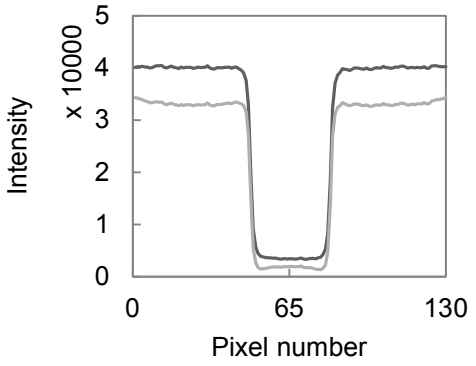

(b) 2 mm disk radius.

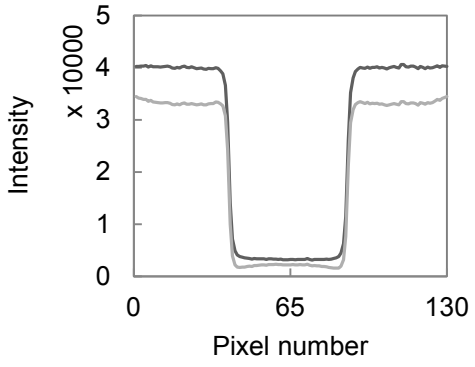

(c) 3 mm disk radius.

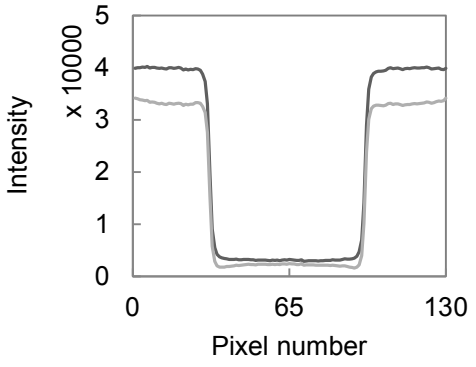

(d) 4 mm disk radius.

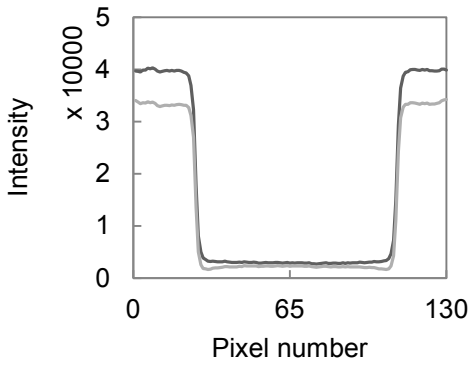

(e) 5 mm disk radius.

Figure 5.22 Intensity profiles from lead disk images before (black line) and after (grey line) veiling glare correction.

5.4.5 Implementing the Beam Stop Array Method

To implement the BSA method a custom acrylic BSA is manufactured, see Figure 5.23. The beam stops are 1 mm in diameter and 3 mm in height; these dimensions match those used in the veiling glare PSF measurements. The beam stops are arranged in a 9×9 grid with a regular 10 mm spacing perpendicular to the rotation axis and 12 mm spacing parallel to the rotation axis since the detector is not square.

A second 'dummy' BSA is also manufactured without the lead beam stops. This dummy BSA is used to ensure the additional scatter signal generated by the acrylic of the BSA is accounted for in scans with the BSA removed.

The BSA is placed between the source and the workpiece on a temporary acrylic mount, see Figure 5.24. A typical projection with the BSA in place is shown in Figure 5.25. The complete BSA scatter correction method is implemented as follows:

1. Conduct flat field correction with the dummy BSA placed on top of the acrylic mount and the workpiece removed.
2. Insert the workpiece and the BSA, conduct a CT scan.
3. Remove BSA, insert dummy BSA, conduct a CT scan.
4. Sample scatter signals from BSA scan (step 2), remove veiling glare from scatter signals and interpolate scatter signals for each projection, these are the scatter estimates.
5. Subtract 4 from 3 to give primary estimates.
6. Reconstruct projections from step 5.

When sampling the scatter signals in step 4, the projections are first pre-processed with a 3×3 median filter to supress faulty pixels. Then the mean of a 3×3 pixel region is evaluated in the shadow of each beam stop. Cubic spline interpolation is used in step 4 to ensure a smooth scatter estimate. All data processing is conducted in MATLAB R2014a. A typical scatter estimate is shown in Figure 5.26.

Step 2 is repeated three times, each time the BSA is translated horizontally and vertically to increase the number of sampling points. Step 3 is also repeated three times to consider repeat measurements. Finally, this entire procedure is repeated but the source pre-filtered with 0.5 mm of copper to evaluate the combined influence of scatter and beam hardening. Source settings for the scans are given in Table 5.2.

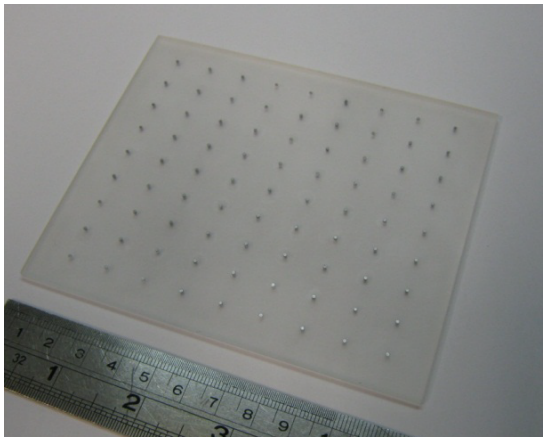

Figure 5.23 Array of lead cylinders 1 mm in diameter, 3 mm in depth, mounted in an acrylic plate, termed a beam stop array (BSA).

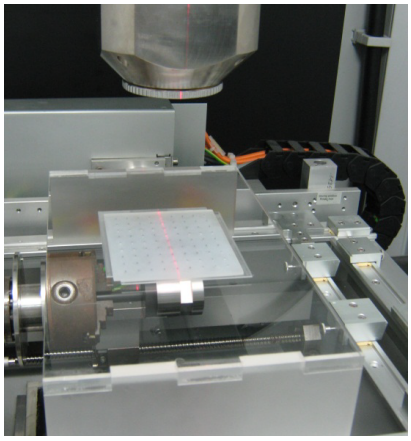

Figure 5.24 BSA positioned between the X-ray source and object on an acrylic mounting table.

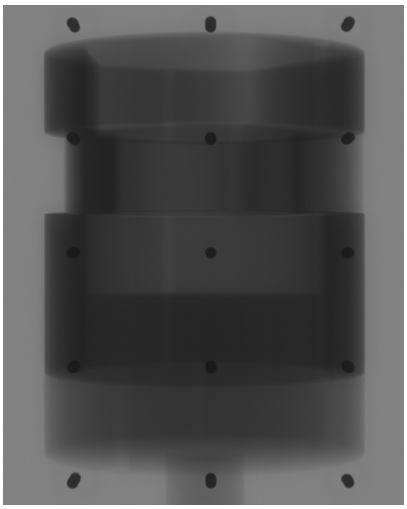

Figure 5.25 Projection of multi cross-section workpiece with BSA.

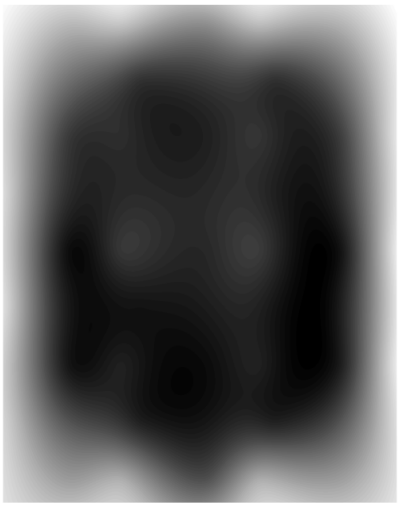

Figure 5.26 Scatter estimate from BSA scatter correction method.

Table 5.2 X-ray source settings for scans with and without the BSA and source pre-filtration.

	Voltage (kV)	Current (μA)
No BSA, no pre-filter	160	14
No BSA, pre-filter	160	25
BSA, no pre filter	160	14
BSA, pre-filter	160	25

5.4.6 Scatter Correction Results

Figure 5.27 compares the scatter signal estimated via collimation in Section 5.2.1 and that estimated via the beam stop array. The two are in good agreement, although discrepancies exist at the outer edges of the workpiece. Compared to the collimator-based estimate, the BSA scatter signal shows a more gradual change in these regions. This is most likely due to the BSA scatter signal being an interpolant. To recover these higher spatial frequency features, a finer scatter sampling strategy would be required. The scatter signal estimated using the BSA appears slightly larger than that of the collimator; this is to be expected as the acrylic BSA and its mount generate additional scatter signals that were not present in the collimator measurements.

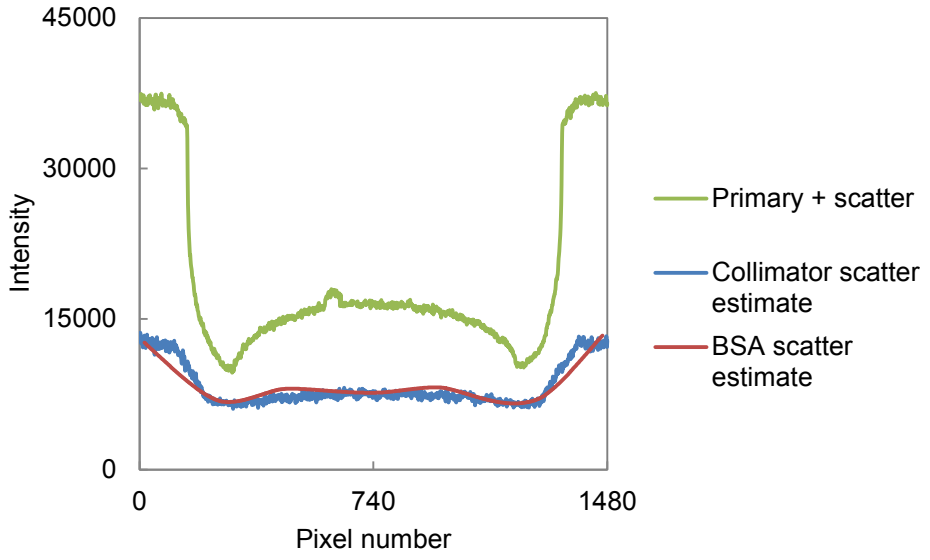

Figure 5.27 Comparison between scatter estimated using collimation and BSA method.

In Figure 5.29 and Figure 5.30 CT images of the three different workpiece cross-sections are shown with and without scatter correction and pre-filtration. A comparison between the data can be made by looking to Figure 5.28 which shows line profiles across the wall of the cylindrical cross-section. The line profiles show the BSA scatter correction has the same effect as collimation. That is, scatter correction raises the reconstructed values, whilst pre-filtration lowers them. Histograms of each CT volume are plotted in Figure 5.31. The histograms show scatter correction is able to unify the material grey value phase as collimation was able to do, Figure 5.31(c). The scatter correction also greatly increases the image contrast. Pre-filtration yields a narrow Gaussian material grey value distribution, but the contrast is the lowest of the four conditions, Figure 5.31(b). The combination of scatter correction and pre-filtration yields both high contrast images and the desired single, narrow, Gaussian material grey value distribution.

In the next section, using the developed scatter correction, the influence scatter and beam hardening have on the accuracy of dimensional measurements is evaluated.

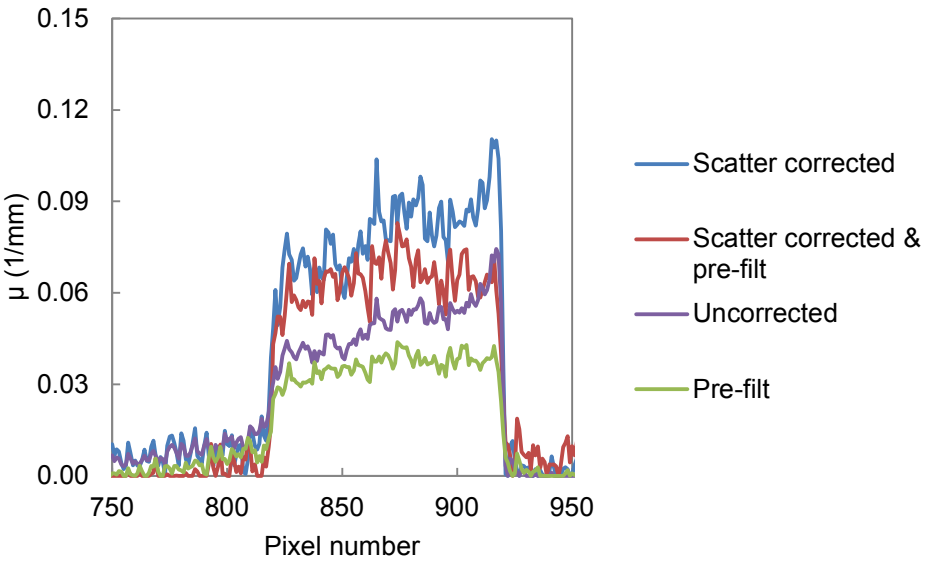

Figure 5.28 Comparison of line profiles drawn across cylinder wall of CT images in Figure 5.29 and Figure 5.30.

No pre-filtration, no scatter correction.

Pre-filtered, no scatter correction.

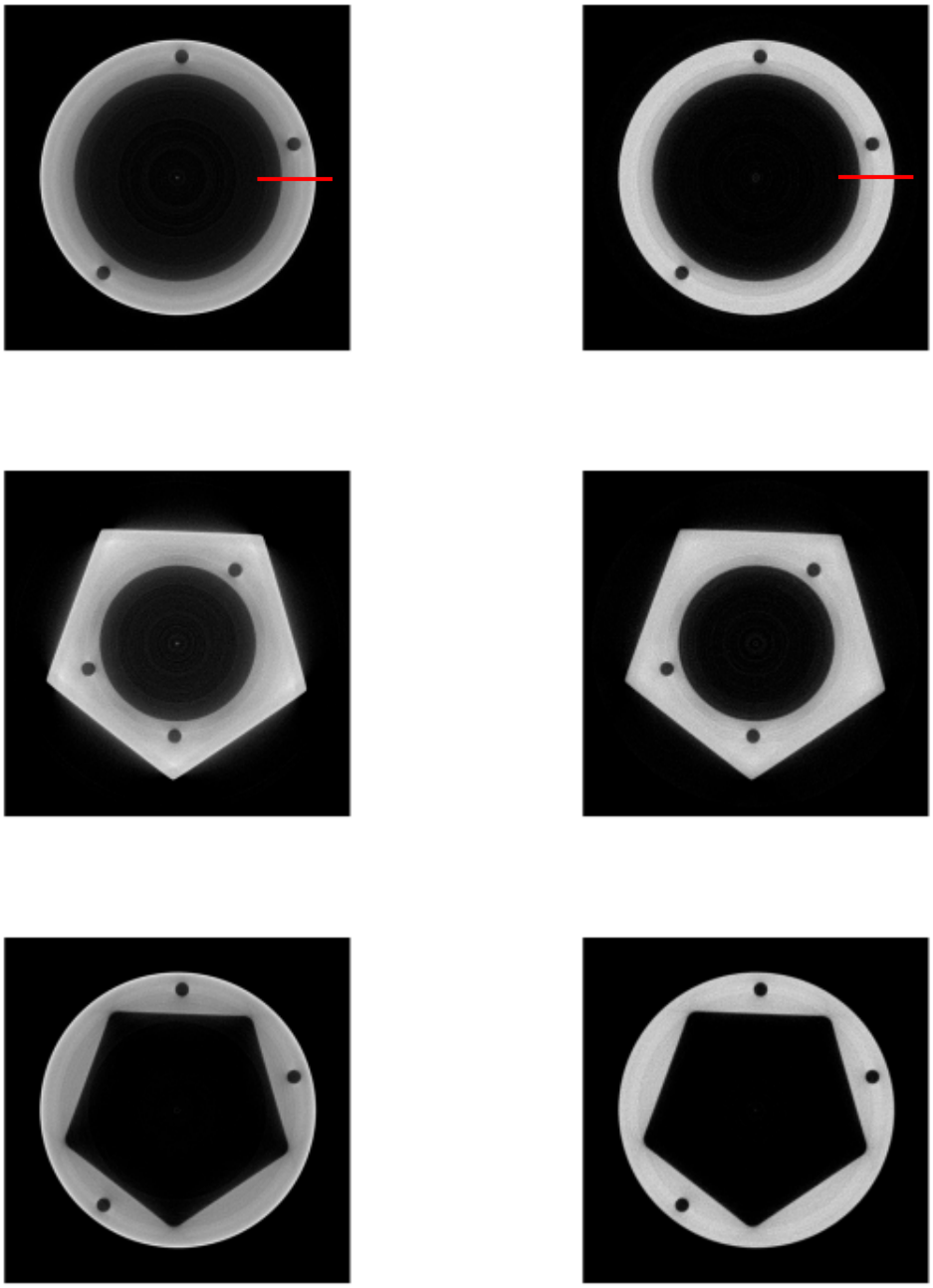

Figure 5.29 Comparison of scatter contaminated CT images with and without pre-filtration. Red lines correspond to line profiles in Figure 5.28.

No pre-filtration, scatter corrected.

Pre-filtered, scatter corrected.

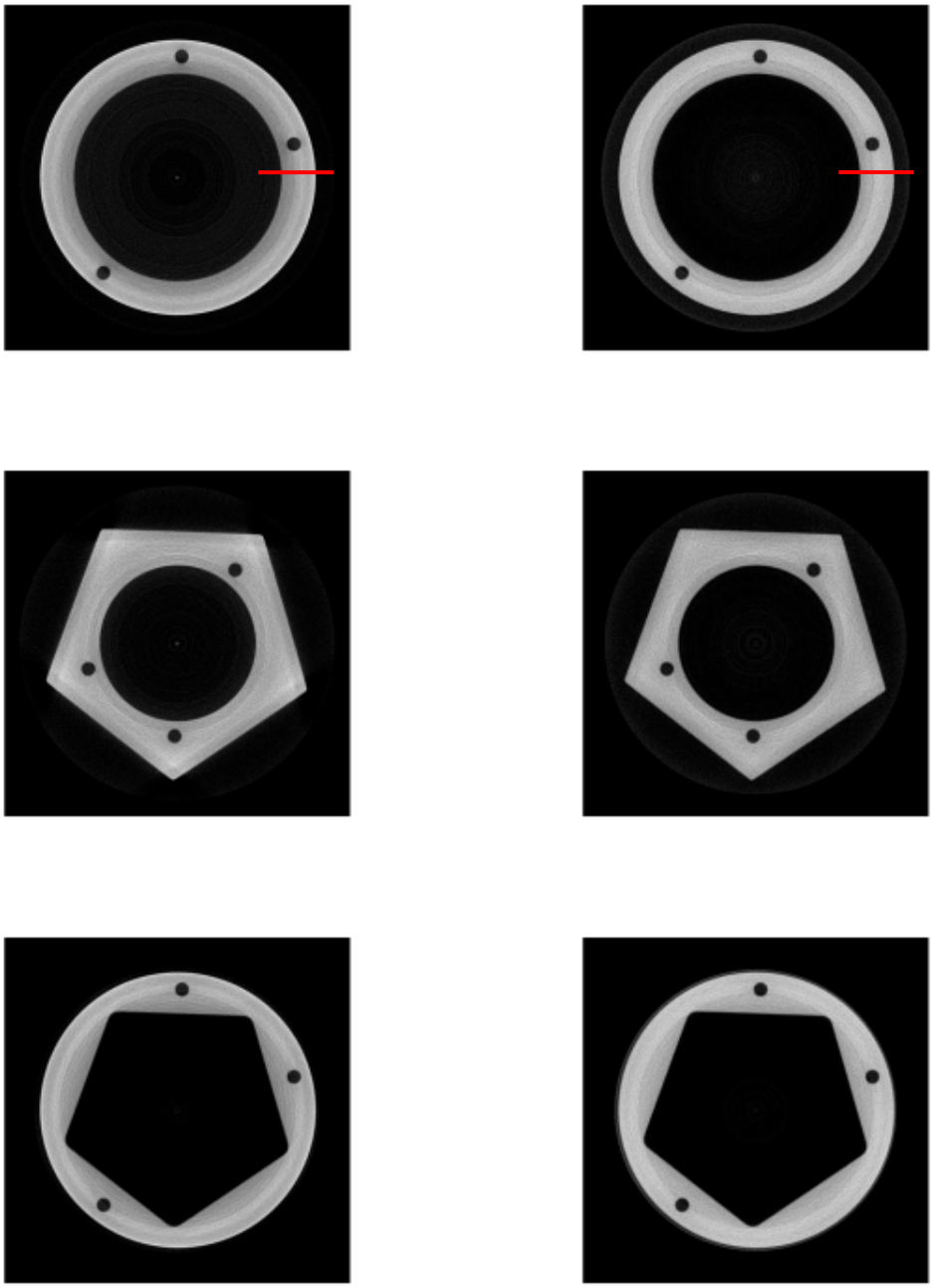

Figure 5.30 Comparison of scatter corrected CT images with and without pre-filtration. Red lines correspond to line profiles in Figure 5.28.

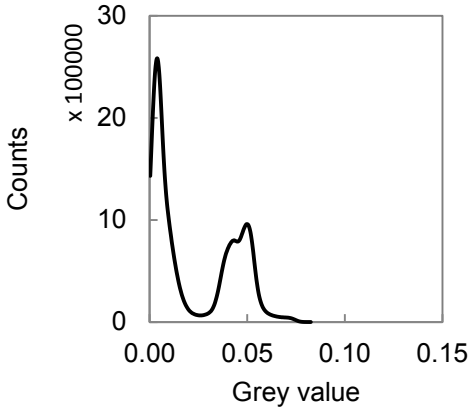

(a) No pre-filter, no scatter correction.

Contrast = 0.045.

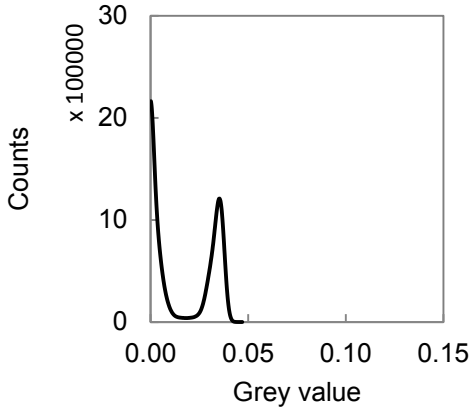

(b) Pre-filtered, no scatter correction.

Contrast = 0.035.

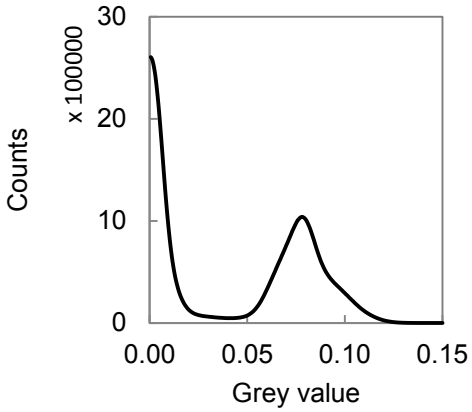

(c) No pre-filter, scatter corrected.

Contrast = 0.077.

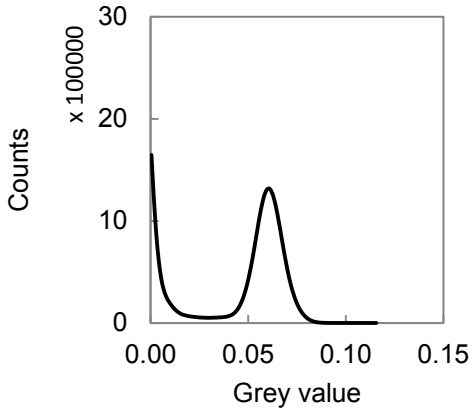

(d) Pre-filtered, scatter corrected.

Contrast = 0.060.

Figure 5.31 Comparison of histograms evaluated from CT volumes with and without pre-filtration and scatter correction.

5.5 Dimensional Measurements with Scatter Correction and Pre-Filtration

In the previous sections the BSA scatter correction was implemented and the impact it had on image quality was evaluated. In this section the influence of scatter correction and pre-filtration on dimensional measurements is evaluated.

5.5.1 Method

The scan results from the previous section are used here. Projections of the aluminium multi cross-section workpiece are acquired under four conditions:

1. With scatter correction.
2. With pre-filtration.
3. With scatter correction and with pre-filtration.
4. Without scatter correction and without pre-filtration.

All scans are repeated three times, the source settings are given in Table 5.2. The workpiece is not removed from the CT system between scans. The ruby sphere workpiece is scanned after the final scan of the multi cross-section workpiece, with the magnification axis unmoved. The voxel size is scaled according to the method described in Section 4.3.

After reconstructing each data-set surface determination is performed using the 3D local method described in Section 2.5. The surface data is then imported to GOM Inspect, aligned as per Chapter 3, and the reference dimensions evaluated by fitting circles using nonlinear least-squares. Exemplary surfaces of the cross-sections evaluated are shown in Figure 5.32. The three cross sections are termed as follows: Outer Circ Inner Circ (OCIC), Outer Circ Inner Pent (OCIP) and Outer Pent Inner Circ (OPIC), see Figure 5.32.

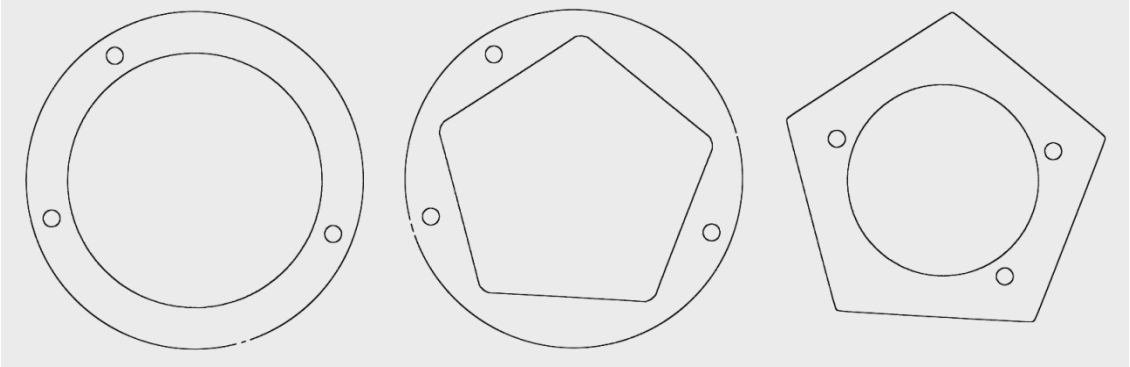

OCIC	OCIP	OPIC
Outer Circ Inner Circ.	Outer Circ Inner Pent	Outer Pent Inner Circ.

Figure 5.32 Surfaces of the multi cross-section workpiece as evaluated in GOM Inspect.

5.5.2 Results

The measurement results for the inner and outer radii for each cross-section are given in Figure 5.33 and Figure 5.34 respectively, the error bars represent the range of the three repeated measurements. The results show the same opposing relationship seen in Section 5.3. That is, both scatter correction and pre-filtration act to increase the inner radius estimate and decrease the outer radius estimate. The influence that scatter and beam hardening have on measurement error however seems to vary. On the one hand, for the OCIP and OPIC cross sections, scatter correction and pre-filtration reduce the measurement error. On the other hand, for OCIC cross sections scatter correction and pre-filtration increase the measurement error. This is a puzzling result that suggests the measurement results for the upper and lower cross-sections of the workpiece act in opposition.

In order to make sense of this outcome consider first the OCIC cross section; with no scatter correction and no pre-filtration the inner radius is measured too large, see Figure 5.33, whilst the outer radius of the same cross section is measured too small, see Figure 5.34. Based on the observation that scatter correction and pre-filtration both act to increase inner dimensions and decrease outer dimensions, it follows that scatter correction and pre-filtration will only increase the measurement error for the OCIC cross-section. On the other hand, with no scatter correction and no pre-filtration the radius of the OPIC cross section is measured too small, whilst the OCIP radius is measured too large; it therefore follows that both scatter correction and pre-filtration will act to reduce the measurement error.

The factor that separates the three cross sections is their relative position on the detector. The OCIP and OPIC cross-sections fall on the upper half of the detector, whilst the OCIC cross-section falls on the centre of the detector. This implies that any one, or a combination of the following factors could induce the observed error: a tilt of the detector or rotation axis, Feldkamp artefacts and wobble of the rotation axis. A detector tilt or rotation axis tilt seem most likely since they will cause the magnification to vary within the CT volume, this is why the measurement error for the upper and lower features of the multi cross section workpiece vary in this manner. In the next chapter it is shown through simulation that scatter and beam hardening increase measurement error. The simulation results therefore support the results for the OCIP and OPIC cross-sections.

Irrespective of this error, the observation that both scatter correction and pre-filtration act to increase the inner radius estimate and decrease the outer radius estimate is in-line with the results from Section 5.3. These results suggest scatter and beam hardening have a systematic and therefore predictable influence on dimensional measurements.

In order to further verify the observations of the experimental study, the influence of scatter and beam hardening are studied in simulation in the next chapter. Furthermore, explanations are given as to why this opposing inner/outer relationship occurs.

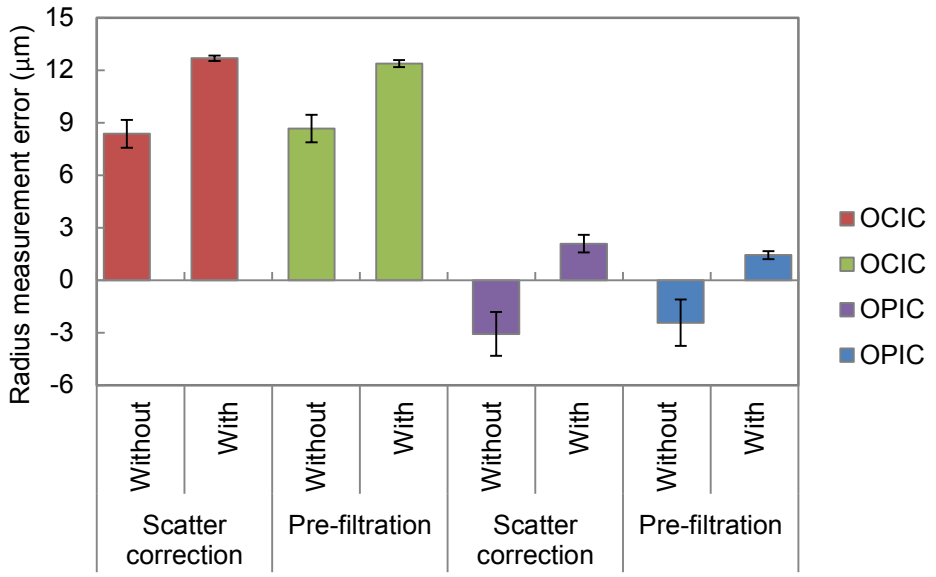

Figure 5.33 Radius measurement error for internal features of the multi cross-section workpiece.

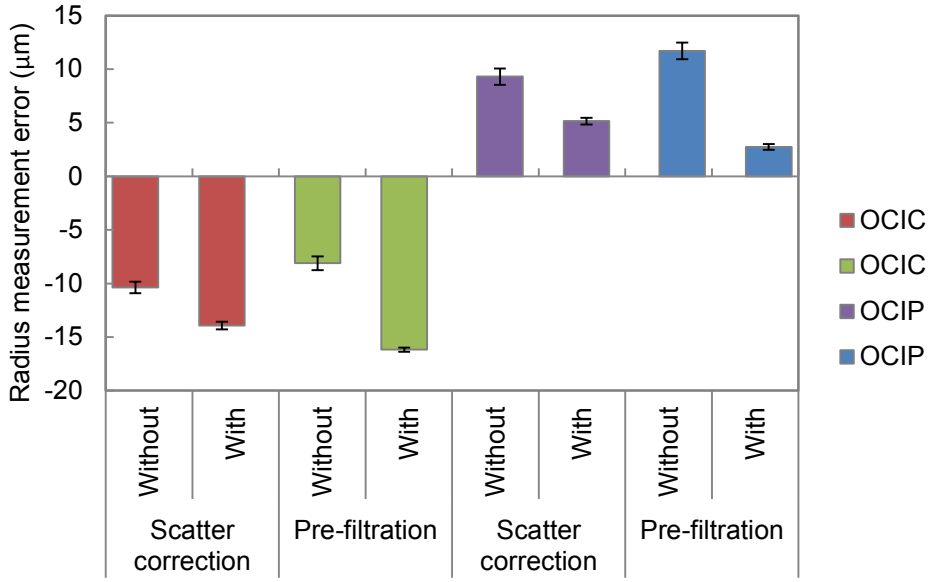

Figure 5.34 Radius measurement error for outer features of the multi cross-section workpiece.

5.6 Chapter Summary

It has been shown that both scatter and beam hardening contribute to the nonlinear relationship between attenuation and material thickness in cone-beam CT. The contribution of scatter has been neglected in previous studies in CT metrology.

It has been shown that scatter and beam hardening severely distort the material phase of grey value histograms. These grey value distortions can be reduced through collimation/scatter correction and pre-filtration, or a combination of the two.

Scatter and beam hardening have been shown to decrease the measured size of internal features and increase the measured size of external features compared to when scatter and beam hardening are minimised/corrected for.

The beam stop array scatter correction method has been extended to consider the impact that veiling glare has on measured scatter signals.

To further verify the observations of the experimental study, the influence of scatter and beam hardening are studied via simulation in the next chapter. Furthermore, explanations are given as to why scatter and beam hardening cause this opposing inner/outer relationship.

Chapter 6 Simulation Studies on Scatter and Beam Hardening

In the previous chapter the influence of scatter and beam hardening was investigated through experimentation. In this chapter these influences are evaluated through the use of a simulation tool.

A number of commercial software packages are available to simulate X-ray CT. Two popular packages are ScorpiusXLab® [152] by Fraunhofer IIS (Erlangen, Germany), and aRTist [153] by BAM (Berlin, Germany). These simulation packages are considered deterministic in nature since they rely on ray-tracing to calculate X-ray path lengths through objects. Monte Carlo methods represent another simulation approach and may rely on general purpose public domain Monte Carlo codes such as Geant4 [154]. Given that deterministic CT simulation methods are well documented in the literature, and a desire to characterise the CT system used experimentally, an in-house simulation tool is developed based on ray-tracing techniques. The simulation tool is largely based on the work of Duvauchelle et al. [155] and Lindgren et al. [156].

The purpose of this chapter is to verify the observations from Chapter 5 and use the simulated data to help explain how scatter and beam hardening influence both the ISO50 and local surface determination methods.

In this chapter the following contributions are made:

- It is shown that the ISO50 method fails to give the ‘correct’ surface position for both inner and outer features in the presence of scatter and/or beam hardening (Section 6.2.3 and 6.3.3).
- It is shown that only when artefacts are minimised/corrected an isovalue threshold can be chosen that minimises measurement error for both inner and outer features (Section 6.2.3).
- Scatter and beam hardening are shown to change the turning point of the edge gradient, this being the property by which surface points are defined for the local method. It is therefore through this change in turning point that scatter and beam hardening influence dimensional measurements (Section 6.2.4 and 6.3.4).
- An explanation is given as to why inner and outer dimensions act in opposition (Section 6.2.4).

In this chapter the simulation tool is first described. Two studies are then presented, one considers the influence of beam hardening on dimensional measurements and the other considers the influence of scatter. Based on the results, the mechanisms through which beam hardening and scatter influence dimensional measurements are identified and discussed.

6.1 Overview of the Simulation Tool

The simulation tool is based on ray-tracing and considers the following characteristics of a CT system and workpiece:

- The finite size of the X-ray focal spot and detector pixels.
- The polychromatic X-ray spectrum.
- Scattered radiation.
- The energy dependence of the detector.
- Noise in the projection images.
- Workpiece geometry and material.

The simulation is performed with fan-beam geometry; this considerably reduces the computational cost of the simulation and subsequent data-processing compared to a cone-beam simulation. The simplification is not expected to influence the results significantly since X-ray path lengths in the central plane are the same for both fan and cone-beam geometry. Evaluating fan-beam data has the additional advantage of mitigating the influence of Feldkamp artefacts.

The basic steps of the simulation are as follows:

- Calculate X-ray path lengths through a workpiece for each angular position using ray-tracing.
- Use the path lengths to calculate X-ray attenuation.
- Add measured scatter signals to the projections.
- Superimpose projections with noise based on an empirical model.

Each of these processing steps is described in detail in the sections that follow.

6.1.1 Ray Tracing

Rays are traced from a point source, through a workpiece, to points in the centre of each pixel of a line detector. The number of pixels perpendicular to the axis of rotation matches that of the detector used experimentally (1480), as does the pixel spacing (0.127 mm).

Fan beam projections of each cross-section of the multi-cross section workpiece are generated. Each cross-section is defined using circles and lines. Based on ray-circle and ray-line intersections, X-ray path lengths through the workpiece are calculated and assigned to each pixel of the detector, see Figure 6.1. For example, the equation of a circle of radius r and centre h, k is:

$$(x-h)^2 + (y-k)^2 = r^2. \tag{6.1}$$

Whilst the equation of a ray cast from the source x_0, y_0 to a detector point x_1, y_1 is:

$$\begin{aligned} x(t) &= (x_1 - x_0)t + x_0 \\ y(t) &= (y_1 - y_0)t + y_0. \end{aligned} \tag{6.2}$$

Substituting Equation 6.2 into 6.1 yields a quadratic equation in t:

$$at^2 + bt + c = 0, \tag{6.3}$$

where:

$$\begin{aligned} a &= (x_1 - x_0)^2 + (y_1 - y_0)^2 \\ b &= 2(x_1 - x_0)(x_0 - h) + 2(y_1 - y_0)(y_0 - k) \\ c &= (x_0 - h)^2 + (y_0 - k)^2 - r^2. \end{aligned} \tag{6.4}$$

The solution of which is:

$$t = \frac{-b \pm \sqrt{b^2 - 4ac}}{2a}. \tag{6.5}$$

The two real roots of the quadratic equation are the entry and exit point of the ray in the circle. The xy coordinates of these intersections are calculated by substituting t back into Equation 6.2. Path lengths through the workpiece are then calculated using trigonometry. This calculation is repeated for each source to pixel ray path, with each pixel assigned the thickness of material the ray traversed.

The finite size of the X-ray focal spot is considered by simulating multiple point sources distributed over an area [155], [156], see Figure 6.2. A 10 μm focal spot size is selected based on look up tables provided by the X-ray source manufacturer. The finite size of the detector pixels is considered by generating each projection at ten times the detector resolution, then taking the mean value of every ten pixels [155], [156]. The resulting projections are then convolved with the veiling glare PSF described in Section 5.4.

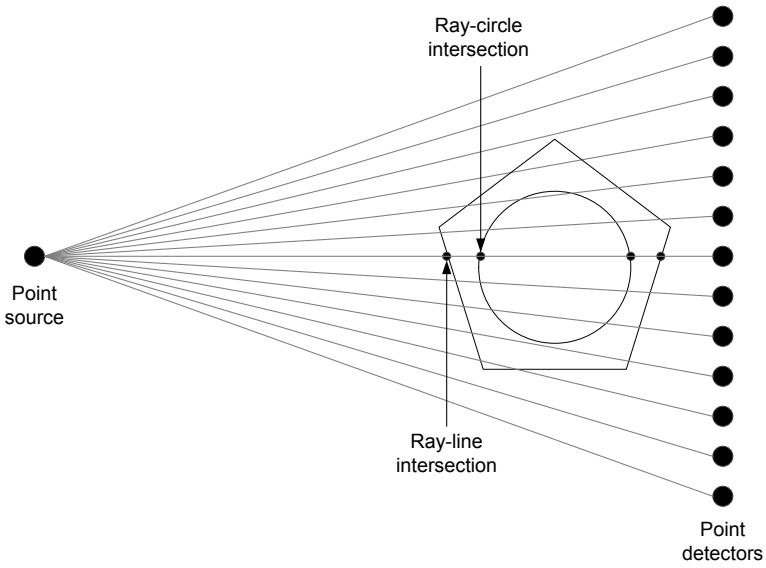

Figure 6.1 Illustration of ray-tracing for calculating X-ray path lengths through each workpiece cross-section.

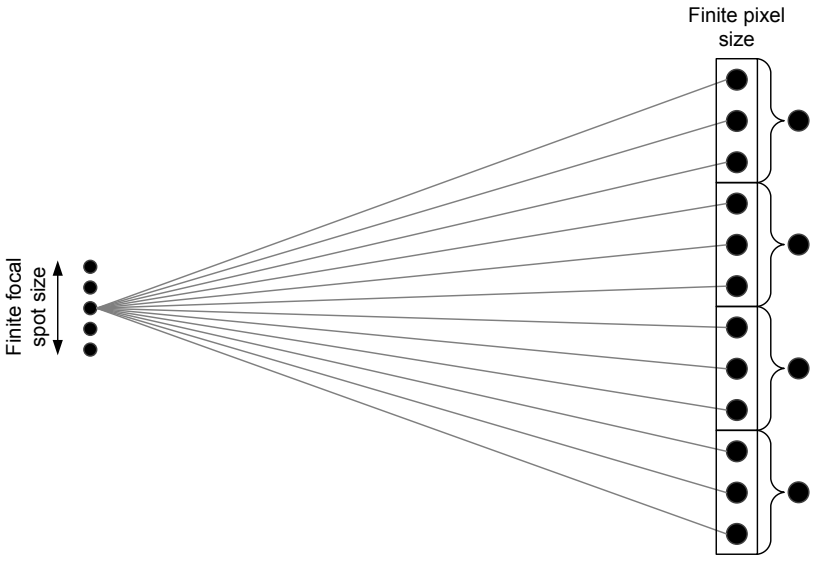

Figure 6.2 Illustration of the finite size of the X-ray source and detector pixels. Rays are traced from multiple point sources whilst point detectors are down-sampled.

6.1.2 X-ray Source and Detector Energy Dependence

Having calculated X-ray path lengths using ray tracing, polychromatic X-ray attenuation is calculated for each ray path using Equation 6.6:

$$-ln(I/I_0) = -ln\left\{\int_0^{E_{max}} W(E)\, e^{-\mu(E)t} dE\right\}, \qquad 6.6$$

where I_0 is the incident X-ray intensity, $\mu(E)$ is the energy dependent linear attenuation coefficient of the workpiece, t is the X-ray path length through the workpiece, and I is the intensity of X-rays emerging from the workpiece having not undergone an interaction.

The term $W(E)$ in Equation 6.6 describes the contribution of each photon energy to the total polychromatic attenuation. It is dependent on both the incident X-ray spectrum and the energy characteristics of the detector. X-ray spectra can be estimated based on analytical models, such as the widely accepted model of Poludniowski et al. [64]. However, such models are generally based on the geometry of a reflection target and are therefore not applicable to the transmission target used here. Estimating the X-ray spectrum via Monte Carlo simulation is another option, however, to do so is beyond the scope of this thesis. The X-ray spectrum could be measured directly [157], however this requires specialist equipment and careful experimental setup.

With regards to the energy dependence of the detector, this has previously been modelled as the scintillator's quantum absorption efficiency $\eta(E)$ [92]:

$$\eta(E) = 1 - e^{-\mu(E)t}, \qquad 6.7$$

where $\mu(E)$ is the linear attenuation coefficient of the scintillator and t is the scintillator thickness. This simple model neglects the energy dependence of subsequent optical detection and signal processing. Again, full scale analytical modelling or Monte Carlo simulation of the energy dependence of the detector are beyond the scope of this thesis.

Due to the ease of implementation, the combined energy dependence of the X-ray spectrum and detector $W(E)$ is estimated from X-ray transmission measurements of an object of known dimensions and composition, such as the step wedges used in Section 5.1. This is a long-standing experimental method for estimating the energy dependence of a CT system; however, the method is known to be unable to recover the fine detail of the source spectra, such as the characteristic peaks (see

Section 2.1.2). This is not a problem in this case as we are interested in the broad bremsstrahlung component of the spectrum which contributes to beam hardening.

The method for estimating $W(E)$ from transmission measurements is derived by discretising Equation 6.6 and rearranging for X-ray transmission, a system of linear equations is thus formed:

$$\frac{I_m}{I_0} = \sum_{n=1}^{N} W_n \exp(-\mu_n t_m), \tag{6.8}$$

where W_n is an unknown vector of N photon energy weights to be estimated, μ_n is a known vector of N linear attenuation coefficients, t_m is a known vector of M material thicknesses, and I_m/I_0 is a vector of M X-ray transmission measurements.
Equation 6.8 is written in matrix notation $b_m = A_{mn}W_n$ accordingly:

$$\begin{bmatrix} I_1/I_0 \\ \vdots \\ I_M/I_0 \end{bmatrix} = \begin{bmatrix} exp(-\mu_1 t_1) & \dots & exp(-\mu_N t_1) \\ \vdots & \ddots & \vdots \\ exp(-\mu_1 t_M) & \dots & exp(-\mu_N t_M) \end{bmatrix} \begin{bmatrix} W_1 \\ \vdots \\ W_N \end{bmatrix}. \tag{6.9}$$

Previous studies have shown the coefficient matrix A_{mn} is typically ill-conditioned. A study by Sidky et al. [158] suggested the condition of A_{mn} can be improved by measuring X-ray transmission for two or more materials. This improvement is seen because X-ray attenuation below the MeV energy range is dominated by two interactions: photoelectric absorption and Compton scattering, see Section 2.1.4. Sidky et al. also showed that more than 20 transmission measurements per material has little impact on the condition of the A_{mn} matrix. Based on Sidky's recommendations, the collimated X-ray transmission measurements of the aluminium and titanium step wedges from section 5.1 are used to build the vector b_m, such that M = 54. Each term in the coefficient matrix A_{mn} is pre-calculated with knowledge of the step wedge thickness t and values of μ. The values of μ are obtained from the NIST XCOM database of photon cross sections [159]. The maximum energy of the X-ray spectrum to be estimated is 160 keV, so with energy bins of 1 keV and a minimum energy of 16 keV, N = 144.

Equation 6.9 is solved iteratively using the expectation maximization (EM) method. The multiplicative update of the EM solver ensures values of the update remain positive or zero upon iteration. The EM update equation used by Sidky et al. [158] and Zhang et al. [160] is adopted here:

$$W_n^{k+1} = \frac{W_n^k}{\sum_m A_{mn}} \sum_m \frac{A_{mn} b_m}{\sum_{n'} A_{mn'} W_{n'}^k} \qquad 6.10$$

where k is the iteration number.

The EM solver requires an initial estimate of $W(E)$, for this, half a sine wave is used, which could be considered a rough approximation of the bremsstrahlung component of the X-ray spectrum. Zhang et al. [160] considered the impact of the initial estimate on the convergence of the solver; half a sine wave was shown to yield the most rapid convergence.

Both Sidky et al. [158] and Zhang et al. [160] have validated this method of estimating $W(E)$ for simulated data. For the sake of completeness, we perform our own validation accordingly. A known 'actual' X-ray spectrum is used to calculate X-ray transmission values for aluminium and titanium using Equation 6.9, the EM solver is then used to estimate the spectrum using the transmission values and the coefficient matrix. The actual and estimated spectra are shown in Figure 6.3, alongside the initial estimate, whilst the actual and estimated transmission values are given in Figure 6.4. Clearly the method is able to estimate the general shape of the X-ray spectrum which is important for simulating beam hardening, but the method fails to recover the spectrum's characteristic lines, as previously mentioned. Even so, the estimated spectrum enables accurate calculation of X-ray transmission, as shown by Figure 6.4.

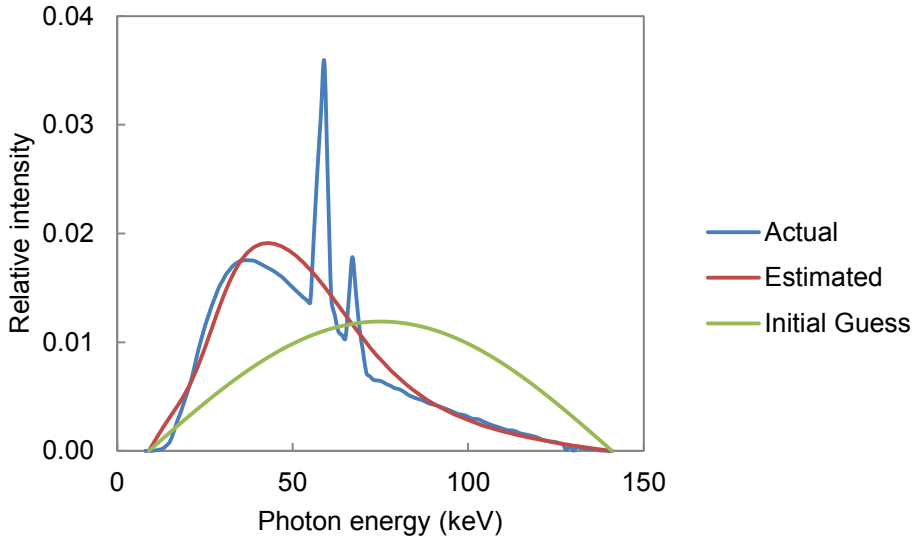

Figure 6.3 Validation of method for estimating $W(E)$. Graph shows a comparison between the actual spectrum, the estimated spectrum and the initial guess.

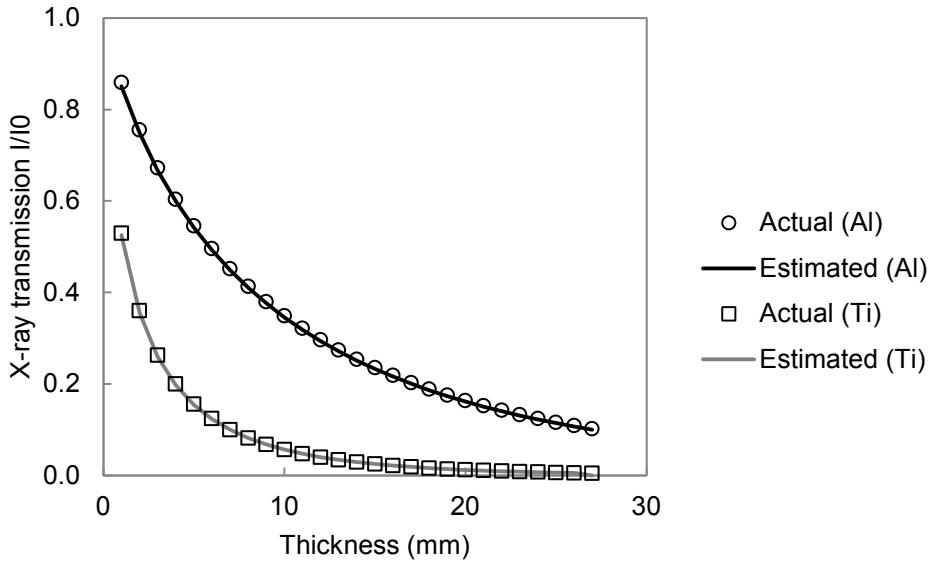

Figure 6.4 Comparison of actual transmission values and those calculated with the estimated spectrum in Figure 6.3.

Figure 6.5 shows the convergence of the EM solver, where the sum of the absolute difference between the actual and estimated transmission values is used to indicate the degree of convergence. The solver quickly finds an initial solution, and then slowly converges, this is similar behaviour to that seen in the previous studies.

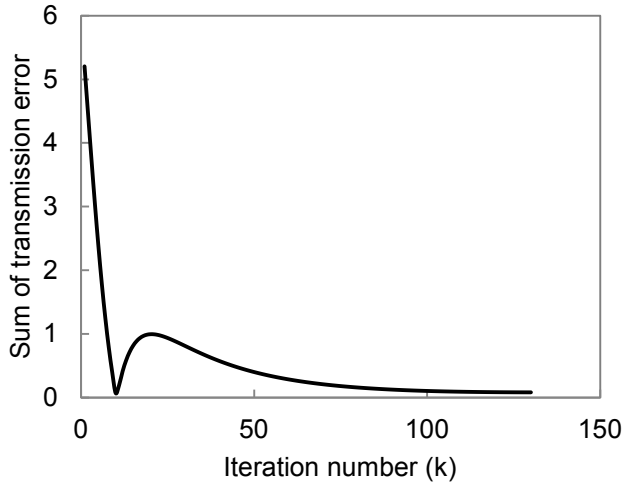

Figure 6.5 Convergence of spectrum estimate, based on the sum of the absolute difference between actual and estimated transmission values in Figure 6.4.

The result of applying the method to the measured transmission values is given in Figure 6.6; the result shown corresponds to the estimate after 50 iterations. A comparison between measured and simulated transmission values is given in Figure 6.7. It is clear the estimate of $W(E)$ can be used to accurately simulate X-ray transmission and therefore X-ray attenuation. To further verify this result, X-ray transmission through steel foils is measured with unchanged X-ray source settings. With the estimate of $W(E)$, X-ray transmission for steel is simulated and plotted alongside the measured transmission in Figure 6.7. Clearly the simulated and measured X-ray transmission values are in good agreement, thus validating the simulation of polychromatic attenuation.

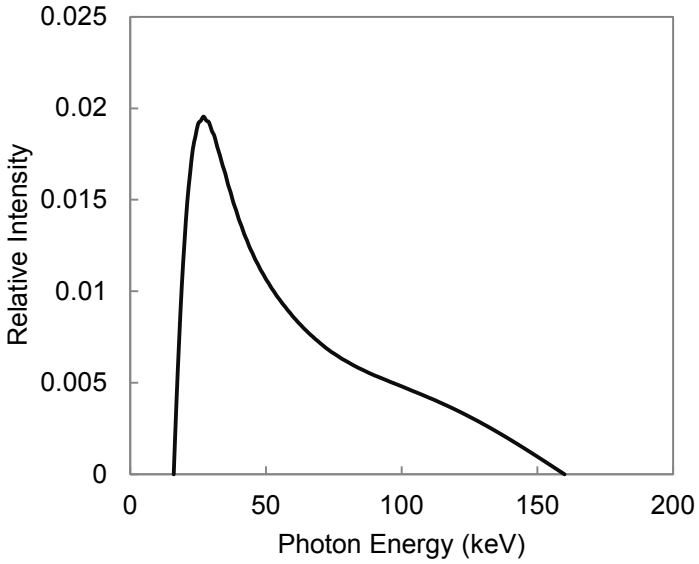

Figure 6.6 Estimate of the energy dependence $W(E)$ of the CT system used in this work.

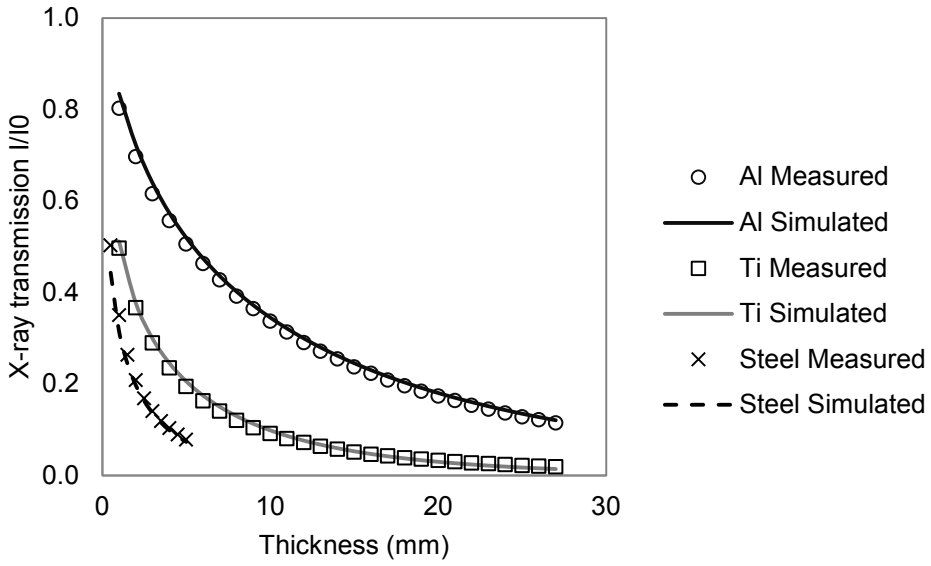

Figure 6.7 Comparison between measured and simulated X-ray transmission for aluminium, titanium and steel.

6.1.3 Scatter

Scattering interactions are stochastic and best simulated using a Monte Carlo approach. Deterministic or 'analytical' scatter simulations do exist, but they are usually based on simplifying assumptions such as: the scattering of X-rays of a single energy, only considering first order interactions, and shift invariance of a scatter PSF. Instead of simulating scatter, the measured scatter signals from Chapter 5 are used.

To incorporate scatter in the simulation, attenuation values are first converted to transmission values:

$$\frac{I}{I_0} = \exp(-\mu x) \qquad 6.11$$

The transmission values are then multiplied by I_0 to give intensity values I, where I_0 is sampled from the measured collimated data in Section 5.2.1. These scatter signals are then added to the intensity values to give the scatter contaminated data. These steps are shown in Figure 6.8 for a projection of the OCIC cross-section.

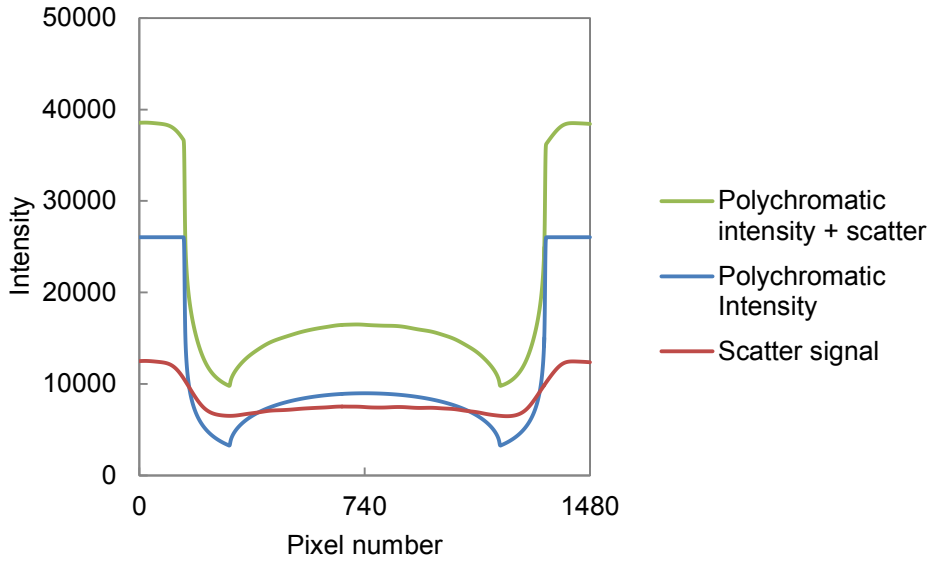

Figure 6.8 Comparison of simulated intensity values with and without scatter.

6.1.4 Noise

Photon detection is a counting process that obeys a Poisson distribution. The standard deviation of the distribution is equal to the square root of the distribution's mean. For a sufficiently large number of events, the Poisson distribution approximates a Gaussian distribution. Projections are therefore superimposed with Gaussian noise, the standard deviation of which is proportional to the square root of a given projection value [155]. This relationship is derived empirically based on the attenuation measurements from Section 5.1; the relationship is shown in Figure 6.9. The gradient m and intercept c of the least-squares line are utilised in the following noise model:

$$I_{x'y'} = I_{xy} + r \tag{6.12}$$

where I_{xy} is a simulated projection value for a given pixel coordinate and r is a random number drawn from a normal distribution with zero mean and a standard deviation of $m \times \sqrt{I_{xy}} + c$.

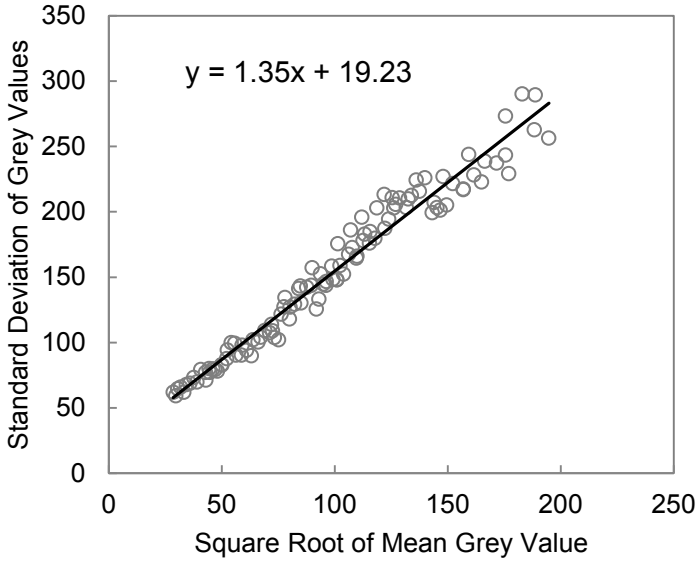

Figure 6.9 Derivation of noise model parameters based on intensity measurements from Section 5.1.

6.1.5 Simulation Validation

To validate the simulation a visual comparison is made between line profiles evaluated from CT images reconstructed from measured and simulated data, see Figure 6.10. The line profiles are drawn across the cylinder wall of the OCIC cross section as per the previous chapters. Very good agreement is seen for the general shape of the profiles alongside the magnitude of the noise. The only minor discrepancies are in Figure 6.10(a) and (c); the reconstructed values at the outer (right hand) edges are slightly larger in the simulated data than the measured data. This may be due to factors such as axial run out, thermal expansion, focal spot drift etc. being omitted from the simulation. As such, the edges are much ‘sharper’ in the simulated data. Nevertheless, a high level of agreement is seen between the measured and simulated data; this is to be expected due to the use of empirically derived spectra, noise and scatter signals.

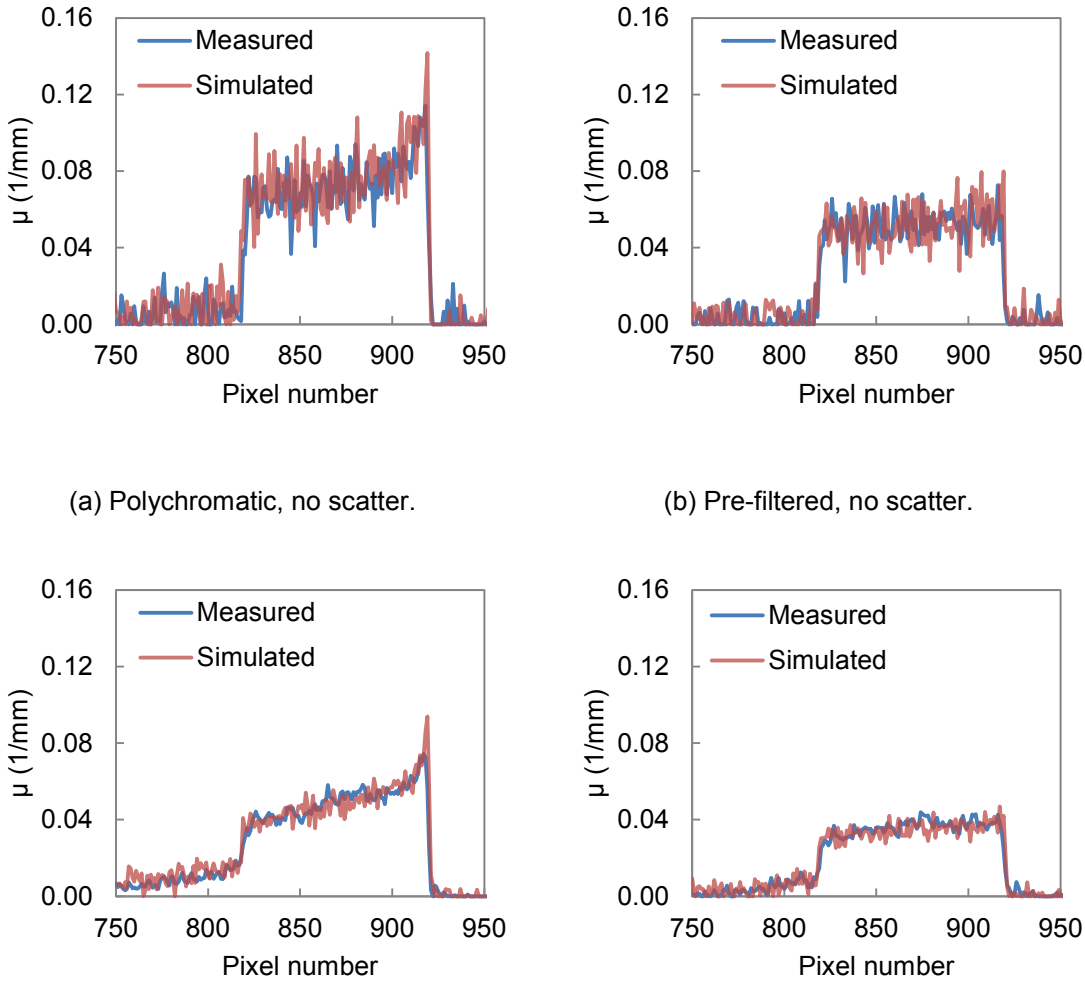

(a) Polychromatic, no scatter.

(b) Pre-filtered, no scatter.

(c) Polychromatic, with scatter.

(d) Pre-filtered, with scatter.

Figure 6.10 Comparison of line profiles drawn across cylinder wall of CT images reconstructed from measured and simulated data.

6.2 The Influence of Beam Hardening on Dimensional Measurements

6.2.1 Method

With the aid of the simulation tool, the inner and outer radius measurement error is evaluated for polychromatic, pre-filtered, monochromatic and beam hardening corrected data. Additional factors that are varied in the simulation include the material of the workpiece and the resolution of the projections.

To simulate spectrum pre-filtration, $W(E)$ is estimated from pre-filtered X-ray transmission measurements in the same manner as described in Section 6.1.2. Monochromatic data is simulated using the Beer-Lambert law (see Section 2.1.5). To consider the material dependence of beam hardening, both aluminium and titanium workpieces are simulated. To consider how pixel and voxel size impact the influence of beam hardening, projections are generated at twice and half the pixel resolution of the actual detector, 254 and 63.5 μm respectively. Finally, to evaluate the influence of beam hardening correction on dimensional measurements, a linearisation beam hardening correction is applied to the polychromatic projections. Beam hardening corrections for both the titanium and aluminium workpieces are derived by fitting a straight line to the respective polychromatic attenuation versus material thickness curves and noting the gradient, see Figure 6.11. The gradient of the best-fit line is the linear attenuation coefficient μ of the monochromatic data. Plotting polychromatic attenuation against the monochromatic attenuation yields the beam hardening correction curve, see Figure 6.12; the function is approximated with a 6^{th} order polynomial.

Projections of each workpiece are generated with an angular increment of 0.5°; the same as used experimentally. The simulation is run three times for each workpiece for each condition. The reconstruction settings are the same as those used experimentally. The 'normal' resolution data is reconstructed into CT images of 1024^2 pixels, whist the higher and lower resolution projections are reconstructed into CT images of 2048^2 and 512^2 pixels respectively. Following reconstruction, surface determination is performed using both the ISO50 and local method.

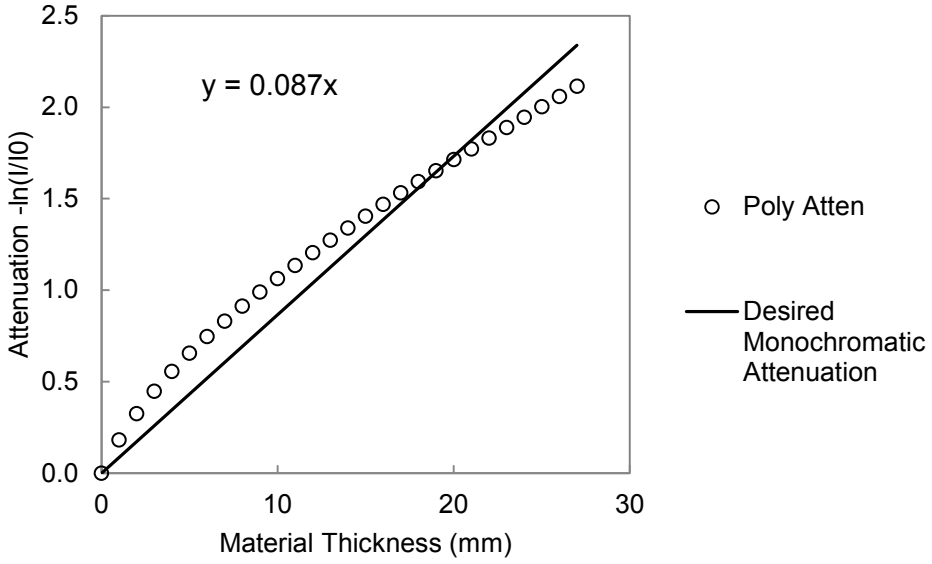

Figure 6.11 Polychromatic and monochromatic attenuation versus material thickness for aluminium.

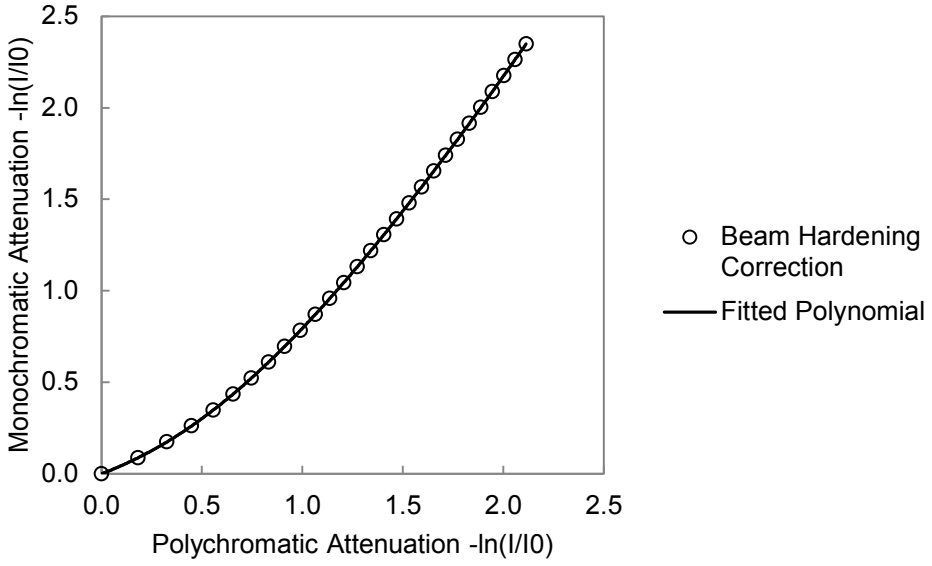

Figure 6.12 Function for correcting polychromatic to monochromatic attenuation for aluminium (beam hardening correction curve) approximated by a 6^{th} order polynomial.

6.2.2 Results

CT images of the polychromatic, pre-filtered, monochromatic and beam hardening corrected (BHC) aluminium workpieces are shown in Figure 6.13(a) to (l). Cupping artefacts are present in the polychromatic data, but these artefacts are suppressed in the pre-filtered data and removed entirely in the beam hardening corrected data. This is shown more clearly in Figure 6.14 where line profiles across noiseless reconstructions of the OCIC cross-section are compared.

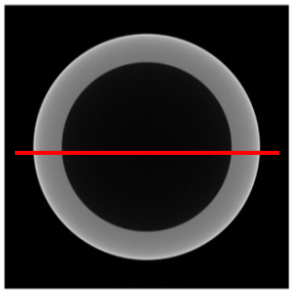

(a) Poly (OCIC)

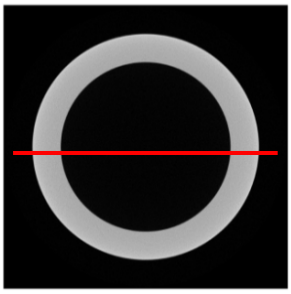

(b) Pre-filt

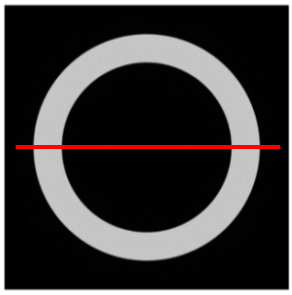

(c) Mono

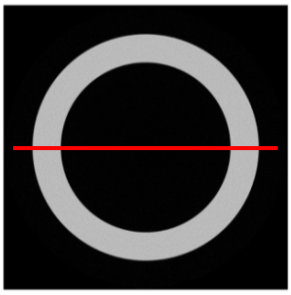

(d) BHC

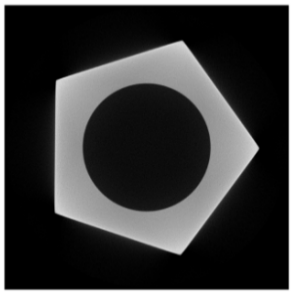

(e) Poly (OPIC)

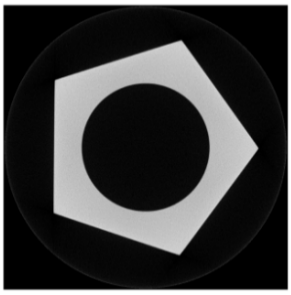

(f) Pre-filt

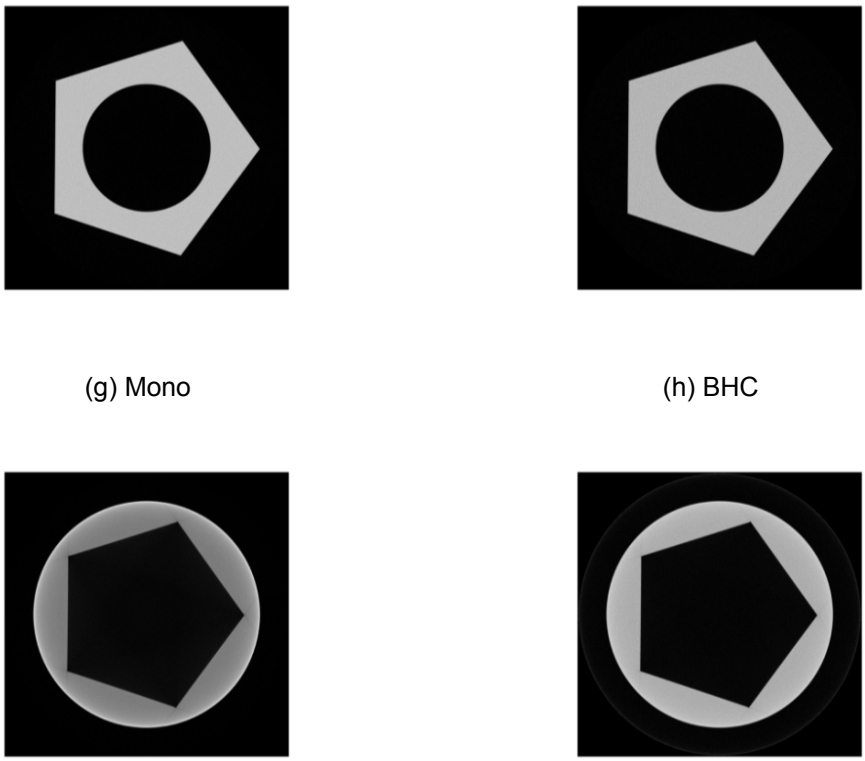

(g) Mono (h) BHC

(i) Poly (OCIP) (j) Pre-filt

(k) Mono (l) BHC

Figure 6.13 CT images reconstructed from simulated data with varying degrees of beam hardening. Red lines correspond to the position of line profiles in Figure 6.14.

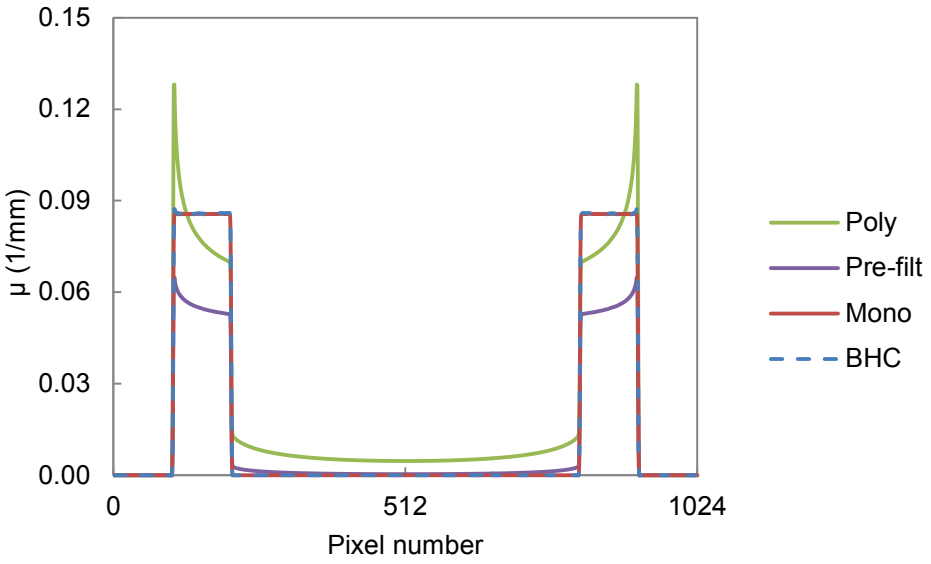

Figure 6.14 Line profiles across CT images of the OCIC cross-section reconstructed from noiseless data with varying degrees of beam hardening.

Figure 6.15(a) to (d) show the radius measurement error for the inner and outer features of the OCIC cross-section, evaluated using the ISO50 and local surface determination methods; the error bars correspond to the range of the three repeated simulations. The trends observed are in line with those seen experimentally. For the inner feature, the radius estimate increases as the data goes from polychromatic to monochromatic, see Figure 6.15(a) and (c). Whilst for the outer feature, the radius estimate decreases as the data goes from polychromatic to monochromatic, see Figure 6.15(b) and (d). The radius measurement error is larger for the external feature than the internal feature, whilst the radius measurement error is larger for the ISO50 method than the local method. To further test these observations, the radius measurement error for the inner and outer features of the OPIC and OCIP cross-sections are evaluated, and again, the same trends are observed (results not shown).

It is interesting to note the pixel size of the reconstructed data is 49 μm, and the maximum error observed is 33.8 μm ± 0.3 μm, see Figure 6.15(b), thus the influence of beam hardening is, at worst, approaching the pixel size.

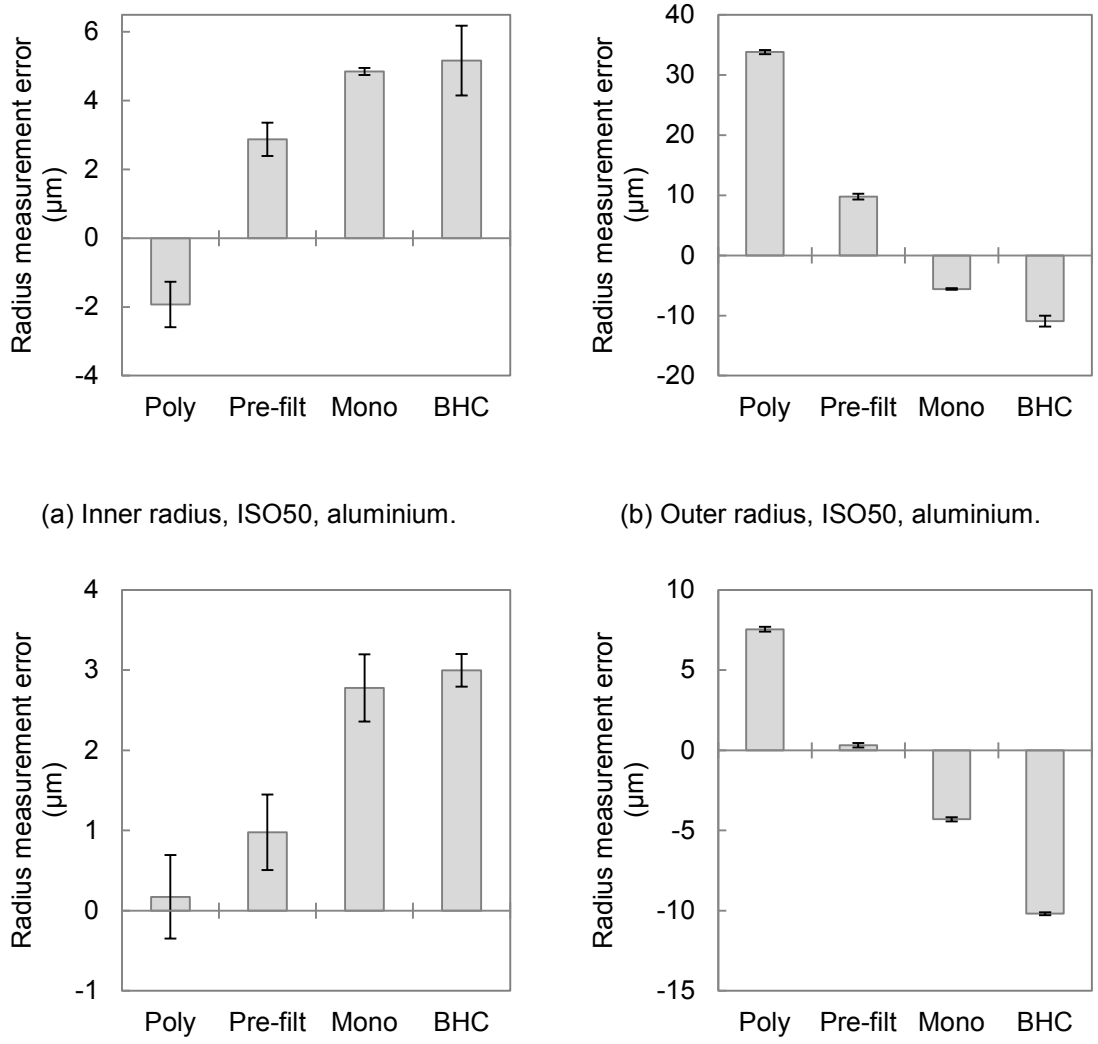

(a) Inner radius, ISO50, aluminium.

(b) Outer radius, ISO50, aluminium.

(c) Inner radius, local, aluminium.

(d) Outer radius, local, aluminium.

Figure 6.15 Comparison of radius measurement error for the OCIC cross-section. Error bars represent the range of the three repeats.

Figure 6.16 (a) to (d) compare the radius measurement error for the OCIC cross-section simulated and reconstructed at twice and half the 'normal' pixel size. It can be seen for all cases, bar Figure 6.16(c), the influence of beam hardening scales with pixel size. This result is to be expected: as the spatial sampling decreases, edges will be spread over fewer pixels making both the ISO50 and local surface determination methods prone to larger errors. Conversely, as the spatial sampling increases, edges will be spread over more pixels and will be more 'well defined'. In simulation this reduces measurement error, in real world measurements other influencing factors will come into play, like focal spot drift, axial run-out and thermal expansion.

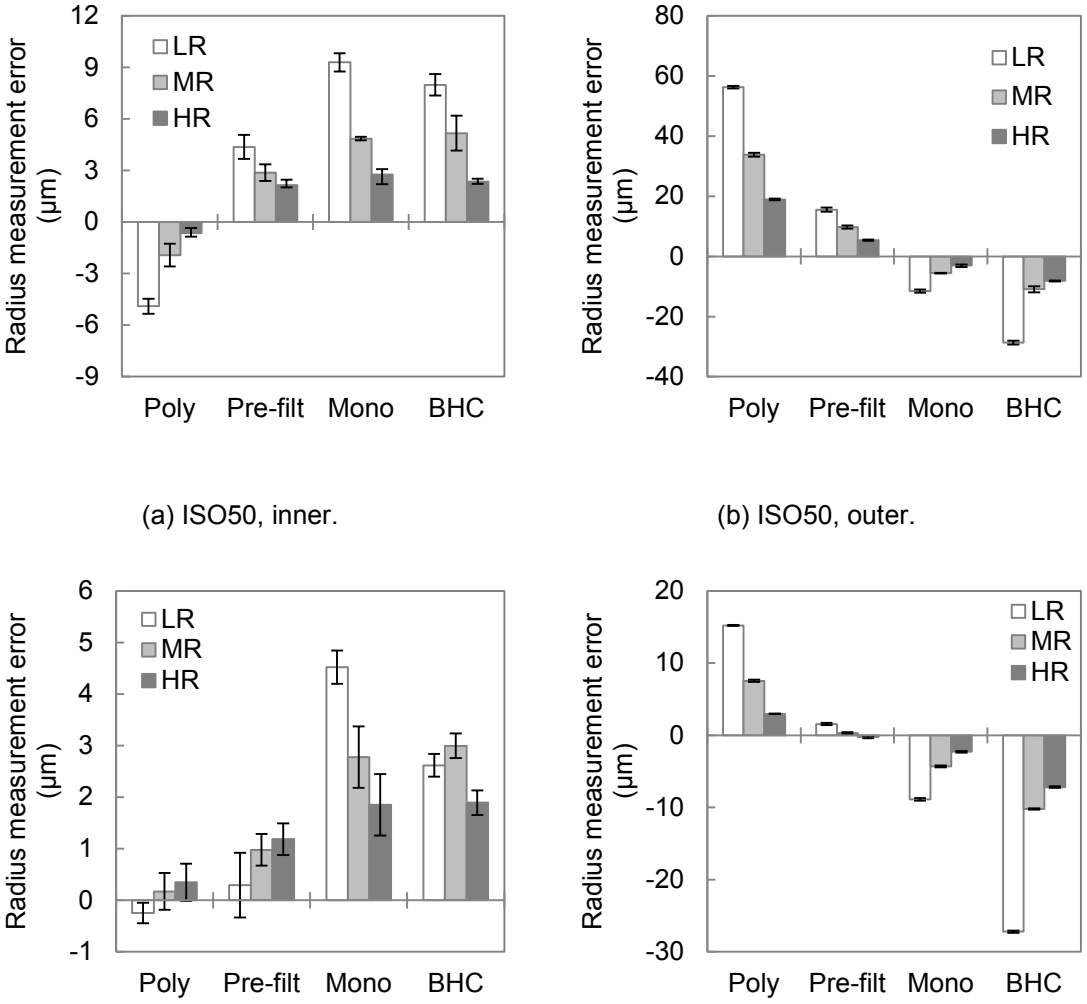

(a) ISO50, inner.

(b) ISO50, outer.

(c) Local, inner.

(d) Local, outer.

Figure 6.16 Comparison of radius measurement error for the OCIC cross-section simulated and reconstructed at three different pixel sizes: low-resolution (LR), medium-resolution (MR) and high-resolution (HR). Respective detector pixel sizes are 254, 127 and 63 µm. Respective CT image pixel sizes are 98, 49 and 24.5 µm.

Figure 6.17(a) to (d) compare the radius measurement error for the OCIC cross-section in aluminium ($Z = 13$, $\rho = 2.7$ g/cm^3) and titanium ($Z = 22$, $\rho = 4.5$ g/cm^3). The results show the radius measurement error is larger for the external features of the titanium workpiece than the aluminium workpiece. This result is to be expected since materials of higher atomic number (Z) and density (ρ) are more attenuating, see Section 2.1.4. On the other hand, the radius measurement error for the internal features does not seem to be so dependent on the workpiece material. This is most likely due to the fact

that internal features are always irradiated by a more monochromatic spectrum than external features since the material surrounding inner features acts as a pre-filter. In addition to this, polychromatic attenuation becomes more linear as material thickness increases (see Figure 6.11), whilst it is most nonlinear for the first few millimetres of material.

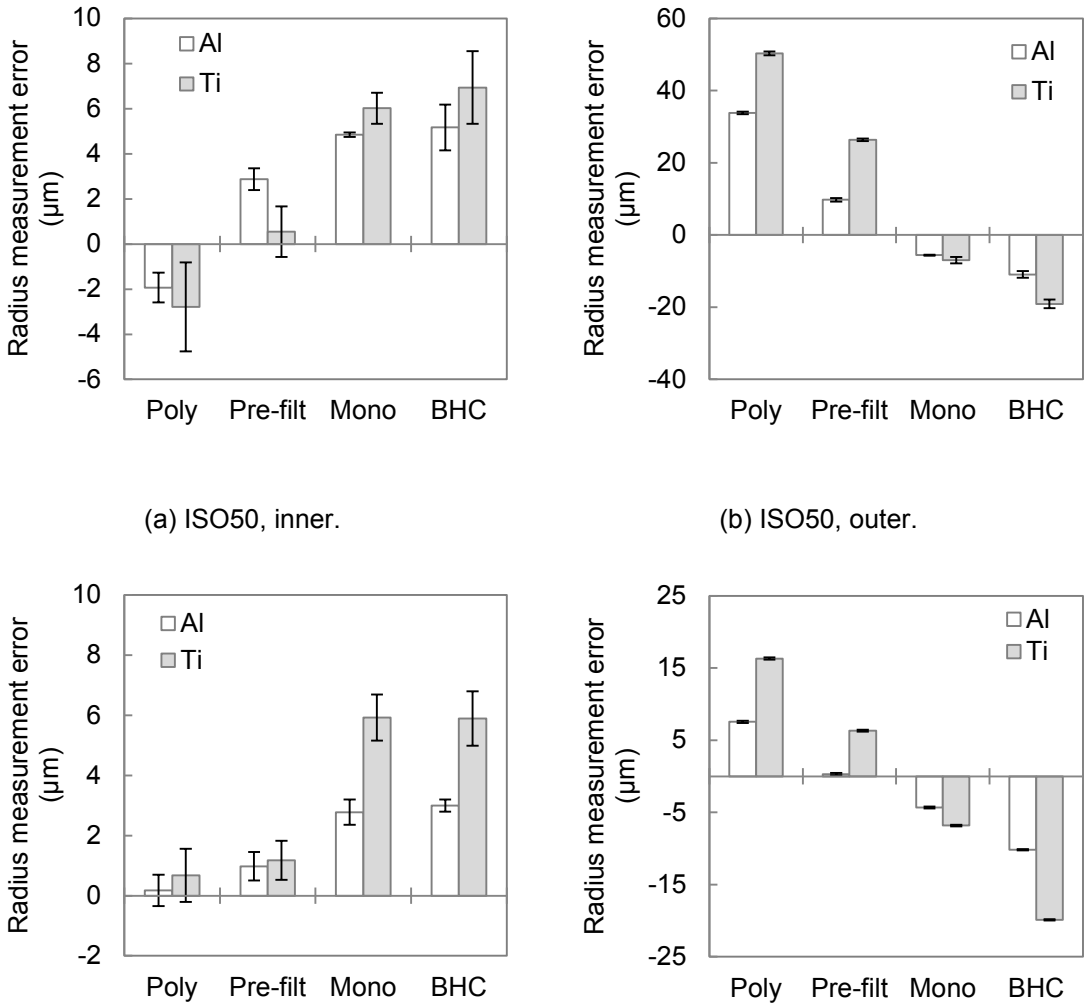

(a) ISO50, inner.

(b) ISO50, outer.

(c) Local, inner.

(d) Local, outer.

Figure 6.17 Comparison of radius measurement error for the OCIC cross-section in aluminium and titanium.

6.2.3 The Influence of Beam Hardening for the ISO50 Method

The results of both the simulation-based study and the experimental study show beam hardening significantly influences measurement results when surface determination is performed using the ISO50 method, particularly external dimensions. This is because beam hardening raises grey values at outer surfaces and reduces grey values at higher penetration depths. The ISO50 method neglects these raised and lowered grey values and defines a global threshold based on the modal material grey value. As such, in the presence of beam hardening the ISO50 threshold can never be ‘correct’ for both internal and external surfaces.

To demonstrate this point, we replicate the experiment of Carmignato et al. [46] who showed that by varying an isovalue threshold and evaluating the inner and outer diameter measurement error of a cylinder, a threshold value can be found to minimise the inner and outer errors simultaneously. The result of such an experiment is shown in Figure 6.18(a), for beam hardening corrected data. Notice the point at which the inner and outer radius measurement error cross coincides with an approximately zero measurement error. The simulation is repeated with polychromatic data, the results are shown in Figure 6.18(b), the crossing point of which is found to be suboptimal for both the inner and outer diameters, thus demonstrating the point: in the presence of beam hardening, no single threshold is ‘correct’ for both inner and outer features. Inner and outer features may however be treated independently, i.e. one threshold value is used for internal features, and another, separate threshold used for external features.

It is also worth noting that according to Figure 6.18(a) the ISO50 value does not represent the ‘correct’ threshold value, even with beam hardening correction. The ISO50 threshold in this case will lead to inner dimensions being measured too large, and outer dimensions being measured too small; looking back to the results in Figure 6.15(a) and (b) this is indeed the case.

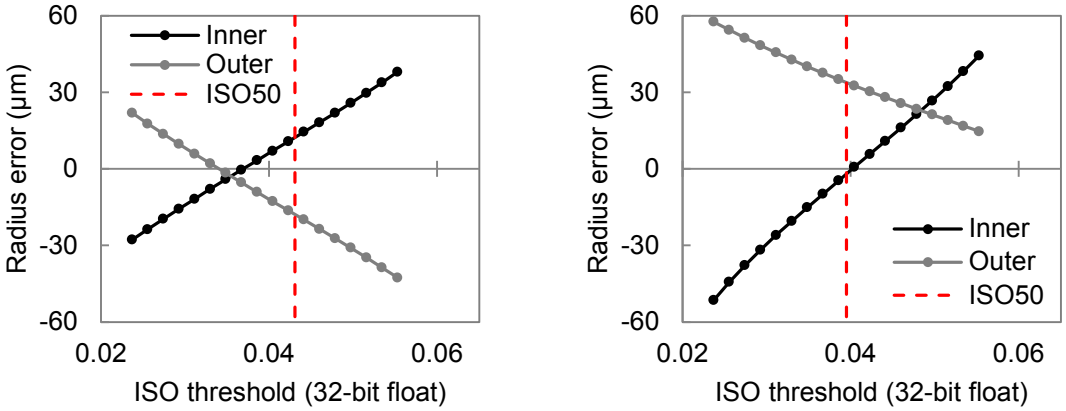

(a) Inner & outer radius measurement error for various threshold values for BHC data. The inner / outer intercept occurs at ~ zero measurement error.

(b) Inner & outer radius measurement error for various threshold values for poly data. In the presence of BH the crossing point is sub-optimal

Figure 6.18 Comparison of inner & outer radius measurement error for various threshold values for BH corrected data and polychromatic data. Experiment replicated from Carmignato et al. [46].

To further illustrate this point the edge response function (ERF) of the inner and outer edges of the polychromatic and monochromatic data are shown in Figure 6.19. The ERF is an imaging system's response to an edge, it is essentially the average of all the edges of a given feature and is evaluated in accordance with ASTM E1685-95 [161].

Figure 6.19 shows that the inner and outer ERFs for the polychromatic data are very different; they differ in both height (contrast) and slope. Furthermore, the point at which they cross is too high for the inner edge, and too low for the outer edge. It is interesting to note that the grey value at which the ERFs cross is equal to the threshold value at which the lines in Figure 6.18(b) cross. Looking now to the monochromatic ERFs, clearly the inner and outer profiles are very similar. It is only when inner and outer edges are similar that the isovalue surface determination method should be used. The 'correct' grey value threshold should be chosen either iteratively as per Carmignato et al. [46] or by plotting the inner and outer ERFs and noting the grey value at which they cross, as per Figure 6.19.

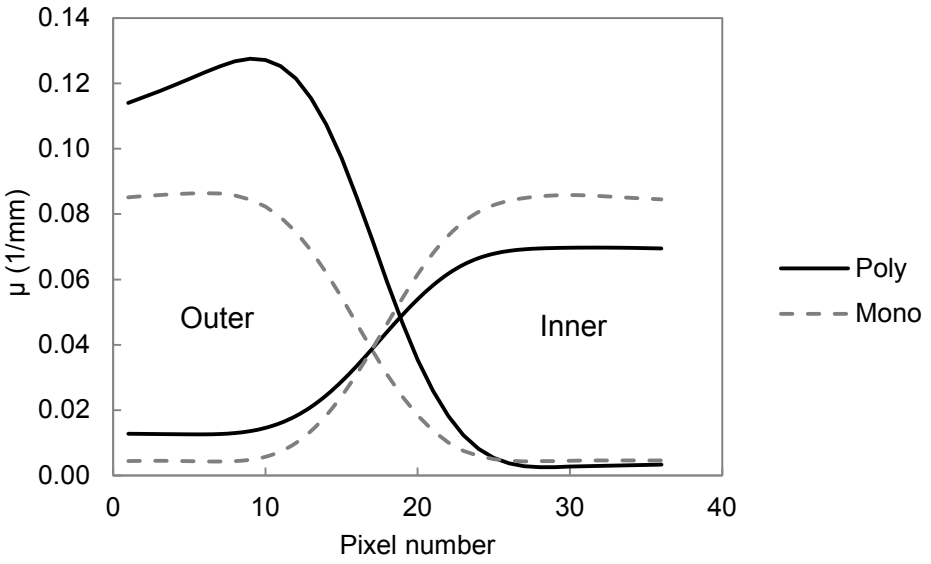

Figure 6.19 Comparison of inner and outer ERFs for polychromatic and monochromatic data.

6.2.4 The Influence of Beam Hardening for the Local Method

The results show the local surface determination method is more robust to the influence of beam hardening compared to the ISO50 method for external features. Even so, beam hardening still significantly influences measurement results evaluated with this surface determination method. To better understand how beam hardening influences the local surface determination method the line spread function (LSF) of the internal and external edges of the OCIC cross-section in aluminium are evaluated. The LSF is the first derivative of the edge response function (ERF). The ERF is considered here as a smooth representation of all the edges in a given CT data set. Based on this reasoning, the LSF is a smooth representation of the gradient of all the edges in the data set. ASTM E1685-95 [161] provides instruction on evaluating the LSF from CT data, the method described in the standard is adopted here.

Figure 6.20(a) and (b) show the ERFs for the inner and outer edges respectively, whist Figure 6.21(a) and (b) show the LSFs for the inner and outer edges respectively. Beam hardening clearly changes the shape of both the internal and external ERFs, whilst the shape of the LSFs is less affected. More importantly though is the turning point of the LSFs. For the local method, turning points of edges represent surface points, so it is

through this change in the turning point that beam hardening influences dimensional measurements.

Beam hardening clearly changes the turning points of the outer LSFs; however, this effect is much smaller for the inner LSFs and explains why the effect of beam hardening is reduced for internal dimensions when compared to external dimensions. It is also interesting to note that there is a clear difference in the turning point of the monochromatic data and the beam hardening corrected data, even though their ERFs appear very similar. This is an important result as it shows that even a near-ideal beam hardening correction will fail to lead to monochromatic edges.

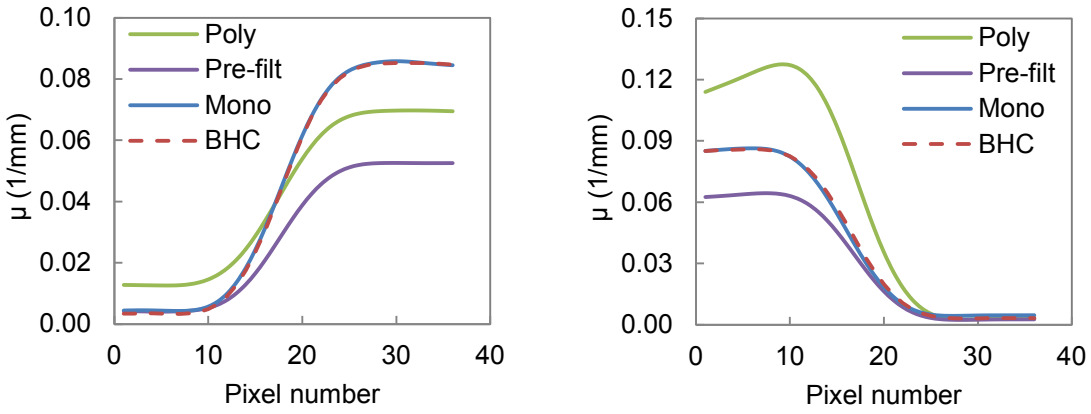

(a) ERFs evaluated from the inner edge of the OCIC cross-section.

(b) ERFs evaluated from the outer edge of the OCIC cross-section.

Figure 6.20 Comparison of ERFs for inner and outer edges of data with various degrees of beam hardening.

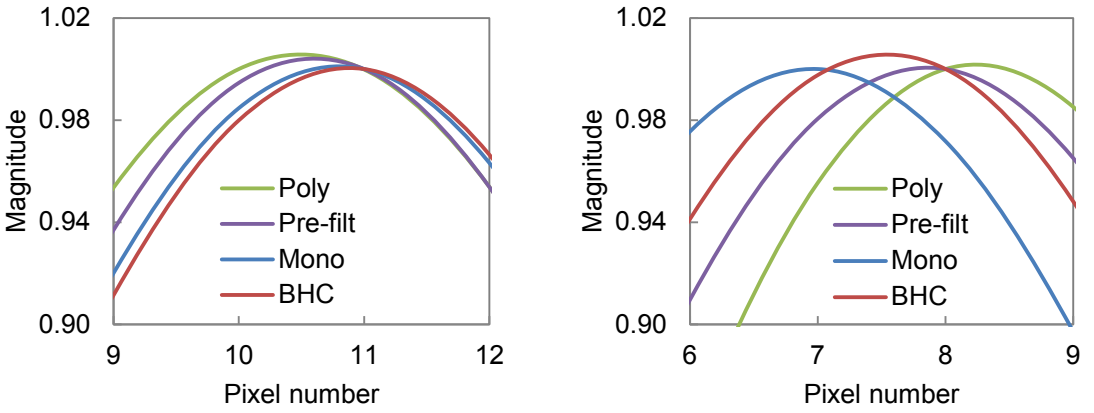

(a) LRFs for the inner edge of the OCIC cross-section.

(b) LRFs for the outer edge of the OCIC cross-section.

Figure 6.21 Comparison of LSFs for inner and outer edges of data with various degrees of beam hardening. The shift in the LSF turning point influences dimensional measurements.

Throughout this work it has been shown that inner and outer dimensions act in opposition. The opposing nature of inner and outer dimensions has previously been observed and discussed by Saewert et al. [37] and Carmignato et al. [46]; however, to the author's best knowledge no explanation of this phenomena has been given in the CT metrology literature. The reason internal and external dimensions act in opposition is because they have opposing grey value gradient directions. This is illustrated in Figure 6.22, whereby an object with an inner and outer edge is depicted alongside the grey value gradient direction, calculated as $\mathrm{atan2}(-Gy/Gx)$, where Gy and Gx are the image gradients in the x and y directions respectively.

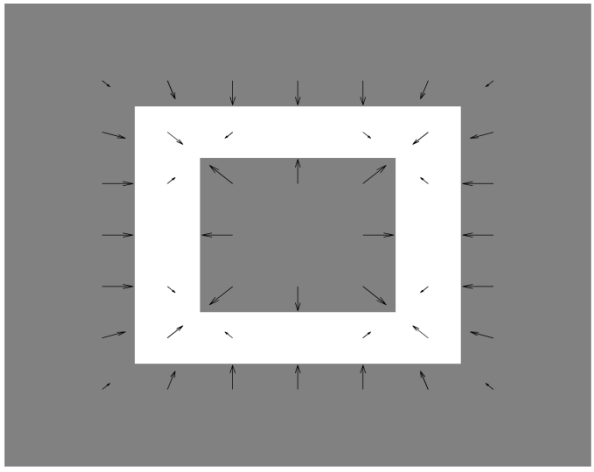

Figure 6.22 Inner and outer dimensions act in opposition because their edges have opposing grey value gradient directions. Illustration of an object with internal and external edges, arrows represent the grey value gradient direction. Figure inspired by Nixon et al. [124].

6.3 The Influence of Scatter on Dimensional Measurements

6.3.1 Method

The influence of scatter on dimensional measurements is evaluated by incorporating the scatter estimates from Section 5.2.1 in the simulation. Since scatter has only been estimated under polychromatic and pre-filtered conditions for the OCIC cross-section, only these data sets are considered. As before, surface determination is performed using both the ISO50 and local methods.

6.3.2 Results

CT images reconstructed from scatter contaminated polychromatic and pre-filtered data are shown in Figure 6.23. Line profiles comparing these reconstructions to the equivalent scatter-free reconstructions from the previous section are plotted in Figure 6.24. The line profiles show the same relationships as the experimental data in the previous chapters (see Figure 5.11 and Figure 5.28). That is, scatter reduces reconstructed values, whilst beam hardening raises reconstructed values.

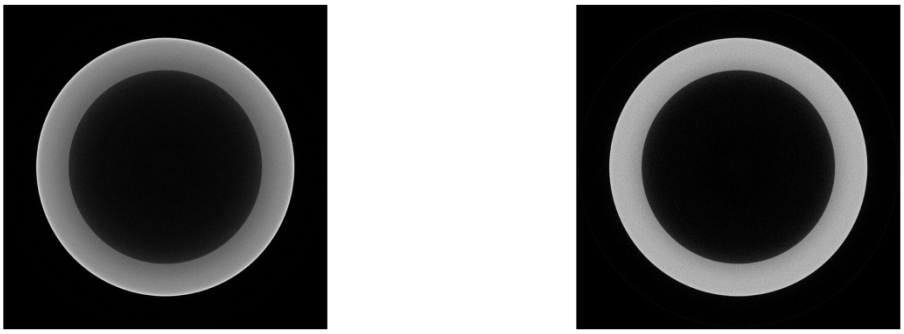

(a) Poly + scatter (b) Pre-filt + scatter

Figure 6.23 CT images reconstructed from simulated scatter-corrupted data.

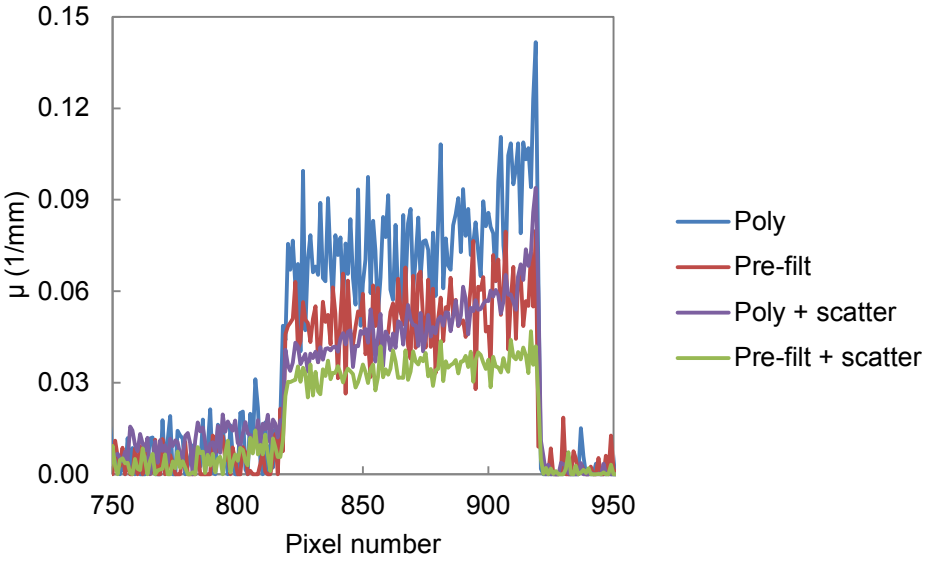

Figure 6.24 Line profiles across CT images reconstructed from simulated data.

Figure 6.25(a) to (d) compare the radius measurement error for polychromatic and pre-filtered data, simulated with and without scatter for both the ISO50 and local surface determination methods; the error bars correspond to the range of three repeated simulations. The trends observed are in line with those seen experimentally. For the inner feature, the presence of scatter reduces the radius estimate, see Figure 6.25(a) and (c). Whilst for the outer feature, scatter increases the radius estimate, see Figure 6.25(b) and (d).

Comparing the inner and outer radius measurements, the measurement error is larger for the external feature than the internal feature, whilst the radius measurement error is larger for the ISO50 method than the local method. The results also show the presence of scatter increases the measurement error; this holds true for both internal and external features, in the presence and in the absence of beam hardening, for both surface determination methods.

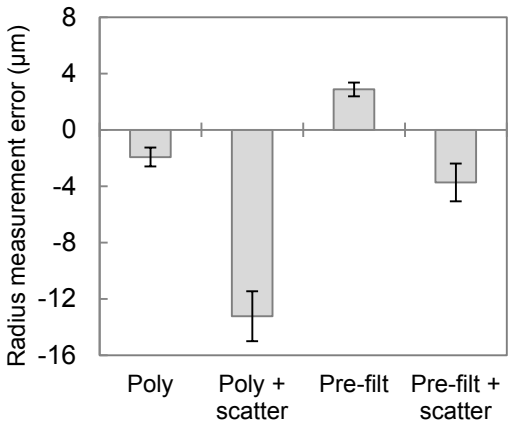

(a) Inner radius, ISO50.

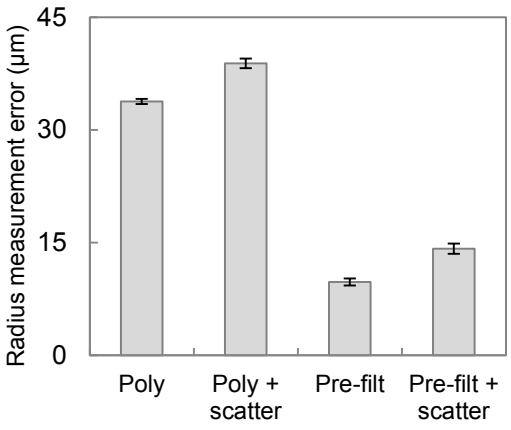

(b) Outer radius, ISO50.

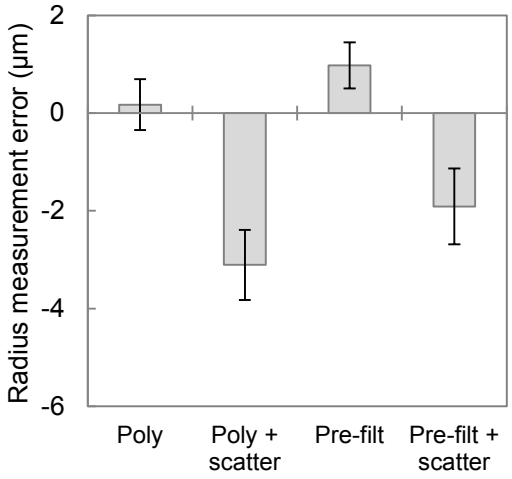

(c) Inner radius, local.

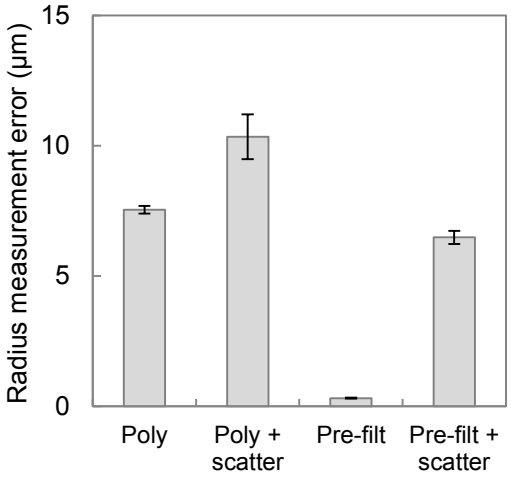

(d) Outer radius, local.

Figure 6.25 Influence of scatter and beam hardening on measurements of the inner and outer features of the OCIC cross-section.

6.3.3 The Influence of Scatter for the ISO50 Method

The results of the simulation-based study and the experimental studies show scatter influences measurement results when surface determination is performed using the ISO50 method, particularly external dimensions. The presence of scatter seems to predominantly lower image contrast. As previously mentioned, the ISO50 method assumes both inner and outer edges have the same contrast, if this isn't the case, no single isovalue will yield a 'correct' edge position for both.

Figure 6.26 shows the influence that scatter has on the inner and outer ERFs evaluated from pre-filtered data. The plot shows that scatter decreases both the inner and outer edge contrast compared to the scatter free data. The difference between the inner and outer contrast in the presence of scatter is 0.017, whilst in the absence of scatter it is 0.013. This shows that the inner and outer edge profiles are more similar in the absence of scatter; the remaining difference is assumed to be due to residual beam hardening. Since the edge profiles are more similar in the scatter free data, it follows that they will lead to more accurate measurements when evaluated via the ISO50 method.

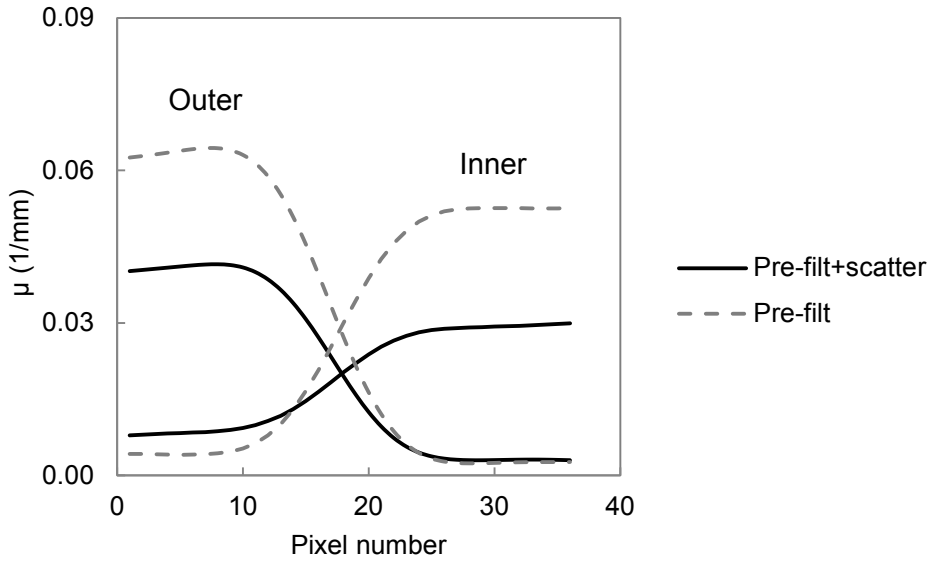

Figure 6.26 Comparison of inner and outer ERFs in the presence and absence of scatter.

6.3.4 The Influence of Scatter for the Local Method

The results show the local surface determination method can lead to more accurate measurements in the presence of scatter compared to the ISO50 method. Even so, scatter still significantly influences measurement results evaluated with this surface determination method.

Following a similar analysis to that presented for beam hardening, the ERFs and LSFs of the polychromatic and pre-filtered data, with and without scatter, are plotted in Figure 6.27 and Figure 6.28. Looking to the LSFs, it is clear that scatter shifts the turning points of the inner and outer LSFs. This shift is in opposite directions for the inner and outer features, and appears to be larger for the outer feature. Based on these observations it appears scatter and beam hardening influence the local surface determination method in a very similar manner. That is, scattered radiation changes the shape of edges, which in turn causes the turning points of edges to shift. It is this shift in turning point that influences dimensional measurements, and is the mechanism through which both scatter and beam hardening influence dimensional measurements.

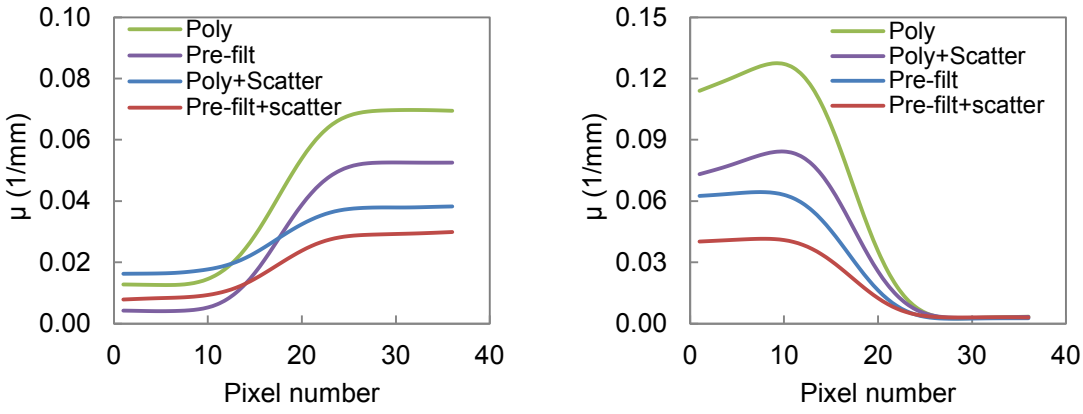

(a) ERFs evaluated from the inner edge of the OCIC cross-section.

(b) ERFs evaluated from the outer edge of the OCIC cross-section.

Figure 6.27 Comparison of ERFs for inner and outer edges evaluated from data with and without scatter and beam hardening.

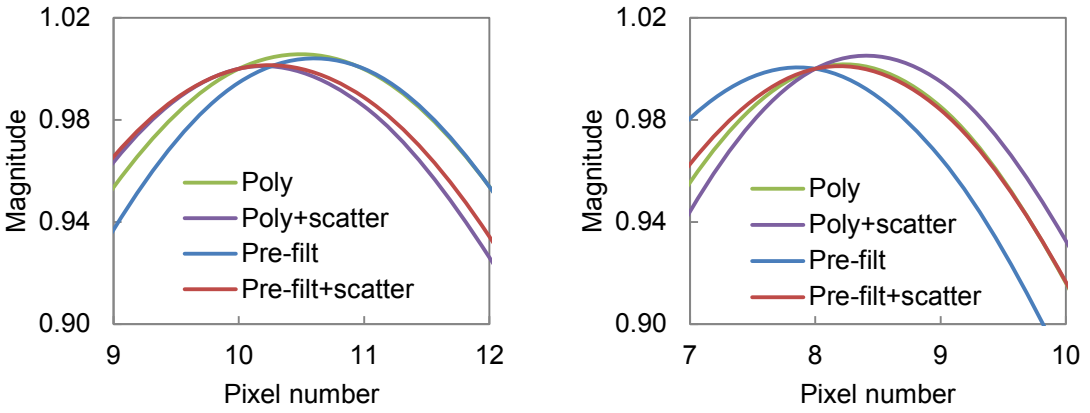

(a) LSFs evaluated from the inner edge of the OCIC cross-section.

(b) LSFs evaluated from the outer edge of the OCIC cross-section.

Figure 6.28 Comparison of LSFs for inner and outer edges evaluated from data with and without scatter contamination. Notice scatter and beam hardening cause the turning points of the LSFs to shift.

6.4 Chapter Summary

In this chapter the key observations from the experimental studies have been verified. Moreover, these observations have been made in the absence of experimental error, such as misalignments, axis run-out, focal spot drift and thermal expansion to name, but a few. As a result, measurement errors as small as a few microns have been achieved. This is a remarkable result considering the nominal voxel size of the reconstructed data is 49 μm, whilst the largest feature measured is a 40 mm diameter.

The simulation results have shown that if beam hardening is present, and neglected by the surface determination algorithm (i.e. the ISO50 method), large measurement errors can occur; at worst, the measurement error approaches the voxel size. However, if scatter and beam hardening are corrected for, and inner and outer edge profiles are similar, a single isovalue threshold can be chosen that leads to accurate measurements of both internal external features, as per Carmignato et al. [46]. It should be noted the ‘correct’ isovalue threshold is not necessarily the 50% value.

In most cases the local surface determination method leads to more accurate measurements than the global ISO50 method; however, such a gradient-based algorithm can still be influenced by scatter and beam hardening artefacts. The results show both scatter and beam hardening influence attenuation values, this in-turn influences edge profiles causing the turning point of an edge to shift. This has been shown by evaluating LSFs from internal and external edges.

Since the turning point of an edge is influenced by artefacts, it is perhaps not such a robust property on which to base a surface determination algorithm. In future work, alternative edge properties could be sought and evaluated with respect to their robustness to artefacts. Irrespective of this, the results suggest the combination of spectrum pre-filtration, scatter minimisation/correction and a local gradient-based surface determination method should lead to more accurate dimensional measurements. This result is supported by the experimental results in Section 5.5 for the OCIP and OPIC cross-sections.

Chapter 7 Measurement Uncertainty due to Surface Determination

In the previous two chapters it was shown that both scatter and beam hardening have a systematic influence on the measurement of inner and outer features. Scatter and beam hardening do not influence dimensional measurements directly, they influence surface determination, which in turn influences dimensional measurements. Obviously surface determination is not exact, meaning that surfaces have an associated uncertainty in their position. The purpose of this chapter is to develop a method to evaluate the measurement uncertainty due to surface determination, then to assess how scatter and beam hardening influence this uncertainty contributor.

The contributions of this chapter are:

- A method for evaluating the measurement uncertainty due to surface determination (Sections 7.2 through 7.6).
- Observations on how scatter and beam hardening influence the measurement uncertainty due to surface determination (Section 7.8).

7.1 Basic Concept

Surface determination is the process of estimating an object's surface from a CT data-set. Due to the finite spatial resolution of the CT data, surfaces may be spread across several voxels in a CT-volume, or pixels in a CT image. Obviously surface determination is not exact, meaning that each estimated surface point has an associated uncertainty. When evaluating the dimensions of an object, geometric features are fitted to surface points using the least-squares approach. Clearly the uncertainties of the surface points used in the least-squares fit will impact the uncertainty of the measurement result.

Figure 7.1 illustrates this idea, and shows the search for the edges of a circle. Each edge point has coordinates x_i, y_i with associated uncertainties $\sigma x_i, \sigma y_i$. Fitting a circle to the coordinates yields an estimate of the circle's radius r; hence the uncertainties of the coordinates directly impact the uncertainty of the fitted radius σr.

In this chapter a method to estimate the uncertainty of surface points is developed, these uncertainties are then propagated through a least-squares geometry fit to the final measurement result in order to evaluate the measurement uncertainty due to surface determination. This method is then used to assess the influence that scatter and beam hardening have on the measurement uncertainty due to surface determination.

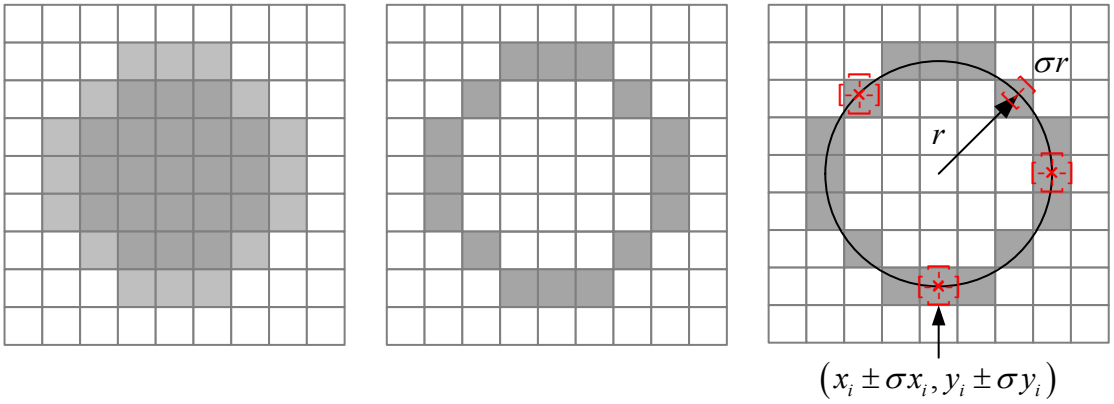

(a) CT image of an object with a circular cross-section.

(b) Edge of object.

(c) A circle fitted to the sub-pixel edge coordinates. Brackets represent uncertainty of surface points.

Figure 7.1 Illustration of the measurement uncertainty due to surface determination.

7.2 Estimating the Uncertainty of Surface Points

To simplify the problem, only 2D CT-images are considered, as illustrated in Figure 7.1. The extension of the problem to 3D is not considered here, but recommendations on how it might be done are given at the end of this chapter.

The error of an edge's position is estimated by simulating an edge with a known position, superimposing the edge with noise, then estimating its position with an edge detector. By repeating this many times in a Monte Carlo simulation, the distribution of the error can be evaluated; the standard deviation of this error distribution represents the uncertainty of a surface point.

In the following sections a discrete 2D ramp edge model is first described followed by a description of the Monte Carlo simulation. The method is then validated by comparing the estimated uncertainty with that evaluated from repeated simulations. Finally, the method is evaluated on measured data to assess the influence that scatter and beam hardening have on the measurement uncertainty due to surface determination.

7.3 Edge Model

Edges in CT images are not step edges, but ramp edges; this is due to the point spread function (PSF) of the imaging system. Figure 7.2 illustrates this point; an internal edge from a CT image is magnified and shows the gradual change that occurs as pixels transition from air to material. In order to generate synthetic 2D edges of this kind the step edge model evaluated by Rockett [120] is adapted, Rockett in turn based the model on that of Lyvers and Mitchell [162].

Rockett's edge model is illustrated in Figure 7.3, the model has three parameters: contrast to noise ratio (CNR) $(I_{HIGH} - I_{LOW})/\sigma_{noise}$, edge orientation θ and edge displacement from the origin t. The intensities of pixels intercepted by the edge are calculated based on the area of high and low intensity regions they occupy. To extend Rockett's step edge to a ramp edge it is simply convolved with a 2D Gaussian function in order to model the PSF of a given measurement.

The CNR used in the model is defined by sampling I_{HIGH}, I_{LOW} and σ_{noise} from a given CT image using ROIs the same size as the edge model (11×11 for all data presented here). Whilst the standard deviation of the PSF used in the model is estimated by fitting a 1D Gaussian function to the line spread function (LSF) evaluated from a given CT data set. The edge parameter t is varied from 0 to 0.4 so as to vary the sub-pixel edge position, whist the parameter θ is varied from 0 to 45°, angles greater than 45° need not be evaluated as the edge model is symmetrical about 45°.

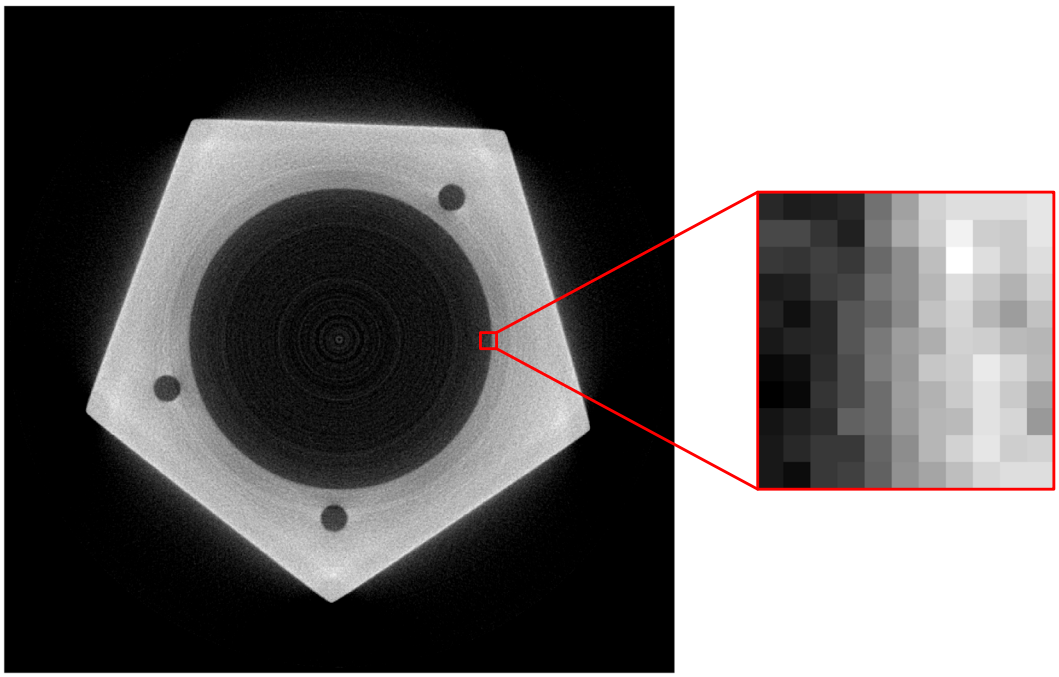

Figure 7.2 Magnified edge from a measured CT image. The edge is not a step edge but is blurred across several pixels.

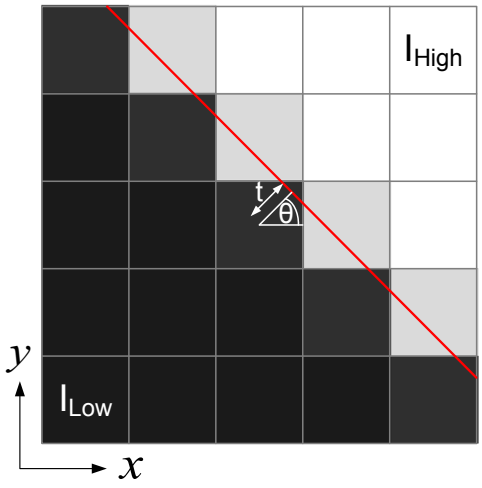

Figure 7.3 Rockett's step edge model [120].

7.4 Monte Carlo Simulation

The edge model is evaluated in a Monte Carlo simulation. Each step in the simulation is shown diagrammatically in Figure 7.4. The parameters t and θ are first defined to build the step edge, the step edge is then convolved with a 2D Gaussian function such that a ramp edge is formed. The ramp edge is next superimposed with zero mean white Gaussian noise, and then passed to the edge detection algorithm to estimate the edge's position. The processes of adding noise and estimating the edge's position are repeated 1000 times such that the error distribution of the edge's position is evaluated. This entire process is then repeated for the different values of t and θ. The number of repeats is chosen by experimentation; no significant change in results is seen for more than 1000 repeats.

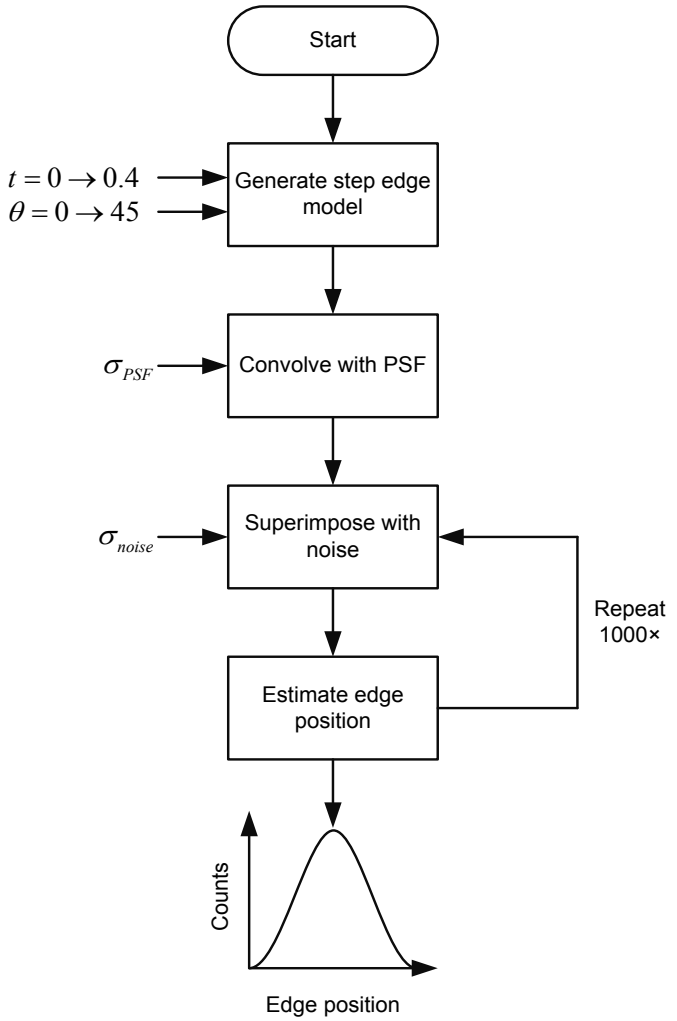

Figure 7.4 Flow chart showing each step in the Monte Carlo simulation for estimating the uncertainty of an edge's position.

7.5 Monte Carlo Simulation Results

The method described in the previous section for estimating the uncertainty of surface points is demonstrated for the simulated CT image shown in Figure 7.5(a). The CNR of the inner edge is estimated as 7.1 based on sampling the mean and standard deviation of grey values in regions of material and air close to the inner edge. Figure 7.5(b) shows the LSF of the inner edge, the standard deviation of the fitted Gaussian is 6.1 pixels. Using these parameters the Monte Carlo simulation is run, an exemplary edge generated by the edge model is shown in Figure 7.5(c).

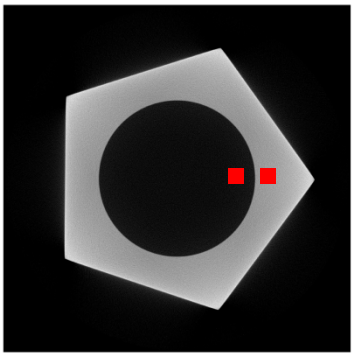

(a) Simulated CT image, red squares show ROIs for CNR calculation (squares not to scale).

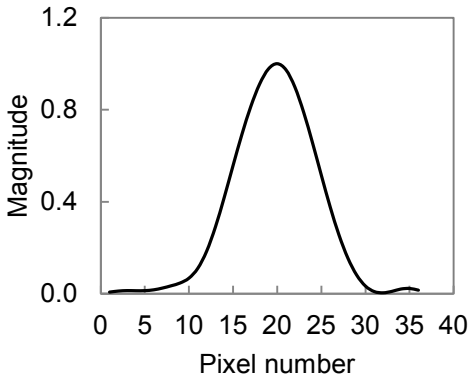

(b) LSF evaluated from the inner edge of the workpiece cross-section.

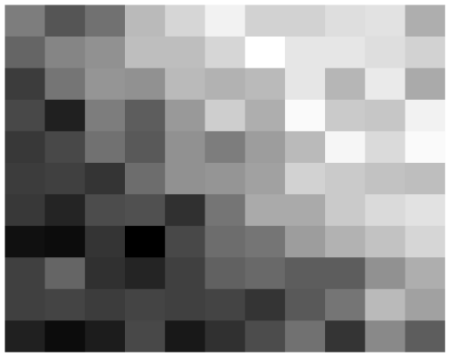

(c) Exemplary noisy ramp edge generated by the edge model in the Monte Carlo simulation.

Figure 7.5 Input and output of the Monte Carlo simulation for estimating the uncertainty of an edge's position.

Figure 7.6(a) shows how the edge's positional error varies as a function of edge displacement t and edge orientation θ in the absence of noise. The error increases with both t and θ and reaches a maximum for t = 0.4 and θ = 35 to 40°. The error is very small, at worst it's approximately 1/25th of a pixel; however, in the presence of noise the error becomes much larger.

Figure 7.6(b) shows how the mean error varies as a function of t and θ in the presence of noise. For values of t that are not equal to 0 a bias is observed and the error becomes independent of θ. This is likely due to the combined effect of the PSF and noise which blur the edge into the neighbouring pixels. In CT this is known as the partial fill artefact which arises due to the finite spatial resolution of the imaging system. This bias may also stem from the edge detector; Mikulastik et al. [163] showed that using polynomials to estimate sub-pixel edge position can introduce a bias similar in size to that seen in Figure 7.6(b).

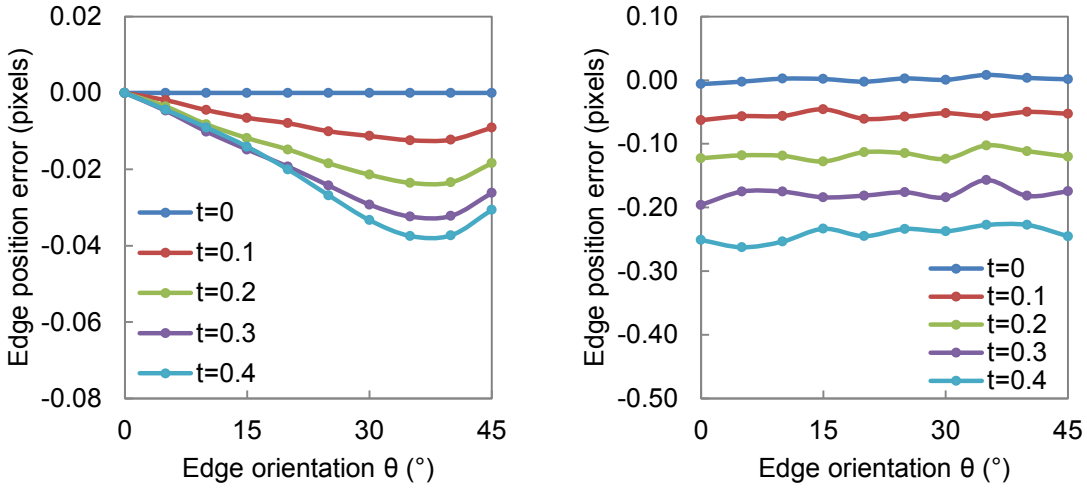

Figure 7.6 Graphs showing how the edge's positional error varies as a function of edge displacement t and edge orientation θ in the absence (a) and presence (b) of noise.

For each run of the Monte Carlo simulation the x and y coordinates of the edge position are estimated. Figure 7.7(a) shows how the standard deviation of these xy coordinates vary as a function of t and θ. It is found the x and y coordinate uncertainties act in opposition and converge at 45˚. Figure 7.7(a) also shows for θ = 0˚ (a vertical edge) the y coordinate uncertainty is minimum whilst the x coordinate uncertainty is a maximum. That is, the coordinate uncertainty is maximum perpendicular to the edge, and minimum parallel to the edge. This result is explained by realising that an edge's sub-pixel position is a function of the x and y gradient components; so if the x and y gradient components are small, their uncertainties will be small, and vice versa. Based on this reasoning, when the x and y gradient components are equal, their uncertainties should be equal, looking again to Figure 7.7(a) this is indeed the case when θ = 45˚.

The results plotted in Figure 7.7(a) are very useful since they enable the uncertainty of an edge's position to be estimated for a given t and θ. If t and θ are known for each surface point in a CT data-set the respective coordinate uncertainties can be estimated. θ is estimated directly by the surface determination algorithm. Unfortunately t cannot be estimated, since for real CT data the actual edge position is unknown. Instead of using t, the maximum envelope of Figure 7.7(a) is used, see Figure 7.7(b). With Figure 7.7(b) the uncertainty of an edge's position can be estimated with only knowledge of its orientation θ. Using the maximum envelope ensures uncertainties are always overestimated rather than underestimated. Figure 7.7(b) forms a look up table (LUT) that is used in the next section to estimate the uncertainty of surface coordinates from simulated CT data. The individual coordinate uncertainties are then propagated through a least-squares fit to the final measurement result.

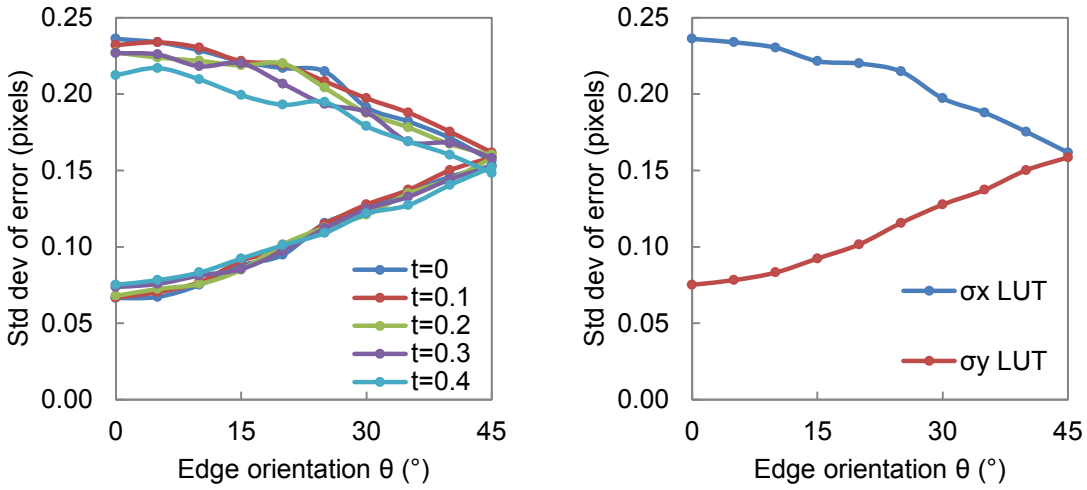

(a) (b)

Figure 7.7 (a) Graph showing how the standard deviation of the xy edge coordinates vary with t and θ. (b) Maximum envelope of (a).

7.6 Uncertainty due to Surface Determination

The results of the Monte Carlo simulation are used in this section to estimate the measurement uncertainty due to surface determination for the inner radius of the CT image shown in Figure 7.5(a). Applying the surface determination algorithm to the CT image yields a vector of surface coordinates x_i and y_i, alongside a vector of edge orientations θ_i for i = 1 to m. Using Figure 7.7(b) the uncertainty of each coordinate, denoted σx_i and σy_i, is estimated. Fitting a circle to the data-set via least-squares yields an estimate of the circle's centre and radius, x_c, y_c and r. The uncertainty of the fitted radius is evaluated via a second Monte Carlo simulation. Random numbers are added to each surface coordinate and a circle fitted to the coordinate set. This is repeated 1000 times in order to evaluate the standard deviation of the radius estimate. The standard deviations of the pseudo-random numbers added to each coordinate are defined by σx_i and σy_i. The coordinate set for each run of the Monte Carlo simulation is therefore:

$$x'_i = x_i + \sigma x_i \cdot n$$
$$y'_i = y_i + \sigma y_i \cdot n \qquad 7.1$$

where n is a random number drawn from the standard normal distribution.

The radius distribution generated from the second Monte Carlo simulation is plotted in Figure 7.8. The mean and standard deviation of the radius estimated from the simulation are 230.324 ± 0.007 pixels respectively. This result suggests the measurement uncertainty due to surface determination is very low indeed. Such a low uncertainty is unexpected, however the result can be rationalised based on the following considerations: firstly, the number of surface points used in the geometric fit is large (m = 987), if m is large than the radius uncertainty will be small. Secondly, for the considered measurement task, the dimension of interest r is large compared to the pixel size; r is nominally 11.3 mm whilst the pixel size is 49 μm. Based on this reasoning, the uncertainty due to surface determination is expected to be larger for features that fill only a small portion of a CT image and for features fitted to few surface points.

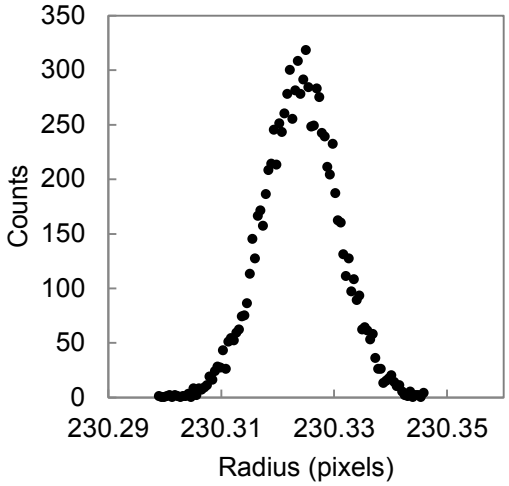

Figure 7.8 Radius distribution based on the output of the second Monte Carlo simulation. Standard deviation is 0.007 pixels which corresponds to 0.343 μm for a 49 μm pixel size.

7.7 Method Verification

To verify the proposed method, the CT simulation tool described in Section 6.1 is further made use of. Twenty sets of polychromatic and pre-filtered data of the OCIC cross-section are generated with and without scatter. Different noise waveforms are used in each simulation such that no two CT images are the same. Twenty repeats per condition are used based on the number of repeated measurements suggested by ISO 15530-3 [142]. Surface determination is performed for each data-set and the inner radius evaluated, the standard deviation of the repeated radius estimates is then calculated. This statistic represents the repeatability of the surface determination method and is assumed equivalent to the measurement uncertainty due to surface determination. As such, the standard deviation of the repeated radius estimate is compared to the results of the proposed method for each of the four data-sets; the results are presented in Figure 7.9.

Close agreement is seen between the model-based estimate and the repeated simulation-based estimate, although the model-based estimate is consistently larger than the simulation-based estimate. This constant overestimation is acceptable as it is preferable to overestimate uncertainty than underestimate it. The results in Figure 7.9 show an interesting trend: the presence of scatter raises the uncertainty due to surface determination, this is discussed further in the next section.

The overestimation of the uncertainty due to the surface determination may stem from the use of the maximum envelope of the coordinate uncertainties, (Figure 7.7), but this is expected to only have a small influence on the propagated uncertainty. Nevertheless, the model is able to follow the trends of the repeated simulations; therefore, the model is used in the next section to estimate the measurement uncertainty due to surface determination for measured data.

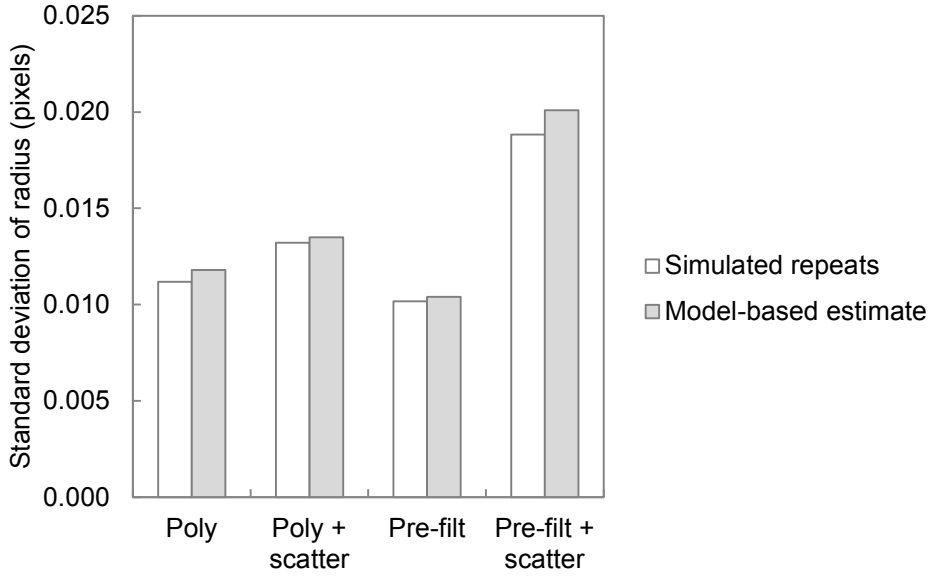

Figure 7.9 Comparison of measurement uncertainty due to surface determination estimated from repeated simulations and the proposed model.

7.8 Evaluation on Measured Data

In this section the proposed method for estimating the measurement uncertainty due to surface determination is evaluated on measured data. Four CT images are utilised and correspond to data acquired with and without pre-filtration and collimation. This allows the influence that scatter and beam hardening have on the measurement uncertainty due to surface determination to be evaluated.

The CT images evaluated are shown in Figure 5.9. The standard deviation of LSFs and the CNRs evaluated from the inner and outer edges are given in Table 7.1 and Table 7.2 respectively, whilst the results of the model-based estimate are plotted in Figure 7.10.

Table 7.1 Monte Carlo edge parameters for inner feature of measured data.

Inner	Poly	Poly + scatter	Pre-filt	Pre-filt + scatter
Std. Dev. LSF (pixels)	7.9	7.3	7.8	8.3
CNR	8.1	7.6	9.9	8.9

Table 7.2 Monte Carlo edge parameters for outer features of measured data.

Outer	Poly	Poly + scatter	Pre-filt	Pre-filt + scatter
Std. Dev. LSF (pixels)	7.6	6.4	6.8	7.4
CNR	30.2	45.9	15.5	25.4

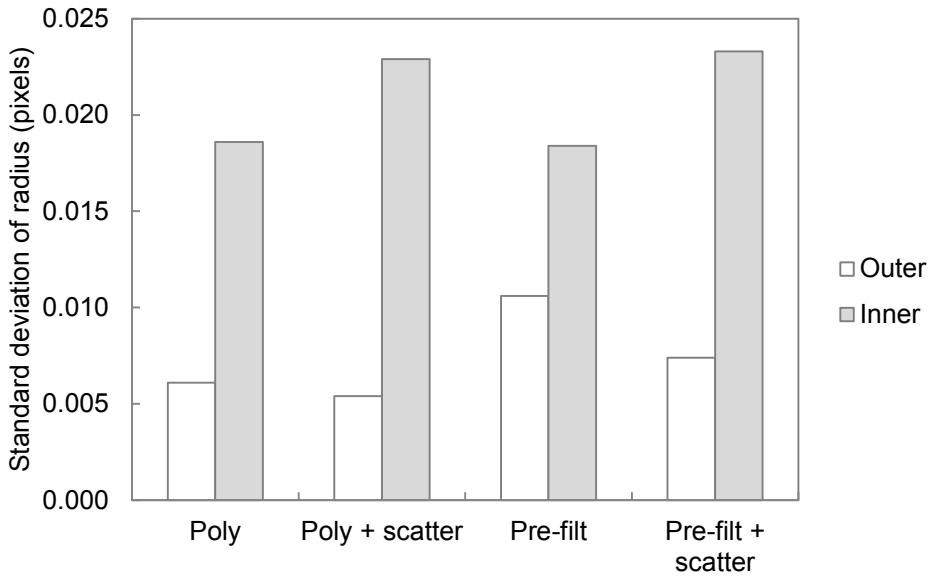

Figure 7.10 Measurement uncertainty due to surface determination for measured data, estimated using proposed model.

Figure 7.10 shows three trends:

- The measurement uncertainty due to surface determination is larger for the inner features than the outer features.
- The presence of scatter raises the measurement uncertainty due to surface determination for inner features and lowers it for outer features.
- Pre-filtering the data raises the measurement uncertainty due to surface determination for outer features.

The first observation can be explained by comparing the CNRs for the inner and outer features in Table 7.1 and Table 7.2 respectively. The CNRs for the inner edges are clearly much lower than those of the outer edges. The low contrast and high noise of the inner edges appears to directly influence the distribution of the surface points, leading to a noisy surface estimate which then impacts the least-squares fit.

The second observation is explained by realising that scatter lowers the contrast of the inner edges, which influences the measurement uncertainty in the same way as just described. On the other hand, for the outer edges, the presence of scatter seems to lower noise more so than it lowers contrast, so scatter raises the CNR of outer edges, see Table 7.2. The lowered noise caused by the presence of scatter acts to reduce the measurement uncertainty due to surface determination. The increase in noise when scatter is suppressed occurs because collimating the source reduces the number of photons incident on the workpiece. This can be overcome by increasing the detector exposure time or increasing the source current, at the cost of increasing scan time or the focal spot size respectively.

The third observation again comes down to noise: pre-filtering the source reduces the number of photons incident on the object's external features thus increasing noise. This trend is not seen for the internal features of the workpiece; this is most likely due to the number of photons irradiating the inner features being similar irrespective of pre-filtration since the surrounding material itself acts as a pre-filter.

7.9 Chapter Discussion

Surface determination defines the coordinate set from which the dimensions of an object are evaluated and thus influences the accuracy and uncertainty of dimensional measurements. It has been shown that with knowledge of the line spread function (LSF) and contrast-to-noise ratio (CNR) of a data-set it is possible to estimate the measurement uncertainty due to surface determination.

It has been shown that for outer features, the presence of scatter increases the CNR compared to data with scatter suppression. This effect has been discussed by Zhu et al. [164] who showed that high spatial frequency scatter noise lowers the CNR of scatter corrected data. Looking back to the histograms in Section 5.2.2 and 5.4.6 it can be seen that both collimation and scatter correction act to increase the spread of the material phase compared to the uncorrected case, which further supports this observation.

The input parameters of the proposed method are the LSF and CNR of the considered data-set. Thus any factors that influence these characteristics will influence the measurement uncertainty due to surface determination. A non-exhaustive list of factors that may influence the LSF and CNR include: X-ray source settings, detector settings, scattered radiation, beam hardening, X-ray focal spot drift, rotational axis run-out and other geometric misalignments, thermal expansion, vibration and reconstruction algorithm. The proposed method therefore considers the entire measurement workflow.

This work is concerned with the influence of scatter and beam hardening on dimensional measurements. It has been shown that because scatter and beam hardening influence the noise and contrast of CT data, they influence the measurement uncertainty due to surface determination. A number of authors have previously discussed the influence scatter and beam hardening may have on the uncertainty of dimensional measurements, but no one has previously quantified the influence. The results presented in this chapter are intuitive, in that factors that increase noise, decrease edge contrast and increase edge blurring will impact the number and distribution of surface points, which subsequently influences the uncertainty of the fitted geometric feature.

It would be useful to correlate a single image quality statistic with the measurement uncertainty due to surface determination. The CNR seems a good choice, but appears to be only half the story. From experimenting with the proposed method it seems other

important factors are the number of surface points used in the fit and the size of the residuals of the least-squares fit. Future work should look to derive an expression relating these fit properties and image quality statistics to the measurement uncertainty due to surface determination.

The obvious limitation of the proposed method is the 2D implementation. Naturally, this approach should next be extended to 3D. One way in which this could be done is by generating a spherical segment; this geometric feature consists of surface points with all possible 3D orientations. By estimating the position of each surface point and calculating its radial distance from the origin, the error of the surface position as a function of edge orientation could be evaluated. By incorporating the measurement PSF and noise characteristics, a similar Monte Carlo approach could be adopted to estimate coordinate uncertainty as a function of surface orientation. The coordinate uncertainties would then be propagated in a similar manner as presented here.

Chapter 8 Summary, Conclusions and Future Work

The aim of this work has been to develop a better understanding of how scatter and beam hardening influence surface determination and hence dimensional measurements, through the use of both measured and simulated data.

This thesis began by looking at systematic errors in geometric magnification. It was shown that after a basic system setup errors in the source-to-detector distance and source-to-object distance can lead to length measurement errors in the order of tens of microns. However, with a one-time voxel size correction these errors were reduced to several microns. This approach to correct systematic scale errors was evaluated such that the influence of scatter and beam hardening could be studied experimentally in Chapter 5.

In Chapter 5 the threshold sensitive dimensions of the multi cross-section workpiece were measured with and without scatter and beam hardening correction/minimisation. Scatter and beam hardening were shown to increase the measured size of external features and decrease the measured size of internal features. This effect was seen for both the ISO50 and local surface determination methods.

In Chapter 6 the systematic influence of scatter and beam hardening was verified via simulation, and explanations were given as to how these artefacts influence both the ISO50 and local surface determination methods.

Finally, in Chapter 7 a method for estimating the measurement uncertainty due to surface determination was developed. This uncertainty contributor was found to be very small, but sensitive to the contrast and noise of CT data.

The results presented in this work clearly show that scatter and beam hardening influence dimensional measurements. Chapter 6 showed that measurements in the absence of scatter and beam hardening were more accurate than those in the presence of scatter and beam hardening. This result was also seen in Chapter 5, but was overshadowed by experimental error.

Scatter and beam hardening do not influence dimensional measurements directly, they influence surface determination, which in turn influences dimensional measurements. Scatter and beam hardening cause inner and outer edges to differ, primarily in

contrast; this means that no single isovalue threshold can lead to a ‘correct’ surface position for both inner and outer features. When scatter and beam hardening are minimised, the difference between inner and outer edge profiles is also minimised; it is only under these conditions that an isovalue surface determination method should be used in CT metrology. It is recommended that prior to performing surface determination using the isovalue method, inner and outer edge profiles be compared; if the edge profiles are in reasonable agreement, then the isovalue method can be used. The results in Chapter 6 suggest that even in the absence of scatter and beam hardening the ISO50 value does not yield the most accurate measurements. It is therefore recommended that the isovalue be selected either using the iterative method proposed by Carmignato et al. [46], or by identifying the grey value at which inner and outer edges cross when plotted on the same axes, as described in Section 6.2.3.

Scatter and beam hardening not only influence edge contrast, but also edge shape, which in turn changes the turning point of the edge gradient. It is through this change in turning point that scatter and beam hardening influence measurements evaluated using the local surface determination method. Even though the local method nearly always leads to more accurate measurements than the ISO50 method, it is still sensitive to the influence of scatter and beam hardening. Based on this important observation it is recommended that in future work alternative approaches to edge detection be considered and assessed with respect to their robustness to artefacts. Another future research direction would be to parameterise the edges of CT data; it seems a simple third order polynomial approximation doesn’t fully describe the shape of edges in CT, nor does an exponential approximation. Further research on characterising the edges in CT data is expected to lead to the development of edge detectors that are better able to deal with the presence of artefacts.

This work has considered the influence of both scatter and beam hardening. In previous studies, nonlinear X-ray attenuation has been wholly attributed to beam hardening. Neglecting the contribution of scatter to this nonlinearity has been the major shortcoming of previous work. Scatter contributes an additional signal to the entire detector output, it should first be estimated, then subtracted. Alternatively, scatter should be minimised through the use of collimation or anti-scatter grids. Beam hardening concerns primary X-rays, and should only be corrected algorithmically after scatter has been dealt with. This is well documented in the industrial CT literature but has been overlooked by the CT metrology community; this may be in part due to the availability of ‘black box’ artefact correction algorithms made available by CT software

companies. It is therefore strongly recommended that commercial artefact correction software be avoided in CT metrology unless provisions have been made to reduce scatter. Failing to do so will result in an over-correction, or invalid correction of beam hardening, which may significantly influence dimensional measurements.

The influence of scatter and beam hardening on the uncertainty of surface determination was evaluated in Chapter 7. It was shown that the measurement uncertainty due to surface determination is very small for all the data considered in this work. However, this uncertainty contributor is expected to be larger for features that fill only a small portion of a CT image, and for features fitted to only a few surface points. The measurement uncertainty due to surface determination has been found to be closely related to the contrast to noise ratio of the data; factors such as the number of points used in the least-squares fit and the size of the fit residual also appear to be important and warrant further investigation. Although these findings are intuitive, in that noisy low contrast data will yield more uncertain surfaces than low noise high contrast data, this uncertainty contributor has not previously been evaluated and is an important contribution of this work. Future work should extend the two-dimensional implementation to three-dimensions, as discussed in Section 7.9.

The limitations of this work include the use of only one CT system, one type of geometric feature, one measurement strategy and a mono-material workpiece. The reason for holding the above constant was to minimise the number of variables in the study. Given the complexity of a CT system and the number of factors that can influence a measurement result it is particularly difficult to isolate any given factor. To further generalise the results presented here, the influence of scatter and beam hardening should be investigated for different types of threshold sensitive dimensions, such as the distance between two planes. Different types of materials should also be considered, such as plastics and multi-material objects. This work has only looked at the measurement of size; other work has suggested that scatter and beam hardening influence form measurements also [94]. This is to be expected as both scatter and beam hardening influence noise in CT data. In future work the influence of scatter and beam hardening on form measurement should be studied in some detail; previous work has shown that errors of form can be much larger than errors of size in CT metrology, this has been attributed to the influence of noise of CT data: size measurements result from fitting and averaging of many measurement points and are therefore less affected by noise than form measurements [131], [165].

In future work, the influence of scatter on dimensional measurements could be further studied through the use of anti-scatter grids; there seems to be little published work on the use of anti-scatter grids in industrial CT. Anti-scatter grids have the disadvantage of requiring longer exposure times or increased source current to compensate for an overall loss of X-ray flux reaching the detector: the former will increase scan time whilst the latter will increase the focal spot size; the improvement in image quality due to reduced scatter will need to be weighed against these two factors. Anti-scatter grids have the advantage of being a permanent fixture to a CT system, rather than requiring an additional scan as per the beam stop array method used here; although, the additional scan required for the beam stop array method could serve as the warm up scan required in CT metrology. Seeing as scatter signals are considered low spatial frequency signals, focal spot drift and thermal expansion aren't likely to have a significant impact of the scatter estimate.

The influence of beam hardening on dimensional measurements has been evaluated here using spectrum pre-filtration and the linearisation beam hardening correction method. It is unlikely the segmentation-based beam hardening corrections described in Section 2.4.1 will be of much value in CT metrology; this is because a poor initial segmentation of the data will only propagate through the iterative correction, which is likely to change material boundaries.

Throughout this work the filtered back-projection (FBP) reconstruction method has been used; in future work the use of iterative reconstruction (IR) methods should be considered. In the first instance, a simple comparison between dimensions evaluated from FBP and IR data should be made; the shape of edges and the noise of the IR data are likely to differ from the FBP data, if this is so, the difference is likely to influence surface determination and hence dimensional measurements. A subsequent study should investigate how including a polychromatic forward projector in the IR method influences dimensional measurements; any advantages or disadvantages of using IR methods in CT metrology should then be discussed.

Edge detection is a long-standing research topic in the field of image processing; as such, there are a large number of papers on the subject describing many different approaches to edge detection. Algorithms have been proposed specifically for medical CT applications [166], but the requirements for accurate and precise edge detection are much higher in metrology. It is therefore suggested that in future work the literature be surveyed and potential edge detection algorithms be identified and their performance for CT metrology characterised. Desirable properties are robustness to

artefacts, speed, precision and accuracy. Possible candidates include a locally adaptive histogram-based edge detector [167]; this approach is similar to the ISO50 method, but rather than defining a single global isovalue, the isovalue is evaluated for small non-overlapping regions. This method should be much more robust to the presence of artefacts than the ISO50 method. Additionally, a feature model-based approach could be considered [168]; the idea is to iteratively match a model of a feature to a set of intensity values, convergence yields a sub-pixel estimate of the model parameters. The two suggested options are at present two-dimensional implementations, but the extension to three-dimensions should be relatively straight forward.

Finally, future work should consider an entirely new workflow for CT metrology. The present workflow has arisen from CT being used to estimate an object's material distribution in a given plane for diagnostic purposes in the medical industry. For metrology, the interest lies in estimating the position of material boundaries, i.e. an object's surface. As such, a more appropriate workflow in CT metrology would to reconstruct an object's surface directly. Such a workflow would avoid surface determination entirely, which can be significantly influenced by the presence of artefacts, noise, and is also influenced by the pixel or voxel resolution of the data. By reconstructing only the surface of an object the number of unknowns in the reconstruction problem reduces significantly, and as such, becomes a task well suited for an iterative reconstruction method. Yin et al. [86] have presented preliminary results for directly reconstructing the surfaces of an object using an iterative reconstruction approach. They combined CT data with additional coordinate points measured with a CMM in order to reconstruct the best-fit surface. Using an iterative reconstruction algorithm in this manner not only allows for the physics of projection acquisition to be incorporated in the forward projection step, but also opens up the possibility for data fusion, which could lead to higher accuracy measurements with lower measurement uncertainties. Direct surface reconstruction has the potential to overcome many of the limitations of the present workflow in CT metrology and should therefore be considered as a future research direction.

List of References

[1] JCGM 200:2012 International vocabulary of metrology — Basic and general concepts and associated terms (VIM). 2012.

[2] D. Flack and J. Hannaford, Measurement good practice guide no. 80: Fundamental good practice in dimensional metrlology, National Physical Laboratory, 2005.

[3] C. J. Evans and J. B. Bryan, “Structured”, “Textured” or “Engineered” Surfaces, *CIRP Ann. - Manuf. Technol.*, vol. 48, no. 2, pp. 541–556, 1999.

[4] K. Harding, Industrial metrology: Engineering precision, *Nat. Photonics*, vol. 2, no. 11, pp. 667–669, 2008.

[5] F. P. León, Evaluation of honed cylinder bores, *CIRP Ann. - Manuf. Technol.*, vol. 51, no. 1, pp. 503–506, 2002.

[6] G. Nicoletto, G. Anzelotti, and R. Konečná, X-ray computed tomography vs. metallography for pore sizing and fatigue of cast Al-alloys, *Procedia Eng.*, vol. 2, no. 1, pp. 547–554, 2010.

[7] B. Bhushan, Biomimetics inspired surfaces for drag reduction and oleophobicity/philicity, *Beilstein J. Nanotechnol.*, vol. 2, pp. 66–84, 2011.

[8] R. Leach, *Fundamental principles of engineering nanometrology*. William Andrew, 2014.

[9] JCGM 100:2008 GUM 1995 with minor corrections, Evaluation of measurement data: Guide to the expression of uncertainty in measurement. 2008.

[10] D. Flack, Measurement good practice guide no. 130: Co-ordinate measuring machine task-specific measurement uncertainties, National Physical Laboratory, 2013.

[11] E. J. C. Bos, Aspects of tactile probing on the micro scale, *Precis. Eng.*, vol. 35, no. 2, pp. 228–240, 2011.

[12] BS EN ISO 25178-601:2010 Geometrical product specifications (GPS) — Surface texture: Areal - Nominal characteristics of non- contact (stylus) instruments. International Organization for Standardization, 2010.

[13] R. Leach, Measurement good practice guide no. 37: The measurement of surface texture using stylus instruments, National Physical Laboratory, 2001.

[14] BS 1134:2010 Assessment of surface texture – Guidance and general information. International Organization for Standardization, 2010.

[15] W. D, J, *Handbook of surface metrology*. IOP Publishing, 1994.

[16] BS EN ISO 10360-4:2001Geometric product specifications (GPS) — Acceptance and reverification tests for coordinate measuring machines (CMM)

— Part 4: CMMs used in scanning measuring mode. International Organization for Standardization, 2001.

[17] M. M. P. A. Vermeulen, P. C. J. N. Rosielle, and P. H. J. Schellekens, Design of a high-precision 3D-coordinate measuring machine, *CIRP Ann. - Manuf. Technol.*, vol. 47, no. 1, pp. 447–450, 1998.

[18] R. K. Leach, J. Claverley, C. Giusca, C. W. Jones, L. Nimishakavi, W. Sun, M. Tedaldi, and A. Yacoot, Advances in engineering nanometrology at the National Physical Laboratory, *Meas. Sci. Technol.*, vol. 23, no. 7, p. 074002, 2012.

[19] J. Petzing, J. Coupland, and R. Leach, Measurement good practice guide no. 116: The measurement of rough surface topography using coherence scanning interferometry, National Physical Laboratory, 2010.

[20] R. Danzl, F. Helmli, and S. Scherer, Focus variation - A robust technology for high resolution optical 3D surface metrology, *J. Mech. Eng.*, vol. 57, no. 3, pp. 245–256, 2011.

[21] P. J. Boltryk, M. Hill, and J. W. McBride, Comparing laser and polychromatic confocal optical displacement sensors for the 3D measurement of cylindrical artefacts containing microscopic grooved structures, *Wear*, vol. 266, no. 5–6, pp. 498–501, 2009.

[22] P. J. Boltryk, M. Hill, J. W. McBride, and A. Nascè, A comparison of precision optical displacement sensors for the 3D measurement of complex surface profiles, *Sensors Actuators, A Phys.*, vol. 142, no. 1, pp. 2–11, 2008.

[23] R. J. Valkenburg and a. M. McIvor, Accurate 3D measurement using a structured light system, *Image Vis. Comput.*, vol. 16, no. 2, pp. 99–110, 1998.

[24] H. Schwenke, U. Neuschaefer-Rube, T. Pfeifer, and H. Kunzmann, Optical methods for dimensional metrology in production engineering, *CIRP Ann. - Manuf. Technol.*, vol. 51, no. 2, pp. 685–699, 2002.

[25] L. Blunt, X. Jiang, and P. J. Scott, Advances in micro and nano-scale surface metrology, *Key Eng. Mater.*, vol. 295–296, pp. 431–436, 2005.

[26] L. De Chiffre, S. Carmignato, J.-P. Kruth, R. Schmitt, and a. Weckenmann, Industrial applications of computed tomography, *CIRP Ann. - Manuf. Technol.*, vol. 63, no. 2, pp. 655–677, 2014.

[27] R. H. Bossi and G. E. Georgeson, X-ray computed tomographic inspection of castings, in *Review of Progress in Quantitative Nondestructive Evaluation*, vol. 10B, 1991, pp. 1783–1790.

[28] N. Schuhmann and H. Okruch, Industrial application of computerized tomography, in *Computerized tomography for Industrial applications and image processing in radiology*, 1999.

[29] S. Van Bael, G. Kerckhofs, M. Moesen, G. Pyka, J. Schrooten, and J. P. Kruth, Micro-CT-based improvement of geometrical and mechanical controllability of

selective laser melted Ti6Al4V porous structures, *Mater. Sci. Eng. A*, vol. 528, no. 24, pp. 7423–7431, 2011.

[30] G. N. Hounsfield, Method and apparatus for measuring x- or gamma-radiation absorption or transmission at plural angles and analyzing the data, Patent No.: 3,778,614 A, 1973.

[31] G. N. Hounsfield, Computerized transverse axial scanning (tomography): I. Description of system, *Br. J. Radiol.*, vol. 46, no. 552, pp. 1016–1022, 1973.

[32] A. M. Cormack, Representation of a function by its line integrals, with some radiological applications, *J. Appl. Phys.*, vol. 34, no. 9, pp. 2722–2727, 1963.

[33] A. M. Cormack, Representation of a function by its line integrals, with some radiological applications. II, *J. Appl. Phys.*, vol. 35, no. 10, pp. 2908–2913, 1964.

[34] The nobel prize in physiology or medicine 1979, *Nobelprize.org*, 2015. [Online]. Available: http://www.nobelprize.org/nobel_prizes/medicine/laureates/1979/.

[35] A. E. Scott, I. Sinclair, S. M. Spearing, M. N. Mavrogordato, and W. Hepples, Influence of voids on damage mechanisms in carbon/epoxy composites determined via high resolution computed tomography, *Compos. Sci. Technol.*, vol. 90, pp. 147–153, 2014.

[36] C. Baldock, S. W. Hughes, D. K. Whittaker, J. Taylor, R. Davis, A. J. Spencer, K. Tonge, and A. Sofat, 3-D Reconstruction of an ancient Egyptian mummy using x-ray computer tomography, *J. R. Soc. Med.*, vol. 87, no. December, pp. 806–808, 1994.

[37] H. Saewert, D. Fiedler, M. Bartscher, and F. Wäldele, Obtaining dimensional information by industrial CT scanning – present and prospective process chain, in *International Symposium on Computed Tomography and Image Processing for Industrial Radiology*, 2003, pp. 163–172.

[38] J. P. Kruth, M. Bartscher, S. Carmignato, R. Schmitt, L. De Chiffre, and a. Weckenmann, Computed tomography for dimensional metrology, *CIRP Ann. - Manuf. Technol.*, vol. 60, no. 2, pp. 821–842, 2011.

[39] P. Müller, J. Hiller, Y. Dai, J. L. Andreasen, H. N. Hansen, and L. De Chiffre, Estimation of measurement uncertainties in x-ray computed tomography metrology using the substitution method, *CIRP J. Manuf. Sci. Technol.*, vol. 7, no. 3, pp. 222–232, 2014.

[40] J. Hiller and L. M. Reindl, A computer simulation platform for the estimation of measurement uncertainties in dimensional X-ray computed tomography, *Meas. J. Int. Meas. Confed.*, vol. 45, no. 8, pp. 2166–2182, 2012.

[41] M. Bartscher, M. Neukamm, U. Hilpert, U. Neuschaefer-Rube, F. Härtig, K. Kniel, K. Ehrig, A. Staude, and J. Goebbels, Achieving traceability of industrial computed tomography, *Key Eng. Mater.*, vol. 437, pp. 79–83, 2010.

[42] P. Müller, Coordinate metrology by traceable computed tomography, Technical University of Denmark, 2012.

[43] M. Bartscher, O. Sato, F. Härtig, and U. Neuschaefer-Rube, Current state of standardization in the field of dimensional computed tomography, *Meas. Sci. Technol.*, vol. 25, no. 6, p. 064013, 2014.

[44] VDI/VDE 2630 Part 1.2:2010 Computed tomography in dimensional measurement - Influencing variables on measurement results and recommendations for computed tomography dimensional measurements. Institute for Innovation and Technology.

[45] F. Welkenhuyzen, K. Kiekens, M. Pierlet, and W. Dewulf, Industrial computer tomography for dimensional metrology: Overview of influence factors and improvement strategies, *Opt. Meas. Tech. Struct. Syst.*, vol. 100, no. 9, pp. 401–410, 2010.

[46] S. Carmignato, D. Dreossi, L. Mancini, F. Marinello, G. Tromba, and E. Savio, Testing of x-ray microtomography systems using a traceable geometrical standard, *Meas. Sci. Technol.*, vol. 20, no. 8, p. 084021, 2009.

[47] G. T. Herman, Correction for beam hardening in computed tomography, *Phys. Med. Biol.*, vol. 24, no. 1, pp. 81–106, 1979.

[48] R. A. Brooks and G. Di Chiro, Beam hardening in x-ray reconstructive tomography, *Phys. Med. Biol.*, vol. 21, no. 3, pp. 390–398, 1976.

[49] O. Nalcioglu and R. Y. Lou, Post-reconstruction method for beam hardening in computerised tomography, *Phys. Med. Biol.*, vol. 24, no. 2, pp. 330–340, 1979.

[50] P. M. Joseph and R. D. Spital, The effects of scatter in x-ray computed tomography, *Med. Phys.*, vol. 9, no. 4, pp. 464–472, 1982.

[51] T. Nishihata, Y. Ohtake, H. Suzuki, and M. Moriguchi, A non-iterative data-driven beam hardening correction for single-material objects, in *Conference on Industrial Computed Tomography (ICT)*, 2012, pp. 135–142.

[52] L. Brabant, E. Pauwels, M. Dierick, D. Van Loo, M. a. Boone, and L. Van Hoorebeke, A novel beam hardening correction method requiring no prior knowledge, incorporated in an iterative reconstruction algorithm, *NDT E Int.*, vol. 51, pp. 68–73, 2012.

[53] Q. Yang, M. Elter, I. Schasiepen, N. Maass, and J. Hornegger, Fast iterative beam hardening correction based on frequency splitting in computed tomography, *SPIE Med. Imaging*, vol. 8668, p. 86682J, 2013.

[54] W. Dewulf, Y. Tan, and K. Kiekens, Sense and non-sense of beam hardening correction in CT metrology, *CIRP Ann. - Manuf. Technol.*, vol. 61, no. 1, pp. 495–498, 2012.

[55] Y. Tan, K. Kiekens, F. Welkenhuyzen, J. Angel, L. De Chiffre, J.-P. Kruth, and W. Dewulf, Simulation-aided investigation of beam hardening induced errors in CT dimensional metrology, *Meas. Sci. Technol.*, vol. 25, no. 6, p. 064014, 2014.

[56] X. Zhang, L. Li, F. Zhang, X. Xi, L. Deng, and B. Yan, Improving the accuracy of CT dimensional metrology by a novel beam hardening correction method, *Meas. Sci. Technol.*, vol. 26, p. 015007, 2015.

[57] K. Schörner, Development of methods for scatter artifact correction in industrial x-ray cone-beam computed tomography, 2012.

[58] K. Schörner, M. Goldammer, and J. Stephan, Comparison between beam-stop and beam-hole array scatter correction techniques for industrial X-ray cone-beam CT, *Nucl. Instruments Methods Phys. Res. Sect. B Beam Interact. with Mater. Atoms*, vol. 269, no. 3, pp. 292–299, 2011.

[59] J. Hsieh, *Computed tomography: principles, design, artifacts, and recent advance*, 2nd ed. SPIE Press, 2009.

[60] J. T. Bushberg, *The essential physics of medical imaging*, 2nd ed. Lippincott Williams & Wilkins, 2002.

[61] R. D. Evans, *The atomic nucleus*. McGraw-Hill, 1955.

[62] R. K. Leach, W. Sun, and S. B. Brown, An overview of industrial X-ray computed tomography, 2012.

[63] C. G. Camara, J. V. Escobar, J. R. Hird, and S. J. Putterman, Correlation between nanosecond X-ray flashes and stick–slip friction in peeling tape, *Nature*, vol. 455, no. 7216, pp. 1089–1092, 2008.

[64] G. G. Poludniowski, Calculation of x-ray spectra emerging from an x-ray tube. Part II. X-ray production and filtration in x-ray targets, *Med. Phys.*, vol. 34, no. 6, pp. 2175–2186, 2007.

[65] J. Lilley, *Nuclear physics: Principles and applications*. John Wiley & Sons, 2001.

[66] B. A. M. Hansson, O. Hemberg, H. M. Hertz, A. Holmberg, and J. Kronstedt, A nanofocus X-ray source, in *Conference on Industrial Computed Tomography (ICT)*, 2014, pp. 343–344.

[67] R. S. Peugeot, Microfocus X-ray system, Patent No.: 4,688,241, 1987.

[68] Technical details microfocus x-ray tubes, 2015. [Online]. Available: http://www.x-ray-worx.com.

[69] G. C. Andrews, Drive assembly for an x-ray tube having a rotating anode, Patent No.: US 6,480,517 B1, 2002.

[70] Metal jet X-ray tube technology, 2015. [Online]. Available: http://www.excillum.com.

[71] J. P. Steffen and T. Fröba, Reducing the focal spot shift of microfocus x-ray tubes to increase the accuracy of CT-based dimensional measurement, in *International Symposium on Digital Industrial Radiology and Computed Tomography*, 2011.

[72] A. Tkachuk, F. Duewer, H. Cui, M. Feser, S. Wang, and W. Yun, X-ray computed tomography in Zernike phase contrast mode at 8 keV with 50-nm resolution using Cu rotating anode X-ray source, *Zeitschrift fur Krist.*, vol. 222, no. 11, pp. 650–655, 2007.

[73] J. Hiller, M. Maisl, and L. M. Reindl, Physical characterization and performance evaluation of an x-ray micro-computed tomography system for dimensional metrology applications, *Meas. Sci. Technol.*, vol. 23, no. 8, p. 085404, 2012.

[74] S. Reisinger, M. Schmitt, and V. Voland, Geometric adjustment methods to improve reconstruction quality on rotational cone-beam systems, *Conf. Ind. Comput. Tomogr. 2012 Proc.*, pp. 261–270, 2012.

[75] F. Vogeler, W. Verheecke, A. Voet, and J. Kruth, Positional stability of 2D X-ray images for computer tomography, in *International Symposium on Digital Industrial Radiology and Computed Tomography*, 2011.

[76] J. A. Seibert, Flat-panel detectors: How much better are they?, *Pediatr. Radiol.*, vol. 36, no. SUPPL. 14, pp. 173–181, 2006.

[77] V. V. Nagarkar, T. K. Gupta, S. R. Miller, Y. Klugerman, M. R. Squillante, and G. Entine, Structured CsI(Tl) scintillators for x-ray imaging applications, *IEEE Trans. Nucl. Sci.*, vol. 45, no. 3, 1998.

[78] D. Weiß, R. Lonardoni, A. Deffner, and C. Kuhn, Geometric image distortion in flat-panel X-ray detectors and its influence on the accuracy of CT-based dimensional measurements, *Conf. Ind. Comput. Tomogr.*, pp. 175–181, 2012.

[79] F. Welkenhuyzen, B. Boeckmans, Y. Tan, K. Kiekens, and W. Dewulf, Investigation of the kinematic system of a 450 kV CT scanner and its influence on dimensional CT metrology applications, *5th Conf. Ind. Comput. Tomogr.*, pp. 217–225, 2014.

[80] J. Hsieh, B. Nett, Z. Yu, K. Sauer, J.-B. Thibault, and C. Bouman, Recent advances in CT image reconstruction, *Curr. Radiol. Rep.*, vol. 1, pp. 39–51, 2013.

[81] A. C. Kak and M. Slaney, *Principles of computerized tomographic imaging*. IEEE Press, 1988.

[82] L. a. Feldkamp, L. C. Davis, and J. W. Kress, Practical cone-beam algorithm, *J. Opt. Soc. Am. A*, vol. 1, no. 6, p. 612, 1984.

[83] J. Hiller, S. Kasperl, T. Schön, S. Schröpfer, and D. Weiss, Comparison of probing error in dimensional measurement by means of 3D computed tomography with circular and helical sampling, *2nd Int. Symp. NDT Aerosp. 2010*, pp. 1–7, 2010.

[84] J. Muders, J. Hesser, A. Lachner, and C. Reinhart, Accuracy evaluation and exploration of measurement uncertainty for exact helical cone beam reconstruction using katsevich filtered backprojection in comparison to circular Feldkamp reconstruction with respect to industrial CT metrology, *Int. Symp. Digit. Ind. Radiol. Comput. Tomogr.*, pp. 1–8, 2011.

[85] M. Beister, D. Kolditz, and W. a Kalender, Iterative reconstruction methods in x-ray CT, *Phys. Medica*, vol. 28, no. 2, pp. 94–108, 2012.

[86] Z. Yin, K. Khare, and B. De Man, Parametric boundary reconstruction algorithm for industrial CT metrology application, *J. Xray. Sci. Technol.*, vol. 17, no. 2, pp. 115–133, 2009.

[87] Y. Zhang, X. Mou, and S. Tang, Beam hardening correction for fan-beam CT imaging with multiple materials, *IEEE Nucl. Sci. Symp. Conf. Rec.*, pp. 3566–3570, 2010.

[88] R. L. McKinley, M. P. Toraai, E. Samei, and M. L. Bradshaw, Initial study of quasi-monochromatic x-ray beam performance for x-ray computed mammotomography, *IEEE Trans. Nucl. Sci.*, vol. 52, no. 5 I, pp. 1243–1250, 2005.

[89] G. Zentai, Signal-to-noise and contrast ratio enhancements by quasi-monochromatic imaging, *IEEE Trans. Instrum. Meas.*, vol. 60, no. 3, pp. 908–915, 2011.

[90] M. Krumm, S. Kasperl, and M. Franz, Reducing non-linear artifacts of multi-material objects in industrial 3D computed tomography, *NDT E Int.*, vol. 41, no. 4, pp. 242–251, 2008.

[91] G. Van Gompel, K. Van Slambrouck, M. Defrise, K. J. Batenburg, J. de Mey, J. Sijbers, and J. Nuyts, Iterative correction of beam hardening artifacts in CT, *Medical Physics*, vol. 38, no. S1. p. S36, 2011.

[92] G. Davis, N. Jain, and J. Elliott, A modelling approach to beam hardening correction, in *Developments in X-ray Tomography VI*, 2008.

[93] I. A. Elbakri and J. A. Fessler, Statistical x-ray-computed tomography image reconstruction with beam-hardening correction, *Proc. SPIE 4322*, vol. 21, no. 1, pp. 1–12, 2001.

[94] M. Bartscher, U. Hilpert, J. Goebbels, and G. Weidemann, Enhancement and proof of accuracy of industrial computed tomography (CT) measurements, *CIRP Ann. - Manuf. Technol.*, vol. 56, no. 1, pp. 495–498, 2007.

[95] P. Wenig and S. Kasperl, Examination of the measurement uncertainty on dimensional measurements by X-ray computed tomography, *Eur. Conf. Non-Destructive Test.*, 2006.

[96] A. Suppes and E. Neuser, Metrology with µCT: precision challenge, in *Developments in X-Ray Tomography Vi*, 2008, vol. 7078G.

[97] P. Hammersberg and M. Mångård, Correction for beam hardening artefacts in computerised tomography, *J. Xray. Sci. Technol.*, vol. 8, no. 1, pp. 75–93, 1998.

[98] J. A. Seibert, O. Nalcioglu, and W. W. Roeck, Characterization of the veiling glare PSF in x-ray image intensified fluoroscopy, *Med. Phys.*, vol. 11, no. 2, pp. 172–179, 1984.

[99] J. A. Seibert, O. Nalcioglu, and W. Roeck, Removal of image intensifier veiling glare by mathematical deconvolution techniques, *Med. Phys.*, vol. 12, no. 3, pp. 281–288, 1985.

[100] S. Z. Shen, A. K. Bloomquist, G. E. Mawdsley, M. J. Yaffe, and I. Elbakri, Effect of scatter and an antiscatter grid on the performance of a slot-scanning digital mammography system, *Med. Phys.*, vol. 33, no. 4, pp. 1108–1115, 2006.

[101] Y. Kyriakou and W. Kalender, Efficiency of antiscatter grids for flat-detector CT, *Phys. Med. Biol.*, vol. 52, no. 20, pp. 6275–6293, 2007.

[102] A. Peterzol, J. M. Létang, and D. Babot, A beam stop based correction procedure for high spatial frequency scatter in industrial cone-beam X-ray CT, *Nucl. Instruments Methods Phys. Res. Sect. B Beam Interact. with Mater. Atoms*, vol. 266, no. 18, pp. 4042–4054, 2008.

[103] J. S. Maltz, B. Gangadharan, M. Vidal, A. Paidi, S. Bose, B. A. Faddegon, M. Aubin, O. Morin, J. Pouliot, Z. Zheng, M. M. Svatos, and A. R. Bani-Hashemi, Focused beam-stop array for the measurement of scatter in megavoltage portal and cone beam CT imaging, *Med. Phys.*, vol. 35, no. 6, pp. 2452–2462, 2008.

[104] R. Thierry, A. Miceli, and J. Hofmann, Hybrid simulation of scattering distribution in cone beam CT, in *International Symposium on Digital Industrial Radiology and Computed Tomography*, 2007.

[105] P. Schuetz, A. Miceli, I. Jerjen, A. Flisch, J. Hofmann, R. Broennimann, and U. Sennhauser, Reducing environmental scattering in industrial computed tomography by system redesign, *NDT E Int.*, vol. 58, pp. 36–42, 2013.

[106] Y. Kyriakou, T. Riedel, and W. a Kalender, Combining deterministic and Monte Carlo calculations for fast estimation of scatter intensities in CT, *Phys. Med. Biol.*, vol. 51, no. 18, pp. 4567–4586, 2006.

[107] H. Li, R. Mohan, and X. R. Zhu, Scatter kernel estimation with an edge-spread function method for cone-beam computed tomography imaging., *Phys. Med. Biol.*, vol. 53, no. 23, pp. 6729–6748, 2008.

[108] M. Sun and J. M. Star-Lack, Improved scatter correction using adaptive scatter kernel superposition, *Phys. Med. Biol.*, vol. 55, no. 22, pp. 6695–6720, 2010.

[109] A. Bub, S. Gondrom, M. Maisl, N. Uhlmann, and W. Arnold, Image blur in a flat-panel detector due to Compton scattering at its internal mountings, *Meas. Sci. Technol.*, vol. 18, no. 5, pp. 1270–1277, 2007.

[110] M. Baer, M. Hammer, M. Knaup, and I. Schmidt, Scatter correction methods in dimensional CT, *Ndt.Net*, vol. 14, no. 1, pp. 41–6, 2012.

[111] H. K. Tuy, An inversion formula for cone-beam reconstruction, *SIAM Journal on Applied Mathematics*, vol. 43, no. 3. pp. 546–552, 1983.

[112] QRM, Mirco-CT multi disk phantom. [Online]. Available: http://www.qrm.de/content/products/microct/microct_multidisk.htm. [Accessed: 09-Apr-2015].

[113] Y. Sun, Y. Hou, F. Zhao, and J. Hu, A calibration method for misaligned scanner geometry in cone-beam computed tomography, *NDT E Int.*, vol. 39, no. 6, pp. 499–513, 2006.

[114] K. Yang, A. L. C. Kwan, D. F. Miller, and J. M. Boone, A geometric calibration method for cone beam CT systems, *Med. Phys.*, vol. 33, no. 6, pp. 1695–1706, 2006.

[115] Y. Sun, Y. Hou, and J. Hu, Reduction of artifacts induced by misaligned geometry in cone-beam CT, *IEEE Trans. Biomed. Eng.*, vol. 54, no. 8, pp. 1461–1471, 2007.

[116] J. Kumar, A. Attridge, P. K. C. Wood, and M. a. Williams, Analysis of the effect of cone-beam geometry and test object configuration on the measurement accuracy of a computed tomography scanner used for dimensional measurement, *Meas. Sci. Technol.*, vol. 035105, 2011.

[117] M. Yang, X.-L. Jin, and X.-L. Li, A new method to determine the projected coordinate origin of a cone-beam CT system using elliptical projection, *Chinese Phys. C*, vol. 34, no. 10, pp. 1665–1670, 2010.

[118] A. Fabijańska, A survey of subpixel edge detection methods for images of heat-emitting metal specimens, *Int. J. Appl. Math. Comput. Sci.*, vol. 22, no. 3, pp. 695–710, 2012.

[119] C. Reinhart, Industrial computer tomography - a universal inspection tool, in *17th World Conference on Nondestructive Testing*, 2008, pp. 25–28.

[120] P. Rockett, The accuracy of sub-pixel localisation in the Canny edge detector, in *BMVC*, 1999, pp. 392–401.

[121] J. F. Canny, Finding edges and lines in images, Massachusetts Inst of Tech, 1983.

[122] N. Otsu, A threshold selection method from gray-level histograms, *IEEE Trans. Syst. Man. Cybern.*, vol. 9, no. 1, pp. 62–66, 1979.

[123] W. E. Lorensen and H. E. Cline, Marching cubes: A high resolution 3D surface construction algorithm, *ACM SIGGRAPH Comput. Graph.*, vol. 21, no. 4, pp. 163–169, 1987.

[124] M. Nixon and A. Aguado, *Feature extraction & image processing for computer vision*. Amsterdam ; London : Elsevier/Academic Press., 2012.

[125] J. Kroll, I. Effenberger, and A. Verl, Adaptive preprocessing and segmentation for a region-based surface extraction method, in *Conference on Industrial Computed Tomography (ICT)*, 2012, pp. 289–295.

[126] C. Heinzl, R. Klingesberger, J. Kastner, and E. Gröller, Robust surface detection for variance comparison and dimensional measurement, *Eurographics/ IEEE-VGTC Symp. Vis.*, 2006.

[127] M. Haitham Shammaa, Y. Ohtake, and H. Suzuki, Segmentation of multi-material CT data of mechanical parts for extracting boundary surfaces, *CAD Comput. Aided Des.*, vol. 42, no. 2, pp. 118–128, 2010.

[128] J. A. Yagüe-Fabra, S. Ontiveros, R. Jiménez, S. Chitchian, G. Tosello, and S. Carmignato, A 3D edge detection technique for surface extraction in computed tomography for dimensional metrology applications, *CIRP Ann. - Manuf. Technol.*, vol. 62, no. 1, pp. 531–534, 2013.

[129] S. Carmignato and A. Pierobon, Preliminary results of the ' CT Audit ' project : First international intercomparison of computed tomography systems for dimensional metrology, *Int. Symp. Digit. Ind. Radiol. Comput. Tomogr. - Mo.2.1*, pp. 1–8, 2011.

[130] G. Schick, Metrology CT technology and its applications in the precision engineering industry, in *Fourth International Conference on Experimental Mechanics*, 2010, vol. 7522.

[131] F. Léonard, S. B. Brown, P. J. Withers, P. M. Mummery, and M. B. McCarthy, A new method of performance verification for x-ray computed tomography measurements, *Meas. Sci. Technol.*, vol. 25, no. 6, p. 065401, 2014.

[132] A. Amirkhanov, C. Heinzl, M. Reiter, and E. Gröller, Visual optimality and stability analysis of 3DCT scan positions, *IEEE Trans. Vis. Comput. Graph.*, vol. 16, no. 6, pp. 1477–1486, 2010.

[133] V. C. Nardelli, F. a Arenhart, G. D. Donatelli, M. C. Porath, C. Niggemann, and R. Schmitt, Feature-based analysis for quality assessment of x-ray computed tomography measurements, *Meas. Sci. Technol.*, vol. 23, no. 10, p. 105006, 2012.

[134] R. Schmitt and C. Niggemann, Method for efficient identification of similar work pieces for X-ray computed tomography, in *International Symposium on Digital Industrial Radiology and Computed Tomography*, 2011, pp. 1–9.

[135] VDI/VDE 2630 Part 1.3:2011 Computed tomography in dimensional measurement - Guideline for the application of DIN EN ISO 10360 for coordinate measuring machines with CT sensors. Institute for Innovation and Technology, 2011.

[136] M. Bartscher, M. Neukamm, M. Koch, U. Neuschaefer-Rube, A. Staude, J. Goebbels, K. Ehrig, C. Kuhn, A. Deffner, and A. Knoch, Performance assessment of geometry measurements with micro-CT using a dismountable work-piece-near reference standard, in *10th European Conference on Non-Destructive Testing*, 2010.

[137] S. Kasperl, Qualitätsverbesserungen durch referenzfreie Artefaktreduzierung und Oberflächennormierung in der industriellen 3D-Computertomographie, University of Erlangen-Nuremberg, 2005.

[138] U. Hilpert, M. Bartscher, and M. Neugebauer, Simulation-aided computed tomography (CT) for dimensional measurements, *Int. Symp. Digit. Ind. Radiol. Comput. Tomogr.*, pp. 1–15, 2007.

[139] C. Heinzl, J. Kastner, B. Georgi, and H. Lettenbauer, Comparison of surface detection methods to evaluate cone beam computed tomography data for three dimensional metrology, *Int. Symp. Digit. Ind. Radiol. Comput. Tomogr.*, 2007.

[140] U. Neuschaefer-rube, M. Bartscher, M. Neukamm, F. Härtig, and P. T. B. P. Bundesanstalt, Dimensional measurements with micro-CT - test procedures and applications, in *Microparts Interest Group Workshop*, 2009.

[141] BS EN ISO 10360-1:2001 Geometrical product specifications (GPS) - Acceptance and reverification tests for coordinate measuring machines (CMM) - Part 1: vocabulary. International Organization for Standardization, 2001.

[142] BS EN ISO 15530-3:2011 Geometrical product specifications (GPS) — Coordinate measuring machines (CMM): Technique for determining the uncertainty of measurement — Part 3: Use of calibrated workpieces or standards. International Organization for Standardization, 2011.

[143] BS EN ISO 14253-2:2011 Geometrical product specifications (GPS) – Inspection by measurement of workpieces and measuring equipment – Part 2: Guidance for the estimation of uncertainty in GPS measurement, in calibration of measuring equipment and in product. International Organization for Standardization, 2011.

[144] BS EN ISO 10360-5:2010 Geometrical product specifications (GPS) — Acceptance and reverification tests for coordinate measuring machines (CMM) — Part 5: CMMs using single and multiple stylus contacting probing systems. International Organization for Standardization, 2010.

[145] D. Flack, Measurement good practice guide no. 42: CMM verification, National Physical Laboratory, 2011.

[146] J. Angel, L. De Chiffre, E. Larsen, J. Rasmussen, and R. Sobiecki, Inter laboratory comparison on industrial computed tomography, 2013.

[147] M3003 2012 The expression of uncertainty and confidence in measurement. United Kingdom Acreditation Service, 2012.

[148] A. Weckenmann and P. Krämer, Assessment of measurement uncertainty caused in the preparation of measurements using computed tomography, in *XIX IMEKO World Congress: Fundamental and Applied Metrology*, 2009, pp. 1888–1892.

[149] J. Angel and L. De Chiffre, Comparison on computed tomography using industrial items, *CIRP Ann. - Manuf. Technol.*, vol. 63, no. 1, pp. 473–476, 2014.

[150] J. G. Salsbury, Pixel size calibration of video probe measuring machines. [Online]. Available: http://www.aspe.net/publications/annual_1999/papers/cmm/salsbury.pdf.

[151] D. Lazos and J. F. Williamson, Impact of flat panel-imager veiling glare on scatter-estimation accuracy and image quality of a commercial on-board cone-beam CT imaging system, *Med. Phys.*, vol. 39, no. 9, p. 5639, 2012.

[152] Fraunhofer, ScorpiusXLab, 2015. [Online]. Available: http://www.iis.fraunhofer.de/en/ff/zfp/leist/algorithmen-und-software/scorpiusxlab.html.

[153] BAM, ARTist - analytical RT inspection simulation tool, 2015. [Online]. Available: http://www.artist.bam.de/en/index.htm.

[154] Geant4: A toolkit for the simulation of the passage of particles through matter, 2015. [Online]. Available: http://geant4.cern.ch.

[155] P. Duvauchelle, N. Freud, V. Kaftandjian, and D. Babot, Computer code to simulate x-ray imaging techniques, *Nucl. Instruments Methods Phys. Res. Sect. B Beam Interact. with Mater. Atoms*, vol. 170, no. 1, pp. 245–258, 2000.

[156] E. Lindgren and H. Wirdelius, X-ray modeling of realistic synthetic radiographs of thin titanium welds, *NDT E Int.*, vol. 51, pp. 111–119, 2012.

[157] P. Hammersberg, M. Stenström, H. Hedtjärn, and M. Mångård, Absolute energy spectra for an industrial micro focal X-ray source under working conditions measured with a Comptonscattering spectrometer: full spectra data, *Linköping Electron. Artic. Mech. Eng.*, vol. 1, no. 1, pp. 1–13, 1998.

[158] E. Y. Sidky, L. Yu, X. Pan, Y. Zou, and M. Vannier, A robust method of x-ray source spectrum estimation from transmission measurements: Demonstrated on computer simulated, scatter-free transmission data, *J. Appl. Phys.*, vol. 97, no. 12, 2005.

[159] XCOM: Photon cross sections database, 2015. [Online]. Available: http://www.nist.gov/pml/data/xcom/.

[160] L. Zhang, G. Zhang, Z. Chen, Y. Xing, J. Cheng, and Y. Xiao, X-ray spectrum estimation from transmission measurements using the expectation maximization method, *2007 IEEE Nucl. Sci. Symp. Conf. Rec.*, no. 1, pp. 3089–3093, 2007.

[161] ASTM E 1695-95 Standard test method for measurement of computed tomography (CT) system performance. ASTM International, 1995.

[162] E. P. Lyvers and O. R. Mitchell, Precision edge contrast and orientation estimation, *IEEE Trans. Pattern Anal. Mach. Intell.*, vol. 10, no. 6, pp. 927–937, 1988.

[163] P. Mikulastik and R. H, Error analysis of subpixel edge localisation, *Technology*, pp. 531–542, 2006.

[164] L. Zhu, J. Wang, and L. Xing, Noise suppression in scatter correction for cone-beam CT, *Med. Phys.*, vol. 36, no. 3, pp. 741–752, 2009.

[165] S. Carmignato, Accuracy of industrial computed tomography measurements: Experimental results from an international comparison, *CIRP Ann. - Manuf. Technol.*, vol. 61, no. 1, pp. 491–494, 2012.

[166] Y. Cao, B. Wang, H. Xiao, H. Jiang, Z. Zhu, and Q. Yin, An efficient sub-pixel edge extraction method for CT brain images, *Proc. - 2009 Int. Conf. Comput. Intell. Softw. Eng. CiSE 2009*, no. 60671050, pp. 3–6, 2009.

[167] M. Khallil and A. Aggoun, Edge detection using adaptive local histogram analysis, *2006 IEEE Int. Conf. Acoust. Speech Signal Process. Proc.*, vol. 2, 2006.

[168] R. Deriche, R. Deriche, T. Blaszka, and T. Blaszka, Recovering and characterizing image features using an efficient model based approach, in *Proceedings of the Conference on Computer Vision and Pattern Recognition, New York, USA*, 1993, pp. 530–535.